HAL
open science

New concepts for the development of polaritonic emitters in the mid-IR and THz range

Paul Goulain

To cite this version:

Paul Goulain. New concepts for the development of polaritonic emitters in the mid-IR and THz range. Quantum Physics [quant-ph]. Université Paris-Saclay, 2022. English. NNT : 2022UPAST056 . tel-03691623

HAL Id: tel-03691623

https://theses.hal.science/tel-03691623v1

Submitted on 9 Jun 2022

HAL is a multi-disciplinary open access archive for the deposit and dissemination of scientific research documents, whether they are published or not. The documents may come from teaching and research institutions in France or abroad, or from public or private research centers.

L'archive ouverte pluridisciplinaire **HAL**, est destinée au dépôt et à la diffusion de documents scientifiques de niveau recherche, publiés ou non, émanant des établissements d'enseignement et de recherche français ou étrangers, des laboratoires publics ou privés.

New concepts for the development of polaritonic emitters in the mid-IR and THz range

Nouveaux concepts d'émetteurs polaritoniques dans les gammes spectrales du moyen-infrarouge et THz

Thèse de doctorat de l'université Paris-Saclay

École doctorale n° 575, Electrical, optical, bio-physics and engineering (EOBE)
Spécialité de doctorat : electronique et optoélectronique, nano- et microtechnologies
Graduate School : Sciences de l'ingénierie et des systèmes
Référent : Faculté des sciences d'Orsay

Thèse préparée au Centre de Nanosciences et de Nanotechnologies, C2N (Université Paris-Saclay, CNRS), sous la direction de Raffaele COLOMBELLI, directeur de recherche (HDR), le co-encadrement de Jean-Michel MANCEAU, chargé de recherche

Thèse soutenue à Paris-Saclay, le 1 avril 2022, par

Paul GOULAIN

Composition du jury

Aristide Lemaître Directeur de recherche (HDR), C2N Palaiseau	Président
Aloyse Degiron Chargé de recherche, MPQ Paris	Rapporteur & Examinateur
Karl Unterrainer Professeur, TU Wien	Rapporteur & Examinateur
Eva Monroy Docteure, NPSC Grenoble	Examinatrice
Raffaele Colombelli Directeur de recherche (HDR), C2N Palaiseau	Directeur de thèse

THESE DE DOCTORAT

NNT : 2022UPAST056

université PARIS-SACLAY

ÉCOLE DOCTORALE
Physique et ingénierie : Electrons, Photons, Sciences du vivant (EOBE)

Titre : Nouveaux concepts d'émetteurs polaritoniques dans les gammes spectrales du moyen-infrarouge et THz

Mots clés : Polaritons intersousbandes, Résonateur LC, Puits quantiques paraboliques, Diffusion phonon-polariton,

Résumé : Le moyen infrarouge et le terahetz sont des bandes de fréquences du spectre électromagnétique dont le domaine applicatif a vu une croissance importante ces dernières années, aussi bien pour les télécommunications que pour les sciences environnementale et médicale. Cet intérêt pousse la demande pour des sources et des détecteurs toujours plus compactes et efficaces. Dans cette optique, la mise au point de sources de photons cohérents utilisant le régime de couplage fort lumière-matière est une voie prometteuse. Deux axes d'étude de telles sources seront explorés dans cette thèse. Dans un premier temps, une nouvelle approche pour obtenir de l'émission de photon dans le moyen infrarouge par le biais du pompage optique résonant de polaritons intersousbandes a été étudié. Ce type d'émission spontanée se base sur l'utilisation de cavités non-dispersives, permettant en principe d'augmenter le taux de diffusion phonons-polaritons et donc d'atteindre plus facilement l'intensité seuil de l'émission cohérente. La démonstration de l'émission de photon dans cette configuration ouvre la possibilité d'explorer cette émission dans le cadre d'un régime de diffusion stimulé en peuplant l'état final du système par le biais d'un faisceau de sonde. Dans un second temps, l'attention sera été portée sur le domaine du THz. Afin de contourner la limitation thermique imposée par la faible énergie des transition THz, des puits quantiques paraboliques interdigités peuvent être utilisés afin d'obtenir une absorption résonante jusqu'à 300K. Pour s'affranchir de l'élargissement qu'introduit la multiplication des interfaces, des puits à gradient d'alliage ont été mis au point en collaboration avec l'université de Waterloo, Canada. Ce design a permis d'obtenir des transition THz de très haute qualité et une amélioration de la température d'opération du régime de couplage fort de 170K. Une particularité des polaritons intersousbandes est la possibilité d'obtenir une constante de couplage élevée par le biais du dopage du semiconducteur. Par conséquent, ces polaritons ont été une plateforme de choix pour la démonstration du régime de couplage ultra-fort, régime dans lequel le niveau fondamental du système se peuple d'une population de photons virtuels non négligeables. Des études théoriques ont prédit qu'une modulation non-adiabatique de l'état fondamental du système, c'est-à-dire sur une échelle de temps plus faible que le temps de vie des polaritons, ce réservoir de lumière peut être accédé. Il est alors possible de voir ces photons virtuels être émis sous forme de photons réels. Pour explorer cet effet, des cavités LC tridimensionnelles ont été fonctionnalisées afin d'obtenir la commutation ultra-rapide de leur fréquence de résonance. Leur développement et caractérisation par spectroscopie THz résolue en temps seront présentés. Par l'utilisation de GaAs épitaxié à basse température, des temps de modulation sous la picoseconde ont été atteints. Enfin, la combinaison de ces interrupteurs ultrarapides avec des puits quantiques paraboliques à gradient d'alliage a permis l'obtention d'un régime de couplage fort lumière-matière entre ces derniers.

ÉCOLE DOCTORALE
Physique et ingénierie : Electrons, Photons, Sciences du vivant (EOBE)

Title : New concepts for the development of polaritonic emitters in the mid-IR and THz range

Keywords : Intersubband polaritons, LC resonator, parabolic quantum wells, phonon-polariton scattering

Abstract : The mid-infrared and terahetz bands of the electromagnetic spectrum have seen significant growth in applications in recent years, both in telecommunications and in the environmental and medical sciences. This interest is driving the demand for ever more compact and efficient sources and detectors. In this context, the development of coherent photon sources using the strong light-matter coupling regime is a promising avenue. Two axes of study of such sources will be explored in this thesis. First, a new approach to obtain mid-infrared photon emission through resonant optical pumping of intersubband polaritons was studied. This type of spontaneous emission is based on the use of non-dispersive cavities, allowing in principle to increase the phonon-polariton scattering rate and thus to reach more easily the threshold intensity of the coherent emission. The demonstration of photon emission in this configuration opens up the possibility of exploring this emission in a stimulated scattering regime by populating the final state of the system with a probe beam. In a second step, the focus will be on the THz domain. In order to overcome the thermal limitation imposed by the low energy of THz transitions, interdigitated parabolic quantum wells can be used to obtain resonant absorption up to 300K. To overcome the broadening introduced by multiple interfaces, alloy gradient wells were developed in collaboration with the University of Waterloo, Canada. This design resulted in very high quality THz transitions and an improvement in the operating temperature of the strong coupling regime by 170K. A particularity of intersubband polaritons is the possibility to obtain a high coupling constant through doping of the semiconductor. Consequently, these polaritons have been a platform of choice for demonstrating the ultra-strong coupling regime, in which the fundamental level of the system is populated by a non-negligible population of virtual photons. Theoretical studies have predicted that a non-adiabatic modulation of the ground state of the system, i.e. on a time scale smaller than the lifetime of the polaritons, this pool of light can be accessed. It is then possible to see these virtual photons being emitted as real photons. To explore this effect, three-dimensional LC cavities have been functionalised to achieve ultra-fast switching of their resonant frequency. Their development and characterisation by time-resolved THz spectroscopy will be presented. By using low temperature epitaxial GaAs, sub-picosecond modulation times have been achieved. Finally, the combination of these ultrafast switches with parabolic graded alloy quantum wells has allowed the achievement of a strong light-matter coupling regime between them.

Nomenclature

Abbreviations

ABCD air biased coherent detection

AR active region

BCB benzocyclobutene

BEC Bose-Einstein condensate

EO electro-optic

FEM finite element method

FIR far-infrared

FTIR Fourier-Transform Infrared

FWHM full width at half maximum

GME guided mode expansion

GMR guided mode resonances

GVD group velocity dispersion

HPQW Half Parabolic Quantum Well

IBE ion beam etching

ICP-RIE inductively coupled plasma – reactive ion etching

IMI Insulator Metal Insulator

ISB Intersubband Transitions

MCT Mercury Cadmium Tellurium

MIM Metal Insulator Metal

MIR mid-infrared

MSP Multisubband Plasmon

NIR near-infrared

PCS Photonic crystal slab

PECVD Plasma-enhanced chemical vapor deposition

PQW Parabolic Quantum Well

QCL quantum cascade laser

QW quantum well

RCWA Rigorous Coupled-wave analysis

RIE Reactive Ion Etching

SEM Scanning electron microscope

SOI silicon on insulator

STEM Scanning Transmission Electron Microscopy

SW switch cavity

TDS time-domain spectroscopy

Remerciements

Je remercie grandement mes encadrants Raffaele Colombelli, Directeur de recherche et Jean-Michel Manceau, Chargé de recherche, de m'avoir donné l'opportunité de travailler sur cette thèse au sein du Centre de Nanosciences et de Nanotechnologies (C2N). Leur présence tout au long de mon parcours au C2N fût extrêmement enrichissant et m'a permis de progresser en tant que chercheur.

Je voudrais aussi remercier Adel Bousseksou, Chargé de recherche et Laurent boulley, ancien doctorant de l'équipe ODIN pour m'avoir ouvert les portes du C2N pour mon stage de 5me année d'école d'ingénieur.

Un grand merci aussi aux ingénieurs des différentes salles blanches dans lesquelles j'ai eu l'occasion de travailler tout au long de ma thèse. Merci à Jean-René Coudevylle, Nathalie Isac, David Bouville, Etienne Herth, Fabien Bayle et Téo Baptiste pour m'avoir initier à la micro-fabrication Merci aussi à Pascal Filloux et Stéphan Suffit de l'université Paris-Diderot pour m'avoir hébergé dans leur salle blanche pendant le déménagement du C2N. Grâce à eux, j'ai pu continuer à produire des échantillons pendant la période de mise en service de la nouvelle salle blanche. Enfin, la réunification des deux sites du C2N m'a permis de rencontrer les ingénieurs de Marcoussis. Parmi eux, je souhaiterai remercier en particulier Abdelmounaim Harouri, Jean-luc Cercus, Stéphane Guilet, Laurence Ferlazzo, Christophe Dupuis, pour les discussions que nous avons pu avoir qui m'ont permis d'enrichir et diversifier mes connaissances en micro-fabrication.

Evidemment, je remercie aussi les post-doctorants et ingénieurs de l'équipe Stefano Pirotta, Mario Malerba, Ngoc-Linh Tran et Marina Yakovleva, dont l'expérience et la sympathie ont donné lieu à des discussions enrichissantes. Je remercie aussi les anciens membres du groupe, Bruno Paulillo, Pierre-Baptiste Vigneron, Claire Abadie, Arnaud Jollivet, François Joint et Ludivine Emeric qui ont été présents à mes débuts pour m'aider lors de mesures et avec qui j'ai apprécié passer du temps.

Durant cette thèse, j'ai eu la chance de travailler en collaboration avec deux équipes de recherche. Je remercie Tasos Koulouklidis, Christina Daskalaki et Stelios Tzortzakis de l'IESL/FORTH en Grèce pour les mesures TDS et les nombreuses discussions qui ont permis l'obtention de résultats De l'équipe MBE de l'université de Waterloo, je voudrais exprimer ma gratitude à Zbig Wasilewski, Wojciech Pasek et surtout Chris Deimert qui nous ont contactés pour développer aider au développement de puits quantiques paraboliques. Chris a eu la possibilité de faire deux séjours en France, durant lesquels nous avons pu faire de nombreuses mesures sur ses échantillons et apprendre énormément sur le domaine de l'épitaxie.

Je souhaite aussi remercier les membres de mon bureau E114, Oussama Ouznali, Tiphaine Mathieu-Pennober et Mathieu Lim-Jeannin, qui m'ont tenu compagnie depuis le déménagement et soutenue pendant la rédaction de mon manuscrit.

Pour finir, je tiens à remercier mes parents, mon freres et ma soeur, et surtout Nina pour avoir été à mes côtés pendant toutes ces années.

Résumé

La gamme spectrale du moyen infrarouge et du térahertz ont vu ces dernières années leur importance augmenter significativement, dans de nombreux domaines allant du médicale aux applications liées aux télécommunications et la sécurité. Pour permettre le développement d'applications dans ces gammes spectrales, des sources et des détecteurs compacts et efficaces sont nécessaires. Jusqu'à présent, la majorité des sources à semiconducteurs dans ces gammes de fréquences repose en grande partie sur l'utilisation de structures à base de puits quantiques. A titre d'exemple, les lasers à cascade quantique (QCL) ont, depuis leur démonstration technique en 1994 dans le MIR et en 2002 dans le THz, grandement amélioré leur efficacité. Des températures cryogéniques, les QCLs MIR fonctionnent de nos jours a températures ambiante et les QCLs THz a des températures accessible a un module Peltier. Le constat est moins reluisant pour les détecteurs a base de puits quantiques, ou les températures de fonctionnement restent limitées à environ 20 K.

Afin de continuer a pousser leurs performances, le concept de dispositifs fonctionnant dans le régime couplage fort lumière-matière a commencé a être exploré. Ce régime est atteint lorsque la force de couplage entre la cavité et l'excitation électronique des puits quantiques est supérieure aux taux d'amortissements des deux systèmes découplés. Quand cette condition est remplie, la dégénérescence des deux états est levée, dont la signature spectrale est un anti-croisement des niveaux à résonance. Ces nouveaux états *hybrides* sont nommés polaritons, et - comme une vaste littérature discute - jouissent de propriétés nouvelles qui les rendent intéressants et pour l'étude de phénomènes physiques fondamentaux, et pour les applications.

Dans cette thèse, nous nous sommes concentrés sur l'utilisation de dispositifs en couplage fort pour l'émission de lumière dans les gammes spectrales du moyen-IR et du THz. En particulier, deux mécanismes d'émission reposants sur l'utilisation du couplage fort ont été explorés.

Dans un premier temps, j'ai mené des travaux sur le développement d'émetteurs reposant sur la diffusion de polaritons intersoubandes par des phonons optiques dans le moyen infrarouge. De façon similaire aux polariton-excitoniques, les polaritons intersoubandes peuvent être considérés comme des bosons, dans certains conditions. Ils peuvent donc être sujet à la stimulation par l'état final, pouvant mener à la création de condensats de Bose-Einstein. Dans le domaine des polariton-excitoniques, la création de condensats a permis la démonstration des lasers a polariton. Reprenant le même concept, un laser a polariton intersoubande a été théorisé. Son principe de fonctionnement est résumé dans la Figure 1.

Par pompage optique résonant, une population de polaritons est créée sur la branche haute. Cette population peut être sujette a une relaxation vers un état final par un mécanisme de diffusion avec un phonon optique. De par leur nature bosonique, le taux de diffusion est proportionnel à la population du dit état, suivant la formule $\Gamma = \Gamma_0(n_{pol} + 1)$ avec Γ_0 le taux de diffusion spontané et n_{pol} la densité de polaritons à l'état final. Si une densité critique est atteinte à cet état final, une accumulation rapide de polaritons intersoubandes mènera à la création d'une population

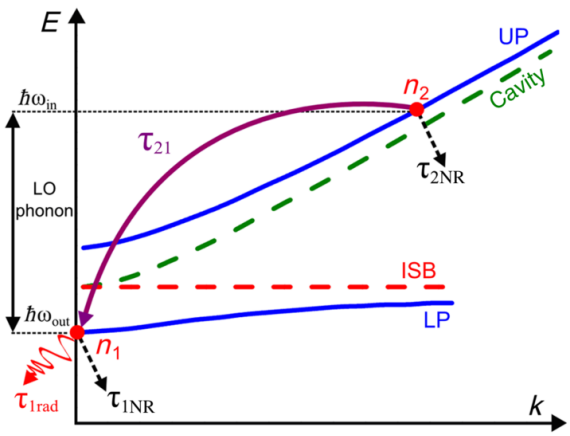

Figure 1.. Principe de fonctionnement d'un laser à polaritons intersoubandes.

polaritonique macroscopique qui rayonnera de façon cohérente. L'étude d'un tel système, utilisant des cavités métal-métal dispersives, a permis il y a quelque temps à notre équipe de montrer la première émission de photons par diffusion de polaritons intersousbandes pompés optiquement. Néanmoins, l'effet laser n'a pas encore été atteint et il a été calculé que la densité de puissance de pompe nécessaire pour l'obtenir était de l'ordre de quelque MW·cm^{-2}, ce qui est hors de portée de notre banc de mesure.

Dans la première partie de ma thèse, j'ai donc étudié deux stratégies pour réduire la densité de puissance optique de seuil pour un éventuel lasers à polaritons intersousbandes.

La première stratégie repose sur l'étude expérimentale de cavités métal-métal non-dispersives. L'utilisation de telles cavités permet en théorie d'augmenter de façon significative le taux de diffusion par les phonons, permettant d'améliorer de façon importante la population a l'état final pour une même puissance de pompe. L'effet net est donc de diminuer la densité de puissance nécessaire pour arriver au seuil.

Afin de tester notre théorie, un échantillon présentant une différence d'énergie entre la branche haute et la branche basse égale à l'énergie du phonon dans le GaAs a été fabriqué. Pour se faire, une dispersion photo-lithographique de cavités non-dispersive a été faite afin de trouver la cavité qui remplie les conditions pour l'étude de la diffusion phonon-polariton (voir Figure 2 (a).

Une fois la cavité fabriquée, des mesures de l'émission de photons par la diffusion phonon-polariton a permis de démontrer le fonctionnement de ce type de cavités. De façon similaire a ce qui a été démontré avec les cavités dispersives, un pompage résonant de la population de polariton sur la branche haute est nécessaire (Figure 2 (b)).

Malgré une augmentation du taux de diffusion et la détection de photons émis sous pompage optique, les résultats expérimentaux n'ont pas montré une amélioration significative de l'émission. La raison probable est la présence de nombreux état finaux, qui diluent la densité de polaritons. Pour pallier ce problème, un schéma de mesure reposant sur un système pompe-sonde est envisagé. Cela permettra d'induire une population préalable de polaritons à un état final spécifique, augmentant le taux de diffusion vers cet état.

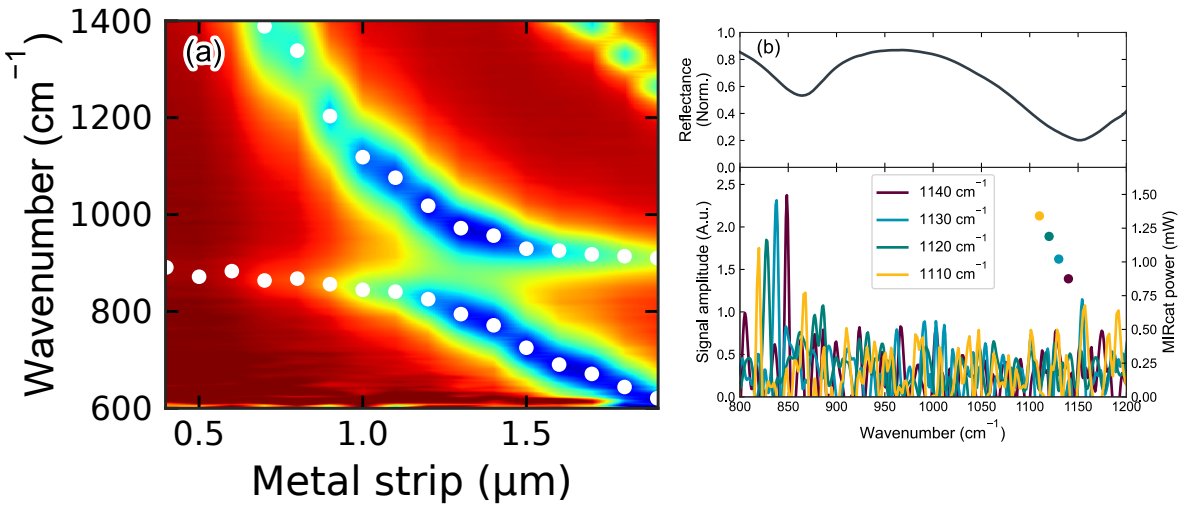

Figure 2.. **(a)**: Dispersion lithographique de cavités non-dispersives afin d'identifier la cavité qui offre une différence d'énergie entre la branche haute et basse égale a l'énergie du phonon optique dans le GaAs. **(b)**: (haut) réflectivité de la cavité non-dispersive. (bas) Fréquence et puissance de la pompe et spectre en amplitude du signal émis par la cavité.

La deuxième stratégie que j'ai étudiée vise à concevoir de cavités avec un facteur de qualité largement amélioré dans la gamme spectrale du moyen-infrarouge. Cette approche repose sur le design et la simulation numérique de cavités qui ne sont pas basées sur l'architecture métal-métal.

Le facteur de qualité de ces dernières est limité par la présence de métal qui introduit des pertes, ce qui réduit le temps de vie des photons, donc des polaritons. Cela a pour effet de limiter la population a l'état final, et donc l'obtention de la densité critique qui mènera a la formation éventuellement d'un condensat. Pour pallier cela, j'ai mené une étude théorique de cavités à cristaux photoniques. De par l'absence de couches métalliques, des facteurs de qualité d'environ 250 ont été obtenus, ce qui est un ordre de grandeur plus élevé que les facteurs de qualité des cavités metal-métal utilisées jusqu'à présent.

Ce résultat théorique/numérique est prometteur et sera développé ultérieurement dans le cadre des activités de l'équipe sur le systèmes polaritoniques.

Dans la suite de ma thèse, l'attention a été portée au domaine fréquentiel du térahertz: j'ai mené des travaux sur le développement d'émetteurs qui fonctionnent sur le principe appelé de "Casimir dynamique". En termes simples, il s'agit de l'émission de photons par la modulation non-adiabatique du régime de couplage fort. Ce travail est très prospectif et de caractère fondamental, mais les contributions que j'ai donné constituent de briques de bases importantes vers cet objectif ambitieux.

Historiquement, cette gamme de fréquence est surnommée le 'Fossé Térahertz' à cause de l'absence de sources compacts fonctionnant a température ambiante. Une des raisons de ce sous-développement vient de la faible énergie des transitions térahertz comparées a l'agitation thermique, ce qui rend l'absorption par les puits quantiques carrés térahertz impossible à température ambiante. En fait, au dessus de 40 K, la transition entre la deuxième et troisième sous bande devient active et au dessus de 150 K aucune transition n'est mesurable.

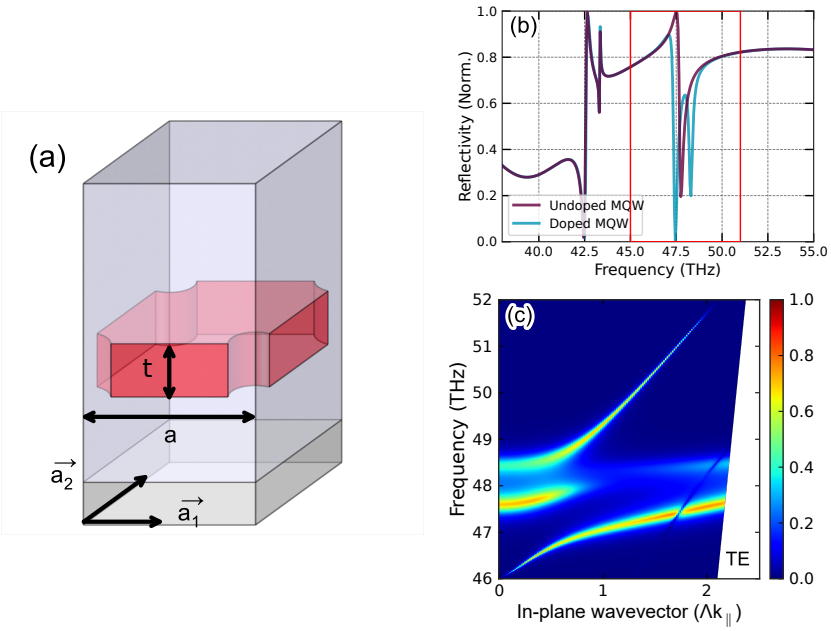

Figure 3.. **(a)**: cellule élémentaire de la cavité à cristaux photoniques étudiée théoriquement. **(b)**: étude d'un mode TM à incidence normale, avec une région active à base de puits quantiques dopés et non dopé. **(c)**: dispersion angulaire de la cavité à cristaux photoniques qui montre de grandes similitudes avec la dispersion obtenue en utilisant des cavités métal-métal dispersives.

(Il faut noter - pour précision - que ce problème affecte principalement les détecteurs. Par contre les lasers, notamment les lasers QCL, ne sont pas strictement contraintes par ces limites car ils sont de systèmes fortement hors équilibre.)

Une façon de pallier ce problème est d'utiliser des puits quantiques paraboliques. Dans ce type de puits, les niveaux d'énergie sont équidistants. Quelque soit la température et le nombre de sous bande actives, une seule absorption est mesurable.

Jusqu'à maintenant, la méthode pour obtenir de tels puits reposait sur l'alternance de puits carrés dont la largeur varie de façon a approximer un potentiel parabolique. Ces puits sont appelés puits inter-digités.

Néanmoins, la multiplication des interfaces du au nombre important de puits introduit une grande quantité d'élargissement menant a de faibles facteurs de qualité.

Afin de contourner ce problème, une nouvelle méthode de croissance a été développée conjointement avec C. Deimert et Z. Wasilewski de l'université de Waterloo. Elle se base sur la croissance de puits quantiques a gradient d'indice. De ce fait, le nombre d'interfaces est réduit au minimum.

Le résultat de cette méthode peut être vu dans la Figure 4. Grâce à cette méthode, des transitions intersousbandes dont la largeur est sous les 5% a 4 K ont été obtenues, un valeur record, et leur élargissement reste inférieur a 10% jusqu'à 150 K. La comparaison entre un puits carré et un puits parabolique est montrée dans la Figure 5. Ces puits paraboliques constituent une première brique importante vers la démonstration d'un émetteur THz basé sur l'effet Casimir dynamique.

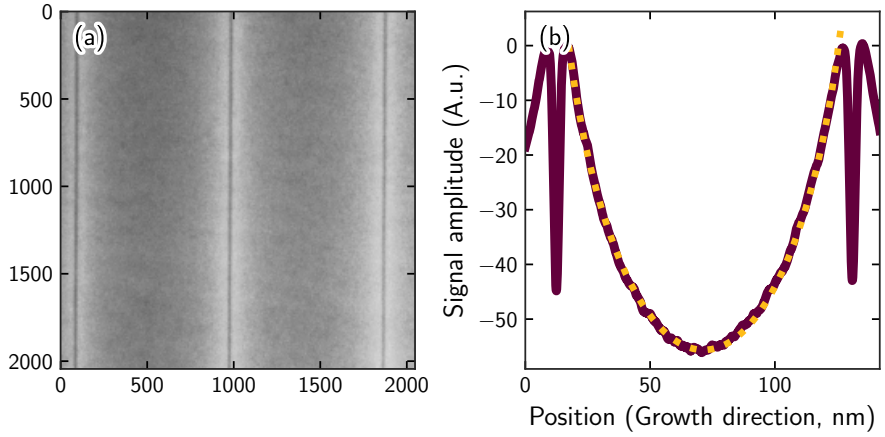

Figure 4.. **(a)** image STEM d'un puit quantique parabolique et **(b)** le profile de l'alliage. La variation continue de l'alliage réduit l'élargissement du aux interfaces.

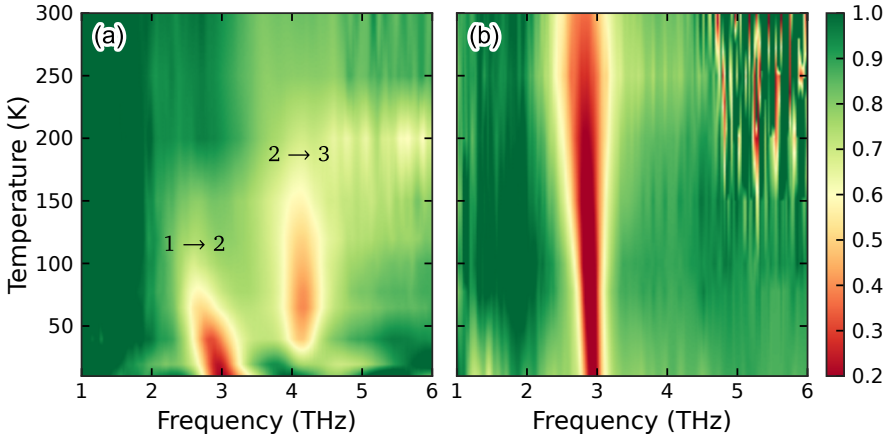

Figure 5.. Figure de la réflectivité en fonction de la température pour **(a)** un puit carré et **(b)** un puit parabolique térahertz.

Dans la dernière partie de cette thèse, j'ai développé la deuxième brique vers l'émission de photons par la modulation non-adiabatique du régime de couplage fort: j'ai conçu et développé de cavités THz dont la densité d'états optiques peut être modulée sur des échelles de temps ultra-rapides.

Pour cela des cavités LC en trois dimension, dont le développement a été initié dans une thèse précédente dans notre équipe, ont été fonctionnalisées (voir Figure 6 (a)). Par l'ajout d'une ouverture dans le plan de masse d'or de du résonateur, j'ai *de facto* modifié la structure circuitale du système. Cela a pour effet d'ajouter un condensateur au circuit équivalent (Figure 6 (b)), qui peut être utilisé comme un interrupteur ultra-rapide.

En exposant le semiconducteur sous le plan d'or, il devient possible de générer des porteurs en les photo-excitant à l'aide d'une impulsion optique par la face avant. Ce faisant, le circuit équivalent change, et avec lui la fréquence de résonance de la cavité (Figure 6 (c) et (d))

Afin de caractériser ces résonateurs et connaître leur réponse temporelle, des mesures par spectroscopie dans le domaine temporel on été effectuées en partenariat avec nos collègues de

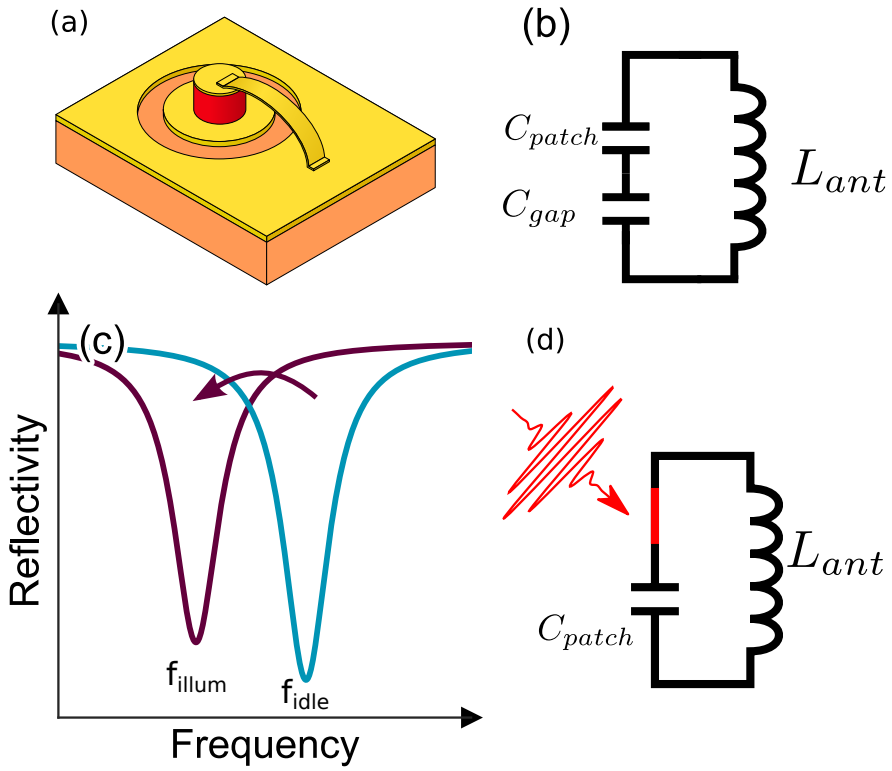

Figure 6.. **(a)** schéma de la cavité LC fonctionnalisée par une ouverture dans le plan d'or. **(b)** circuit équivalent de la cavité LC fonctionnalisée. L'ajout d'un condensateur supplémentaire change la fréquence de résonance comparé au résonateur LC classique. **(c)** et **(d)**: modulation de la fréquence de résonance du résonateur LC avant et après la photo-excitation.

IESL/FORTH en Grèce. Par l'utilisation d'arséniure de gallium dont la croissance a été faite à basse température comme substrat et d'une cavité composée de SiO_2, une dynamique ultra-rapide de la recombinaison des photo-porteurs est obtenue. Avec ce système, j'ai pu démontrer des modulations de la densité optique d'états sur des échelles de temps sous la picoseconde.

Fort de ce résultat, j'ai procédé à la conception, fabrication et caractérisation de résonateurs avec une région active constitué des puits paraboliques développés dans la partie précédente de la thèse. Ces dispositifs pourraient, en principe, être utilisés pour des premières mesures de radiation de Casimir dynamique.

Pour cela, une région active composée de quatre puits quantiques paraboliques a été utilisée. Afin de ne pas générer de porteurs aussi dans la partie active du dispositifs (le patch), un échantillon reposant sur un substrat de saphir a été fabriqué pour permettre de effectuer le pompage optique par la face arrière. Ainsi, la région active n'est pas perturbée. Cet échantillon a été mesuré de façon passive et a montré du couplage fort jusqu'à une température de 100 K (voir Figure 7). Il a ensuite été envoyé a nos collègues de l'IESL/FORTH afin d'être mesuré dynamiquement.

Nous ne savons pas encore si ce premier échantillon complet pourra déjà amener à l'observation de l'effet Casimir dynamique, mais le résultat important de mon travail de thèse - c.a.d. d'avoir

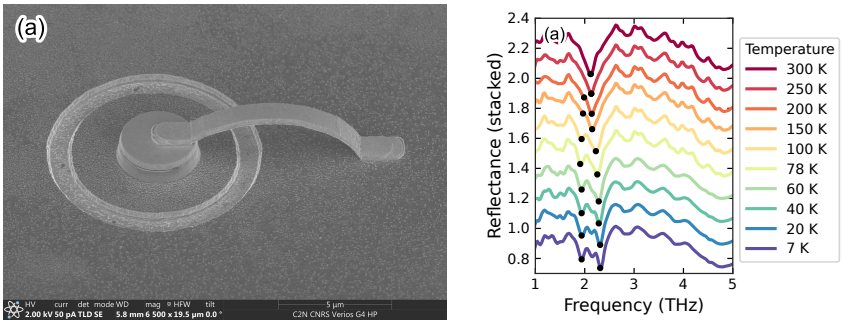

Figure 7.. (a) image MEB d'un résonateur LC fabriqué sur un substrat de saphir et **(b)** la mesure par spectroscopie infrarouge à transformée de Fourier.

construit et demontré expérimentalement les deux briques de base fondamentales - a été obtenu.

Contents

1. Introduction **2**

1.1. The frequency range of interest : MIR and FIR 2
1.1.1. General description and definition 2
1.1.2. Applications in MIR and FIR frequency ranges 3
1.1.3. State of the art 4

1.2. Electronic states in a semiconductor quantum well 5
1.2.1. The III-V compounds 5
1.2.2. Electrons in a periodic crystal 5
1.2.3. The concept of effective mass 6
1.2.4. Determination of the bandstructure : the k.p method 7
1.2.5. Toward the heterostructure band structure: the envelope function formalism 8
1.2.6. Infinite quantum well 9

1.3. Optical properties of material 10
1.3.1. The Lorentz oscillator model 11
1.3.2. The Gallium Arsenide permittivity 13
1.3.3. The Drude model for free electrons 14
1.3.4. Extension of the relative permittivity of doped GaAs 16

1.4. Intersubband absorption in quantum wells 16
1.4.1. The interaction Hamiltonian 17
1.4.2. Transition rate: Fermi's golden rule 18
1.4.3. Absorption in a quantum well 20
1.4.4. Many body effects in a quantum well: the depolarization shift 20
1.4.5. The effective medium approximation 21

1.5. The concept of intersubband polaritons 22
1.5.1. Light-matter interaction and weak coupling 22
1.5.2. Strong light matter coupling 23
1.5.3. Strong coupling in the Jaynes-Cummings model 23
1.5.4. Ultra-Strong coupling regime description 28
1.5.5. Virtual photon cavity 32

2. Novel approaches for the demonstration of final state stimulation in ISB polaritons under resonant injection of light **34**

2.1. Metal-metal cavity 34
2.1.1. The parallel plates waveguide 34

2.1.2. MIM patterned cavity . . . 37
2.1.2.1. Metal Insulator Metal (MIM) dispersive cavity . . . 38
2.1.2.2. Metal Insulator Metal (MIM) non-dispersive cavity . . . 40

2.2. Lasing without population inversion: The polariton laser . . . 41
2.2.1. Exciton-polariton lasers . . . 41
2.2.2. Extension of the polariton lasing concept to ISB-polaritons . . . 43
2.2.3. ISB-polariton scattering within a dispersive MIM cavity . . . 45

2.3. Intersubband Transitions (ISB) polaritons spontaneous emission under resonant optical pumping within a non-dispersive MIM cavity . . . 47
2.3.1. Possible improvement of the polariton scattering rate . . . 47
2.3.2. Design and fabrication of the non-dispersive cavity . . . 48
2.3.3. Improvements on the optical pumping experimental setup. . . . 49
2.3.4. LO-phonon scattering in a non-dispersive cavity . . . 50
2.3.4.1. Pump frequency dependence on the polariton emitted light . . . 50
2.3.4.2. Pump angle dependence on the polariton emitted light . . . 51
2.3.4.3. Difficulties linked to the non-dispersive final state . . . 52
2.3.5. Conclusions on the phonon-polariton scattering process within non-dispersive cavities . . . 53

2.4. Improved cavity Q-factor: all dielectric photonic crystal slab . . . 54
2.4.1. Generalities on photonic crystals . . . 55
2.4.2. Simulation of the photonic crystal slab cavity . . . 56
2.4.3. Strong light-matter coupling regime with ISB transition embedded in Photonic crystal slab (PCS) . . . 58

2.5. Conclusions . . . 60

3. Parabolic quantum wells for room temperature operation in the THz . . . 62

3.1. Theory . . . 62
3.1.1. The shortcomings of the THz square quantum well . . . 62
3.1.2. The parabolic potential . . . 64
3.1.3. Methods to grow quantum wells a with parabolic energy potential . . . 65
3.1.3.1. Interdigitated PQWs . . . 66
3.1.3.2. Continuously-graded alloy PQWs . . . 67
3.1.4. Modelisation of a Parabolic Quantum Well (PQW) structure . . . 68

3.2. Experimental Characterization setup . . . 70
3.2.1. Multipass geometry and measurements . . . 70
3.2.2. High resolution transmission measurements . . . 72
3.2.3. The effective medium model to fit the experimental absorption . . . 74

3.3. Performances of the Parabolic Quantum Wells . . . 77
3.3.1. First generation: 18-well repetition . . . 77
3.3.1.1. Design choices for a PQW structure . . . 77
3.3.1.2. Experimental results . . . 77

3.3.2. Second generation: 18-well regrowth and doping level study 78
3.3.2.1. TEM measurements 80
3.3.3. Third generation: corrected Alloy vs bandgap 82

3.4. Half Parabolic Quantum Wells 83

3.5. Strong light-matter coupling regime with PQWs 86
3.5.1. 54 PQWs within dispersive cavities: strong-coupling 86
3.5.2. 4 PQWs in non-dispersive cavity: strong-coupling up to 200 K 88
3.5.3. The strong coupling regime with Half-PQWs inserted in non-dispersive resonators 89

3.6. Conclusion 90

4. Toward dynamical Casimir: ultrafast switching of a subwavelength THz cavity . . . 92

4.1. Subwavelength resonators: The 3D LC circuit meta-atom 92
4.1.1. The Lambda/2n patch resonator 92
4.1.1.1. The square patch resonator 92
4.1.1.2. The round patch 95
4.1.1.3. The diffraction limit 97
4.1.2. The concept of meta-material 97
4.1.3. Toward the LC resonator 98
4.1.3.1. Lumped elements 98
4.1.3.2. The patch cavity as a capacitance 99
4.1.3.3. Energy conservation in a patch cavity 100
4.1.3.4. The air bridge antenna 101
4.1.4. Considerations on the THz LC resonator 103
4.1.4.1. Circuit tuning of an LC cavity 103
4.1.4.2. Coupling 104

4.2. Functionalization of the LC resonator 107
4.2.1. Frequency modulation of the optical properties of metasurfaces 107
4.2.2. Optical switching implementation on an LC resonator 107
4.2.2.1. Clean room fabrication of state-of-the-art LC resonators 109
4.2.2.2. Numerical simulation of the LC resonator device 110

4.3. Time domain characterization of the LC switch dynamic 111
4.3.1. Time domain spectrometer and the generation of THz pulses 111
4.3.1.1. THz pulses generation 112
4.3.1.2. Electric-field sampling of the THz pulses 113
4.3.1.3. Pump-Probe experiments 113
4.3.2. First attempt of cavity photoswitching: the SOI based device 114
4.3.2.1. Semiconductor photo-excitation capabilities 114
4.3.2.2. Ultrafast-Switching of the cavity under illumination 115
4.3.3. Toward sub-picosecond photoswitching dynamics 116
4.3.3.1. Addressing the dynamics hurdles using LT-GaAs 116
4.3.3.2. The importance of the setup configuration for the ultrafast dynamics measurements 118

4.3.3.3. Observation of the full switching dynamics 120

4.4. PQW LC cavity 121
4.4.1. Backside illumination geometry 122
4.4.1.1. Front side illumination issue with GaAs substrate and cavity material 122
4.4.1.2. LT-GaAs on Sapphire: dynamics measurements 123
4.4.2. LC strong coupling measurements with PQWs 124
4.4.2.1. Fabrication of the LC resonators on LT-GaAs and on sapphire substrate 124
4.4.2.2. Static Fourier-Transform Infrared (FTIR) measurements 126

4.5. Conclusions and perspectives 127

5. Conclusions 128

A. Active region growthsheets 130

A.1. L1006 Interdigitated PQWs 130

A.2. G0413 18 PQWs 133

A.3. G0489 18 PQWs 134

A.4. G0490 54 PQWs 135

A.5. G0642 4 PQWs 136

A.6. G0643 8 PQWs 137

A.7. G0645 43 HPQWs bulk doped 138

A.8. G0712 43 HPQWs mod. dop. 139

A.9. HM4162 140

Bibliography 142

Chapter 1

Introduction

In this chapter, the fundamental concepts used to describe the results throughout this thesis will be introduced.

1.1. The frequency range of interest : MIR and FIR

1.1.1. General description and definition

The mid-infrared (MIR) and far-infrared (FIR), the latter one also named terahertz (THz), correspond to adjacent frequency ranges of the electromagnetic spectrum. The exact boundaries of these two frequency ranges depend on the references, but they are often defined from 0.3 THz to 30 THz for the FIR and 30 THz to 300 THz for the MIR. These two frequency bands are surrounded by the near-infrared (NIR) band also referred as the telecommunication band and the microwave band on the other side which is the entry point of the electronic realm. Fig. 1.1 (a) shows the atmospheric absorption from the optical frequencies to the millimeter waves, and Fig. 1.1 (b) and (c) put the emphasis on the two frequency ranges that will be studied throughout this thesis.

The range between 8 µm to 13 µm, called the 3rd atmospheric window, is surrounded by two absorption regions due to H_2O molecule vibrational modes at 6.4 µm and CO_2 vibrational modes at 13 µm and presents a narrow absorption line at 6.4 µm created by O_3 molecules [3]. MIR measurements can then be performed in the ambient atmosphere. On the contrary, the THz is a more complicated frequency range to work with. Over the range spanning from 1 to 3 THz, the different gas that enter into the composition of the atmosphere possess several vibrational modes which make the atmosphere almost opaque to THz radiation over long distances [4]. If one wants to carry out measurements in this frequency window, those have to be done under dry air purging or vacuum environment.

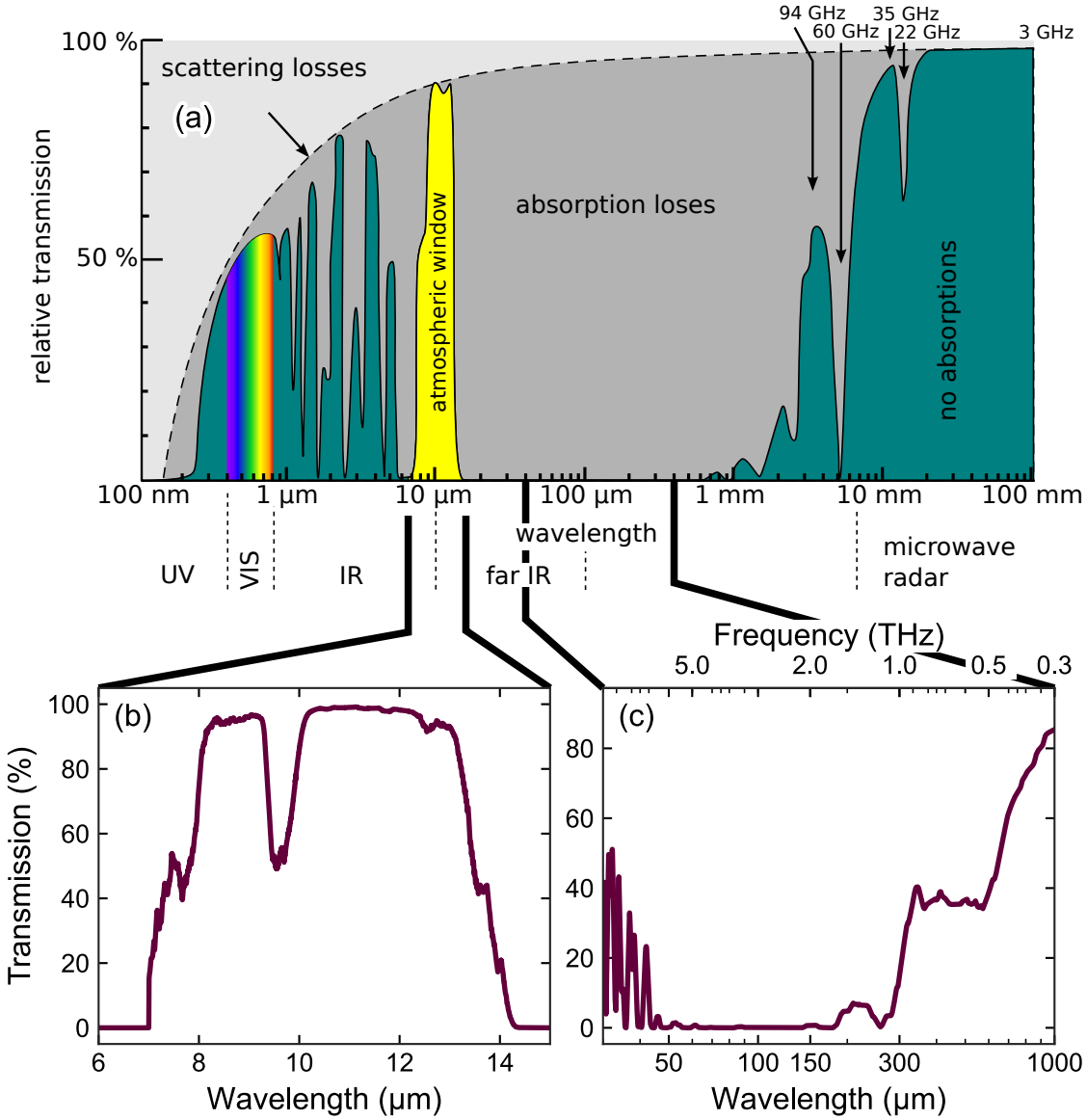

Figure 1.1.. **(a)**: simplified representation of the atmospheric transmission ranging from the visible to the millimeter frequency. **(b)** and **(c)**: atmospheric transmission of the two frequency ranges of interest of this thesis for the MIR and THz measured at the Gemini South telescope in Chile and the Concordia Research Station at the South Pole (data from [1, 2]). The transmission was measured though 1.6 mm of air for MIR and 0.2 mm for THz

1.1.2. Applications in MIR and FIR frequency ranges

The MIR has found over the years many applications in science, especially in trace gas spectroscopy due to the strong interaction between MIR radiation and molecular vibrational transitions, allowing to efficiently analyze chemicals. One particularly interesting application is the development of

miniaturized gas sensors for in situ analysis, which play a vital role in the industry for process control [5], or portable devices for atmospheric measurement and pollution detection [6]. Another widely used application of this frequency band can be found in thermal imaging, as it corresponds to the emission spectra of bodies at ambient temperature. Here the primary applications are for military use with night vision [7] and guiding systems, as well as in astronomy [8]. This led to a surge of interest and research during the last two decades which resulted in the development of a wide range of efficient and compact sources and detectors. The current shift of the community is toward the development of integrated systems, with for instance the source and the detector on the same chips [9].

On the other hand FIR did not receive as much attention despite the tremendous potential this frequency band possesses, gaining the name of "THz gap" to emphasize its underdevelopment. Like MIR frequencies, THz finds applications in astronomy and cosmology [10] as well as spectroscopy due to its strong absorption in water. Security is another field where the terahertz band found application opportunities thanks to its high transmission through non-metallic or non-polar materials (cloths, cardboard, etc.), its distinctive absorption spectra in many drugs and explosive materials, while presenting minimal health risks [11]. The next big terahertz application is communication as FIR is seen as a potential candidate for 6G communication [12].

1.1.3. State of the art

As explained before, MIR and FIR did not receive the same level of attention during the last two decades. This created a wide difference of device performances between these two frequency bands.

For MIR emission, several coherent sources are available. The most emblematic of them is the quantum cascade laser (QCL) introduced in 1994, limited at first at a temperature of 88 K for 8 mW of optical power in pulsed mode [13]. Since its demonstration, MIR QCLs have seen a tremendous development achieving continuous wave operation at room temperature (RT) with multi-watt output power [14]. Nowadays, several manufacturers provide QCL sources integrated in a compact form factor [15]. On the detection side, Mercury Cadmium Tellurium (MCT) [16] is the most used detector for this spectral range, offering an extremely high sensitivity with the downside of requiring nitrogen cooling. Later, Quantum Well Photo-Detectors (QWIP) were demonstrated and proved to be good alternative to MCT for selected applications . They exhibit a fast response time even at room temperature, albeit with reduced sensitivity [17, 18, 19].

Things are more complicated on the THz side of the spectrum. THz waves can be generated using different systems. One of them relies on the use of a NIR laser pulse to produce a THz pulse through electron acceleration [20], or non-linear effects in gases like air or nitrogen with a low output power of a few microwatts. Another is, like in the MIR, the THz QCL which was first demonstrated in 2002 [21], 8 years after the MIR QCL. Recently, the operating temperature of a THz QCL was pushed up to 250 K (−23 °C), enabling the development of TEC-cooled systems. Concerning the detection, there is a real challenge for achieving fast and sensitive room temperature detection in a compact format. The most used systems are currently based on a thermal detection of the photons: semiconductor bolometer, pyroelectric or thermocouple. THz QWIPs were demonstrated in 2005 by Luo et al. [22] with an operating temperature of 17 K. Since this publication, operating

temperature stagnated with only marginal gain until recently with a 60 K THz detection using QW transitions and a metamaterial cavity being reported [23].

1.2. Electronic states in a semiconductor quantum well

1.2.1. The III-V compounds

The term III-V material refers to a chemical compound with at least one atom from the third column and one atom from the fifth column of the periodic table. In optoelectronics the most used ones are the gallium based (GaAs, AlGaAs, GaSb, ...) and indium based (InP, InAs, InSb) compounds. Most of the III-V materials possess a Zinc Blend crystal structure, with the notable exception of GaN and its alloy InGaN which have a wurtzite structure. Thanks to its crystalline structure, a semiconductor can be described as an infinite repetition of an elemental lattice defined by its fundamental vectors $\boldsymbol{a}_1$, $\boldsymbol{a}_2$ and $\boldsymbol{a}_3$. The atomic environment is the same by the translation of a Bravais lattice vector $\boldsymbol{R} = n_1\boldsymbol{a}_1 + n_2\boldsymbol{a}_2 + n_3\boldsymbol{a}_3$ where $n_{1,2,3}$ are integers.

In this thesis, the only alloys used were the GaAs and AlGaAs, thus the emphasis will be onto this material. In a perfect GaAs crystal without dopants, also called intrinsic, the bonds between the fifth column arsenic and third column gallium form mixed covalent and ionic bonds: the arsenic atoms delocalize one of its electrons to a gallium atom. Both atoms possess then 4 electrons and form covalent bonds between each other [24].

1.2.2. Electrons in a periodic crystal

In the general case, the electronic states of an electron, wavefunction and energy, are solutions of the Schrödinger equation:

$$H\Psi(\boldsymbol{r}) = E\Psi(\boldsymbol{r}) \tag{1.1}$$

In a crystal, the Hamiltonian of one electron can be written:

$$H_{cry} = \frac{\boldsymbol{p}^2}{2m_0} + V(\boldsymbol{r}) \tag{1.2}$$

with $V(\boldsymbol{r})$ the background potential experienced by the electron. This potential has the same periodicity of the crystal, i.e. for any Bravais lattice vector $\boldsymbol{R}$, $V(\boldsymbol{r}) = V(\boldsymbol{r}+\boldsymbol{R})$.

In the particular case where $V(\boldsymbol{r}) = 0$, which corresponds to the free electron case, the solution of the Schrödinger equation in a volume V is:

$$\Psi(\boldsymbol{r}) = \frac{1}{\sqrt{V}} e^{i\boldsymbol{k}\cdot\boldsymbol{r}} \tag{1.3}$$

and the energy is:

$$E = \frac{\hbar^2 k^2}{2m_0} \tag{1.4}$$

If a periodic crystal is now considered, the Bloch theorem under the Born-von Karman boundary condition states that the electron wavefunctions are the product of a plane wave and a function with the same periodicity as the crystal [25]:

$$\Psi_{n,\boldsymbol{k}}(\boldsymbol{r}) = u_{n,\boldsymbol{k}}(\boldsymbol{r}) \frac{\mathrm{e}^{\mathrm{i}\boldsymbol{k}\cdot\boldsymbol{r}}}{\sqrt{V}} \tag{1.5}$$

where $u_{n,\boldsymbol{k}}(\boldsymbol{r}+\boldsymbol{R}) = u_{n,\boldsymbol{k}}(\boldsymbol{r})$ with $\boldsymbol{R}$ a Bravais lattice vector. Similarly to the free electron case, $\boldsymbol{k}$ is the wavevector of the associated plane wave, and n is the band index that arises from the quantization introduced with the Born-von Karman boundary conditions: for a given $\boldsymbol{k}$ value there are several solutions of the Schrödinger equation. For a given band index number, the set of $E_{n,\boldsymbol{k}}$ is called an energy band [26].

1.2.3. The concept of effective mass

One of the important implications of the Bloch theorem is the picture it provides to understand the behavior of an electron in a crystal. If one considers the forces experienced by this electron, they can be decomposed in two terms: one corresponding to the internal force created by the crystal and one representing the external force applied to the electron. By defining the group velocity of a wavepacket $\boldsymbol{v}_\mathrm{g} = \frac{1}{\hbar}\frac{\mathrm{d}E}{\mathrm{d}k}$, and considering the work of an external force on the electron, it can be demonstrated that:

$$\hbar \frac{\mathrm{d}\boldsymbol{k}}{\mathrm{d}t} = \boldsymbol{F}_\mathrm{ext} \tag{1.6}$$

Using the Newton's second law, the effective mass $m^* = \hbar^2 \left(\frac{\mathrm{d}^2 E}{\mathrm{d}k^2}\right)^{-1}$ can be defined, which depends on the dispersion relation of the electron. This effective mass is the result of the interactions of the electron with the crystal potential, and allows to rewrite the Schrödinger equation in a simpler form:

$$\frac{\boldsymbol{p}^2}{2m^*}\Psi(\boldsymbol{r}) = E\Psi(\boldsymbol{r}) \tag{1.7}$$

It means that if the dispersion relation is quadratic (which means the effective mass m^* is constant), then the motion of an electron in a crystal can be solved as it was a free electron with a mass m^* in free space. The solutions are then plane waves and its energy has the same form as the free electron Eq. (1.4) with the effective mass m^*. This quadratic dispersion approximation is often used when one is only interested in the band structure around the Γ point.

1.2.4. Determination of the bandstructure : the k.p method

As the previous section highlighted it, knowing the bandstructure is a key ingredient to solve the Schrödinger equation for an electron in a crystal. Several methods exist to calculate the whole bandstructure of a crystal (The tight binding or the pseudopotential methods for example). However, the knowledge of the bandstructure around the Γ point of the bandstructure is often enough for describing the optical and electronic properties of a semiconductor quantum well.

Starting from the one electron Hamiltonian in a crystal, and substituting the Bloch eigenstate into it , one can find that:

$$\left(\underbrace{\frac{p^2}{2m_0}+V(\boldsymbol{r})}_{H(\boldsymbol{k}=0)}+\underbrace{\frac{\hbar\boldsymbol{K}\cdot\boldsymbol{p}}{m_0}+\frac{\hbar^2k^2}{2m_0}}_{W(\boldsymbol{k})}\right)u_{n\boldsymbol{k}}(\boldsymbol{r})=E_{n\boldsymbol{k}}u_{n\boldsymbol{k}}(\boldsymbol{r}) \tag{1.8}$$

which is a Schrödinger like equation whose solutions are the periodic Bloch functions. For $\boldsymbol{k}=0$, Eq. (1.8) is reduced to exactly the one electron Schrödinger equation $H(\boldsymbol{k}=0)$ for the periodic functions $u_{n,0}$. The idea behind the $\boldsymbol{k}\cdot\boldsymbol{p}$ method is to solve Eq. (1.8) in perturbation theory, where the $\boldsymbol{k}$-dependant terms can be approximated as perturbation of the system as long as small values of $\boldsymbol{k}$ are considered. The solutions are built using the periodic functions $u_{n,0}$ as a basis.

From this point, the resolution of the Schrödinger equation will depend on how many bands are considered. More bands mean more accurate solution at the expense of solution and resolution complexity. The simplest case is for a non-degenerate band, which is the case for the GaAs conduction band, weakly coupled with the other bands. The energy of a state near the Γ-point can be expressed [24]:

$$E_{n,\boldsymbol{k}}=E_{n,0}+\frac{\hbar^2k^2}{2m}+\frac{\hbar^2}{m^2}\sum_{n\neq n'}\frac{\left|\langle u_{n,0}|\boldsymbol{k}\cdot\boldsymbol{p}|u_{n',0}\rangle\right|^2}{E_{n,0}-E_{n',0}} \tag{1.9}$$

The energy at a finite $\boldsymbol{k}$ value of the conduction band is modified by the influence of the other bands through the matrix element $\langle u_{n,0}|\boldsymbol{k}\cdot\boldsymbol{p}|u_{n',0}\rangle$. For small values of $\boldsymbol{k}$ (which is implied due to the perturbative approximation), Eq. (1.9) can be cast into the following form:

$$E_{n,\boldsymbol{k}}=E_{n,0}+\frac{\hbar^2k^2}{2m^*} \tag{1.10}$$

where m^* is an effective mass with the expression:

$$\frac{1}{m^*}=\frac{1}{m_0}+\frac{2}{m_0^2k^2}\sum_{n\neq n'}\frac{\left|\langle u_{n,0}|\boldsymbol{k}\cdot\boldsymbol{p}|u_{n',0}\rangle\right|^2}{E_{n,0}-E_{n',0}} \tag{1.11}$$

with m_0 the free electron mass. The solution of the Schrödinger equation using the single band $\boldsymbol{k}\cdot\boldsymbol{p}$ are similar to the solution of a free electron with the mass m^*. The single band $\boldsymbol{k}\cdot\boldsymbol{p}$ is often called the effective mass approximation [27].

Other formulations of the $\boldsymbol{k} \cdot \boldsymbol{p}$ were developed over the years, taking into account more bands, degeneracy and spin coupling in order to provide more accurate bandstructure descriptions. Applied to bulk and quantum well semiconductor, the most notable are the Kane [28] and Luttinger-Kohn models (ref here).

1.2.5. Toward the heterostructure band structure: the envelope function formalism

So far, the Schrödinger equation of the one electron was solved for a bulk III-V continuous crystal, which allowed us to obtain the band structure. To pursue of the goal of developing new optoelectronics devices, tailoring the energy bands of the crystal is necessary. The development of new epitaxial methods (MBE [29], MOCVD) made possible the study of high quality heterostructures with close to perfect lattice matching conditions, making a virtually perfect continuation between different material. One of the most famous heterostructure systems is the quantum well, which consists of a small gap material cladded by a material with a larger gap. A representation can be seen Fig. 1.2 (a) for a GaAs/AlGaAs quantum well.

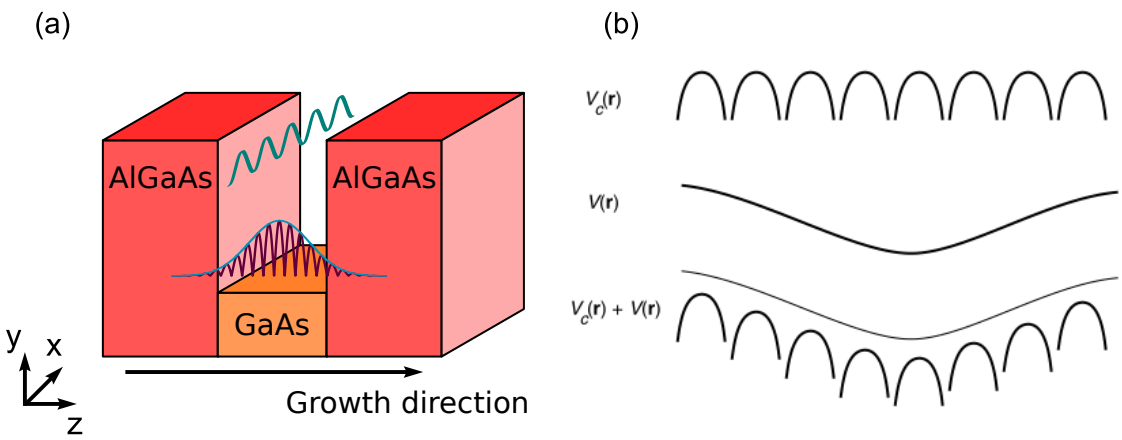

Figure 1.2.. **(a)**: energy potential of a GaAs/AlGaAs heterostructure. **(b)**: crystal potential V_c created by the lattice atoms, material potential V due to the different material composing the heterostructure.

The growth axis direction, i.e. the direction in which the material periodically changes, is the z-axis. In the x,y-plane at a given z position the material is uniform.

The formalism developed up to know provides solutions of electron Schrödinger equation that take the form of a plane wave multiplied by a Bloch function. This formalism can be expended to obtain the electron wavefunctions in the case of a heterostructure, and is called the envelope function formalism. The Schrödinger equation for an heterostructure can be written:

$$H = \frac{\boldsymbol{p}^2}{2m_0} + V_c(\boldsymbol{r}) + V(\boldsymbol{r}) \tag{1.12}$$

where V_c is the crystal potential and $V(z)$ is the band offset in th z-direction. It can be shown that the form of Eq. (1.12) solutions is:

$$\Psi_{n,\boldsymbol{k}}(\boldsymbol{r}) = F_n(\boldsymbol{r})u_{n,0}(\boldsymbol{r}) \tag{1.13}$$

where F_n is the envelope function describing the electron motion of the nth subband, and $u_{n,0}(\boldsymbol{r})$ the periodic Bloch function assumed to be identical for both materials [30]. The Schrödinger equation for the envelope function reads:

$$\left[-\frac{\hbar^2}{2}\boldsymbol{\nabla}\left(\frac{1}{m^*(z)}\boldsymbol{\nabla}\right) + V(z)\right]F_n(\boldsymbol{r}) = E_{n,\boldsymbol{k}}F_n(\boldsymbol{r}) \tag{1.14}$$

with $m^*(z)$ the effective mass defined previous section, which includes the crystal potential $V_c(\boldsymbol{r})$. To solve Eq. (1.14), the envelope function can be separated into two components: an in-plane component which is a solution of Eq. (1.14) with a constant effective mass and band offset V and a z-dependent function which describe the electron confinement. The envelope function becomes:

$$F_n(\boldsymbol{r}) = \frac{1}{\sqrt{S}}\mathrm{e}^{\mathrm{i}\boldsymbol{k}_{\parallel}\cdot\boldsymbol{r}}\Phi_n(z) \tag{1.15}$$

The function $\Phi_n(z)$ is the wavefunction of the electron in the confinement direction. It is the solution of the one-dimensional Schrödinger equation:

$$\left[-\frac{\hbar^2}{2}\frac{\partial}{\partial z}\left(\frac{1}{m^*(z)}\frac{\partial}{\partial z}\right) + V(z)\right]\Phi_n(z) = E_n\Phi_n(z) \tag{1.16}$$

and must fulfil the following boundary conditions:

$$\Phi_n(z)\big|_{z\to z_0^-} = \Phi_n(z)\big|_{z\to z_0^+} \quad \text{and} \quad \left(\frac{1}{m^*(z)}\frac{\partial\Phi_n(z)}{\partial z}\right)\Big|_{z\to z_0^-} = \left(\frac{1}{m^*(z)}\frac{\partial\Phi_n(z)}{\partial z}\right)\Big|_{z\to z_0^+} \tag{1.17}$$

with z_0 the boundary between the two materials, and the exposant - and + denoting the left- and right-hand side of the boundary. These boundary conditions are known as the BenDaniel and Duke boundary conditions [31] and ensure the probability current continuity across the heterojunction.

1.2.6. Infinite quantum well

In general, Eq. (1.16) cannot be solved analytically, numerical solvers are needed. However, a simple yet important case study that can be solved exactly is the infinite quantum well. The idea is to consider a geometry where inside the well for $|z| \leq L/2$, $V(z) = 0$, and $V(z) = \infty$ everywhere else. Also, the electron mass is supposed to be constant. Under these conditions, the Schrödinger equation Eq. (1.16) becomes:

$$\frac{\partial^2\Phi_n}{\partial z^2} + \frac{2m^*}{\hbar^2}E_n\Phi_n = 0 \tag{1.18}$$

It can be noticed that since the barrier are infinitely high, the probability of finding an electron in the barriers is null. Solving Eq. (1.18) with the boundary conditions $\Phi(\pm L/2) = 0$ yields the normalized wavefunctions:

$$\Phi_n(z) = \sqrt{\frac{2}{L}} \sin\left(k_n z + \frac{n\pi}{2}\right) \quad \text{with} \quad k_n = \frac{n\pi}{d} \tag{1.19}$$

where n is an integer indexing the energy levels in the conduction quantum well. The three first wavefunctions are plotted in Fig. 1.3 (a). Φ describes a standing wave with nodes at the interface between the well and the barrier. The energy associated with the nth energy level is:

$$E_n = \frac{\hbar^2 k_n^2}{2m^*} = \frac{\hbar^2 \pi^2 n^2}{2m^* d^2} \tag{1.20}$$

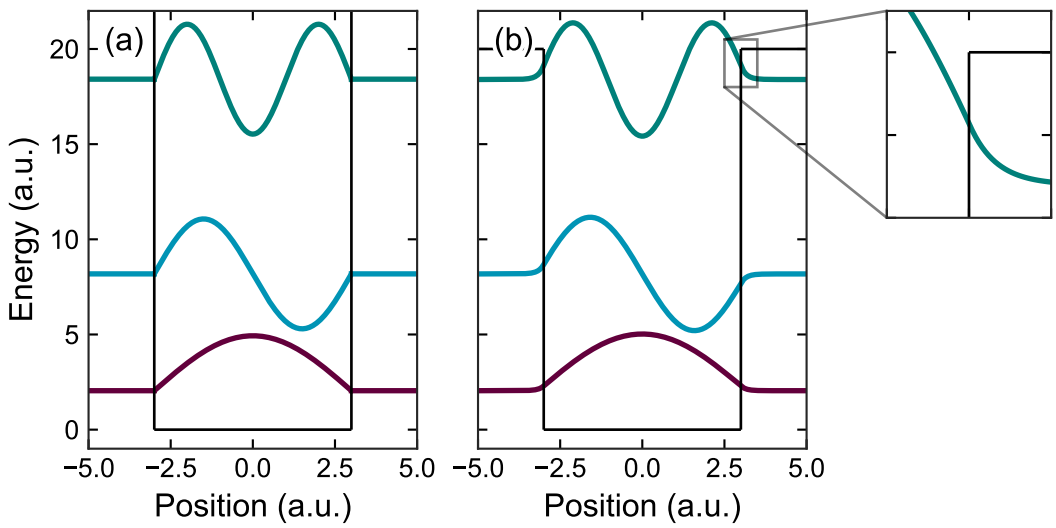

Figure 1.3.. Energy levels and wavefunctions of **(a)** an infinite and **(b)** a finite quantum well. The inset highlights the extension of the wavefunction in the barrier for a finite quantum well.

While being unrealistic, the infinite quantum well provides an intuitive picture close to the reality. In Fig. 1.3 (b) the three first wavefunctions of a finite quantum well with the same effective mass for both the well and the barrier are shown. The main difference is that in the case of the finite well, the wavefunctions penetrate on a short distance inside the barrier.

1.3. Optical properties of material

In this section we discuss the different approaches to model the optical properties of different materials. The goal is to find equations describing the propagation of light in a dense medium. The knowledge of these equations is important if one wants to model material behavior, either in a simulation tool or to fit data.

1.3.1. The Lorentz oscillator model

In general, it is assumed that the optical properties of a material arise from the interaction between an electromagnetic wave and dipole oscillators, the most important contributor being the bound electrons of the atoms. These electrons can be seen as masses connected to their atoms with a spring. When a light wave interacts with the electrons, it disturbs them from their idle positions and in turn they start to oscillate around their initial positions. The Coulomb interaction between the electrons and their respective atom nucleus acts as a restoring force.

Using this analogy, it is possible to derive a macroscopic relation using a semi-classical model. Let's consider the interaction between an electromagnetic wave and an atom. The bound electrons constitute an electric dipole of charge e, with a resonant frequency ω_0 and a damping parameter γ. The nucleus is assumed to have a much greater mass than the electrons, thus it can be considered immobile. The system is depicted in Fig. 1.4 (a).

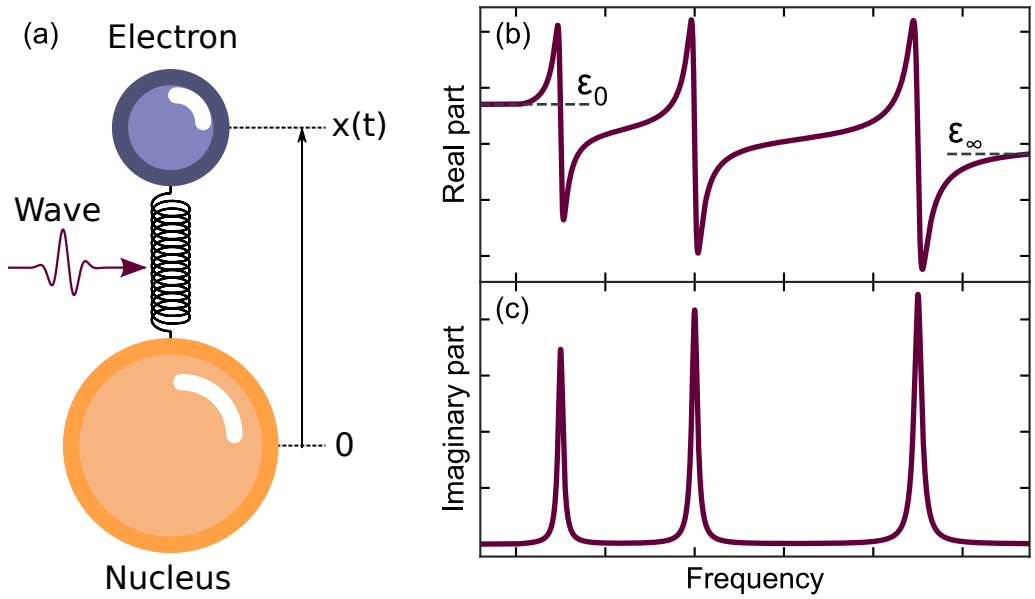

Figure 1.4.. **(a)**: Schematic of the Lorentz oscillator model. **(b)**: Real part and **(c)**: imaginary part of a fictive permittivity

Using the equation of motion, the displacement of a dipole can be written:

$$m_0 \frac{\mathrm{d}^2 \boldsymbol{x}}{\mathrm{d}t^2} + m_0 \gamma \frac{\mathrm{d}\boldsymbol{x}}{\mathrm{d}t} + m_0 \omega_0^2 \boldsymbol{x} = -e\boldsymbol{E} \tag{1.21}$$

where m_0 is the electron mass, γ is the damping rate, e the electron charge, E the electric field of the electromagnetic field. In the case of a harmonic driving electric field $E(t) = E_0 e^{-i\omega t}$, the solution of the equation of motion is:

$$x(t) = X_0 e^{-i\omega t} \quad \text{with} \quad X_0 = \frac{-eE_0}{m_0} \frac{1}{\omega_0^2 - \omega^2 - i\gamma\omega} \tag{1.22}$$

where X_0 is the amplitude of the electron oscillation.

By moving away from its nucleus, an electron induces a dipole moment $p(t) = ex(t)$, which adds up to the macroscopic polarization of the medium. For N atoms per unit volume, the total polarization contribution is:

$$\boldsymbol{P}_{res} = -Ne\boldsymbol{x}(t) = -\frac{Ne}{m_0}\frac{1}{\omega_0^2 - \omega^2 - i\gamma\omega}\boldsymbol{E}(t) \tag{1.23}$$

A quick analysis of $\boldsymbol{P}_{res}$ shows that this resonant contribution to the medium polarization is small unless the light wave frequency ω is close to the resonant frequency of the oscillator ω_0. The electric displacement is then written:

$$\boldsymbol{D} = \varepsilon_0\boldsymbol{E} + \boldsymbol{P}_{background} + \boldsymbol{P}_{res} \tag{1.24}$$

where ε_0 is the vacuum permittivity and $\boldsymbol{P}_{background}$ corresponds to the non-resonant term of the total polarization of the medium and can be expressed in terms of electrical susceptibility with the relation $\boldsymbol{P}_{background} = \varepsilon_0\chi\boldsymbol{E}$. All the terms of the Eq. (1.24) depend on the electric field $\boldsymbol{E}$, thus the relation can be written:

$$\boldsymbol{D} = \varepsilon_0\varepsilon_{\mathrm{r}}\boldsymbol{E} \quad \text{with} \quad \varepsilon_{\mathrm{r}} = 1 + \chi + \frac{Ne^2}{\varepsilon_0 m_0}\frac{1}{\omega_0^2 - \omega^2 - \mathrm{i}\gamma\omega} \tag{1.25}$$

where ε_r is called the relative permittivity, and contains the optical response of a medium for a light wave of frequency ω. By defining:

$$\varepsilon_{\mathrm{st}} = \varepsilon_{\mathrm{r}}(0) = 1 + \chi + \frac{Ne^2}{\varepsilon_0 m_0\omega_0^2} \tag{1.26}$$

$$\varepsilon_\infty = \varepsilon_r(\infty) = 1 + \chi \tag{1.27}$$

then the relative permittivity can be written:

$$\varepsilon_{\mathrm{r}}(\omega) = \varepsilon_\infty + (\varepsilon_{\mathrm{st}} - \varepsilon_\infty)\frac{1}{\omega_0^2 - \omega^2 - \mathrm{i}\gamma\omega} \tag{1.28}$$

This derivation was done under the assumption that the medium has one oscillator at the frequency ω_0, the rest of the polarization is included in the $\boldsymbol{P}_{background}$ vector. In reality, this background polarization also comes from resonant polarizations occurring at other frequencies and can then be treated by the Lorentz oscillator model. The polarization vector and relative permittivity become:

$$\boldsymbol{P} = \left(\sum_j \frac{N_j e^2}{m_0}\frac{1}{\omega_j^2 - \omega^2 - \mathrm{i}\gamma_j\omega}\right)\boldsymbol{E} \tag{1.29}$$

$$\varepsilon_r = 1 + \sum_j \frac{N_j e^2}{\varepsilon_0 m_0}\frac{1}{\omega_j^2 - \omega^2 - \mathrm{i}\gamma_j\omega} \tag{1.30}$$

with the subscript j indexing the different resonant oscillations with the respective resonance frequency ω_j and damping factor γ_j. Fig. 1.4 shows a hypothetical relative permittivity of a material with 3 resonant Lorentz oscillators at 3 different frequencies.

1.3.2. The Gallium Arsenide permittivity

Considering that GaAs is the material of interest in this thesis work, being able to model its dielectric function accurately is of great importance. The crystalline structure of this III-V compound has already been detailed in Section 1.2.1. As a reminder, the bonds are partially ionic which create a slightly asymmetric electron cloud between the column V and column III atoms. This property makes the crystal itself a dipole, which upon interaction with the transverse electric field of an impinging light wave induces oscillations of the entire lattice. This results in a transverse vibration of the crystal, whose modes are called Transverse Optical (TO) phonons. These modes are notoriously active in the THz and the IR frequency range.

Using the oscillator model developed in the previous section, the following relative permittivity can be derivated:

$$\varepsilon_{\mathrm{r}}(\omega) = \varepsilon_{\infty} + (\varepsilon_0 - \varepsilon_{\infty}) \frac{\omega_{\mathrm{TO}}^2}{\omega_{\mathrm{TO}}^2 - \omega^2 - \mathrm{i}\gamma_{\mathrm{ph}}\omega} \tag{1.31}$$

From the Lyddane-Sachs-Teller relation [32], it can be obtained:

$$\frac{\omega_{\mathrm{LO}}^2}{\omega_{\mathrm{TO}}^2} = \frac{\varepsilon_{\mathrm{lf}}}{\varepsilon_{\mathrm{hf}}} \tag{1.32}$$

where ω_{LO} is the Longitudinal Optical (LO) phonon frequency. The Eq. (1.31) can then be written:

$$\varepsilon_{\mathrm{r}}(\omega) = \varepsilon_{\mathrm{hf}} \left(1 + \frac{\omega_{\mathrm{LO}}^2 - \omega_{\mathrm{TO}}^2}{\omega_{\mathrm{TO}}^2 - \omega^2 - i\gamma_{\mathrm{ph}}\omega} \right) \tag{1.33}$$

The values of the longitudinal, transversal optical phonon and the damping coefficient can be found in the literature [33, 34, 35]. The following values were used : $\nu_{\mathrm{TO}} = 8.05\,\mathrm{THz}$, $\gamma_{\mathrm{TO}} = 75.2\,\mathrm{GHz}$ and $\nu_{\mathrm{LO}} = 8.75\,\mathrm{THz}$. An important result obtained from the phonon model is that between ν_{TO} and ν_{LO}, the real part of the relative permittivity is negative thus the reflectivity, calculated using the formula:

$$R = \left| \frac{\sqrt{\varepsilon_{\mathrm{r}}} - 1}{\sqrt{\varepsilon_{\mathrm{r}}} + 1} \right|^2 \tag{1.34}$$

yields a reflectivity close to 1. This band of frequency is called the Reststrahlen (residual rays in German), a frequency range in which light can not propagate in polar semiconductor. The reflectivity from 1 to 15 THz is plotted in Fig. 1.5. For GaAs, the Reststrahlen is between the TO- and LO-phonon frequency (8.05 and 8.75 THz).

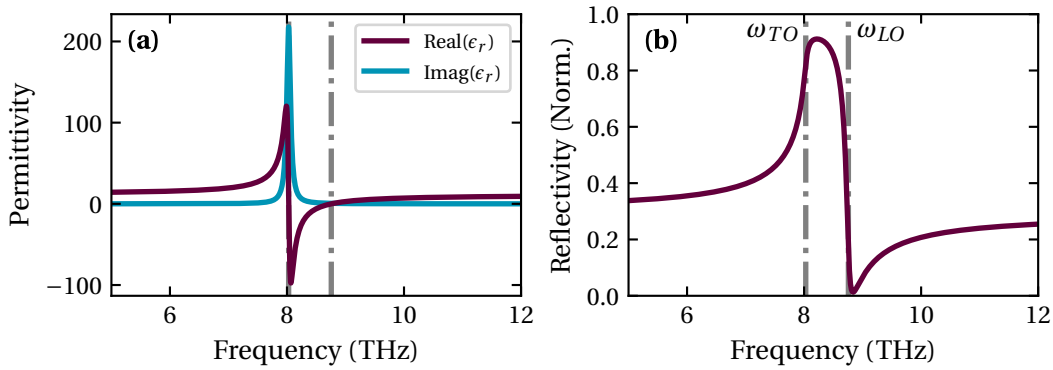

Figure 1.5.. **(a)**: Real and imaginary part of the GaAs permittivity. **(b)**: Gallium arsenide reflectivity in the THz range. The Reststrahlen band is the region between the TO- and LO-phonon frequency.

1.3.3. The Drude model for free electrons

The Lorentz oscillator model provides a way to understand the response of the bound electrons and the lattice to an optical pulse, but does not take into account the contribution of the free electrons. These electrons, which do not experience restoring forces from the lattice, can be found in metals and doped semiconductors, and contribute strongly in the optical response. They can be described as a plasma, a neutral gas of charged particles with the free electrons acting as negative charges, and the donor atoms as positive ions. When electrons are accelerated by an external electric field, they will undergo collisions with the heavy crystal atoms, bouncing and losing momentum with a characteristic time between collision events τ known as the scattering rate.

The derivation of the Drude model is somewhat similar to the Lorentz oscillator model, with the difference that no restoring force is considered in the motion equation. The damping term of the equation is the inverse of the scattering rate $\gamma = 1/\tau$. Using the same notation for the electric field used for the Lorentz oscillator model, the equation is:

$$m_0 \frac{\mathrm{d}^2 \boldsymbol{x}}{\mathrm{d}t^2} + m_0 \gamma \frac{\mathrm{d}\boldsymbol{x}}{\mathrm{d}t} = -e\boldsymbol{E} \tag{1.35}$$

Using similar arguments, the relative permittivity for a medium with free electron is:

$$\varepsilon_\mathrm{r}(\omega) = 1 - \frac{N e^2}{\varepsilon_0 m_0} \frac{1}{\omega^2 + \mathrm{i}\gamma\omega} = 1 - \frac{\omega_\mathrm{p}^2}{\omega^2 + \mathrm{i}\gamma\omega} \tag{1.36}$$

$$\text{with} \quad \omega_\mathrm{p} = \sqrt{\frac{N e^2}{\varepsilon_0 m_0}} \tag{1.37}$$

Here, N is the concentration of free electrons in a metal, or the dopant concentration in a semiconductor. ω_p is the plasma frequency and has an important meaning: it is the resonant frequency of the electron gas. Optically, this frequency marks the transition between two regimes: below the plasma frequency the plasma reflects the light, above it is transparent (see Figure Fig. 1.6 (b)).

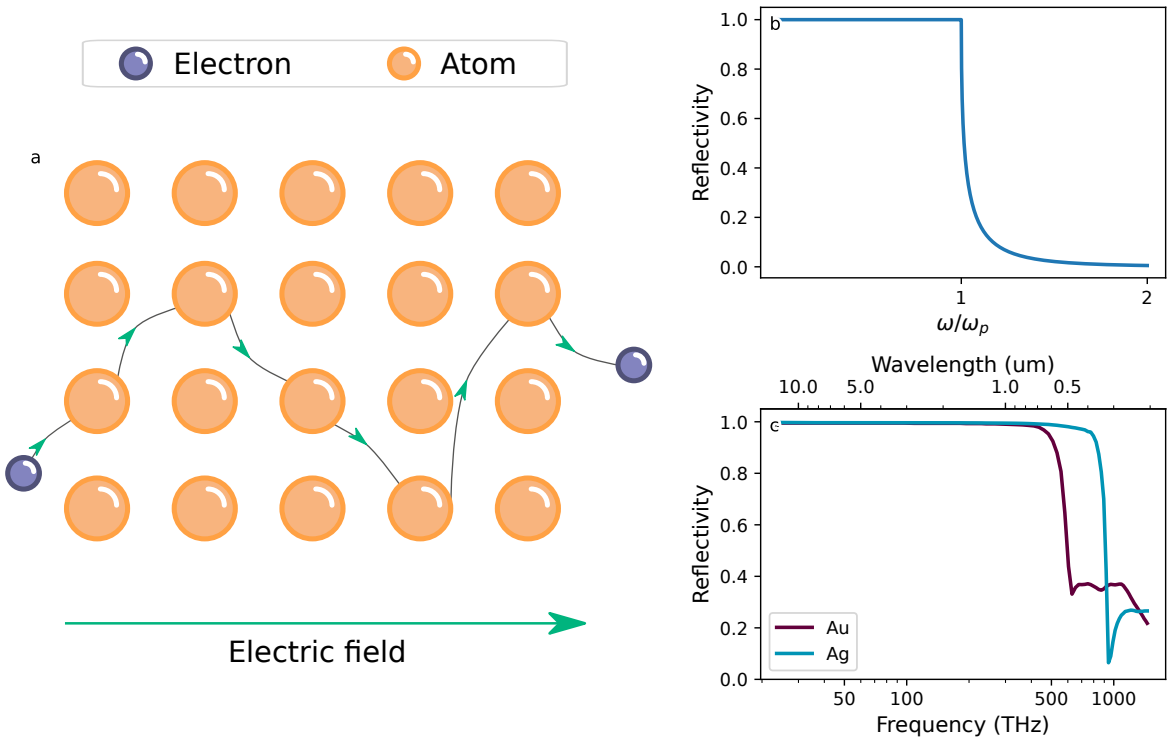

Figure 1.6.. (a): Movement of a free electron in a crystal lattice. The electron jitters between each bounce while having a net displacement in the same direction as the electric field. **(b)**: Experimental reflectivity of gold and silver.

Experimentally, such transition occurs, for instance for gold or silver, in the UV frequency range (see Fig. 1.6 (b)).

Eq. (1.35) can also be solved not in terms of the electron position, but in terms of the electron momentum $\boldsymbol{p} = m_0 \boldsymbol{v}$. In doing so, an interesting value can be extracted: the frequency dependent conductivity σ expressed as follows:

$$\sigma(\omega) = \frac{\sigma_0}{1 - i\omega\tau} \quad \text{with} \quad \sigma_0 = \frac{N e^2 \tau}{m_0} \tag{1.38}$$

σ_0 is the DC conductivity. An alternative form of Eq. (1.36) can be deduced:

$$\varepsilon_r(\omega) = 1 + \frac{i\sigma(\omega)}{\varepsilon_0 \omega} \tag{1.39}$$

Calculating the attenuation using this new expression of the relative permittivity, one can find:

$$\alpha = \sqrt{2\sigma_0 \omega \mu_0} \tag{1.40}$$

where μ_0 is the vacuum permeability. It is then possible to define the skin depth δ which is the penetration depth at which the amplitude E_0 of an impinging electromagnetic wave is decreased to E_0/e, e being the exponential constant such that $ln(e) = 1$. The skin depth is given by:

$$\delta = \sqrt{\frac{1}{\sigma_0 \omega \mu_0}} \tag{1.41}$$

For gold, the skin depth is around $\delta = 50\,\text{nm}$ in the THz range, and $\delta = 15\,\text{nm}$ in the MIR range. As a rule of thumb, using 4 or 5 times the skin depth for a metallic layer thickness ensures that the electromagnetic wave of a given frequency can not go through.

1.3.4. Extension of the relative permittivity of doped GaAs

When the relative permittivity of Gallium Arsenide was derived in Section 1.3.2, the Lorentz oscillator model was used, taking into account only the optical response of the lattice which is sufficient for an intrinsic GaAs medium. However, if this semiconductor is doped then the Drude model is mandatory to take into account the effect of the electron gas contribution. Using similar methods as done previously for the Drude model in a metal, the following expression of the relative permittivity can be obtained:

$$\varepsilon_\text{r}(\omega) = \varepsilon_\text{ph}(\omega) - \frac{\omega_\text{p}}{\omega^2 + i\gamma\omega} = \varepsilon_\infty \left(1 + \frac{\omega_\text{LO}^2 - \omega_\text{TO}^2}{\omega_\text{TO}^2 - \omega^2 - i\gamma_\text{ph}\omega}\right) - \frac{\omega_\text{p}}{\omega^2 + i\gamma\omega} \tag{1.42}$$

In this equation, ε_{ph} is the dielectric constant of the undoped medium, and ω_p is the plasma frequency which has one important difference compared to the expression derived Section 1.3.3:

$$\omega_\text{p} = \sqrt{\frac{N e^2}{\varepsilon_0 m^*}} \tag{1.43}$$

m^* is the electron mass in GaAs, and is equal to $0.067 m_0$, with m_0 the free electron mass.

1.4. Intersubband absorption in quantum wells

In Section 1.2 the band structure and wavefunctions of a semiconductor was derived from the Schrödinger equation, which describes the behavior of the electron in the structure. The goal of this section is to elucidate the interaction between an electromagnetic wave and an electron in a quantum well using a semi-classical approach.

1.4.1. The interaction Hamiltonian

The starting point of this demonstration is the interaction Hamiltonian between an electric field and an electron. Considering an electromagnetic plane wave defined by:

$$\boldsymbol{E}(\boldsymbol{r},t) = E_0 \hat{e} cos\left(\omega t - \boldsymbol{q}\cdot\boldsymbol{r}\right) \tag{1.44}$$

where E_0 is the wave amplitude, $\boldsymbol{e}$ is the polarization vector and $\boldsymbol{q}$ is the wavevector, the Hamiltonian of an electron in a quantum well structure can be written as:

$$H = \frac{\left(\boldsymbol{p} - e\boldsymbol{A}(\boldsymbol{r},t)\right)^2}{2m^*} + V(\boldsymbol{r}) \tag{1.45}$$

In this equation, $\boldsymbol{p}$ is the momentum operator $-i\hbar\nabla$, $\boldsymbol{A}(\boldsymbol{r},t)$ is the vector potential defined by the relation $\boldsymbol{E}(\boldsymbol{r},t) = -\frac{\partial \boldsymbol{A}(\boldsymbol{r},t)}{\partial t}$, e the electron charge, m^* the electron mass in the quantum well and $V(\boldsymbol{r})$ is the crystal potential.

Eq. (1.45) can be expended into:

$$H = H_0 + H_{\text{int}} \tag{1.46}$$

$$H_0 = \frac{\boldsymbol{p}^2}{2m^*} + V \tag{1.47}$$

$$H_{\text{int}} = -\frac{e}{2m^*}\left(\boldsymbol{p}\cdot\boldsymbol{A} + \boldsymbol{A}\cdot\boldsymbol{p}\right) + \frac{e^2\boldsymbol{A}^2}{2m^*} \tag{1.48}$$

H_0 is the atomic Hamiltonian and H_{int} is the interaction Hamiltonian resulting from the electromagnetic plane wave. H_{int} can be simplified by considering two things:

- Using the Coulomb gauge ($\nabla\boldsymbol{A} = 0$), the momentum operator $\boldsymbol{p}$ and potential vector $\boldsymbol{A}$ commute thus $\boldsymbol{p}\cdot\boldsymbol{A} = \boldsymbol{A}\cdot\boldsymbol{p}$ [36].
- At the considered wavelength (in the micron range and more), the momentum of the electron is much bigger than the light momentum, thus $|e\boldsymbol{A}| \ll |\boldsymbol{p}|$. The quadratic term is then negligible compared to the linear term as long as only low intensity fields are considered.

The interaction Hamiltonian can then be written:

$$H_{\text{int}} = \frac{e}{m^*}\boldsymbol{p}\cdot\boldsymbol{A} \tag{1.49}$$

1.4.2. Transition rate: Fermi's golden rule

The interaction Hamiltonian can be considered as a weak harmonic perturbation, thanks to the fact the vector potential $\boldsymbol{A}$ is a plane wave, and that the amplitude of the electric field was chosen to be small to make the quadratic term negligible. It is then possible to use the Fermi's golden rule to calculate the transition rate $W_{i\to f}$ between two eigenstates Ψ_i and Ψ_f, respectively the initial and final state. Using the envelope function formalism introduced Section 1.2.5, the eigenstates can be expressed as follows:

$$\Psi_i(\boldsymbol{r}) = \frac{1}{\sqrt{S}} e^{i\boldsymbol{k}_{\parallel,i}\cdot\boldsymbol{r}} u_i(\boldsymbol{r})\Phi_i(z) \tag{1.50}$$

$$\Psi_f(\boldsymbol{r}) = \frac{1}{\sqrt{S}} e^{i\boldsymbol{k}_{\parallel,f}\cdot\boldsymbol{r}} u_f(\boldsymbol{r})\Phi_f(z) \tag{1.51}$$

Using Fermi's golden rules it can be recast as:

$$W_{i\to f} = \frac{2\pi}{\hbar} \left|\langle\Psi_i(\boldsymbol{r})|H_{int}|\Psi_f(\boldsymbol{r})\rangle\right|^2 \delta\left(E_f - E_i - \hbar\omega\right) \tag{1.52}$$

$$= \frac{2\pi}{\hbar} \frac{e^2 E_0^2}{4m^{*2}\omega^2} \left|\langle\Psi_i(\boldsymbol{r})|\boldsymbol{e}\cdot\boldsymbol{p}|\Psi_f(\boldsymbol{r})\rangle\right|^2 \delta\left(E_f - E_i - \hbar\omega\right) \tag{1.53}$$

Taking a closer look at the matrix element, it can be expended into two terms:

$$\langle\Psi_i(\boldsymbol{r})|\boldsymbol{e}\cdot\boldsymbol{p}|\Psi_f(\boldsymbol{r})\rangle = \langle u_i(\boldsymbol{r})|\boldsymbol{e}\cdot\boldsymbol{p}|u_f(\boldsymbol{r})\rangle\langle\Phi_i(z)|\Phi_f(z)\rangle + \langle u_i(\boldsymbol{r})|u_f(\boldsymbol{r})\rangle\langle\Phi_i(z)|\boldsymbol{e}\cdot\boldsymbol{p}|\Phi_f(z)\rangle \tag{1.54}$$

The first term corresponds to inter-band transitions, and is expected to vanish as the systems of interest are supposed to exhibit only intersubband transitions with a Fermi level at least between the first and second subband. The second term describes the intersubband transition rate. Several interesting properties can be obtained by expending this term. First, the overlap integral of the Bloch function $\langle u_i|u_f\rangle$ is equal to unity because transitions from states within the same subband are considered, thus $u_i = u_f$. Also, the transitions conserve the electron wavevector, i.e. $\boldsymbol{k}_{\parallel,i} = \boldsymbol{k}_{\parallel,f}$. Following these rules and remembering that the envelope function depends only on the confinement direction z, the matrix element becomes:

$$\langle\Psi_i(\boldsymbol{r})|\boldsymbol{e}\cdot\boldsymbol{p}|\Psi_f(\boldsymbol{r})\rangle = \langle\Phi_i(z)|p_z|\Phi_f(z)\rangle\,\boldsymbol{e_z} \tag{1.55}$$

Finally, by employing the electric-dipole approximation, it can be further simplified [37, 38]:

$$\langle\Phi_i(z)|p_z|\Phi_f(z)\rangle\,\boldsymbol{e_z} = i\frac{m^*}{\hbar}\left(E_f - E_i\right)\langle\Phi_i(z)|\hat{z}|\Phi_f(z)\rangle\,\boldsymbol{e_z} \tag{1.56}$$

This result highlights two important rules about intersubband transitions:

- Only the vector component along the z-direction of the EM wave remains after the scalar product between $\boldsymbol{e}$ and the electron momentum operator $\boldsymbol{p}$. It means that in order to couple to an intersubband transition, the electric field must have a non-zero component along the growth axis (here chosen to be the z-axis).
- Considering a quantum well wavefunction having the form of Eq. (1.19), the matrix element $\langle\psi_i|\hat{z}|\psi_f\rangle$ imposes a condition of parity on the initial and final wavefunctions. The position operator $\hat{z}$ is an odd function, which implies that $\Psi_i^*\Psi_f$ needs to also be an odd function. This condition is fulfilled only when one of the wavefunction is odd and the other even (at least for the special case where potentials with mirror symmetry are considered). This is the case when the difference of band index is an odd number (for example $1 \to 2$, $2 \to 3$ or $1 \to 4$ are allowed, but $1 \to 3$ or $1 \to 5$ are not)

Inserting Eq. (1.56) into Eq. (1.52), the Fermi's golden rule can be cast as follows:

$$W_{i\to f} = \frac{\pi e^2 I_z f_{i\to f}}{2m^*\omega\varepsilon_0 c\sqrt{\varepsilon_r}}\delta\left(E_f - E_i - \hbar\omega\right) \tag{1.57}$$

where $f_{i\to f}$ and I_z are respectively the oscillator strength of the transition and the incident beam intensity of the electromagnetic wave defined as follows:

$$f_{i\to f} = \frac{2m^*\omega}{\hbar}\langle\Psi_i|\hat{z}|\Psi_f\rangle \quad \text{and} \quad I_z = \frac{\varepsilon_0 c\sqrt{\varepsilon_r}E_0^2}{2} \tag{1.58}$$

In order to make the link between Eq. (1.57) and the experiment easier, two refinements can be done:

- The current expression of the transition rate is for a single electron. By introducing the electronic density per unit surface N_i and N_j, and making the assumption that the electrons do not interact with each other (which is true for small density), then the transition rate can be weighted by the number of possible transitions $(N_i - N_j)S$ with S the surface of the sample.
- Experimentally, the transition can occur at wavelengths different from the transition energy due to the natural homogeneous broadening of the energy levels. The sources are numerous: electron-electron scattering, electron-phonon scattering, interface roughness ... To take these effects into account, the delta function can be replaced with a Lorentzian function centered at the transition frequency ω_{21} and Full Width at Half Maximum (FWHM) γ: $L(\omega) = \frac{\frac{\gamma}{\pi}}{(\omega-\omega_{21})^2+\gamma^2}$

Therefore, the final expression of the transition rate becomes:

$$W_{i\to f} = \frac{(N_i - N_j)Se^2 I_z f_{i\to f}}{2m^*\omega\varepsilon_0 cn}\frac{\gamma}{(\omega-\omega_{21})^2+\gamma^2} \tag{1.59}$$

In the context of a square quantum well, only the transition between the first and second subband is meaningful. The reason is that the oscillator strength of the transition $1 \to 2$ is way higher

than any other transitions ($f_{1\to 2} = 0.96$ while $f_{1\to 4} = 0.03$). In the following sections, only the first subband will be considered populated, with a density N ($N_1 - N_2 = N$).

1.4.3. Absorption in a quantum well

In general, the absorbance α_{3D} of a medium is defined as the ratio of the absorbed electromagnetic energy per unit volume divided by the electromagnetic field intensity. Applied to a quantum well structure, $\alpha_{3d} = \hbar\omega W_{i\to f}/VI_z$ with V the effective volume where the absorption occurs. While this formula is general, it remains unsuited for a system like a quantum well due to the quasi-two-dimensional absorption area. In that case, a more convenient quantity can be defined: the 2D absorption α_{2D} which is related to the 3D absorption through the relation $\alpha_{2D} = \alpha_{3D} L_{\text{eff}}$. L_{eff} is the length over which the electromagnetic wave is effectively absorbed by the quantum well. A good first approximation is to consider $L_{\text{eff}} \approx L_{\text{well}}$. The 2D absorption can then be written [38]:

$$\alpha_{2D}(\omega) = \frac{N e^2 \hbar f_{12}}{2m^* \varepsilon_0 c \sqrt{\varepsilon_r}} \frac{\gamma}{(\omega - \omega_{21})^2 + \gamma^2} \tag{1.60}$$

From the expression of the absorption, and remembering that $\alpha_{3D} = \frac{\omega}{c\sqrt{\varepsilon_r}} Im[\varepsilon(\omega)]$ [37], the permittivity with the ISB transition contribution can be written:

$$\varepsilon_{\text{ISB}} = \varepsilon_r \left(1 - \frac{\omega_{p,QW}^2}{\omega^2 - \omega_{21}^2 + i\gamma\omega}\right) \tag{1.61}$$

with $\omega_{\text{p,QW}} = \sqrt{\frac{N_s e^2 f_{12}}{\varepsilon_0 \varepsilon_r m^* L_{eff}}}$ is the ISB transition plasma frequency.

1.4.4. Many body effects in a quantum well: the depolarization shift

In the previous section, the ISB absorption was derived under the assumption that the electrons were independent. While this may be a valid approximation in very low doping quantum well, standard structures used for strong-coupling have a 2D doping ranging from 10^{11} cm^{-2} to $5 \cdot 10^{12}$ cm^{-2}. This implies a strong interaction between the electrons. When an electron is promoted from its initial subband to another, the whole electromagnetic environment seen by the 2D electron gas changes, which impact the optical response of the material.

To take into account this effect in the absorption, the electron density interacting with an external electromagnetic field can be treated as an oscillating current density which follows the formula $j_z = \tilde{\sigma}_{zz} E$ where $\tilde{\sigma}_{zz}$ is the two-dimensional conductivity [38]. Without entering into the details (see Ref. [39, 40] for a complete walkthrough), the effective conductivity can be written:

$$\tilde{\sigma}_{zz} = \frac{N_s e^2 f_{12}}{\varepsilon_r m^*} \frac{i\omega}{\omega^2 - \tilde{\omega_{21}}^2 + i2\gamma\omega} \tag{1.62}$$

where $\tilde{\omega}_{21} = \sqrt{\omega_{21}^2 + \omega_p^2}$ is ISB resonance frequency shifted by a contribution due to the electron gas. Using the Drude-Lorentz oscillator model (see Section 1.3.3), a permittivity taking into account the depolarization shift can be obtained:

$$\frac{1}{\varepsilon_{\mathrm{ISB}}} = \varepsilon_r^{-1}\left(1 + \frac{\omega_{p,\mathrm{QW}}^2}{\omega^2 - \tilde{\omega}_{21}^2 + i\gamma\omega}\right) \tag{1.63}$$

and the 2D absorption becomes:

$$\alpha_{2D}(\omega) = -\frac{\omega\sqrt{\varepsilon_r}L_{\mathrm{eff}}}{c} Im\left[\frac{1}{\varepsilon_{\mathrm{ISB}}(\omega)}\right] \tag{1.64}$$

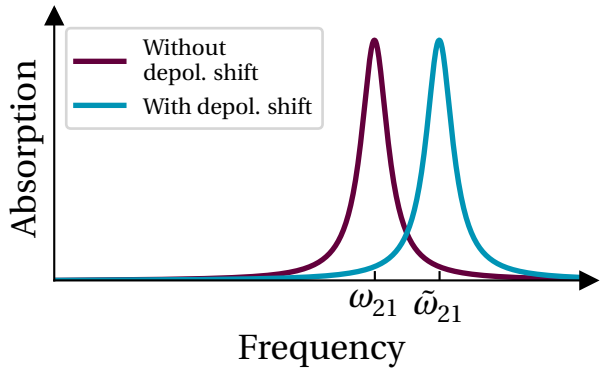

Figure 1.7.. Absorption of an ISB transition of a doped quantum well with and without taking into account the depolarization shift

In Fig. 1.7, the schematized absorptions of a quantum well with the isolated electron picture and when the many body effects are taken into account are shown. The corrected resonance frequency $\tilde{\omega}_{21}$ is effectively the new frequency at which the quantum well absorbs.

1.4.5. The effective medium approximation

The permittivity derived from the many body effect allows to model an ISB transition in a quantum well. Using this permittivity is equivalent to treat an active region as a uniform medium, without taking into account the barrier and the interferences coming from the multiple reflections at the well/barrier interfaces. While Eq. (1.63) is a good approximation when the barrier and well permittivity are close, a more accurate picture may be needed for active region with a high number of quantum well (QW). In Ref. [41], an effective medium approach taking into account the superlattice structure is developed. The expressions of the permittivity tensor are:

$$\varepsilon_{xx,yy}(\omega) = \langle \varepsilon(\omega, z) \rangle - \frac{\omega_{\mathrm{p}}^2}{\omega^2 + \mathrm{i}\gamma\omega} \tag{1.65}$$

$$\frac{1}{\varepsilon_{zz}(\omega)} = \left\langle \frac{1}{\varepsilon(\omega, z)} \right\rangle + \frac{\omega_{\mathrm{p,QW}}^2}{\omega^2 - \tilde{\omega}_{21}^2 + \mathrm{i}\gamma_{\mathrm{QW}}\omega} \tag{1.66}$$

where ω_{p} and $\omega_{\mathrm{p,QW}}$ are respectively the bulk and quantum well plasma frequency, $\varepsilon(\omega, z)$ the Lorentz permittivity of the material at the z-position in the quantum well stack, and $\langle . \rangle$ the average over a quantum well period.

For a square quantum well, these permittivity averages are:

$$\langle \varepsilon(\omega, z) \rangle = (1 - f_{\mathrm{w}})\varepsilon_{\mathrm{b}} + f_w \varepsilon_{\mathrm{w}} \tag{1.67}$$

$$\left\langle \frac{1}{\varepsilon(\omega, z)} \right\rangle = \frac{1 - f_{\mathrm{w}}}{\varepsilon_{\mathrm{b}}} + \frac{f_{\mathrm{w}}}{\varepsilon_{\mathrm{w}}} \tag{1.68}$$

with $f_{\mathrm{w}} = L_{\mathrm{well}}/(L_{\mathrm{well}} + L_{\mathrm{barrier}})$ is the quantum well overlap factor.

1.5. The concept of intersubband polaritons

1.5.1. Light-matter interaction and weak coupling

An optical cavity is a structure whose purpose is to confine light into a defined volume. In 1947, Purcell demonstrated that the light-matter interaction can be enhanced in presence of a photonic cavity [42]. This effect led to a new research field named cavity Quantum Electrodynamics (cQED) [43]. In general, the transition rate between states of a two level system is proportional to the density of states (DOS). The introduction of a cavity allows to "engineer" the number of final states, thus increasing the DOS compared to a two-level system in free space. A frequently used picture is the two oscillators coupled system. Each oscillator possesses a damping rate, and interact with each other through a coupling constant g.

In the case where the coupling constant is smaller than the damping rates of both oscillators, the emitted photons leave the cavity after a specific decay time. This regime is called the weak coupling regime. There is a negligible probability for the photon to be recaptured by the two-level system and thus the probability to recover the system in an excited state decays exponentially after the emission.

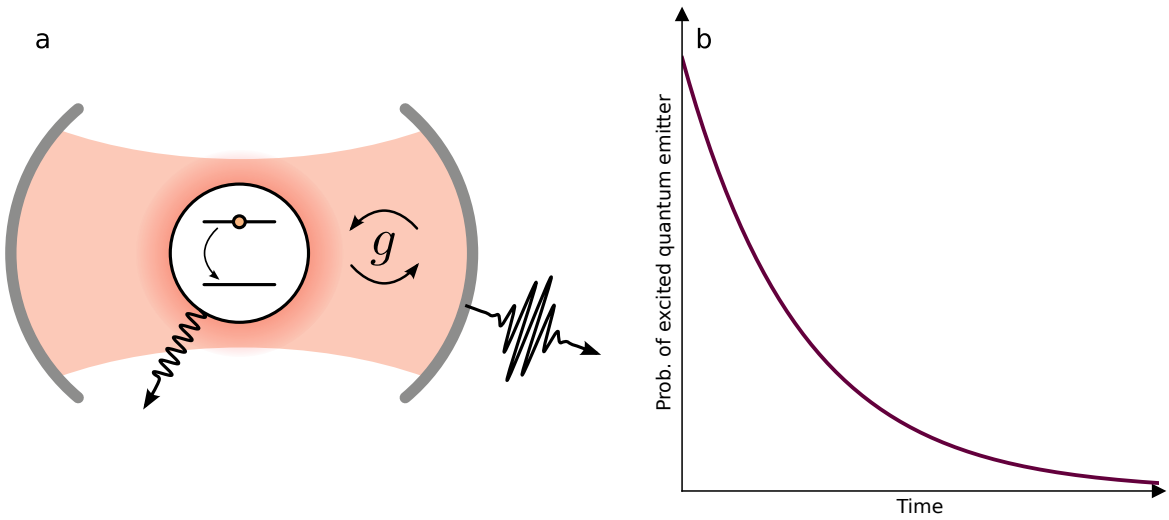

Figure 1.8.. **(a)**: Cavity in the weak coupling regime. After the quantum emitter relaxation, the emitted photon is not recaptured. **(b)**: Probability of having the quantum emitter in the excited state vs time.

1.5.2. Strong light matter coupling

In order to increase the probability of recapturing the emitted photon, one may engineer the system in such a way that the coupling constant of the two oscillators dominates the damping of the two isolated oscillators, which leads to a periodic exchange of energy between the two level system and the cavity. This regime, where the probability of having the excited state is not exponentially decaying, is called the strong coupling regime. The eigenstates of the system are no longer dipolar excitation and light, but a mixture of both called polaritons. Such a state was first observed for atoms [44, 45].

The first study of the strong coupling regime in a solid-state system originates from Hopfield in 1958 [46] and further studied by Jaynes and Cummings [47]. It was later observed in a quantum well microcavity [48], and a decade later for intersubband transitions [49].

1.5.3. Strong coupling in the Jaynes-Cummings model

In order to obtain a simple description of the strong light-matter coupling, the most basic system is considered. It is composed of a cavity and a single electron in a quantum well. The electron can be seen as a two level system with the two states $\langle g|$ and $\langle e|$. $\langle g|$ refers the state where the electron is in the ground state, and $\langle e|$ to the excited state and defines the Hilbert space of the two level system. Similarly, the cavity photon can be described by the states $\langle 0|$ and $\langle 1|$, corresponding respectively to the state where zero or one photon is present in the cavity

The Hamiltonian of the system has the form:

$$\widehat{H} = \widehat{H}_{\text{cav}} + \widehat{H}_{\text{ISB}} + \widehat{H}_{\text{int}} \tag{1.69}$$

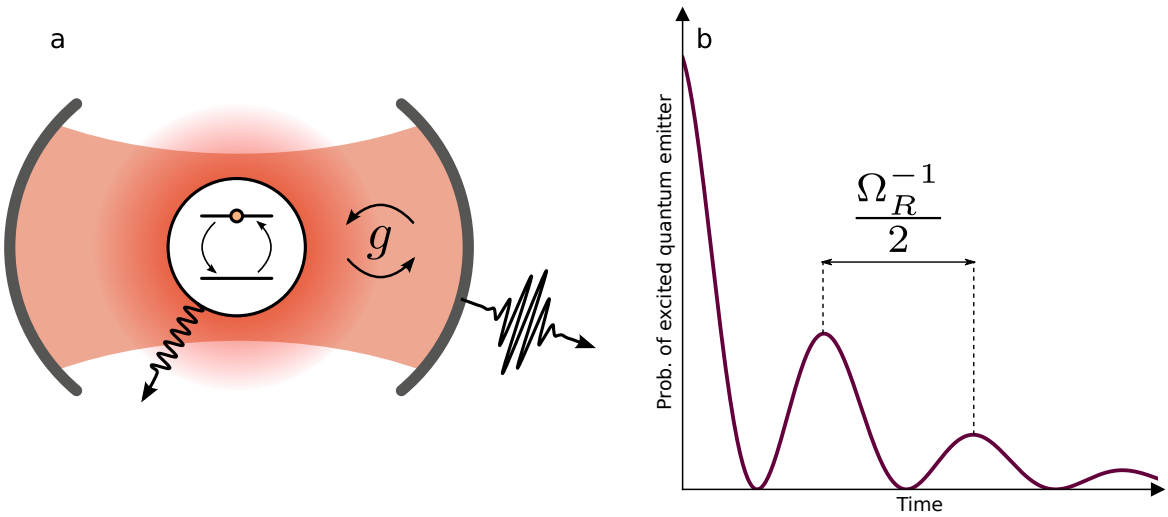

Figure 1.9.. (a): Cavity in the strong coupling regime. After the quantum emitter relaxation, the emitted photon will not exit the cavity but instead will be reabsorbed by the quantum emitter. **(b)**: Probability of having the quantum emitter in the excited state vs time.

where $\widehat{H}_{\text{cav}}$, $\widehat{H}_{\text{ISB}}$ and $\widehat{H}_{\text{int}}$ are respectively the cavity, the electron in a quantum well and the interaction Hamiltonian. In the second quantization, the cavity photon Hamiltonian takes the following form:

$$\widehat{H}_{\text{cav}} = \hbar\omega_{\text{cav}}(\widehat{a}^{\dagger}\widehat{a}) \tag{1.70}$$

where $\widehat{a}^{\dagger}$ and $\widehat{a}$ are the creation and annihilation operators of a cavity photon. The Hamiltonian of the two level system has the expression:

$$\widehat{H}_{ISB} = \hbar\omega_0 \left|g\right\rangle\left\langle g\right| + \hbar\omega_1 \left|e\right\rangle\left\langle e\right| \tag{1.71}$$

with ω_0 and ω_1 the frequency of the ground and excited states. To simplify this Hamiltonian, the fermionic operators $\widehat{\sigma}^{\dagger} = \left|e\right\rangle\left\langle g\right|$ and $\widehat{\sigma} = \left|g\right\rangle\left\langle e\right|$ can be defined. The operator $\widehat{\sigma}^{\dagger}$ is the promotion of an electron from the ground state to the excited state. By using these operators, and choosing the energy of the ground state to be zero, the ISB Hamiltonian reads:

$$\widehat{H}_{\text{ISB}} = \hbar\omega_{12}\widehat{\sigma}^{\dagger}\widehat{\sigma} \tag{1.72}$$

with ω_{12} the frequency difference between the ground and excited states.

For the interaction Hamiltonian, an electric dipole interaction is considered. The expression is:

$$\widehat{H}_{\text{int}} = -\widehat{\boldsymbol{d}} \cdot \widehat{\boldsymbol{E}} \tag{1.73}$$

with $\hat{\boldsymbol{d}}$ and $\hat{\boldsymbol{E}}$ are the dipole and electric field operators. Both operators can be expressed in the second quantization picture. Starting with the dipole operator, for a moment along the z-direction (to be consistent with the notation used Section Fermi golden rule for ISB), $\hat{\boldsymbol{d}} = -q\hat{\boldsymbol{z}}$. Using the fact that $|g\rangle$ and $|e\rangle$ form a complete basis of the two level system, the dipole operator becomes:

$$\hat{\boldsymbol{d}} = -q(|g\rangle\langle g| + |e\rangle\langle e|)\hat{\boldsymbol{z}}(|g\rangle\langle g| + |e\rangle\langle e|) \tag{1.74}$$
$$= -q(|e\rangle\langle g|\langle e|\hat{\boldsymbol{z}}|g\rangle + |g\rangle\langle e|\langle g|\hat{\boldsymbol{z}}|e\rangle) \tag{1.75}$$
$$= \hat{\sigma}^\dagger \boldsymbol{d}_{eg} + \hat{\sigma}\boldsymbol{d}_{eg}^* = \boldsymbol{d}_{eg}(\hat{\sigma}^\dagger + \hat{\sigma}) \tag{1.76}$$

where $\boldsymbol{d}_{eg}$ is the dipole moment vector, and the dipole matrix element $\langle g|\hat{\boldsymbol{z}}|g\rangle$ and $\langle e|\hat{\boldsymbol{z}}|e\rangle$ are assumed to be null. In second quantization, the electric field operator reads $\hat{\boldsymbol{E}} = \mathrm{i}\mathscr{E}_0(\hat{a} - \hat{a}^\dagger)$ where $\mathscr{E}_0 = \sqrt{\frac{\hbar\omega_c}{2\varepsilon_0\varepsilon_r V_{\text{mode}}}}$ with V the mode volume and ε_r the relative permittivity. Substituting the terms in the interaction Hamiltonian yields:

$$\hat{H}_{\text{int}} = -\mathrm{i}d_{eg}\mathscr{E}_0(\hat{\sigma}^\dagger + \hat{\sigma})(\hat{a} - \hat{a}^\dagger) \tag{1.77}$$

To obtain a more practical form of the interaction Hamiltonian, the coupling constant $g = d_{eg}\mathscr{E}_0/\hbar$ is introduced. Recalling the expression of the dipole matrix element of an intersubband transition (see Eq. (1.58)), the coupling constant becomes:

$$g = \sqrt{\frac{q^2 f_{1\to 2}}{4\varepsilon_r\varepsilon_0 m^* V_{\text{mode}}}} \tag{1.78}$$

The total interaction Hamiltonian is:

$$\hat{H} = \hbar\omega_{\text{cav}}(\hat{a}^\dagger\hat{a}) + \hbar\omega_{12}\hat{\sigma}^\dagger\hat{\sigma} + \mathrm{i}\hbar g(\hat{\sigma}^\dagger + \hat{\sigma})(\hat{a} - \hat{a}^\dagger) \tag{1.79}$$

This form of the Hamiltonian is called the quantum Rabi model, historically used to describe the nuclear spin of an atom, modeled as a two level system, with varying magnetic field.

The interaction Hamiltonian can be further expanded into:

$$\hat{H}_{\text{int}} = \mathrm{i}\hbar g(\hat{\sigma}^\dagger\hat{a} - \hat{\sigma}^\dagger\hat{a}^\dagger + \hat{\sigma}\hat{a} - \hat{\sigma}\hat{a}^\dagger) \tag{1.80}$$

The terms $\hat{\sigma}^\dagger\hat{a}$ and $\hat{\sigma}\hat{a}^\dagger$ are called resonant terms and represent the energy exchange between light and matter. The two other terms $\hat{\sigma}^\dagger\hat{a}^\dagger$ and $\hat{\sigma}\hat{a}$ are called non-resonant or counter-rotating terms and represent the process of creation or destruction of both light and matter excitations at the same time. A very common approximation, called the Rotating Wave Approximation (RWA) states that in a case where the coupling constant is small compared to the cavity and two level system frequency ($|g| \ll \omega_{\text{c,ISB}}$) and the detuning between the cavity and the two level system frequency is small ($|\omega_c - \omega_{\text{ISB}}| \ll \omega_c + \omega_{\text{ISB}}$) then the counter-rotating terms can be neglected. In this approximation, the total Hamiltonian reads:

$$\widehat{H} = \hbar\omega_{\text{cav}}(\widehat{a}^{\dagger}\widehat{a}) + \hbar\omega_{12}\widehat{\sigma}^{\dagger}\widehat{\sigma} + \text{i}\hbar g(\widehat{\sigma}^{\dagger}\widehat{a} - \widehat{\sigma}\widehat{a}^{\dagger}) \tag{1.81}$$

This form of the quantum Rabi Hamiltonian in the RWA approximation is known as the Jaynes-Cummings model and represents one of the simplest models for studying the interaction between a two level system (atom, ISB transition, ...) and a field.

To diagonalize this Hamiltonian, it is cast in a matrix representation, in the basis $|0, e\rangle$ and $|1, g\rangle$. One obtains:

$$\widehat{H} = \begin{pmatrix} \hbar\omega_{\text{cav}} & \text{i}\hbar g \\ -\text{i}\hbar g^{*} & \hbar\omega_{\text{isb}} \end{pmatrix} \tag{1.82}$$

In this current representation, the system does not take into account damping. In order to complete the model, they can be introduced by adding a complex phenomenological term γ_{cav} and γ_{ISB} to the cavity and ISB energy:

$$\widehat{H} = \begin{pmatrix} \hbar\omega_{\text{cav}} - i\hbar\gamma_{\text{cav}} & \text{i}\hbar g \\ -\text{i}\hbar g^{*} & \hbar\omega_{\text{ISB}} - \text{i}\hbar\gamma_{\text{ISB}} \end{pmatrix} \tag{1.83}$$

This matrix representation can be diagonalized in order to find the eigenstates and eigenenergies arising from the coupling of the cavity photon and the ISB transition. Let's define these eigenstates $|\Phi_{\text{UP}}\rangle$ and $|\Phi_{\text{LP}}\rangle$ and the eigenenergies E_{UP} and E_{LP}. The eigenenergies can be found by solving the equation:

$$\det\left(\widehat{H} - E\right) = 0 \tag{1.84}$$

The calculation yields the following eigenenergies:

$$E_{\text{UP/LP}} = \frac{E_{\text{cav}} + E_{\text{ISB}} - \text{i}\hbar(\gamma_{\text{cav}} + \gamma_{\text{ISB}})}{2} \pm \frac{\sqrt{4\hbar^2 g^2 + \hbar^2(\omega_{\text{cav}} - \omega_{\text{ISB}} - i(\gamma_{\text{cav}} - \gamma_{\text{ISB}}))^2}}{2} \tag{1.85}$$

From this result, two different regimes can be distinguished. By considering $E_{\text{UP/LP}}$ with zero detuning between the cavity and the ISB transition ($\omega_{\text{cav}} = \omega_{\text{ISB}}$), the energies of the system become:

$$E_{\text{UP/LP}} = \frac{E_{\text{cav}} + E_{\text{ISB}} - \text{i}\hbar(\gamma_{\text{cav}} + \gamma_{\text{ISB}})}{2} \pm \frac{\sqrt{4\hbar^2 g^2 - \hbar^2(\gamma_{\text{cav}} - \gamma_{\text{ISB}})^2}}{2} \tag{1.86}$$

In the case where $2g < |\gamma_{\text{cav}} - \gamma_{\text{ISB}}|$, the part under the square root is negative thus the two eigenenergies are the cavity and ISB transition energies. The cavity and ISB transition dispersion depending on the detuning can be seen Fig. 1.10 (a). At zero detuning, the system is degenerate. The cavity and ISB transition energy differ only by their imaginary part, corresponding to their respective losses. This state is called the weak coupling and is characterized by an enhancement of the spontaneous emission called the Purcell effect [42].

On the contrary when $2g > |\gamma_{\text{cav}} - \gamma_{\text{ISB}}|$, the system possesses two eigenenergies separated by the Rabi splitting $\hbar\Omega_{\text{R}} = \sqrt{(\hbar g)^2 - \hbar^2(\gamma_{\text{cav}} - \gamma_{\text{ISB}})^2}$. This state is called the strong-coupling regime.

In these conditions, the new eigenstates of the system can be written:

$$|\Psi\rangle_{\text{UP}} = \alpha_{\text{UP}}|g,1\rangle + \beta_{\text{UP}}|e,0\rangle \tag{1.87}$$

$$|\Psi\rangle_{\text{LP}} = \alpha_{\text{LP}}|g,1\rangle + \beta_{\text{LP}}|e,0\rangle \tag{1.88}$$

where the coefficients $\alpha_{\text{UP/LP}}$ and $\beta_{\text{UP/LP}}$ are called the Hopfield coefficients [46]. They correspond to the light and matter parts of the renormalized states. Those coefficients are obtained by diagonalizing the Hamiltonian matrix without the complex damping Eq. (1.82) and their expressions depending on the detuning between the cavity and the ISB frequency $\Delta E = \hbar\omega_{\text{c}} - \hbar\omega_{\text{ISB}}$ are:

$$\alpha_{\text{UP}}^2 = \beta_{\text{LP}}^2 = \frac{\Delta E + \sqrt{\Delta E^2 + (2\hbar g)^2}}{2\sqrt{\Delta E^2 + (2\hbar g)^2}} \tag{1.89}$$

$$\alpha_{\text{LP}}^2 = \beta_{\text{UP}}^2 = \frac{(2\hbar g)^2}{2\sqrt{\Delta E^2 + (2\hbar g)^2}(\Delta E + \sqrt{\Delta E^2 + (2\hbar g)^2})} \tag{1.90}$$

The solid lines of Fig. 1.10 (a) and (b) are the eigenenergy dispersions and Hopfield coefficients in the strong-coupling regime depending on the detuning. The color change represents the photonic and matter fraction of the renormalized states depending on the detuning. At negative detuning, the upper polariton is mostly a matter excitation mode and the lower polariton a photonic mode. When the cavity is getting resonant with the matter excitation, the two modes become mixed states up to the zero detuning where both modes are half matter / half light with a minimum energy splitting.

Up to now, the derivation of the system was done using a single quantum emitter (one electron in a well). For a real quantum well, several electrons participate to the process. It is possible to adapt our simple model in order to take into account these numerous 2-level systems. Let's consider a quantum well with two parabolic subbands E_1 and E_2. The well has a surface density of electrons N_{s}, thus a total number of electrons $N = N_{\text{s}}S$ with S the surface of the cavity.

In this basis, the system Hamiltonian can be written:

$$\widehat{H} = \widehat{H}_{\text{cav}} + \sum_{n=1}^{N} \hbar\omega_{\text{ISB}}\widehat{\sigma}_n^{\dagger}\sigma_n + \text{i}\sum_{n=1}^{N} \hbar g(\widehat{\sigma}_n\widehat{a}^{\dagger} + \widehat{\sigma}_n^{\dagger}\widehat{a}) \tag{1.91}$$

Using the matrix representation, omitting the imaginary damping to make the calculation easier, the system is described as:

$$\widehat{H} = \begin{pmatrix} \hbar\omega_{\text{cav}} & \text{i}\hbar g & \text{i}\hbar g & \cdots & \text{i}\hbar g \\ -\text{i}\hbar g^* & \hbar\omega_{\text{ISB}} & 0 & \cdots & 0 \\ -\text{i}\hbar g^* & 0 & \hbar\omega_{\text{ISB}} & \ddots & \vdots \\ \vdots & \vdots & \ddots & \ddots & 0 \\ -\text{i}\hbar g^* & 0 & \cdots & 0 & \hbar\omega_{\text{ISB}} \end{pmatrix} \tag{1.92}$$

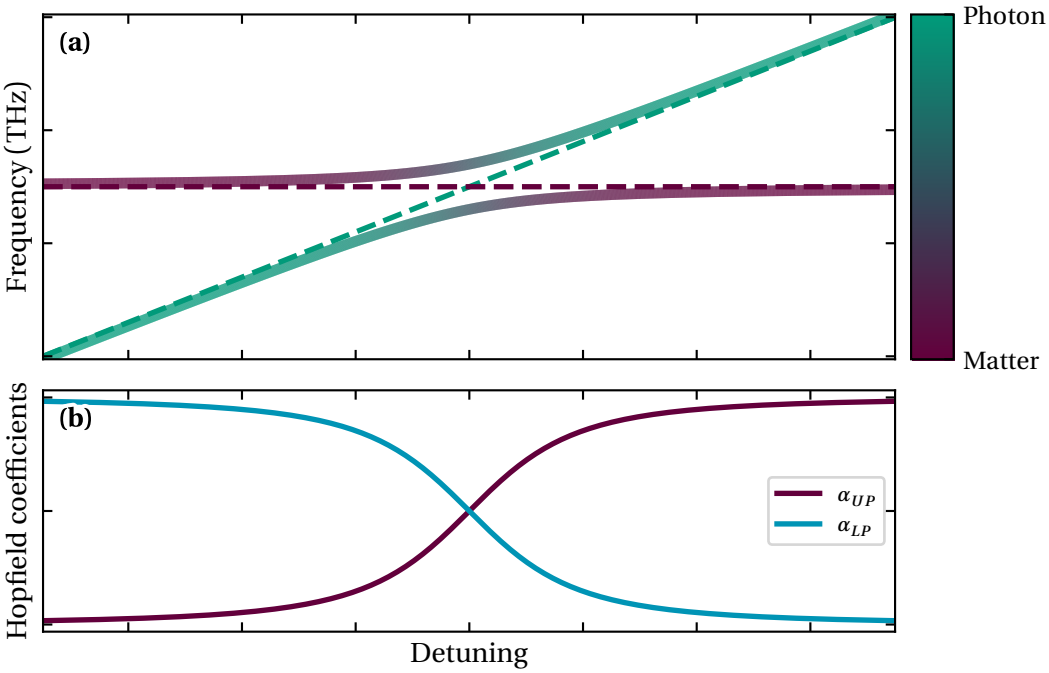

Figure 1.10.. **(a)**: frequency dispersion of the renormalized states (solid lines) depending on the detuning. Dashed lines are the cavity and ISB transition dispersion. **(b)**: Hopfield coefficients of the upper states depending on the detuning.

Diagonalizing this matrix, the following equation is obtained:

$$det(\widehat{H} - E) = (\hbar\omega_{\text{ISB}} - E)^{N-1}[(\hbar\omega_{\text{cav}} - E)(\hbar\omega_{\text{ISB}} - E) - N\hbar^2 g^2] = 0 \tag{1.93}$$

The characteristic equation highlights two interesting properties when N quantum emitters are introduced in a cavity. First, the system has one state that is actually coupled to cavity photonic mode, and $N-1$ degenerate states not coupled with electromagnetic field. The coupled mode is referred as bright state while the $N-1$ uncoupled mode are named dark states. Second, the coupling constant in the case of the N oscillator case becomes $\Omega_{\text{R}} = \sqrt{N}g$ and has the expression :

$$\Omega_{\text{R}} = \sqrt{\frac{N_{\text{s}} N_{\text{QW}} e^2 f_{12}}{\varepsilon_0 \varepsilon_{\text{r}} m^* L_{\text{cav}}}} \tag{1.94}$$

Compared to the single emitter case, the Rabi splitting is enhanced by a factor $\sqrt{N}$. This collective enhancement is similar to the observation of the superradiance phenomenon observed by Dicke when a collection of molecules interact with the same field [50].

1.5.4. Ultra-Strong coupling regime description

While the Jaynes-Cummings model allows deriving fundamental properties of a strongly coupled quantum well with a cavity, assumptions were made on the coupling constant value. For the RWA

approximation to hold, Ω_R needs to be negligible compare to the ISB and the cavity frequencies. However, for a highly doped quantum well structure, this condition is not fulfilled anymore. A more accurate model is needed.

The Hamiltonian for a doped quantum well embedded in a microcavity can be expressed in the Coulomb gauge as follows:

$$H = \sum_i \frac{(\boldsymbol{p}_i - e\boldsymbol{A}(\boldsymbol{r},t))^2}{2m_i} + V(\boldsymbol{r}) + \frac{1}{2}\iiint \left(\varepsilon_0\varepsilon_r \boldsymbol{E}^2 + \mu_0 \boldsymbol{H}^2\right) dr \tag{1.95}$$

$$= \underbrace{\sum_i \frac{\boldsymbol{p}_i^2}{2m_i}}_{\text{matter}} + \underbrace{\frac{1}{2}\iiint \left(\varepsilon_0\varepsilon_r \boldsymbol{E}^2 + \mu_0 \boldsymbol{H}^2\right) dr}_{\text{cavity}} - \underbrace{\sum_i \frac{q\boldsymbol{p}_i \cdot \boldsymbol{A}}{m_i} + \sum \frac{q^2\boldsymbol{A}^2}{2m_i} + V(\boldsymbol{r})}_{\text{interaction}} \tag{1.96}$$

where $V(\boldsymbol{r})$ is the Coulomb potential arising from the electron-electron interactions. This was the path followed in Ref. [51] when they provide detailed model describing the ultra strong-coupling regime between an ISB transition and a cavity mode. However, this treatment discards the electron-electron interactions which create the depolarization shift of the ISB transition when highly doped quantum wells are considered.

Another way to treat this system is to consider the Hamiltonian in the dipole gauge Ref. [52]. The advantage of this treatment is that the system is not described by a dipole moment, but by the polarization of the medium (thus the distribution of the charges). The transformation of the Coulomb gauge Hamiltonian is called the Power-Zienau-Woolley transformation [53] and yields the following Hamiltonian:

$$\widehat{H} = \underbrace{\sum_i \frac{\boldsymbol{p}_i^2}{2m_i}}_{\text{matter}} + \underbrace{\frac{1}{2}\iiint \left(\frac{\boldsymbol{D}^2}{\varepsilon_0\varepsilon_r} + \mu_0 \boldsymbol{H}^2\right) dr^3}_{\text{cavity}} - \underbrace{\iiint \frac{\boldsymbol{D}\cdot\boldsymbol{P}}{\varepsilon_0\varepsilon_r} dr^3 + \iiint \frac{\boldsymbol{P}^2}{2\varepsilon_0\varepsilon_r} dr^3}_{\text{interaction}} \tag{1.97}$$

with $\boldsymbol{D}$ and $\boldsymbol{P}$ are the electric displacement and the polarization density vector. The first term of the interaction part of the Hamiltonian corresponds to the light-matter interaction (term proportional to the coupling constant in the simple Hamiltonian model derived in the previous section). The second term describes the electron self interaction. It can be noted that the Coulomb potential $V(\boldsymbol{r})$ is included into this term.

In order to diagonalize this Hamiltonian, we need to express it in second quantization. To keep the expression as simple as possible, the summation over the in-plane wavevectors will be omitted.

Using the conventional quantization procedure for the electric displacement vector, the cavity Hamiltonian reads:

$$\widehat{H}_{\text{cav}} = \hbar\omega_{cav}\widehat{a}^\dagger\widehat{a} \tag{1.98}$$

The matter Hamiltonian needs more attention. Under the assumption that only the $1 \rightarrow 2$ transition occurs and parabolic subbands are considered, the matter Hamiltonian can be written:

$$\widehat{H}_{\text{matter}} = \sum_{\boldsymbol{k}} \hbar\omega_{21,\boldsymbol{k}} c^{\dagger}_{2,\boldsymbol{k}} c_{1,\boldsymbol{k}} \tag{1.99}$$

where $c^{\dagger}_{i,\boldsymbol{k}}$ and $c_{i,\boldsymbol{k}}$ are the fermionic creation and annihilation operators of an electron in the ith subband with the wavevector $\boldsymbol{k}$. The energy of the electron on the ith subband with in plane momentum wavevector $\boldsymbol{k}$ is $\hbar\omega_{i,\boldsymbol{k}} = \hbar\omega_i + \frac{\hbar^2\boldsymbol{k}^2}{2m^*}$ To further study the system, and obtain a readily diagonalizable Hamiltonian, it is interesting to treat the fermionic electron population as a bosonic field. This bosonization operation is done by defining the creation operator $\widehat{b}^{\dagger}$ which reads:

$$\widehat{b}^{\dagger} = \frac{1}{\sqrt{\Delta N}} \sum_{|\boldsymbol{k}|<\boldsymbol{k}_F} c^{\dagger}_{2,\boldsymbol{k}} c_{1,\boldsymbol{k}} \tag{1.100}$$

with $\Delta N = N_1 - N_2$ the difference between the subband populations. This operator is indeed bosonic as long as the number of excited electrons is small in front of the total number of electron.

In the bosonic picture, the matter Hamiltonian becomes:

$$\widehat{H}_{\text{matter}} = \hbar\omega_{21} \widehat{b}^{\dagger}\widehat{b} \tag{1.101}$$

with ω_{21} the frequency difference between the two subbands (more detail about the bosonization procedure can be found in Ref. [54, 55]).

Finally, the interaction Hamiltonian is composed of two parts and can be expressed using the bosonic operator $\widehat{b}^{\dagger}$ [55]. The first, linear with the polarization vector, is the light matter interaction term. Its expression is:

$$\widehat{H}_{\text{lm}} = \mathrm{i}\frac{\hbar\omega_p}{2}\sqrt{f_w \frac{\omega_{\text{c}}}{\omega_{21}}}(\widehat{a}^{\dagger} - \widehat{a})(\widehat{b} + \widehat{b}^{\dagger}) \tag{1.102}$$

where ω_p is the plasma frequency and f_w is the electromagnetic overlap of the cavity mode with the electron distribution. The second term describes the electron-electron coupling. Its expression is:

$$\widehat{H}_{\text{e-e}} = \frac{\hbar\omega_{\text{p}}^2}{4\omega_{21}}(b + b^{\dagger})^2 \tag{1.103}$$

Combining Eqs. (1.98) and (1.101) to (1.103), the Hamiltonian of the system becomes:

$$H = \hbar\omega_{\text{c}}(a^{\dagger}a + \frac{1}{2}) + \hbar\omega_{21} b^{\dagger}b + \mathrm{i}\frac{\hbar\omega_{\text{p}}}{2}\sqrt{f_w \frac{\omega_{\text{c}}}{\omega_{21}}}(\widehat{a}^{\dagger} - \widehat{a})(\widehat{b} + \widehat{b}^{\dagger}) + \frac{\hbar\omega_{\text{p}}^2}{4\omega_{21}}(b + b^{\dagger})^2 \tag{1.104}$$

In order to find the modes of this Hamiltonian, it is necessary to diagonalize it. This will be achieved by doing successively two Bogoliubov transformations. The first one is done introducing the operator intersubband plasmon p with the expression:

$$\hat{p} = \frac{\tilde{\omega}_{21} + \omega_{21}}{2\sqrt{\tilde{\omega}_{21}\omega_{21}}}\hat{b} + \frac{\tilde{\omega}_{21} - \omega_{21}}{2\sqrt{\tilde{\omega}_{21}\omega_{21}}}\hat{b}^{\dagger} \tag{1.105}$$

where $\tilde{\omega}_{21} = \sqrt{\omega_{21}^2 + \omega_{\mathrm{p}}^2}$ is the plasma shifted transition frequency. The Hamiltonian becomes:

$$\widehat{H} = \hbar\tilde{\omega}_{21}\hat{p}^{\dagger}\hat{p} + \hbar\omega_{\mathrm{cav}}\hat{a}^{\dagger}\hat{a} + i\frac{\hbar\omega_{\mathrm{p}}}{2}\sqrt{f_w\frac{\omega_c}{\tilde{\omega}_{21}}}(\hat{a}^{\dagger} - \hat{a})(\hat{p} + \hat{p}^{\dagger}) \tag{1.106}$$

The second one is done using the polariton operator π:

$$\pi_j = x_j\hat{a} + y_j\hat{a}^{\dagger} + z_j\hat{p} + t_j\hat{p}^{\dagger} \tag{1.107}$$

where $j \in \{\mathrm{LP}, \mathrm{UP}\}$ and x, y, z and t are the Hopefield coefficients. The Hamiltonian, cast into a matrix form, is:

$$\widehat{H} = \begin{pmatrix} \omega_{\mathrm{cav}} & 0 & \mathrm{i}\Omega_{\mathrm{R}} & \mathrm{i}\Omega_{\mathrm{R}} \\ 0 & -\omega_{\mathrm{cav}} & \mathrm{i}\Omega_{\mathrm{R}} & \mathrm{i}\Omega_{\mathrm{R}} \\ -\mathrm{i}\Omega_{\mathrm{R}} & \mathrm{i}\Omega_{\mathrm{R}} & \tilde{\omega}_{\mathrm{ISB}} & 0 \\ \mathrm{i}\Omega_{\mathrm{R}} & -\mathrm{i}\Omega_{\mathrm{R}} & 0 & -\tilde{\omega}_{\mathrm{ISB}} \end{pmatrix} \tag{1.108}$$

with $\Omega_{\mathrm{R}} = \frac{\omega_{\mathrm{p}}}{2}\sqrt{f_{\mathrm{w}}\frac{\omega_{\mathrm{c}}}{\tilde{\omega}_{21}}}$ the coupling constant.

Solving for the eigenenergy of the Hamiltonian yields the transcendental equation:

$$\left(\omega^2 - \tilde{\omega}_{21}^2\right)\left(\omega^2 - \omega_{\mathrm{c}}^2\right) = f_w\omega_{\mathrm{p}}^2\omega_{\mathrm{c}}^2 \tag{1.109}$$

whose solutions are :

$$\omega_{\mathrm{UP/LP}}^2 = \frac{\omega_{\mathrm{c}}^2 + \tilde{\omega}_{21}^2 \pm \sqrt{\left(\omega_{\mathrm{c}}^2 - \tilde{\omega}_{12}^2\right)^2 + 4f_{\mathrm{w}}\omega_{\mathrm{p}}^2\omega_{\mathrm{c}}^2}}{2} \tag{1.110}$$

In Fig. 1.11 (a) the polariton frequency ω_{UP} and ω_{LP} are plotted as a function of the detuning $\Delta\omega = \omega_{\mathrm{c}} - \tilde{\omega}_{\mathrm{ISB}}$. Compared to the strong-coupling dispersion obtained using the Jaynes-Cummings, a few differences can be seen.

First the two asymptotes of the upper branch for $\omega_{\mathrm{c}} \ll \tilde{\omega}_{21}$ and the lower branch for $\omega_{\mathrm{c}} \gg \tilde{\omega}_{21}$ are different, opening an energy gap whose width depends on the plasma frequency. This feature is a signature of the ultra strong-coupling regime. The width of the gap depends on the doping though ω_{p}. Also, the minimum splitting $2\Omega_{\mathrm{R}} = \omega_{\mathrm{p}}\sqrt{f_{\mathrm{w}}}$ does not occur at zero-detuning.

In Fig. 1.11 (c), the upper and lower polariton frequencies for the model developed in this section and the simple Jaynes-Cummings model are plotted depending on the plasma frequency ω_{p}. At low value of ω_{p}, corresponding to lightly doped quantum wells, both models have a good agreement. However, as ω_{p} reaches 30 % of the bare ISB frequency, the Jaynes-Cummings model starts to diverge. The reason is two-fold. One of the fundamental assumptions made during the derivation

of the Jaynes-Cummings model is that the coupling constant is negligible in front of the resonance frequency of both the cavity and the ISB transition. With the increasing plasma frequency value, this assumption becomes less and less true. The other reason is that the ISB transition in the Jaynes-Cummings does not include the depolarization shift, which blue shifts the ISB transition as the plasma frequency increases.

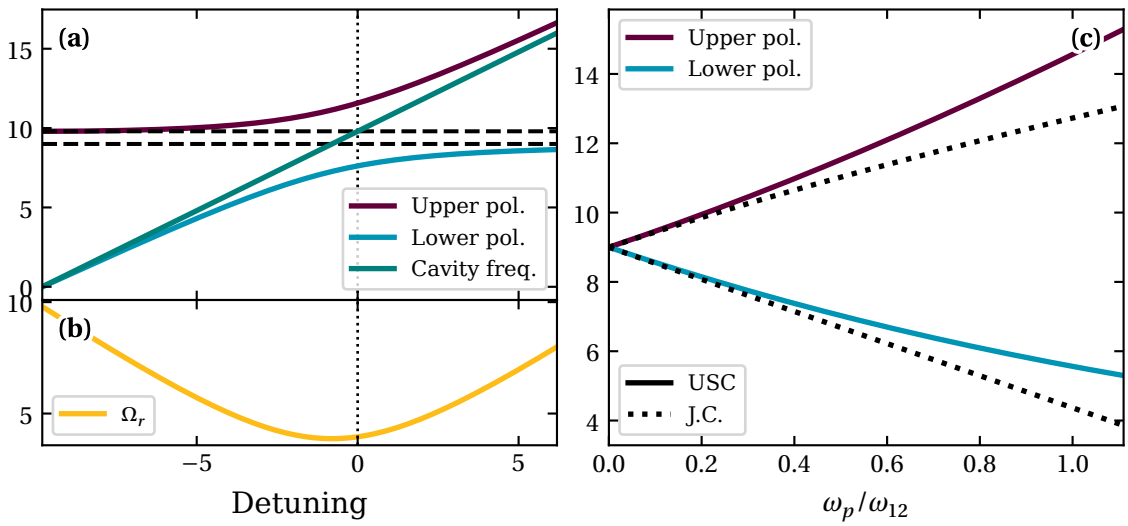

Figure 1.11.. **(a)**: frequency dispersion of the USC coupling. **(b)**: frequency splitting depending on the detuning Schematic of the two possible states of the coupled system. **(c)**: upper and lower polariton frequency depending on the plasma frequency electrical dipole model and the Jaynes-Cummings model.

1.5.5. Virtual photon cavity

An interesting property arises from the fact that the destruction operator of a polariton contains the creation operator of a photon. In general, the vacuum state is the state with the lowest energy and contains no particles. It is the case for the system in the weak and strong-coupling regime. However, entering the ultra strong-coupling regime, the nature of the ground state changes. Calculating the expectation value of the photon ground level population, one can find that [51]:

$$\langle G|\hat{a}^{\dagger}\hat{a}|G\rangle = |y_{\mathrm{LP}}|^2 + |y_{\mathrm{UP}}|^2 \tag{1.111}$$

Fig. 1.12 (a) shows the total virtual photon population of the ground state depending on the normalized coupling constant. For $\Omega_{\mathrm{R}} \leq 0.1\omega_{21}$, which corresponds to the strong-coupling regime, the ground state population is negligible. For $\Omega_{\mathrm{R}} \geq 0.1\omega_{21}$, the probability to find a photon in the ground state increases exponentially with the coupling constant.

Ref. [51] theorized that it is possible to access this reservoir by an abrupt change of the coupling constant Ω_R, from the ultra strong-coupling to the weak coupling regime, on a timescale shorter than the polariton lifetime. In doing so, the cavity modes of the ground state don't have the time to react to the change. These photons become cavity mode of an excited state. As the weakly coupled

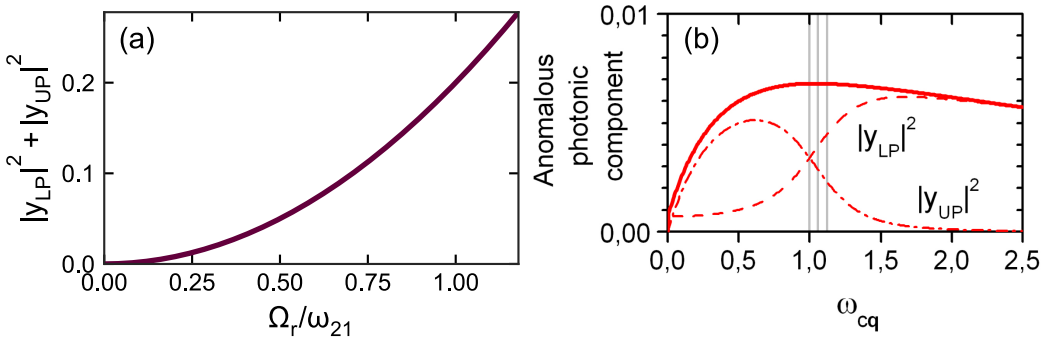

Figure 1.12.. **(a)**: Total virtual photon population of the ground state depending on the coupling constant. **(b)**: mixing fraction of the virtual photon population of the ground state depending on the detuning of the cavity with the ISB transition (from Ref. [56]).

system relaxes to its new ground state, the cavity photons will be emitted. Experimentally, the presented solution relies on a depletion of the two-dimensional electron gas by applying a voltage to the active region, turning off the USC [57, 58]. However, this approach proved to be inadequate as it does not meet the speed requirement to provide sub-cycle change of the coupling constant [59]. Optical methods were explored to obtain this coupling constant modulation by using optical pumping to promote electrons from the valence band to the first subband of the conduction band of a quantum well structure [60].

The idea behind the coupling constant modulation is similar to the dynamical Casimir effect (DCE). The first description of the DCE was made by Moore which showed that the motion of the boundaries of a 1D cavity can result in a quanta of EM field generation from the vacuum state [61]. For that reason, the DCE is often named the mirror induced Casimir effect. While this initial description involved mechanical modulation, it was then realized that no physical motions were necessary. A non-adiabatic change of the refractive index [62], the eigenfrequency of the system [63] or the effective length of the cavity [64] were predicted to be enough to activate the DCE. The first report of DCE photon emission was done by modulating the electrical length of a superconducting circuit [65].

In fact, Ref. [51] mention the possibility to leverage the non-adiabatic switching of the resonance frequency to emit photon using the dynamical Casimir effect. One of the goal of my thesis was to devise a system to enable the observation of the DCE in the THz range. This effort is the topic of Chapter 4. The foundation of this system is based on the 3D LC resonator, 3D equivalent of the split ring resonator which has been developed over the year by our team.

Chapter

2

Novel approaches for the demonstration of final state stimulation in ISB polaritons under resonant injection of light

In this chapter, the topic of light emission from ISB polaritons under resonant optical pumping will be discussed. First, the typical MIM cavities used for this work will be described in details, along with the previous work of the team on this subject. In this respect, a different approach for enhancing the scattering rate has been explored with a different cavity system and will be presented. Finally, I will conclude this chapter with some exploratory work of photonic crystal based cavities in conjunction with a full dielectric configuration.

2.1. Metal-metal cavity

Metal Insulator Metal (MIM) or Metal Dielectric Metal (MDM) cavities are a category of photonic structures largely used in conjunction with quantum well based devices thanks to their capability to confine modes with a non-zero electric field component in the z-direction. In this section, three different cavities will be presented. The first is the parallel plates waveguide, which is the basic block of the two other cavities presented later on. Then, the MIM dispersive cavity obtained by patterning one of the metallic mirror will be studied. Finally, the non-dispersive regime obtained when each slab of the patterned mirror behaves like isolated resonators will be discussed.

2.1.1. The parallel plates waveguide

Waveguides are structures designed to guide waves whether they are electromagnetic or sound. They are commonly used in several fields. For electromagnetic waves, guiding is achieved thanks to boundary conditions created by metallic planes restricting the propagation direction. These waveguides saw an important interest during the World War II, where they were used for radar and microwave applications.

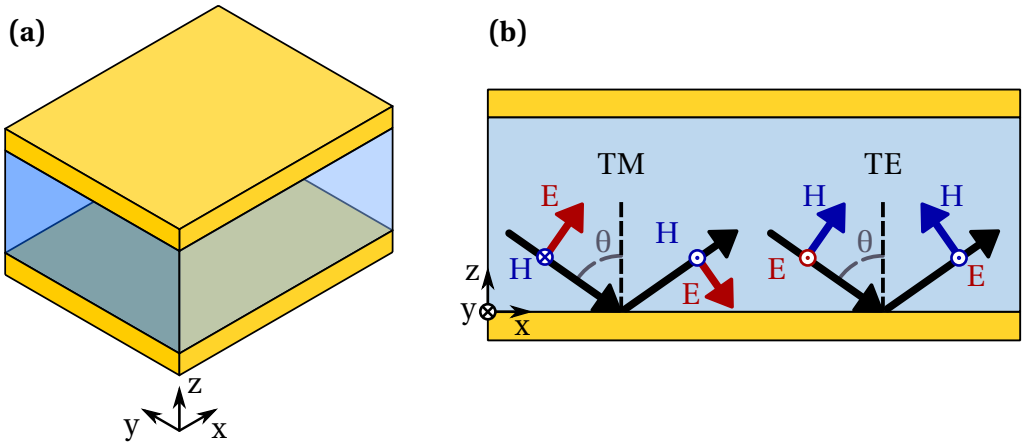

Figure 2.1.. **(a)**: Parallel plates waveguide geometry which extends infinitely in the x- and y-direction. **(b)**: Polarization configuration for the TM- and TE-polarized propagation for a wave propagating in the x-direction.

The structure that will be studied here is a Metal-Insulator-Metal (MIM) structure. The guided optical mode in this structure can be obtained using different methods. One is to solve the Helmoltz's equation using an eigen-solution for the form of the electric field that respect the cavity boundary conditions or symmetries. Another method, which is the one used here, is to consider a propagating polarized electromagnetic wave bouncing back and forth between two perfectly conducting layers.

In order to find the modes, it will be assumed that the wave propagates in the x-direction, with an angle θ. First, the transverse electric (TE) case is treated. The incident and reflected electric fields can be formulated:

$$\boldsymbol{E}_i = \boldsymbol{y} E_i e^{\mathrm{i}k_z z - \mathrm{i}k_x x} \tag{2.112}$$

$$\boldsymbol{E}_r = \boldsymbol{y} E_r e^{-\mathrm{i}k_z z - \mathrm{i}k_x x} \tag{2.113}$$

At z=0, the boundary condition at the metal interface implies that the tangential component of the electric field is continuous for every x-value. Thus, $E_i + E_r = 0$ The total electric field in the cavity becomes:

$$\boldsymbol{E} = \boldsymbol{y} 2\mathrm{i} E_i \sin(k_z z) e^{-\mathrm{i}k_x x} = \boldsymbol{y} E_0 \sin(k_z z) e^{-\mathrm{i}k_x x} \quad \text{with} \quad E_0 = 2\mathrm{i}E_i \tag{2.114}$$

Using the second boundary condition at z=d, $E(z = d) = 0$ for any x. Thus, $sin(k_z d) = 0$ i.e. $k_z = m\pi/d$ with $m \geq 1$ a positive integer. m is the mode index. It can be noted that for $m = 0$ the electric field becomes null, which leads to a non-physical solution. For a transverse electric mode, there is no TE_0 mode. The magnetic field can be obtained using the Faraday's law:

$$\boldsymbol{H}(x,z) = -\frac{\boldsymbol{\nabla}\times\boldsymbol{E}}{\mathrm{i}\omega\mu} = \frac{1}{\mathrm{i}\omega\mu}\left(\partial_z E_y \boldsymbol{x} - \partial_x E_y \boldsymbol{z}\right) \tag{2.115}$$

$$= -\mathrm{i}\frac{E_0 k_z}{\omega\mu}\cos\left(k_z z\right)\mathrm{e}^{-\mathrm{i}k_x x}\boldsymbol{x} + \frac{E_0 k_x}{\omega\mu}\sin\left(k_Z z\right)e^{-\mathrm{i}k_x x}\boldsymbol{z} \tag{2.116}$$

The propagation condition of a TE mode in this cavity is :

$$k_x = \sqrt{k_0^2 - k_Z^2} = \sqrt{k_0^2 - \left(\frac{m\pi}{d}\right)^2} \quad m \geq 1 \tag{2.117}$$

Because the propagation constant must be a real value, then $k_0 > m\pi/d$. As explained earlier the first allowed mode is TE_1. The minimal frequency above which a signal can propagate is for the m-th mode is :

$$f_c = \frac{m}{2d\sqrt{\mu\varepsilon}} \tag{2.118}$$

This frequency is called the cut off frequency.

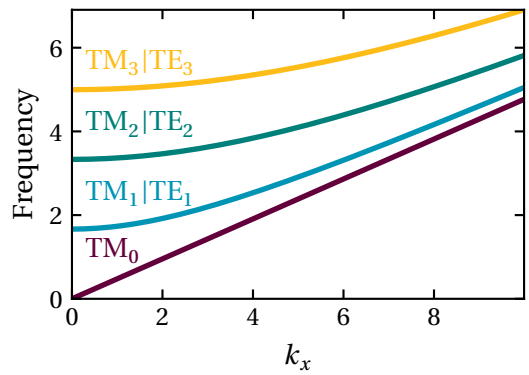

Figure 2.2.. Frequency dispersion of the TM and TE modes of an arbitrary parallel plate waveguide.

Using a similar method, the TM modes can be derived using the reflection of a y-polarized magnetic field :

$$\boldsymbol{H}_i = \boldsymbol{y}H_i\mathrm{e}^{\mathrm{i}k_z z - \mathrm{i}k_x x} \tag{2.119}$$

$$\boldsymbol{H}_r = \boldsymbol{y}H_r\mathrm{e}^{-\mathrm{i}k_z z - \mathrm{i}k_x x} \tag{2.120}$$

Using this time the Ampere's law $\mathrm{i}\omega\varepsilon\boldsymbol{E} = \boldsymbol{\nabla}\times\boldsymbol{H} = \partial_x E_y \boldsymbol{z} - \partial_z E_y \boldsymbol{x}$, the total electric field after the reflection is:

$$E_x = \frac{k_z}{\omega\varepsilon}\left(-H_i e^{ik_z z} + H_r e^{-ik_z z}\right) e^{-ik_x x} \tag{2.121}$$

$$E_z = -\frac{k_x}{\omega\varepsilon}\left(H_i e^{ik_z z} + H_r e^{-ik_z z}\right) e^{-ik_x x} \tag{2.122}$$

The continuity of the tangential electric field at the metal interface gives $H_i = H_r = H_0/2$. So the fields in the cavity are :

$$H_y = H_0 \cos\left(k_z z\right) e^{-ik_x x} \tag{2.123}$$

$$E_x = -iH_0 \frac{k_z}{\omega\varepsilon} \sin\left(k_z z\right) e^{-ik_x x} \tag{2.124}$$

$$E_z = -H_0 \frac{k_x}{\omega\varepsilon} \cos\left(k_z z\right) e^{-ik_x x} \tag{2.125}$$

Using the second boundary condition at $z = d$, a similar formulation of the z wavevector can be obtained: $k_z = m\pi/d$ with m an integer. It can be noted that on the contrary of the TE modes, the 0-th TM mode is an allowed mode. The propagation condition is the same for the TE mode and shows that the 0-th order mode has no cutoff frequency.

This kind of waveguide can couple the TM modes with an intersubband transition but are not practical. In fact, the problem is to couple an external wave within the waveguide. The thickness of a typical active region is in the order of hundredth of nanometers in the MIR, and a few microns in the THz. Coupling light in such a reduced area can be a challenge.

2.1.2. MIM patterned cavity

To overcome the problem of coupling the free space radiation to the cavity, a solution is the patterning of the top mirror. The geometry of such a cavity is pictured Fig. 2.4. Two different regimes can be obtained using this cavity geometry, which possess different dispersion relations. One is dispersive while the other is not. The transition between the two regimes depends on the cavity thickness. A thorough study of this property in the THz can be found in Ref. [66, 67]. These properties can be translated to the MIR.

The impedance mismatch arises from a difference effective index between the metal-metal and air-metal regions. The reflectivity ρ at this interface can be written:

$$\rho = \frac{n_s - n_g}{n_s + n_g} \tag{2.126}$$

where n_s is the index of the single metal region, equal to material index, and n_g the effective guided mode index which is a function of the cavity thickness. In Fig. 2.3 (b), the modulus of the reflectivity ρ is plotted as a function of the cavity thickness h for a guided mode wavelength $\lambda = 100\,\mu m$. For a cavity thickness below 1 µm, the reflectivity at the interface is close to 1. Such a cavity presents a non-dispersive behavior. On the contrary, a cavity with a thickness greater than 10 µm has a reflectivity modulus almost null thus is a dispersive cavity. As a rule of thumb, a cavity is dispersive for a slab thickness greater than $\lambda/10$, and is non-dispersive for a thickness lower than $\lambda/30$.

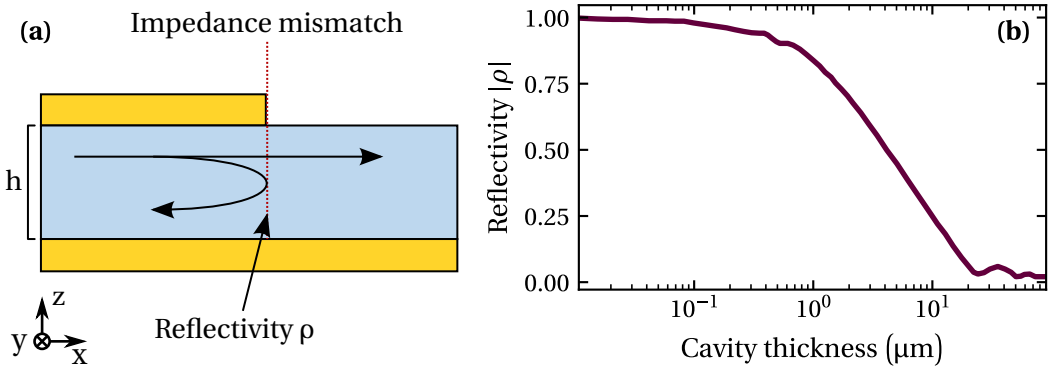

Figure 2.3.. **(a)**: schematic of the metal-metal to the metal-air interface. The impedance mismatch induces a reflectivity of the guided mode. **(b)**: plot of the reflectivity modulus of the impedance mismatch as a function of the cavity thickness for wavelength of 100 µm ($\nu = 3\,\text{THz}$). From Ref. [67]

2.1.2.1. MIM dispersive cavity

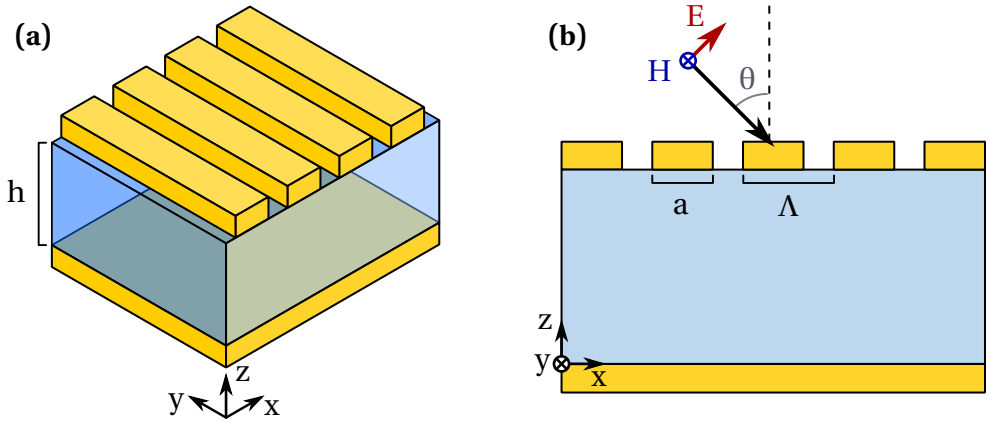

Figure 2.4.. **(a)**: typical 1D MIM cavity geometry which extends infinitely in the x- and y-direction. **(b)**: xz-plane view of the cavity.

The treatment of the dispersive MIM cavity can be done by considering the patterning as a perturbation of the parallel plate waveguide mode. Such an approximation is valid when the patterning filling factor $ff = a/\Lambda$ is important (around 80 %) An external wave of wavevector $\boldsymbol{k}_0$ can couple to a mode in this periodically patterned cavity when the in-plane wavevector $\boldsymbol{k}_x$ matches a guided mode wavevector β_x with the following condition [68, 56]:

$$\left|k_x + mg\right| = k_0\sqrt{\varepsilon} \tag{2.127}$$

with m an integer and $g = 2\pi/a$ a reciprocal lattice vector. The propagating mode in the cavity becomes a parallel plate waveguide mode modulated by a Bloch-Floquet envelope function $\exp(-i2\pi x/a)$. Due to the periodicity of the grating, the translational symmetry along the x-axis leaves the system in the same state for a translation of a vector $m\boldsymbol{g}$. Thus, for a given frequency

value, several wavevectors are associated. It means that all the information about the dispersion is contained into the reduced zone between $k_x = 0$ and $k_x = \pi/a$ called the Brillouin zone. The dispersion can be folded into this zone to form optical branches. An example of such a dispersion can be calculated using numerical tool.

Fig. 2.5 (a) shows the dispersion of a MIR cavity of $\Lambda = 4\,\mu$m periodicity, filling factor $ff = 70\,\%$ and thickness $h = 1.1\,\mu$m. The black dashed curve is the TM_0 mode folded in the first Brillouin zone. For wavevectors far from the band edge, the periodically patterned mode are parallel to the unpatterned waveguide mode. At the band edge of the Brillouin zone, a distinct behavior occurs where the real value of the eigenfrequency becomes constant while the imaginary part is non-zero. This leads to a strong attenuation materialized by photonic bandgaps, frequency zones in which there is no wave propagation.

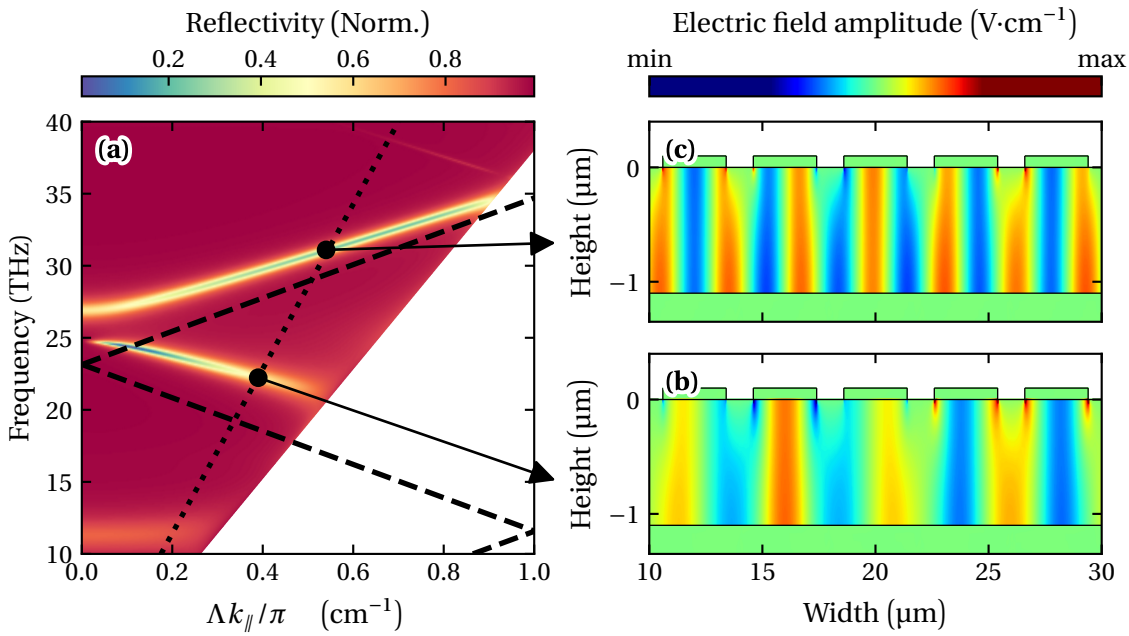

Figure 2.5.. **(a)**: Reflectivity dispersion of dispersive MIR cavity. The black dashed curve is the TM_0 mode of the equivalent parallel plate waveguide folded in the first Brillouin zone. The purple dotted line highlights the reflectivity at an angle of 41°. **(b)**: plot of the reflectivity at an angle of 41°. **(c)** and **(d)**: electric field E_z of the mode on the first and second photonic branch.

Fig. 2.5 **(b)** depicts the reflectivity for an incident angle $\theta = 41°$ and Fig. 2.5 **(c)** and **(d)** show the z-component of the electric field on the first and second photonic branch, calculated using COMSOL Multiphysics. The electric field in the cavity is not strictly confined under the metal-metal region. The dispersive behavior of the cavity mode with the incidence angle arises from this mode delocalization [69].

2.1.2.2. MIM non-dispersive cavity

As it was explained earlier, the transition between the dispersive and non-dispersive regime for a cavity with a given period and filling factor can be obtained by simply reducing the cavity thickness. To illustrate this property, the same cavity used previous section is modeled, except the cavity thickness is $h = 200\,\text{nm}$. Fig. 2.6 **(a)** shows a color plot of the cavity dispersion. Flat photonic branches can be observed, the cavity is non-dispersive which indicates that modes are not delocalized anymore.

An observation of the electric field confirms it. Fig. 2.6 **(b)** and **(c)** show the electric field in the z-direction for the TM_{01} and TM_{02} modes. For both of them, the field is strictly confined under the metal slab: each slab is an independent resonator. In Section 4.1.1.1 a detailed study of this type of cavity, called patch cavity, in the 2D is given. For the case of a 1D patch cavity, the mode resonance frequencies depend on the slab width and follows the formula:

$$\nu_n = \frac{Kc}{2n_{\text{m}}a} \tag{2.128}$$

where K is the mode index, n_m the effective refractive index of the mode and a the slab width.

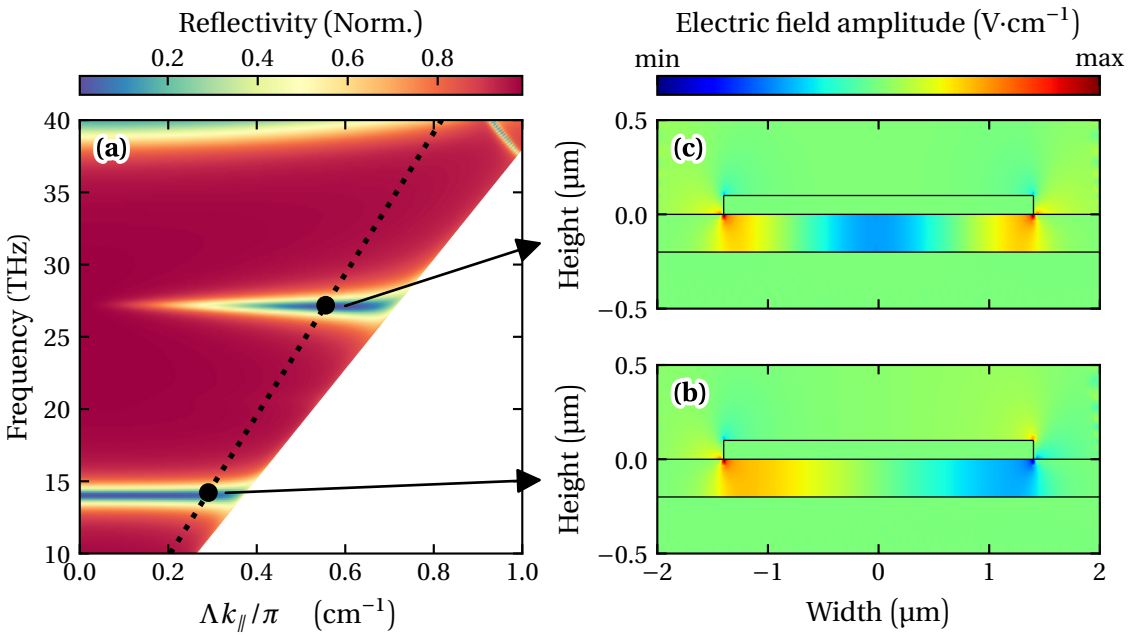

Figure 2.6.. **(a)**: reflectivity dispersion of a MIR non-dispersive cavity. MIR non-dispersive cavity Electric field E_z for **(b)** the TM_{01} and **(c)** TM_{02} mode.

2.2. Lasing without population inversion: The polariton laser

2.2.1. Exciton-polariton lasers

In semiconductors, the absorption of a photon promotes an electron from the valence band to the conduction band, leaving behind a hole. Being of opposite charge, these two particles attract each other through Coulomb interactions to form a pair. This pair is called an exciton [37]. An exciton is a quasi-particle showing bosonic properties.

Similarly to ISB transitions, excitons can couple with cavity modes to form exciton-polaritons. In the achievement of condensate, exciton-polaritons present a clear advantage over atoms and excitons. The reason comes to the condition for the lift of degeneracy. For a fixed condensate density, the condition for achieving condensation depends on the mass of the boson and its temperature. The lighter the boson is, the higher the maximum temperature condensation can occur. That is why, compared Bose-Einstein condensate (BEC) of atoms which were achieved in the nK/μk temperature range [70, 71], BEC was achieved in the mK range with excitons [72]. And thanks to its photon part, exciton-polariton can achieve BEC at even higher temperature.

Exciton-polariton lifetime and effective mass can be calculated using the following formulae:

$$\frac{1}{\tau_{\mathrm{LP,UP}}} = \frac{\alpha_{\mathrm{LP,UP}}}{\tau_{\mathrm{C}}} + \frac{\beta_{\mathrm{LP,UP}}}{\tau_{\mathrm{X}}} \tag{2.129}$$

$$\frac{1}{m_{\mathrm{LP,UP}}} = \frac{\alpha_{\mathrm{LP,UP}}}{m_{\mathrm{C}}} + \frac{\beta_{\mathrm{LP,UP}}}{m_{\mathrm{X}}} \tag{2.130}$$

where $\alpha_{\mathrm{LP,UP}}$ and $\beta_{\mathrm{LP,UP}}$ are the photon and exciton fraction of the polariton, and τ_{C} and m_{C} (τ_{X} and m_{X}) are respectively the lifetime and the effective mass of the cavity photon (exciton). The most favorable case for achieving a BEC occurs then for a high photon fraction.

The operating principle of a polariton laser was proposed by Imamoglu et al. in 1996. Fig. 2.7 (a) presents the working principle and can be summarized as follows [74]. Through non-resonant pumping an electron-hole pair plasma is generated. As the plasma relaxes, these pairs start to occupy polariton states on the lower polariton branch, creating an excitonic reservoir. These polaritons with a high exciton fraction can relax further down toward the bottom of the lower polariton branch by phonon or exciton-exciton scattering [75]. Due to its high cavity photon fraction, the polariton decay is followed by a photon emission at an angle θ which corresponds to the in-plane wavevector of the decaying polariton $k_{/\!/} = (E/\hbar c)\sin(\theta)$ [76]. The scattering toward the state close to $k_{/\!/} = 0$ is proportional to the population of the said state and can be expressed as follows [77, 78]:

$$\Gamma_{\mathrm{scat}} = \Gamma_0 (n_{\mathrm{pol}} + 1) \tag{2.131}$$

where Γ_0 is the probability a polariton relaxes to the state $k_{/\!/} = 0$, and n_{pol} the polariton population at the final state. Equation Eq. (2.131) predicts that a threshold population exists at which the scattering probability Γ_{scat} increases exponentially. Scattering toward the final state becomes the

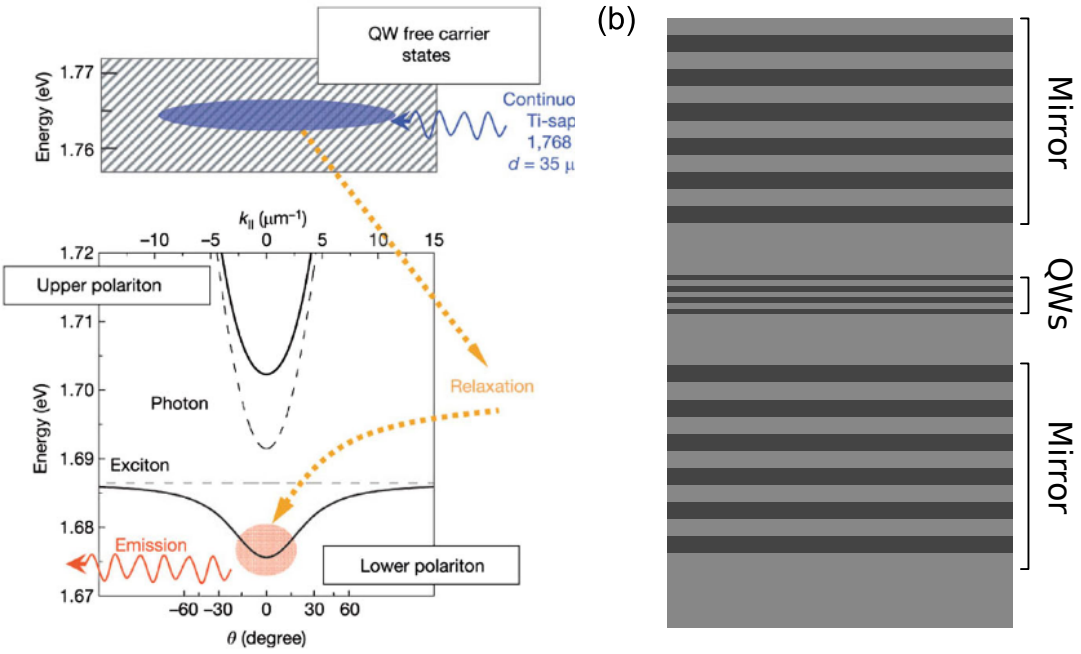

Figure 2.7.. (a): Schematic of the exciton-polariton laser principle. A hot carrier population is built up using a laser source. These carriers relax toward polariton states on the lower polariton branch. Through acoustic phonon scattering, polaritons reach the final state and eventually decay with a photon emission. From [73]. **(b)**: schematic of a Bragg mirror cavity typically used to achieve polariton lasing

favored over any other state leading to an increase of the population, which increases further the probability of scattering toward the final state, and so on.

One advantage exciton-polaritons have over their intersubband counterpart is the possibility to use high Q-factor cavities. Because the Intersubband Transitions (ISB) transition selection rule does not have to be fulfilled, dielectric cavities can be used. These cavities offer very long polariton lifetimes which allow to more easily build up the necessary population to achieve condensation. Fig. 2.7 (b) represents the schematic of a typical Bragg mirror cavity used for exciton-polariton scattering experiments.

The topic of excitonic polariton laser has been widely investigated over the last decade, with the demonstration of coherent emission with optically pumped devices at low temperature [76], and later at room temperature [79]. Emission was then achieved under electrical pumping at cryogenic temperature [80, 81] and at room-temperature [82].

While the lasing was achieved, the performance of the polariton laser based on exciton-polariton devices faces several problems. First, in order to build up the polariton population at the final state, the lifetime of the polariton must be longer than the scattering time. But as the polariton comes closer to the bottom of the LP branch, its photon fraction increases. According to Eq. (2.129), the polariton lifetime becomes more and more dominated by the photon cavity lifetime which depends on the cavity Q-factor. Moreover, exciton-polaritons are subject to the 'bottleneck' effect: as the exciton fraction decreases, the effective mass of the polariton decreases as well making

the acoustic phonon mechanism necessary to reach the final state less and less effective [83] increasing the scattering time. Also, the output power of such an emitter is fundamentally limited by the Mott transition density, which defines an upper limit above which polaritons lose their bosonicity. The output power is:

$$P_{out} = \frac{\hbar\omega N_S}{\tau_C} S \tag{2.132}$$

where ω is the photon frequency, N_S is the 2D polariton density, τ_C is the lifetime of the photon cavity and S the surface of the device. One advantage is the lower threshold at which occurs coherent emission, which in turn could be promising in the general trend of miniaturized sources for photonic circuits.

2.2.2. Extension of the polariton lasing concept to ISB-polaritons

Following the first observation of intersubband-polariton in microcavity [49], the proposal of using the bosonic properties of this quasi-particle for observing final state stimulation arrived shortly after [84]. The first attempts to create light emitting devices using ISB polaritons relied almost exclusively on electrical injection to create a polariton population [85, 86, 87, 88]. However, this approach suffers from the presence of the numerous dark states which do not couple with the electromagnetic field, thus do not participate in the strong-coupling regime. Only a fraction of the injected electrons tunneled into a bright state which hampers the performance of the device. That is why recent attempts to achieve polariton scattering was done under optical injection, by resonantly pumping in a polariton state [89].

While the goal of an ISB-polariton laser is similar to the exciton-polariton laser (obtaining a final state stimulation regime at $k_{/\!/} = 0$ and coherent emission of light), the operating principle is quite different. QW ISB transitions have a well-defined resonance frequency: non-resonant pumping will not populate polariton states [84]. Instead of relying on a relaxation mechanism to populate an exciton-polariton reservoir, ISB-polariton population is created by resonantly pumping the upper polariton branch. This is summarized in Fig. 2.8.

By resonantly pumping, a polariton population is built on the upper branch at a state separated by the LO-phonon energy with the lower polariton state at $k_{/\!/} = 0$. Two phenomena can occur: either a polariton decays through non-radiative channels, or is scattered by an LO-phonon. The scattered polaritons accumulate at $k_{/\!/} = 0$, building this time a polariton population on the lower branch. Here, the decay channels are either non-radiative or radiative with a photon emission.

This dynamic can be summarized with the following dynamic rate equations [90]:

$$\frac{\mathrm{d}n_2}{\mathrm{d}t} = \frac{AP_{\mathrm{in}}}{\hbar\omega_{in}} - \frac{n_2}{\tau_{21}} - \frac{n_2}{\tau_{2,\mathrm{NR}}} \tag{2.133}$$

$$\frac{\mathrm{d}n_1}{\mathrm{d}t} = \frac{n_2}{\tau_{21}} - \frac{n_1}{\tau_{1,\mathrm{NR}}} - \frac{n_1}{\tau_{1,\mathrm{rad}}} \tag{2.134}$$

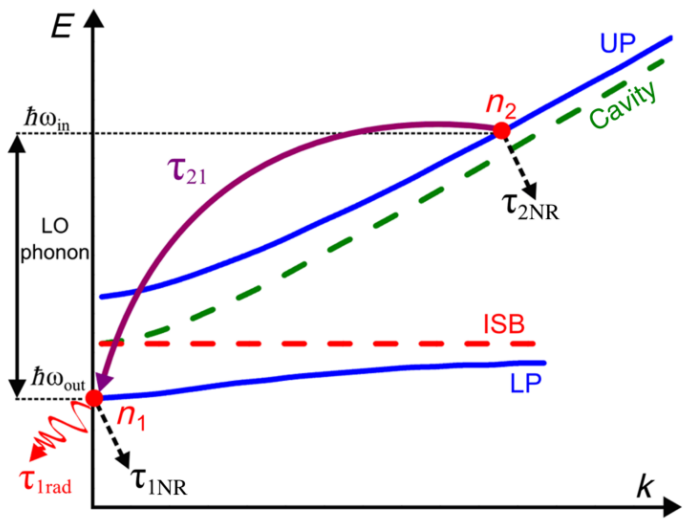

Figure 2.8.. Schematic of the ISB-polariton laser principle. Upper polariton branch is resonantly populated using a coherent light source.

where $n_{i,f}$ is the injection and final state polariton density, A is the upper polariton absorption of the injection state, P_{in} is the pump incident power, ω_{in} is the pump frequency, $\tau_{21} = 1/\Gamma_{\text{scat}}$ is the LO-phonon scattering time, $\tau_{2,\text{NR}}$ the non-radiative recombination time of the upper polariton at the injection state, $\tau_{1,\text{rad}}$ and $\tau_{1,\text{NR}}$ the radiative and non-radiative recombination times of the lower polariton at the final state. The emitted power follows the same rule as exciton-polariton lasers Eq. (2.132), but since the density of ISB-polaritons can be relatively elevated, it could result in a fairly powerful coherent source of light [90].

In the context of ISB-polaritons, the scattering rate of an upper polariton by an LO-phonon can be expressed as follows [89]:

$$\Gamma_{\text{ph}} = \frac{\pi\omega_{\text{LO}} e^2 k_{\text{f}} L_{\text{QW}} f \left|\alpha^i_{\text{ISB}} \alpha^f_{\text{ISB}}\right|^2}{\hbar v^{gr}_{\text{f}} \varepsilon_{\text{p}}} \tag{2.135}$$

where ω_{LO} is the frequency of the LO-phonon, L_{QW} is the quantum well width, k_f is the wavevector of the final state, $\alpha^{i,f}_{ISB}$ are the Hopefield coefficients of the ISB plasmon Hopefield weights of the initial and final polaritonic state, v^{gr}_f the group velocity of the final state at $k_{\parallel} = 0$, $\varepsilon_p = \left[\varepsilon_\infty^{-1} - \varepsilon_s^{-1}\right]^{-1}$ and f is a numerical factor between 0.01 and 0.03.

For a given cavity, it is possible to estimate the pump intensity to reach the population threshold for obtaining lasing. The expression of the intensity is [91]:

$$I_{th} = \frac{\hbar^2 \Gamma_{\text{LO}} \Gamma_{UP} \Gamma_{LP} \omega_{pump} \varepsilon_\rho N_{QW}}{4\pi |\alpha^i_{ISB}| |\alpha^f_{ISB}| \omega_{\text{LO}} f e^2 L_{QW}} \tag{2.136}$$

with Γ_{LO} the LO-phonon damping rate, Γ_{UP} (Γ_{LP}) is the upper (lower) polariton damping rate, ω_{pump} the pump frequency and N_{QW} the number of quantum wells. It can be noted that, unlike QCL, the lasing threshold of polariton lasers decreases with a decreasing number of wells.

2.2.3. ISB-polariton scattering within a dispersive MIM cavity

The results presented here used an MIM dispersive cavity to achieve photon emission through ISB polariton scattering. The active region was 36 repetitions of 8.3 nm GaAs wells and 20 nm $Al_{30}Ga_{70}As$ barriers. At 78 K, the ISB transition was measured at 29.8 THz. This active region was embedded in a dispersive MIM cavity with a grating period of 4.26 µm and a filling factor of 72 %. The experimental dispersion measurement and the configuration which provides the LO-phonon energy difference between the upper and the lower polariton state at $k_{//} = 0$ are shown Fig. 2.9 (b). In GaAs, the LO-phonon frequency is $\omega_{\mathrm{LO}} = 293.5\,\mathrm{cm}^{-1}$.

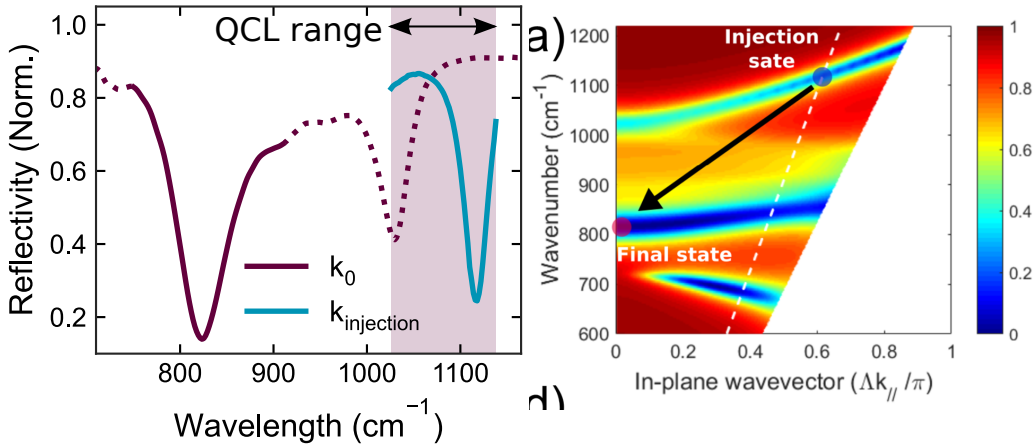

Figure 2.9.. (a): reflectivity of the injection state (solid blue line) and the final state (solid purple line). **(b)**: color plot of the reflectivity as a function of the angle of the sample presented in Ref. [89].

For the pumping experiment, a commercial quantum cascade laser (QCL) from Daylight was used. Its tuning range extends from 1026 to 1040 cm^{-1}. The tuning range is plotted in solid dark purple, with the injection state reflectivity in Fig. 2.9 (a). The upper polariton at the angle $\theta = 41°$ is the injection state, where the polariton population will be created by resonant pumping and the lower polariton at $k_{//} = 0$, which is the final state, is around 294 cm^{-1} from the injection state.

A schematic of the experiment setup can be seen Fig. 2.10 (a). The QCL signal is shined upon the sample at a 41° angle. A $\lambda/2$ waveplate is used to ensure the TM polarization to couple with the cavity. The specular reflection is recovered on a power meter while the normal emitted light is collected by a ZnSe lens and send through a Bruker 70v Fourier-Transform Infrared (FTIR). The light is then focused and measured by a nitrogen cooled MCT detector. One key element of the detection system is the long wave filter (LWP) inserted between the output lens and the MCT. It is design to offer a 30 dB attenuation above 1000 cm^{-1}. This attenuation is necessary due to the pump stray light from the grating that is collected at $\theta = 0°$, which is orders of magnitude more intense than the emitted signal.

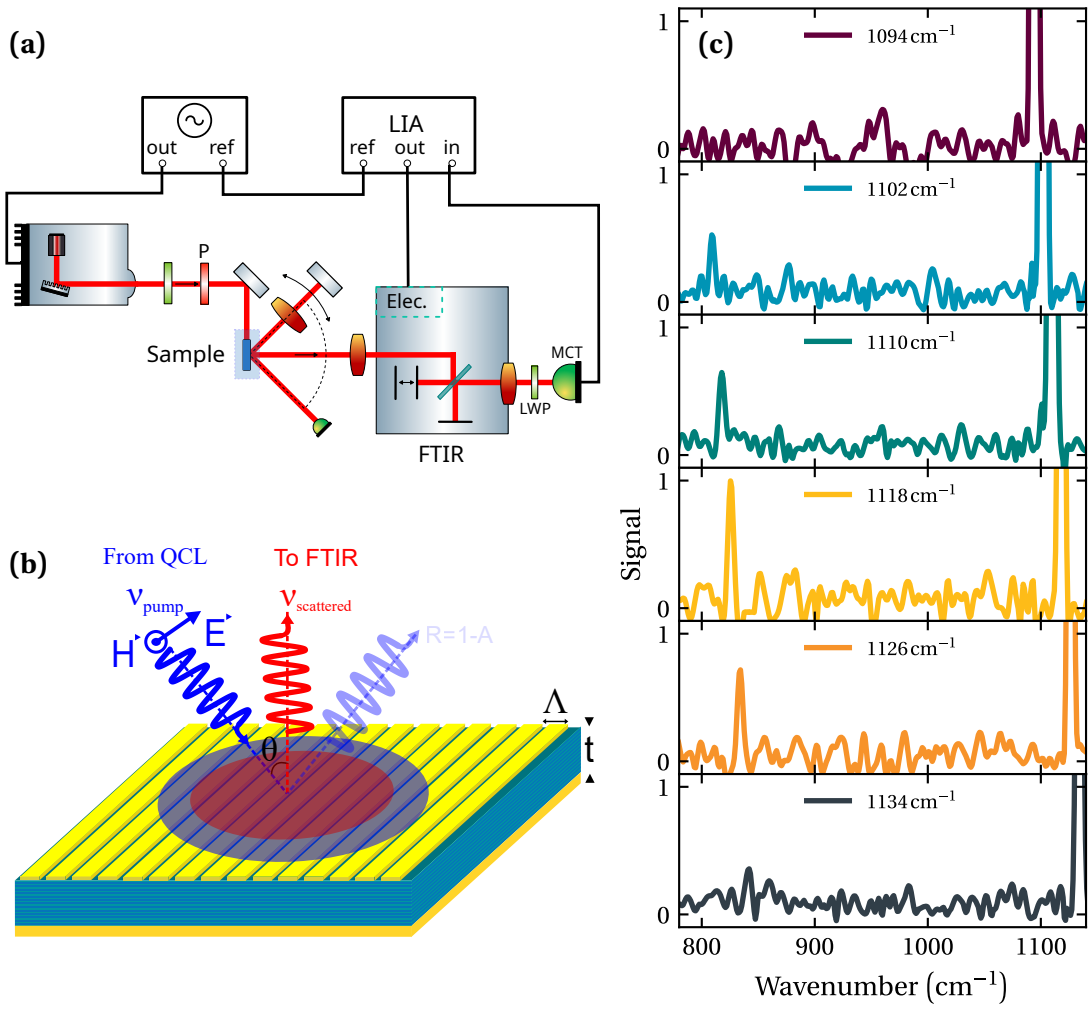

Figure 2.10.. **(a)**: experiment schematic. **(b)**: optical configuration for the pump coupling with the cavity. **(c)**: measured signal depending on the frequency for several pump frequencies.

The results of these measurements for different pumping frequencies can be seen Fig. 2.10 (c). The high intensity peak is the scattered light from the QCL, the low intensity one is the emitted signal. Despite the LWP, the source signal remains intense. The first important thing to note is that for the different pump frequencies, the frequency difference between the pump and the emitted signal is exactly ω_{LO} the LO-phonon frequency in GaAs which prove its involvement in the emission process. The second observation is that the peak intensity of the scattered signal depends on the upper polariton absorption. At 1118 cm^{-1}, which correspond to the maximum of absorption of the upper polariton 41°, the scattered signal is maximum. Detuning the pump from this frequency decreases the peak intensity. Finally, the frequency difference between the stray light from the pump and the scattered light is exactly 293 cm^{-1}, the LO-phonon frequency. Note that the demonstration was also done using the InGaAs−AlInAs system, where the separation between the pumped and scattered polaritons was equal to 271 cm^{-1}, corresponding to the value of the LO-phonon of this material system [89]. Using Eq. (2.136), an estimate of the lasing threshold for the cavity used in

Ref. [89] is around 70 kW·cm^{-2} per well, which corresponds to an average pump power of ≈ 20 W per well. Reaching the lasing regime would have required a pump able to deliver an average power of ≈ 720 W

Despite being far from the required power to obtain lasing, these results are an important milestone. It is the first conclusive demonstration of photon emission from phonon scattering of optically pumped ISB polaritons.

2.3. ISB polaritons spontaneous emission under resonant optical pumping within a non-dispersive MIM cavity

While the results on dispersive cavities conclusively demonstrated the photon emission, the system remains far from the potential lasing threshold. If one wishes to keep the measurement setup with a limited pump power, it is not possible to build a large enough the population density at the final state. Improvements on the sample are necessary.

According to Eqs. (2.135) and (2.136), several knobs are available to increase the population density at the final state for a constant pump power. In this section, the emphasis will be set on a method that could improve the LO-phonon scattering rate Γ_{scat}. In this respect, a different MIM cavity geometry will be explored.

2.3.1. Possible improvement of the polariton scattering rate

Independently to the polariton lifetime, increasing the amount of scattered polaritons toward the final state would increase the final state occupation. According to Eq. (2.135), a possible course of action is to reduce the group velocity of the final state at $k_{/\!/} = 0$. The group velocity is:

$$v_f^{gr} = \frac{\partial \omega}{\partial k} \tag{2.137}$$

The group velocity is related to the curvature of the lower polariton near $k_{/\!/} = 0$. The curvier it is, the higher the group velocity and the lower the polariton scattering is. On the other hand, a flatter lower polariton branch leads to a smaller group velocity which would increase the scattering rate. A good candidate to explore this idea is the non-dispersive cavity introduced Section 2.1.2.2. The advantage of this type of cavity is the similarity with the dispersive one in terms of conception, fabrication and measurement method.

Another advantage of the non-dispersive cavity comes from the active region design. The strategy to obtain the non-dispersive behavior is to reduce the active region thickness in order to obtain an impedance mismatch confining the optical mode under the metallic slabs [67], as discussed previously. Using a similar active region design as the one used for the LO-phonon experiment presented Section 2.2.3, a compatible active region with a non-dispersive sample is achieved by reducing the amount of quantum wells. According to Eq. (2.136), this is beneficial for the lasing threshold as this number is proportional to N_{QW} the number of quantum wells in the active region. A lower pumping power would in principle be necessary to reach the final state stimulation.

2.3.2. Design and fabrication of the non-dispersive cavity

To explore this design, a similar active region used for the demonstration of polariton scattering in [89] was used (HM4162). The only difference is the number of quantum wells (7 instead of 36) to reduce stack thickness which goes from 1.1 µm to 288 nm. The growthsheet can be found in Appendix A.9 and a multipass transmittance measurement along with its Voigt fit are plotted in Fig. 2.11.

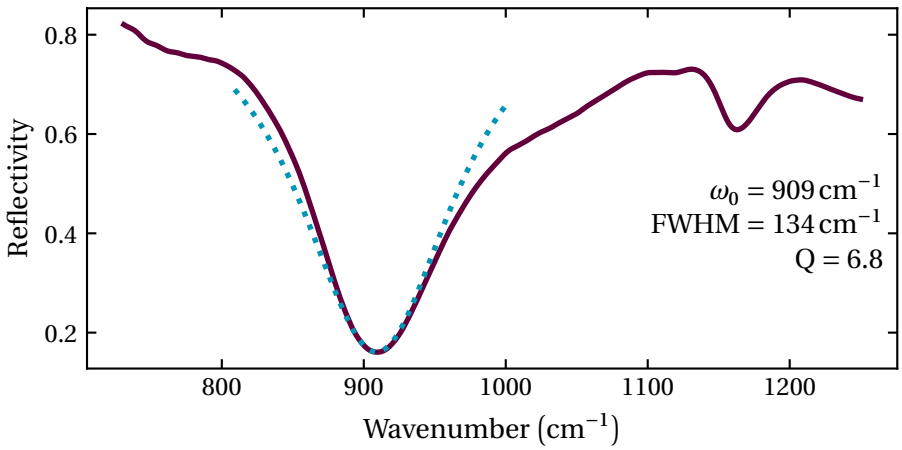

Figure 2.11.. Multipass transmittance measurement of HM4162 active region

To design the cavity parameters, a RCWA code was used.

A major difference exists between the development of a suitable cavity for observing the phonon-polariton scattering between a dispersive and a non-dispersive cavity. In the dispersive case, the frequency separation between the injection state and the final state at $k_{\parallel} = 0$ changes with the injection angle. Any deviations between the simulated and fabricated sample can be recovered using the dispersion of the photonic mode. However in the non-dispersive case, the dispersion remains constant with the incident angle. There is no possibility to recover from fabrication imperfections. To make a sample suitable for studying phonon-polariton scattering (with an energy difference between upper and lower polariton branches of 293 cm^{-1}) with the upper polariton branch in the frequency range of the MIRcat QCL unit, an array of non-dispersive cavities with a varying strip width on a waferbonded HM4162 active region was made and measured (see Fig. 2.12 (a)). The strip width ranges from 0.4 to 1.9 µm, with a constant gap of 1.4 µm. The sample was made using e-beam lithography and Ti/Au evaporation. Each of the resonators composing the array are 200 µm^2.

The sample was measured in reflectivity on a Nicolet microscope FTIR, with an objective at 20°. The reflectivity was then normalized by the reflectivity of a plane gold mirror. The results of the measurements are shown in Fig. 2.12 (b).

From the polariton splitting energy as a function of the metal strip width, plotted in Fig. 2.12 (c), the most suitable cavity for the phonon-polariton scattering can be identified. Here, the LO-phonon frequency is crossed for samples with stripes between 0.9 µm and 1 µm. Using the same e-beam parameters for the fabrication, three resonators of 1 mm^2 with the metallic slab width of 0.925, 0.5 and 1 um were made. In Fig. 2.12 (d), the Hopfield coefficients for the resonator array, depending

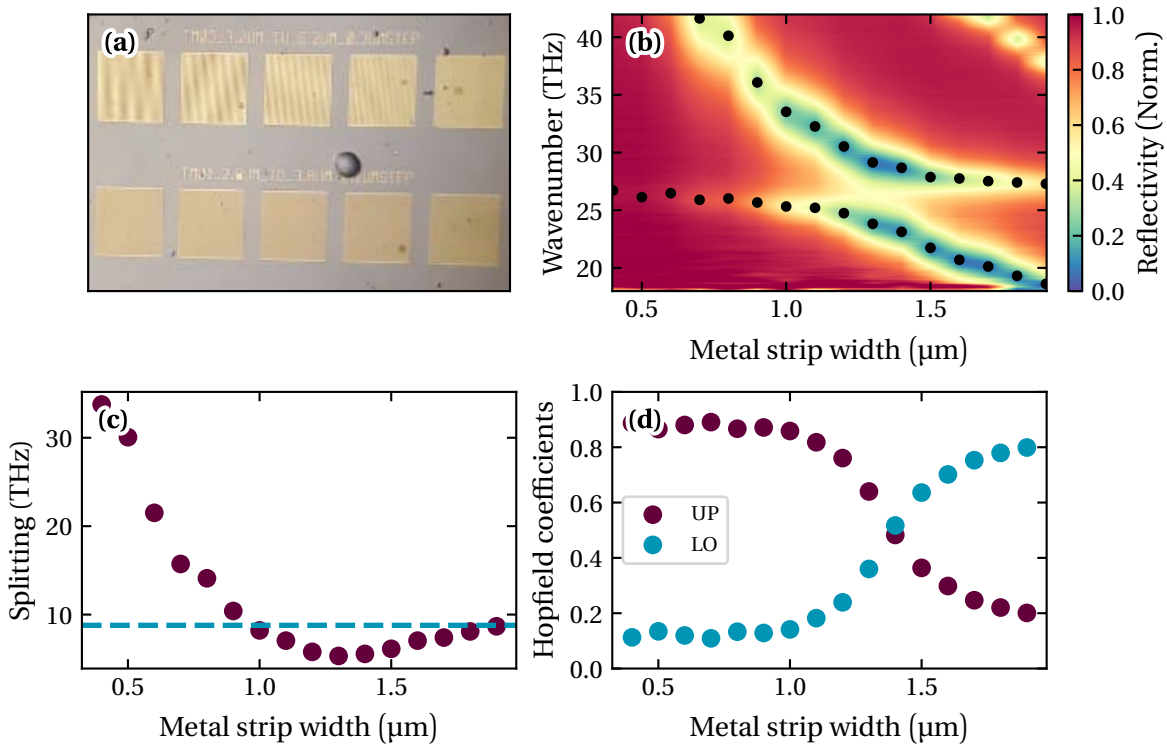

Figure 2.12.. **(a)**: Picture of the MIM cavity array. **(b)**: Color plot of the photolithographic dispersion. **(c)**: Frequency splitting between the upper and lower polariton depending on the metal slab width. The solid blue line is the LO-phonon frequency in GaAs ω_{LO}. **(d)**: Hopefield coefficient

on the metal slab width is plotted. For the samples fabricated for the pumping experiments, the coefficients are $\alpha^i_{\mathrm{ISB}} = 0.84$ and $\alpha^f_{\mathrm{ISB}} = 0.16$. While this does not correspond to the most favorable configuration (according to Eq. (2.135), the best case is $\alpha^i_{\mathrm{ISB}} = \alpha^f_{\mathrm{ISB}} = 0.5$), fabricating a sample with the right polariton splitting, with the Hopfield coefficients $\alpha^i_{\mathrm{ISB}} = \alpha^f_{\mathrm{ISB}} = 0.5$ would have required a new active region growth.

2.3.3. Improvements on the optical pumping experimental setup.

The measurements of the scattered signal emission from the non-dispersive cavities was done on the same setup used for the dispersive cavities experiments [89]. However, a few changes were made in order to make the setup better suited and easier to use. The first change was the introduction of a goniometer. Up to now, the scattering experiments were done at a fixed angle of 41°, which corresponds to the optimal angle for the sample used for the experiment. The samples of interest here are expected to be insensitive to the incidence angle. However, the fixed system used previously lacked flexibility optimizing the optical alignment which turned out to be an important task to obtain results. The development and integration of a homemade goniometer opened the possibility to explore several angles of incidence, and optimize the alignment.

The second change was the introduction of a second LWP filter before the MCT detector. Fig. 2.13

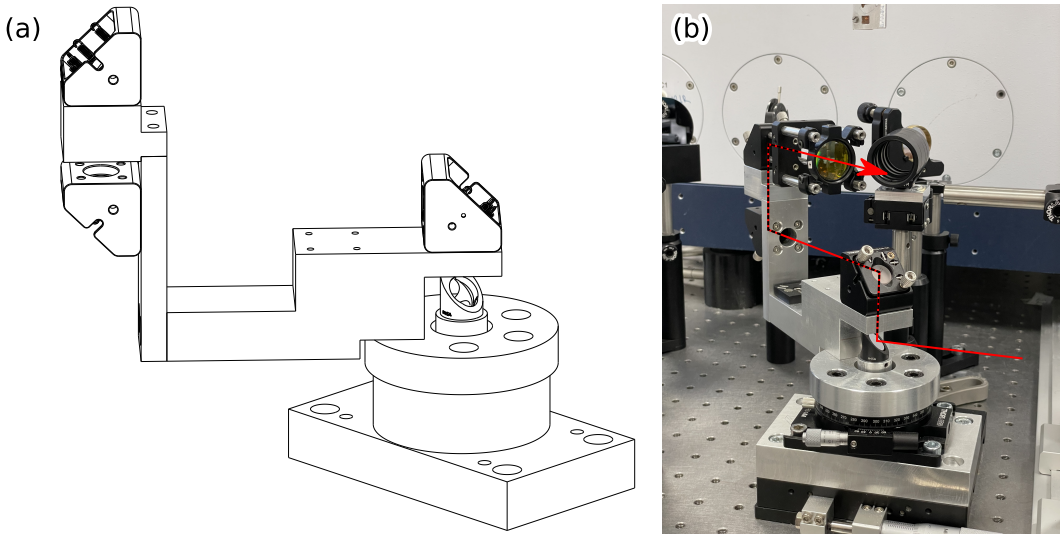

Figure 2.13.. (a): CAD schematics of the goniometer unit. **(b)**: Picture of the goniometer unit, with the light path.

shows two measurements done on the 0.95 µm metallic slab non-dispersive cavity sample, with exactly the same parameters, but the number of LWP. Two major observations can be extracted from this measurement comparison. The first is that adding a second LWP successfully attenuated completely the pump signal. The second is that the relative amplitude of the scattered signal is higher on the 2 LWP measurement, compared to the 1 LWP measurement. The reason of this effect comes from the non-linearity of the cooled MCT detector [92].

2.3.4. LO-phonon scattering in a non-dispersive cavity

2.3.4.1. Pump frequency dependence on the polariton emitted light

The first experiment that has been performed was to confirm photons can be emitted and measured using a non-dispersive cavity. The goniometer arm was set at 45° and the pump at 1140 cm^{-1} which coincides with the maximum of absorption of the upper polariton (see Fig. 2.14 (a)). The result of this measurement can be seen in Fig. 2.14 (b). The effect of the stacked LWP appears clearly: no signal coming from the stray light scattered by the sample was measured at the pump frequency. As expected, the wavelength separation between the QCL pump and the measured signal is 293 cm^{-1}. These results are similar to what is observed with dispersive cavities. The energy difference corresponds to the LO-phonon frequency.

To confirm this result, the measurement was repeated at different pump frequencies in order to assess if the frequency separation remains constant. Also, this will allow to observe the measured signal amplitude evolution depending on the pumping state absorption. The results are visible in Fig. 2.14 (b).

Similarly to the dispersive cavity, there is a correlation between the absorption of the pumped upper polariton state and the amount of emitted light, in agreement with Eq. (2.133). For every pump wavelength, the emitted signal wavelength separation is locked at 293 cm^{-1}.

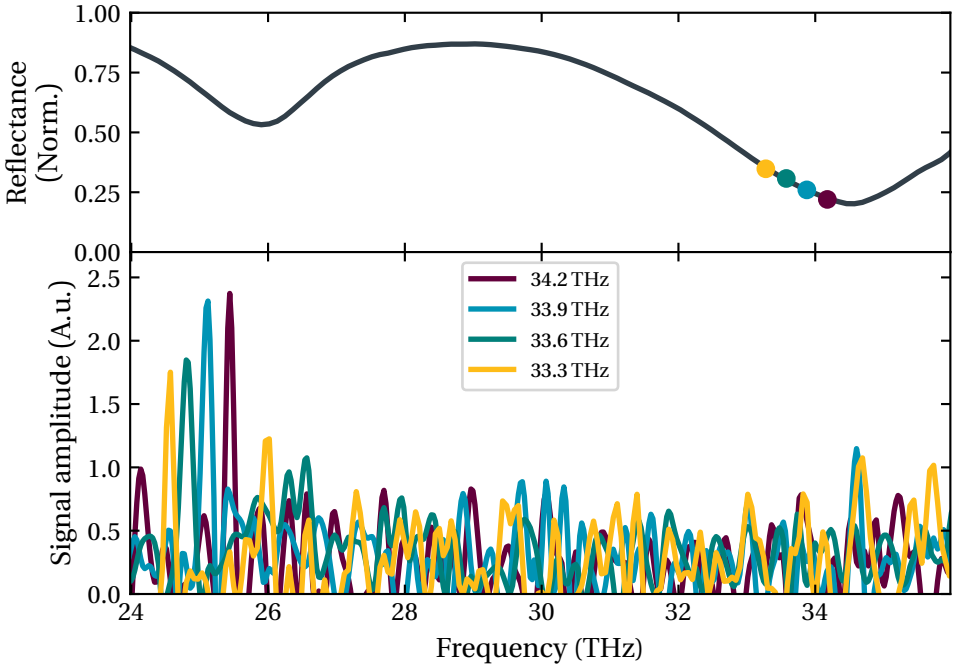

Figure 2.14.. **(a)**: FTIR measurement of the sample reflectivity. The two absorption peaks are the lower and upper polariton. **(b)**: scattered signal for different pump wavelength. The dots are the source output power depending on the frequency.

Fig. 2.14 (a) shows the sample reflectivity measured using the microscope FTIR Nicolet at 27°. Fig. 2.14 (b) depicts the pump power and frequency (dots) and the measured signal (solid lines). The results on the non-dispersive cavities share several similarities with the dispersive one [89]. The first observation is that the frequency difference between the pump and the scattered signal remains constant for every measured frequency of 293 cm^{-1}. It confirms that the LO-phonon plays a role in the light emission process.

The second observation is the impact of the injection and final state absorption on the scattered signal intensity. For a given pump fluence, the number of polaritons generated at the injection state follows Eq. (2.133) and it depends on the absorption at the said state. The measured output amplitudes followed this trend: at 1140 cm^{-1}, which correspond to the highest absorption frequency of the sample accessible by our QCL unit, the measured signal amplitude is the highest. The amplitude decreases as the pump frequency detunes from the maximum of absorption.

2.3.4.2. Pump angle dependence on the polariton emitted light

To confirm the non-dispersive property of the cavity and the impact on the scattered light frequency, we took advantage of the home built goniometer to explore the signal evolution when different pumping angles are used. Because of the 2 inches collection lens, and the reduced clearance due to the cryostat window, the accessible angle range by the goniometer's arm is limited between 34°

and 50°. For each angle, the light collection was done at normal angle. The pump wavelength was 1130 cm^{-1}. The results are shown in Fig. 2.15.

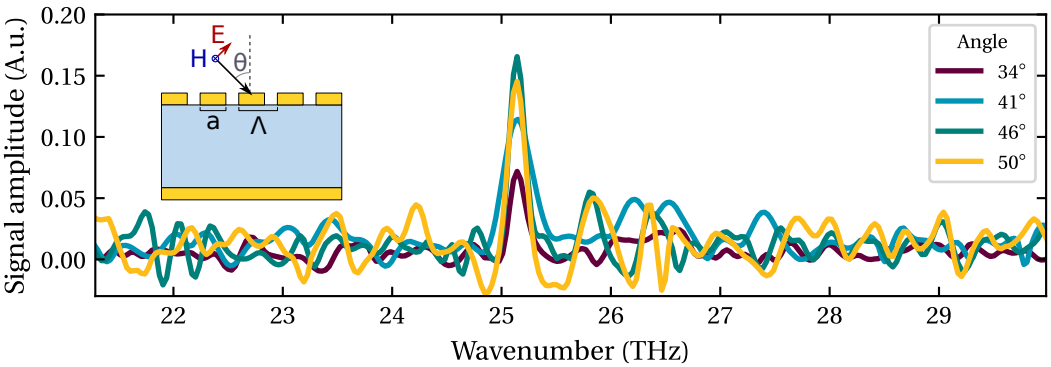

Figure 2.15.. Measured signal amplitude at different pump beam impinging angles.

Interestingly, the signal wavelength remains constant with the pump beam angle, locked at the LO-phonon separation ($\omega_{LO} = 293.5\,cm^{-1}$), which confirms the non-dispersive nature of the fabricated cavity. For the different angles measured, no trend on the emitted signal intensity can be extracted. The slight changes in amplitude come possibly from the noise of the measurement and most probably a slight misalignment due to the geometrical spreading of the pump beam. Despite the relatively weak level of the output signal, these measurements are the demonstration that the phonon-polariton scattering can also occur using non-dispersive cavities. However, it can be observed that by comparing the output signal with the background noise amplitude, the transition to a non-dispersive cavity did not lead to expected improvement of the emitted signal.

Nonetheless, it is very likely that the scattering rate Γ_{ph} increased. The quality factor of a dispersive and non-dispersive cavity are different: $Q_{disp} \approx 50$ while $Q_{non-disp} \approx 30$. The reason of this difference comes from the mode confinement: in a non-dispersive cavity, all the electromagnetic field is confined in a smaller volume, The mode penetrates deeper in the metal, increasing the losses. Despite this decreased Q-factor, a similar output signal is measured, which can be explained by an increase amount of scattered polariton to the final state.

2.3.4.3. Difficulties linked to the non-dispersive final state

In Section 2.2.3, it was explained that one key ingredient of the dispersive cavity design was that the state at $k_{\parallel}$ has to be the state of lower energy. The reason is to make this state the most favorable one for scattered polaritons to accumulate. Due to the nature of the non-dispersive system, no such state exists. The flat dispersion means that there is a continuum of possible final states with different $k_{\parallel}$ values.

To confirm this hypothesis, a measurement was performed at the same pumping angle, frequency and power but with a different collection lens: a 1 inch ZnSe lens instead of the 2 inches used previously. In theory, reducing the collection angle should reduce the amount of signal measured (see Fig. 2.16).

Despite several attempts of measurements with the 1-inch lens, no signal was ever measured in this configuration. It is very likely that the reduced collection angle (and in turn the reduced number

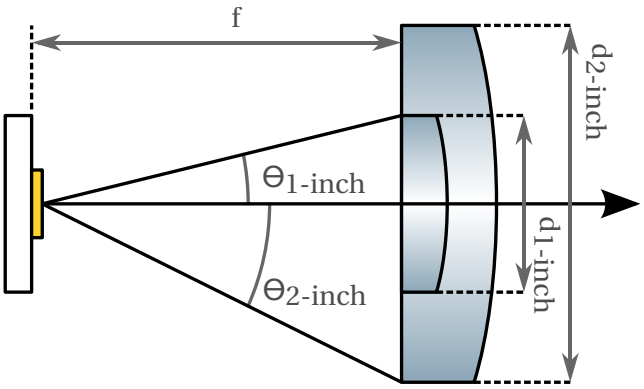

Figure 2.16.. Difference of collection angle with a 1-inch and 2-inch lens.

of wavevectors) does not allow to measure a signal high enough to emerge from the background noise.

This result highlights the necessity to find a way to favor one specific final state for polariton scattering. This can be achieved using a different measurement setup.

In either case (dispersive or non-dispersive cavities), using a coherent pump to populate the upper state and relying on the phonon scattering rate does not allow to reach the necessary population to enter the final state stimulation regime. Recently, another approach was used to demonstrate an increased efficiency of the polariton-polariton scattering process using a dispersive cavity, by building a polariton population at the final state at $k_{\parallel} = 0$ [93] using a probe beam.

Borrowing the idea, a similar experiment can be applied to the non-dispersive cavities. The idea is summarized in Fig. 2.17.

Fig. 2.17 (c) shows the dispersion of the reflectivity of a non-dispersive cavity. Fig. 2.17 (a) and (b) depicts the reflectivity at 10° and 40°, and a theoretical polariton population if a probe and a pump were shined at respectively 10° and 40°. This population is calculated by multiplying the absorption by a uniform arbitrary value (here 1) for the probe, and a delta function for the probe (here 2). We know, according to Eq. (2.131), that the scattering rate toward a specific state is proportional to the population of said state. Using a probe to build an initial population would help to overcome the fundamental problem that no particular state is favored in the case of non-dispersive cavity. With this method, coupled with the improved phonon-polariton scattering rate obtained using non-dispersive cavities, one could expect that gain or even condensation would be observed.

2.3.5. Conclusions on the phonon-polariton scattering process within non-dispersive cavities

While sharing the same mechanism for the photon emission (LO-phonon scattering), the non-dispersive cavities have one major difference. First, no state is favored as final state compared to dispersive cavities that are designed to exhibit the lowest energy state at $k_{\parallel} = 0$. However, this issue can be circumvented using a different measurement approach. By inducing a polariton population first at a state on the lower polariton branch, that state becomes the most probable one polariton scattering. This can be achieved with a pump-probe measurement setup [93]. Combined with the

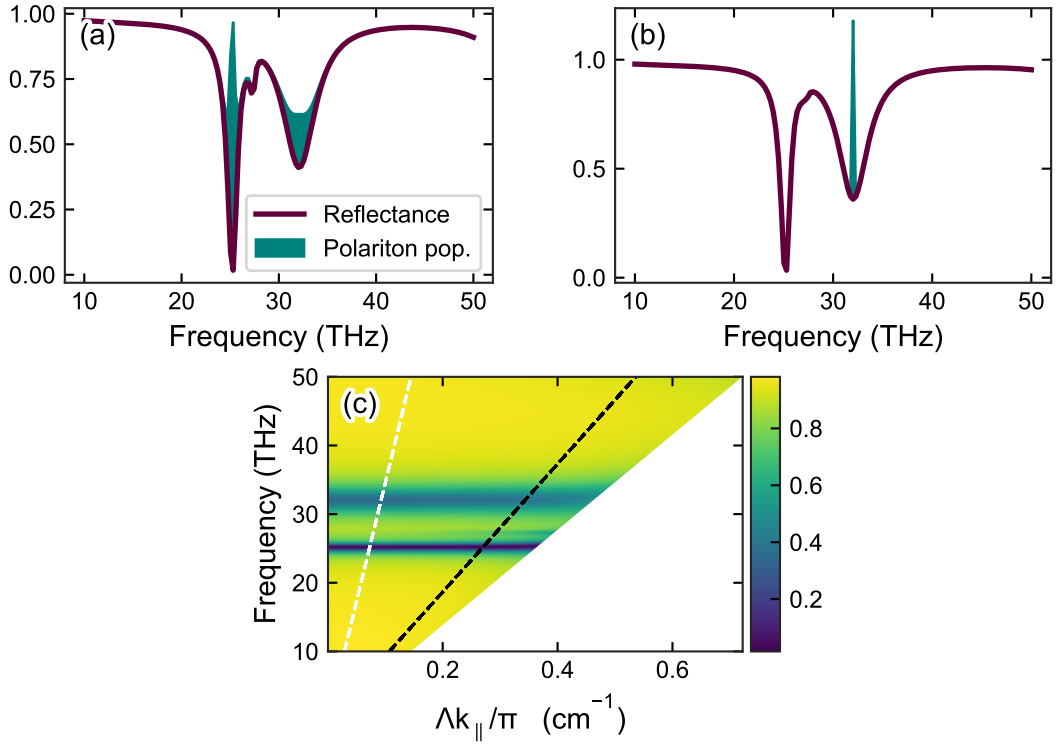

Figure 2.17.. **(a)**: Reflectivity of at the probing angle, and the polariton population generated by the probe. **(b)**: Reflectivity of at the pumping angle, and the polariton population generated by the pump. **(c)**: Angular dispersion of the simulated non-dispersive cavity. The probing and pumping angles are respectively the white and black dashed lines.

increased scattering rate due to the flat dispersion, the non-dispersive cavity could be a promising platform for the demonstration of the final state stimulation regime within ISB polaritonic systems.

2.4. Improved cavity Q-factor: all dielectric photonic crystal slab

In the previous section, the strategy to reach a final state regime that has been studied was to improve the phonon-polariton scattering rate. Another strategy, in the continuation of the work done by our team on the phonon-polariton and the polariton-polariton scattering [93], is to improve the cavity quality factor. A higher quality factor implies a longer photon lifetime thus an improved polaritonic lifetime. For a dispersive cavity with an energy minimum at $k_{\parallel} = 0$, it means that a scattered polariton will stay longer at the final state before decaying, hence the population at the final state will build up more easily. The main problem with the MIM cavities is the presence of gold, which introduces losses but necessary to obtain modes that can coupled with ISB transitions

To expect an improvement on the cavity Q-factor, cavities without metal layers are necessary. One example of such cavities, which exhibits extremely high Q-factor is the photonic crystal cavities. It

is this category of cavities that will be theoretically explored in this section in order to improve the photon and polariton lifetime.

2.4.1. Generalities on photonic crystals

Photonic crystals are structures that present periodic variation of their permittivity. The variation can either be 1-, 2- or 3-dimensionnal with infinite dimensions in all directions. They offer tremendous possibility to control, guide and confine electromagnetic wave using only dielectric materials, thus with intrinsic very low losses. Using these properties, application were found for developing waveguides [94], beam splitters [95] or cavities [96]. The translation of these infinite structure to real structures with finite thickness are called photonic crystal slabs.

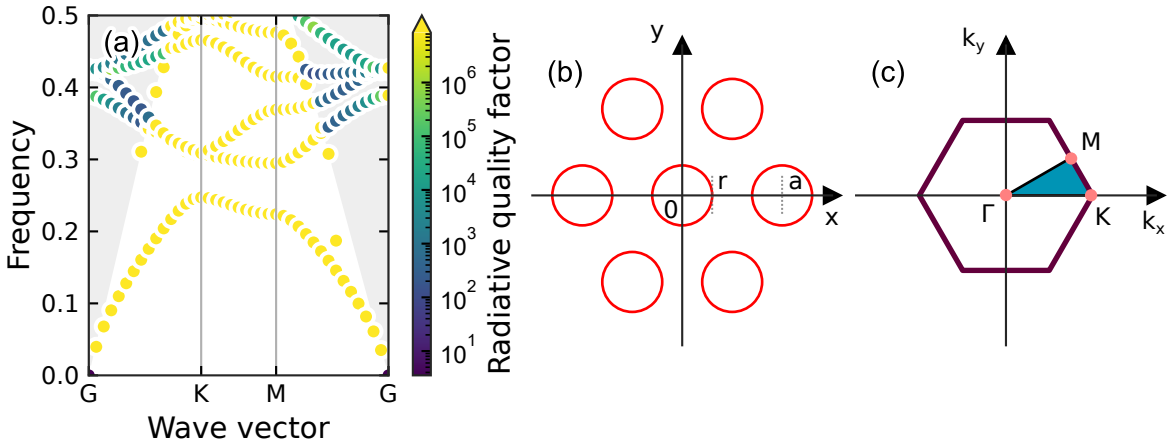

Figure 2.18.. **(a)**: guided mode expansion simulation of Photonic crystal slab (PCS) with triangular lattice holes. **(b)**: top view of the triangular lattice. a and r denote respectively the lattice constant and the radius of the air holes. **(b)**: first Brillouin zone of the reciprocal lattice, and the highly symmetric points Γ, M and K

To illustrate, the emphasis is set on a Photonic crystal slab (PCS) with a triangular lattice of cylindrical air holes. In Fig. 2.18 (b) and (c) depict the top view and the reciprocal lattice are plotted. The lattice is defined by the parameters a and r, which are respectively the lattice constant and the air holes' radius.

In Fig. 2.18 (a) shows a simulation of a PCS using the guided mode expansion (GME) method. The gray areas represent the light cone, and the color dots the modes and their quality factor.

PCS can support two kinds of mode. The first ones are guided modes which are confined modes by the cladding layers due to total internal reflections [97]. Fig. 2.18 (a), these modes correspond to the modes lying below the light line, thus cannot be probed by an external field. These modes posse high Q-factor. The second category is the quasi-guided mode. These modes posse a finite Q-factor due to radiation losses. They are often called leaky modes or guided mode resonances (GMR) due to their ability to couple with external radiation.

In the following pages, the emphasis will be set on the triangular photonic crystal slab. In a perfect infinite 2D photonic crystal, the TE (TM) mode can only be excited by a TE (TM) polarized source.

It is a consequence of the in-plane symmetry of the crystal. However, for a finite thickness slab this symmetry is not exactly respected, which implies polarization mixing. A consequence is that in-plane TM mode can be excited by TE polarized source and vice versa [98]. In the context of the strong-coupling regime, these TM modes will be the focus of the next part as they are the only mode coupling with an ISB transition.

2.4.2. Simulation of the photonic crystal slab cavity

To investigate the use of PCS structures in conjunction with ISB transitions in QWs, two numerical tools were used. The reflectivity dispersion was calculated using S^4 (for Stanford Stratified Structure Solver) [99], a freely available Rigorous Coupled-wave analysis (RCWA) code while the mode profiling was performed using COMSOL Multiphysics.

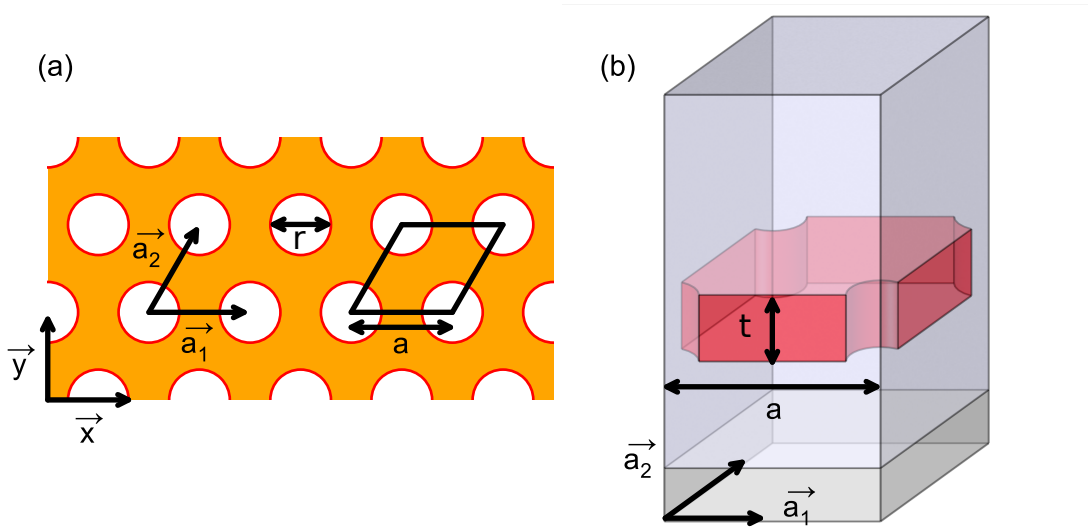

Figure 2.19.. (a): schematic of the triangular lattice. **(b)**: COMSOL model view of the simulated unit cell.

For both softwares, a model implementing a single unit cell of the PCS was created, with Floquet boundary conditions. The axis definitions as well as the lattice constant a and the hole radius r and thickness t can be seen in Fig. 2.19 (a) and (b). The lattice vectors are defined as follows:

$$\boldsymbol{a}_1 = a\boldsymbol{x} \tag{2.138}$$

$$\boldsymbol{a}_2 = a\left[\cos\left(\frac{pi}{3}\right)\boldsymbol{x} + \sin\left(\frac{pi}{3}\right)\boldsymbol{y}\right] \tag{2.139}$$

As a starting point, a similar structure to the one used in [100] was used with a lattice constant $a = 3.675\,\mu\text{m}$, a hole radius $r = 0.16a$ and a thickness $t = 0.34a$. In fact, such slab has already been successfully used in conjunction with ISB QWIP active regions. Using S^4, an angle resolved simulation in the Γ-to-K direction was run for a TE- and TM-polarized incident wave. The results are plot in Fig. 2.20.

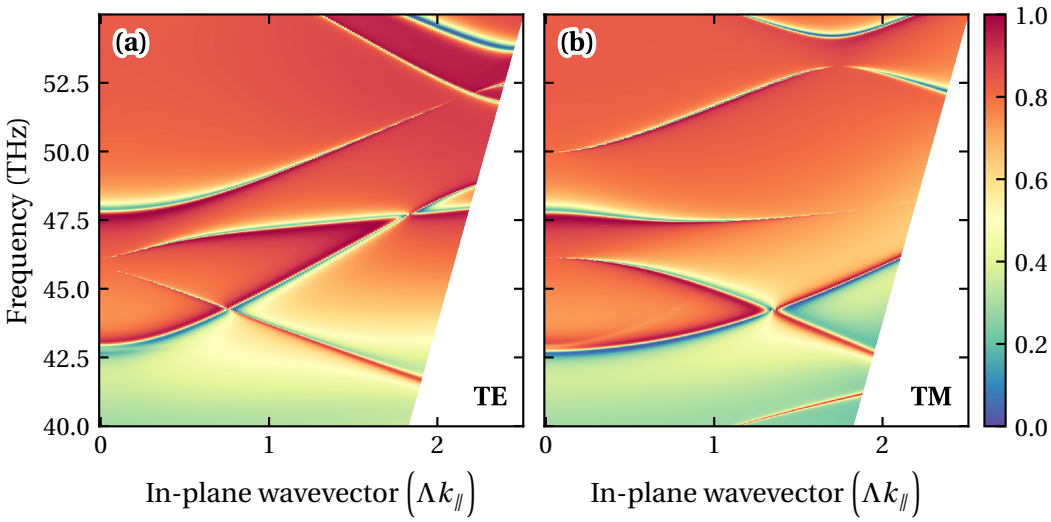

Figure 2.20.. Simulation of the angle resolved reflectivity for **(a)** a TE- and **(b)** a TM-polarized incident light source.

We focus our attention to the photonic mode at 48 THz. As the study of the electric field reveal it, it is a TM mode of the PCS, thus can couple with an ISB transition. The electric field at $k_{\parallel} = 0$ taken in the middle of the slab in the xy-plane is plotted in Fig. 2.21 (c). At $k_{\parallel} = 0$, this mode is degenerated. As the incident angle increases, the degeneracy is lifted: with the TE-polarized source the mode blue shifts while it red shifts with the TM-polarized source. Interestingly, the TE-polarized reflectivity presents a similar dispersion as the MIM dispersive cavity (see Section 2.1.2.1).

In Fig. 2.21 (a), the reflectivity at $k_{\parallel} = 0$ is shown. It presents a modulated background with Fano like resonances. First, the origin of the modulation of the reflectivity is investigated. It arises from the Fabry-Perot interferences within the slab [101]. As a consistency check, the reflectivity of a uniform slab (without the holes) was simulated. The permittivity of the uniform slab was changed to be equal to the average permittivity of the photonic crystal slab which is equal to:

$$\varepsilon_{\text{avg}}(\omega) = \frac{\varepsilon_{\text{GaAs}}(\omega)(\sin(60) - \pi(r/a)^2) + \varepsilon_{\text{air}}\pi(r/a)^2}{\sin(60)} \tag{2.140}$$

The result is plot in Fig. 2.21 (a) (blue dashed line). The unpatterned slab reflectivity overlaps almost perfectly the PCS reflectivity, without the Fano shaped features.

Then, the emphasis was set on the TM mode at 48 THz. To quantify the Q-factor of this mode, the reflectivity was fitted using the Fano lineshape equation [102]:

$$F(\omega) = A_0 + F_0 \frac{[q + 2(\omega - \omega_0)/\Gamma]^2}{1 + [2(\omega - \omega_0)/\Gamma]^2} \tag{2.141}$$

Here, A_0 and F_0 are constants, ω_0 the mode frequency, Γ the mode linewidth and q a dimensionless parameter describing the shape of the Fano resonance. The mode reflectivity and its fit are shown in Fig. 2.21 (b). A Q-factor of 250 is obtained, which is around an order of magnitude higher than

what is achievable with MIM cavities, and on a par with other works on ISB embedded in PCS [103].

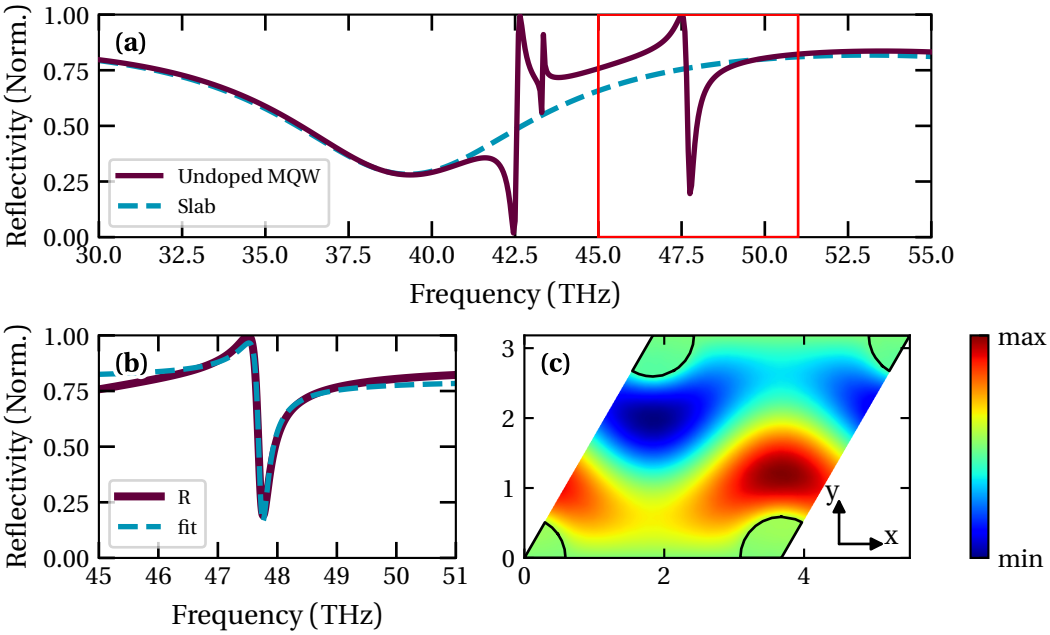

Figure 2.21.. **(a)**: numerically simulated reflectivity of an undoped PCS (solid line) and the equivalent unpatterned slab (dashed line) **(b)**: Fano fit of the TM mode reflectivity. **(c)**: E_z electric field in the xy-plane

2.4.3. Strong light-matter coupling regime with ISB transition embedded in PCS

To pursue the study of the PCS cavity, the strong-coupling regime in such cavities was numerically simulated. An effective medium permittivity (see Section 1.4.5) was used to model the ISB absorption. For this numerical simulation, a doping $n = 10^{12}\,\mathrm{cm}^{-2}$, a quantum well overlap $f_w = 0.12$ and a resonance frequency $\tilde{f}_{21} = 48\,\mathrm{THz}$ was used. In Fig. 2.22 (a) is presented a simulation at $\theta = 0°$ for the doped and undoped PCS. At the TM mode frequency, a strong coupling regime is obtained. It can also be observed that the reflectivity keeps the Fano shaped resonance.

Compared to the dispersion plot of MIM cavities, it makes the PCS spectra more complicated to analyze. Also, compared to MIM cavities that either absorb or reflect an impinging wave, the absence of mirror under the slab means that a part of the wave is transmitted. A way to clarify the coupling between the active region and the PCS mode is to calculate the absorption $A(\omega) = 1 - (R(\omega) + T(\omega))$. Fig. 2.22 (b) put the emphasis on the frequency range where the strong-coupling regime takes place. Compared to the reflectivity, which highlights a Fano like shape for the renormalized modes, the absorption shows a conventional Lorentzian lineshape.

Using S^4, an angle resolved simulation in the incident TE polarization was done. The results are presented in Fig. 2.23.

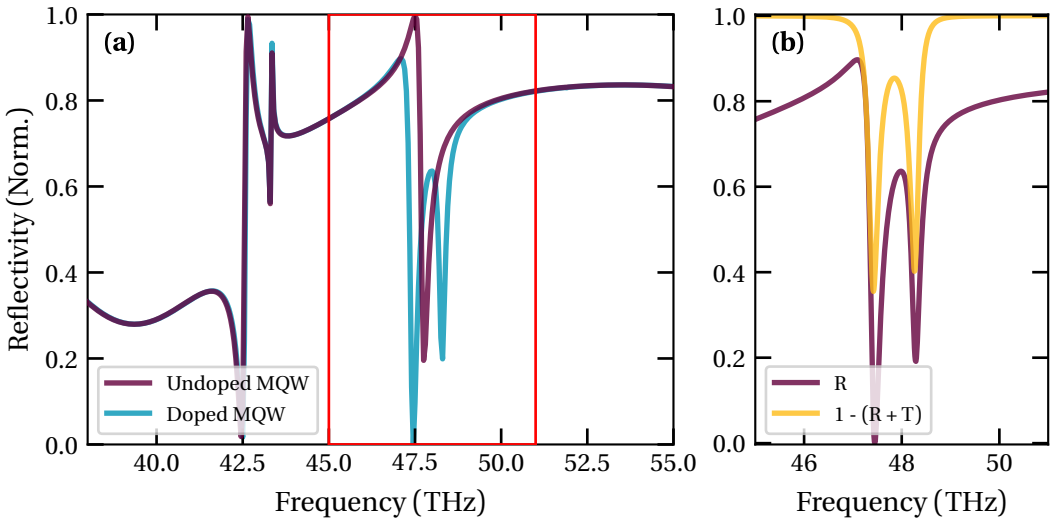

Figure 2.22.. **(a)**: numerically simulated reflectivity of a doped and undoped PCS. **(b)**: comparison between the reflectivity and 1 minus the absorption around the ISB transition frequency.

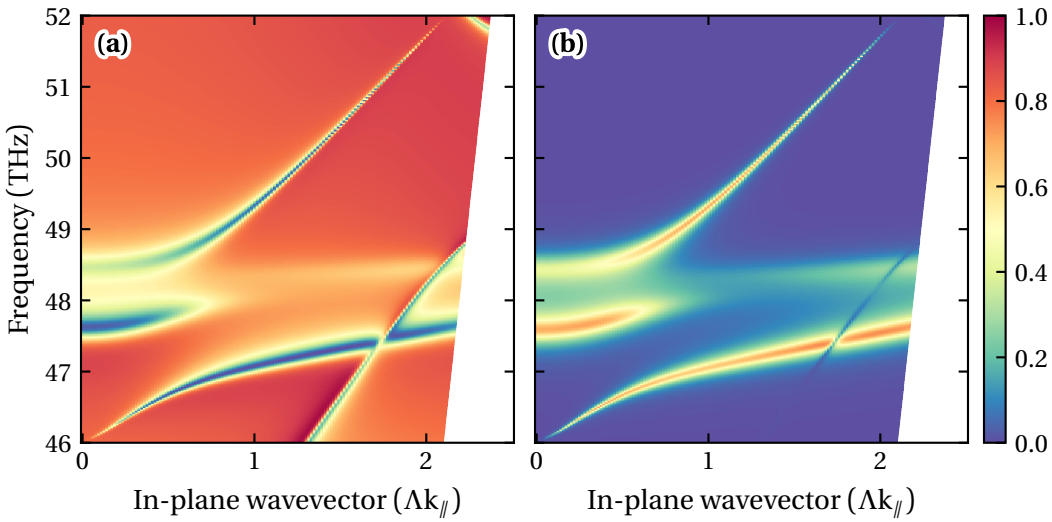

Figure 2.23.. Simulation of the angle resolved reflectivity for a TM-polarized incident light source. **(a)** the reflectivity and **(b)** the absorption are plot.

The absorption plot exhibits a strong dispersion which shares similar features with the dispersive MIM cavities. The lower branch has a flat dispersion with a minimum of energy at $k_{\parallel} = 0$, which is favorable for increasing the dispersion rate in the context of the phonon-polariton scattering. Furthermore, PCS are highly flexible in terms of design. Using the scalability property of photonic crystals, the optical response of a design can be shifted in frequency by scaling the whole geometry and keeping constant ratios between the period of the crystal, the hole radius and the slab thickness [104]. Once good ratios are found, the design can be adapted to several operating frequencies.

To assess the improvement using such a cavity would bring to the total system, one can calculate

the total Q-factor of the ISB transition and the cavity. Assuming a typical cavity and ISB transition Q-factor of 10, the total Q-factor is 10. However, using the PCS cavity modeled above, the total Q-factor is around 19. This corresponds to almost a factor two on the polariton lifetime. From simulations done on the results of a recent paper from our team on polariton-polariton scattering in MIM dispersive cavity, such an increase of the polariton lifetime would almost allow to observe gain [93].

2.5. Conclusions

In this chapter, two strategies were developed to improve ISB polariton emitters relying on phonon-polariton scattering.

The first one was to use non-dispersive cavities to improve the scattering rate. Evidence of photon emission with these cavities was demonstrated. However, no particular improvement on the signal amplitude was found. The reason might be that, contrary to the dispersive cavities, there is a multitude of final states on the lower branch. This issue can be circumvented by measuring the sample using a pump-prob scheme, to induce a polariton population on the lower branch and favor a final state with a specific wavevector. A pump-probe setup is currently being installed to explore this strategy.

The second strategy was the numerical simulation study of photonic crystal cavities as a replacement for the MIM dispersive cavities. Due to the absence of metal, these cavities have a better Q-factor, leading to a longer polariton lifetime. This improvement of the lifetime may be one of the key ingredient to reach the lasing threshold to demonstrate ISB polariton lasers.

Chapter

3

Parabolic quantum wells for room temperature operation in the THz

This chapter describes the work that has been done to develop high quality parabolic quantum wells operating in the THz frequency range using an innovative epitaxial technique in collaboration with the QNC-MBE epitaxy group of Dr. Z.R. Wasilewski at the University of Waterloo, Canada. Part of the theoretical framework, as well as the growths, were realized by C. Deimert, PhD student within the QNC-MBE group, while the experimental characterizations were performed at C2N, France. This partnership has led iterative improvements of the samples, via a thorough analysis of the experimental data. This synergy allowed us to set a record linewidth for a THz ISB transitions competing with square wells up to 150 K, along with a clear absorption line at room temperature. In this chapter, epitaxial growth concepts will be introduced, but not detailed in depth. A more complete description can be found in C. Deimert's manuscript, which is solely dedicated to the Parabolic Quantum Well (PQW) growth.

3.1. Theory

In this first section some basic principles related to THz ISB transitions will be introduced. Then there will be a discussion on the parabolic potential applied to quantum wells at these frequencies. Finally, two methods allowing to grow them are described.

3.1.1. The shortcomings of the THz square quantum well

As discussed in the introductory chapter Section 1.1.2, THz waves are low energy radiation with a photon energy $E = h\nu$ spanning from 4 to 40 meV, which is of the same order of the thermal agitation at room temperature $E = k_b T_{300\,\mathrm{K}} \simeq 25\,\mathrm{meV}$, while MIR radiation covers photon energies between 120 and 620 meV. It is instructive to have a look at the Fermi-Dirac distribution for these two wavelength range to grasp the inherent problem with square quantum wells at THz frequencies which hindered the development of THz devices, especially for the achievement of

room temperature operation. The distribution gives the probability to find an electron at a specific energy, for a given temperature. Its expression is:

$$f(E) = \frac{1}{1 + \exp\left(\frac{E - E_f}{k_b T}\right)} \tag{3.142}$$

where E if the energy, E_f is the Fermi energy, T is the temperature and k_b is the Boltzmann constant.

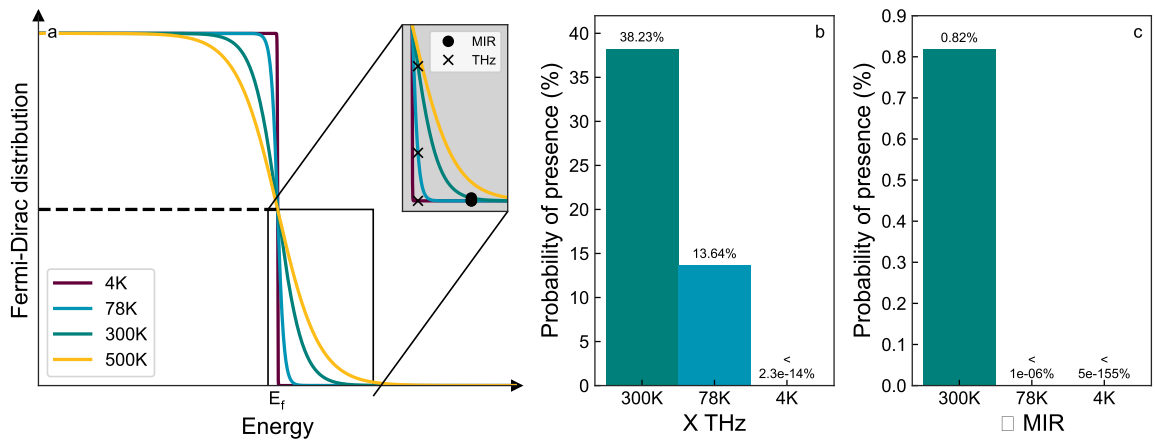

Figure 3.1.. (a): Fermi-Dirac distribution for various temperatures. The Fermi level corresponds to the energy where there is a 50 % probability of presence of an electron. **(b)** and **(c)**: Probability of presence of an electron in the second subband for a THz and MIR transition at respectively 3 and 30 THz.

Fig. 3.1 (a) represents this distribution for four different temperatures: 4, 78, 300 and 500 K. The Fermi energy is the highest energy state that can be populated by an electron at 0 K. Most of the time, its position is engineered to be between the first and second subband to ensure the first subband is populated by electrons. Let's suppose a situation where the Fermi level is at the first subband, and two transitions: a THz one at $\nu_{THz} = 3$ THz and a MIR one at $\nu_{MIR} = 30$ THz. The inset of Fig. 3.1 indicates the transition energies with respect to the first subband position, and Fig. 3.1 (b) and (c) the corresponding probability of presence of an electron at 4, 78 and 300 K. In the MIR case, the probability of presence remains close to zero on the whole temperature range. On the contrary in the THz case, the electron probability at 300 and 78 K are not negligible. Only cryogenic temperature brings the probability below 1 %. It means a standard THz quantum will not exhibit a resonant absorption at 78 K and 300 K.

In fact, such effect can be confirmed by a Schrodinger-Poisson simulation. During this thesis, the commercial software Nextnano++ was used. Here a square well designed to exhibit an absorption at 3 THz is simulated. Its wavefunctions, occupation levels of the confined states and calculated absorption at different temperatures are plotted in Fig. 3.2. At 4 K, only the lowest energy state is populated thus only a single strong absorption peak is visible around 3 THz. As the temperature increases, the second and third energy levels start to be populated which enables higher energy transitions, with a weaker contrast. It should be noted that this simulation shows a perfect picture of the situation. Experimentally, no absorptions are measured above 150 K due to a

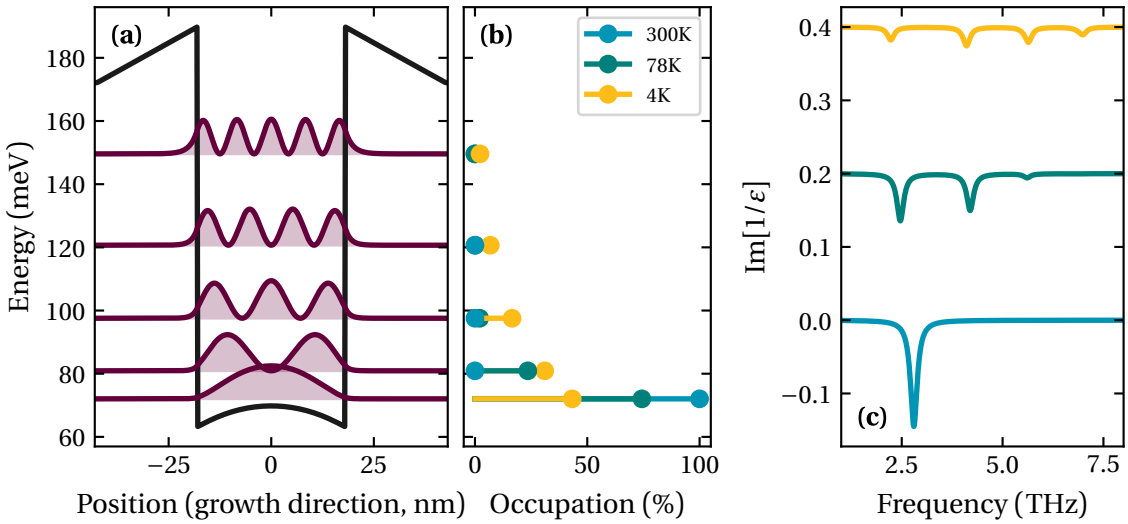

Figure 3.2.. **(a)**: Simulated squared quantum well conduction band and wavefunctions. **(b)**: Energy level occupations at 4, 78 and 300 K. **(c)**: Calculated absorption.

significant broadening, which flattens the peaks making them harder to spot (See Fig. 3.16 left for an absorption vs temperature of a real THz square well structure).

For this reason, current THz technology mostly need to be operated under liquid He cooling, either close cycle or continuous flow. There have been improvements in the operating temperature of THz lasers, with devices that can be operated up 250 K [105], but detectors remain bound to temperatures below nitrogen cooling.

3.1.2. The parabolic potential

In the end the whole problem with THz square wells at temperatures above 30 K is that absorption at several different energies occurs at the same time. If the different confined states were to be separated by the same energy, then only one absorption peak would appear. A well known system, often used to introduce quantum mechanics in textbooks, exhibits such property: the harmonic oscillator. If one solves the Schrödinger equation for a particle inside a parabolic potential, the possible energy levels are :

$$E_n = \left(n + \frac{1}{2}\right)\hbar\omega \quad \text{with} \quad n = 0, 1, 2, \ldots \tag{3.143}$$

In a parabolic potential, energy levels are evenly spaced. In theory, translating such concept to a quantum well structure would allow to have an active region that would undergo several transitions at the same energy. In that case the THz ISB transition is no longer dependent on the thermal distribution of electrons. Fig. 3.3 shows a Schrodinger-Poisson simulation of a parabolic well with a target ISB transition of 3 THz.

Similarly to the square well presented in the previous section, the electron population occupies only the first subband. However, despite having several subbands populated at higher temperature,

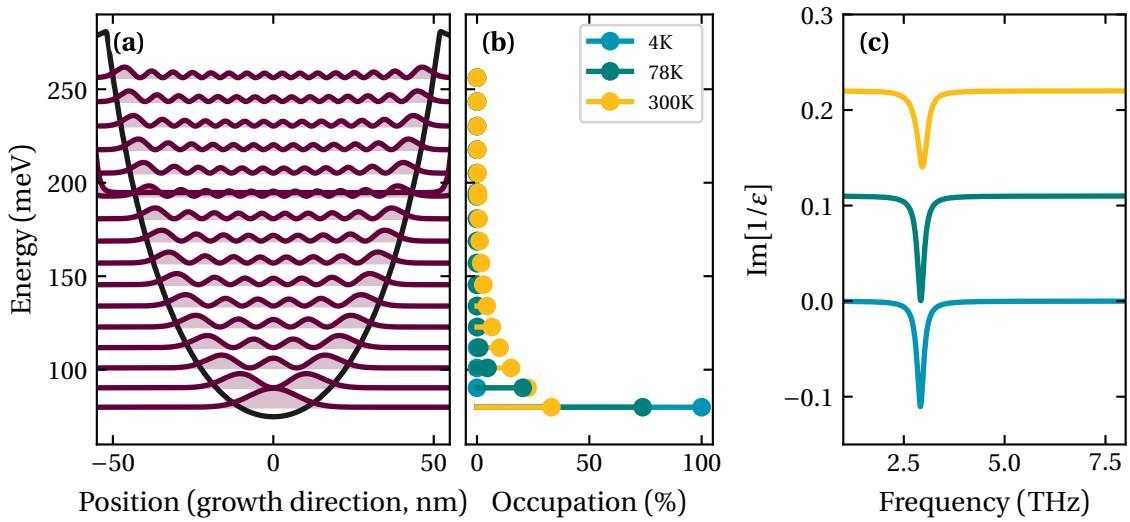

Figure 3.3.. (a): simulated parabolic quantum well conduction band and wavefunctions. **(b)**: energy level occupations at 4, 78 and 300 K. **(c)**: calculated absorption.

the calculated absorption does not change significantly. Instead of having several peaks, only one stable absorption is visible.

Furthermore, in a parabolic potential the Kohn theorem is respected [106]. This theorem predicts that the dipole excitations are not impacted by the electron-electron interactions. In a conventional square well, these electron-electron interactions induce a blue-shift of the ISB transition: the so-called depolarization shift (See Section 1.4.4), which is proportional to the number of electrons within the well. But thanks to the Kohn theorem, the observed transition of a PQW should remain unchanged no matter the number of carriers confined in the well, at least for an infinite parabolic quantum well. For a realistic PQW the potential profile has to be truncated at some point, but as long as the electrons see a parabolic potential the theorem should hold. In other word, if the well is deep enough to accommodate all the carriers, then a PQW is not affected by the depolarization shift. This effect was already observed experimentally in the FIR [107] with Landau levels.

3.1.3. Methods to grow quantum wells a with parabolic energy potential

In the coming paragraph, I will describe two different approaches to grow quantum wells with a parabolic energy potential. Despite the numerous advantages that were listed in the previous section, PQWs are not that commonly used. The main reason that slowed down development was the difficulty of growing them: in order to have a fairly close to parabolic conduction band, it is necessary to have a very accurate control of the epitaxial process.

In this part, two kinds of PQW implementations will be described: the first one is the interdigitated structure, a sequence of square quantum wells that mimics a parabolic energy level. The second kind is the result of C. Deimert work during his thesis, and is based on a continuously graded alloy.

3.1.3.1. Interdigitated PQWs

While the natural way to obtain a parabolic conduction band would be to change continuously the composition of the alloy with the position, the difficulty to do it reliably explains why the first parabolic quantum well attempts were not continuously graded but interdigitated structures [108]. The idea is to use the average energy value of well/barrier couples to mimic the desired parabolic potential [109, 110, 111]. This value can be calculated using the following equation:

$$E = \frac{E_{\text{well}} W_{\text{well}} + E_{\text{barrier}} W_{\text{barrier}}}{W_{\text{well}} + W_{\text{barrier}}} \tag{3.144}$$

where E_{well} and W_{well} (respectively E_{barrier} and W_{well}) are the well material energy and thickness (respectively of the barrier). To illustrate this equation, Fig. 3.4 (a) shows the average potential energy for fraction of GaAs/$Al_{30}Ga_{70}As$ well/barrier with a period of 4 nm. By doing the right sequence, it is possible to approximate any potential profile that is in the range of the well and barrier energies. The development of this growth method made semiconductor parabolic potential systems available, and proved to be a very interesting playground for fundamental studies. Examples are numerous: 3-dimensionnal electron gas thanks to an almost homogeneous electron distribution over a wide width [112, 113], light scattering to investigate the subband transitions [114], cyclotron effective mass measurements [115], resonant tunneling [116, 117], light emission [118], photoluminescence [119] or inverse parabolic quantum wells [120, 121]. More recently, these structures were used to achieve the strong-coupling regime at room temperature in the THz [122, 123].

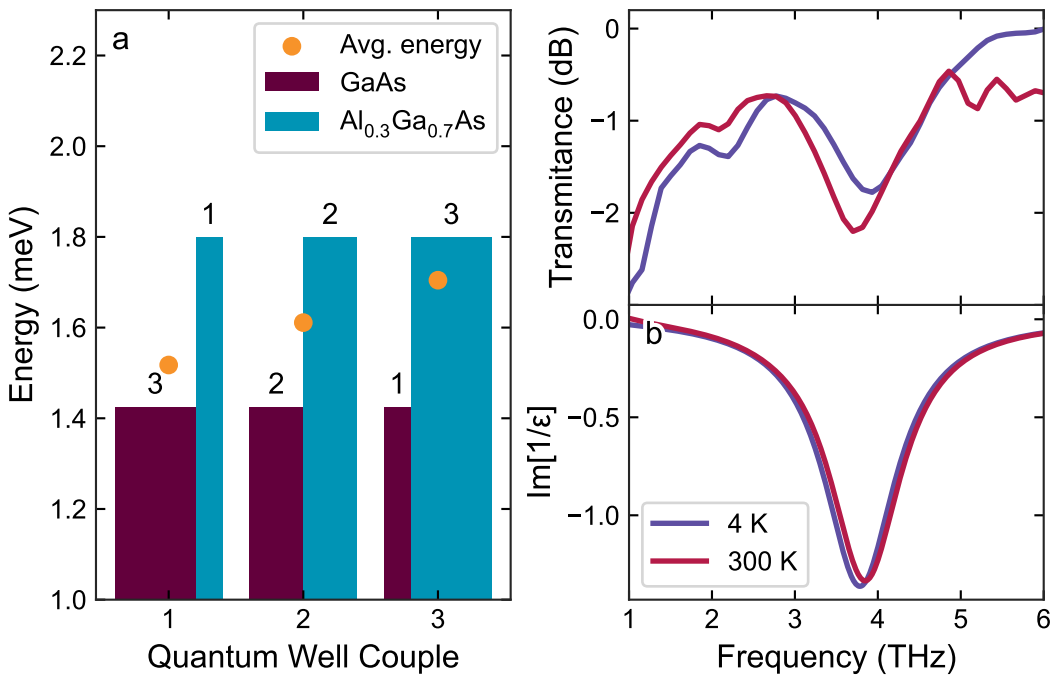

Figure 3.4.. **(a)**: average energy of different well/barrier couples of total width 4 nm. **(b)**: experimental and simulated absorption of the sample L1006 at liquid He and room temperature.

To obtain a deeper understanding of the performance of digital PQWs for ISB transition, the same active region used in Ref. [122, 123] was simulated and experimentally measured. This structure has been grown several years ago by our long term collaborators from the University of Leeds in the UK, in the team of Prof. E. Linfield. The growth sheet as well as the bandstructure can be found in Appendix Appendix A.1. The bandstructure shows evenly spaced energy levels. The calculated absorption (top panel of Fig. 3.4 (b)) predicts a stable ISB transition, even at room temperature. The multipass measurements confirms this prediction with a discrepancy for the 4 K measurement, which is blue-shifted with respect to the experimental results, while red-shifted on the simulation.

Also, a broad linewidth of almost 30 % for both temperatures is measured. While it was expected that high temperature absorption broadens due to phonon scattering, no improvements occurred at 4 K. The reason comes from the very design idea of the interdigitated structure: the repetition of square quantum wells. A common problem with the growth of thin layers is interface roughness: at the interface between two materials, a small mismatch between the lattices create strains and defects, which in return induce non-homogeneous broadening [124, 125, 126]. For a classical square quantum well structure, this source of broadening is not the major contributor because the number of interfaces is small enough. But in interdigitated wells, this is not the case: for sample L1006, each parabolic quantum well contains 23 interfaces. The interface roughness dominates every other broadening mechanisms, and does not depend on the temperature which explains why there are no improvements with cooling.

3.1.3.2. Continuously-graded alloy PQWs

The concept of PQW works as it was demonstrated earlier, but suffers from an interface roughness problem. The best way to avoid this limitation would be to reduce to a minimum the number of interfaces. One method to achieve that is to generate the energy profile not by doing an average over the thickness of square wells, but by varying the alloy composition along the growth direction. This was already successfully achieved in the past [127]. However, no general method exists to gain the necessary control over the aluminum flux in an MBE reactor. Developing such a method was part of the C. Deimert PhD thesis, under the supervision of Z. Wasilewski and what will follow is an outline of this method. A complete walkthrough can be found in these Ref. [128, 129].

In an MBE reactor, material cell fluxes are temperature dependent: the higher the temperature, the higher the flux. It means that during the growth it is theoretically possible to change in real time the alloy composition, to make it match the desired value. However, the flux control is not as straightforward as directly feeding a composition profile to the temperature controller. When a temperature is set as target to the PID, it takes time to the cell to reach it: there is lag. The whole problem is then how to set the right temperature cell $T_{\text{cell}}(t)$ to obtain the desired alloy profile using only the PID temperature $T_{\text{PID}}(t)$?

The chosen solution is to describe this relationship using a transfer function $H(f)$ in the frequency domain :

$$T_{\text{cell}}(f) = H(f)\,T_{\text{PID}}(f) \tag{3.145}$$

Here, $H(f)$ is a second order linear transfer function. Its value was derived from mock growths, where step functions were fed to the PID controller and the resulting flux measured using an ion

gauge. From the flux, the cell temperature was retrieved using the flux vs temperature formula. This operation yields $T_{\text{cell}}(t)$ and $T_{\text{PID}}(t)$ in the time domain. Using Fourier transforms, these values are converted to the frequency domain and $H(f)$ is then calculated using Eq. (3.145).

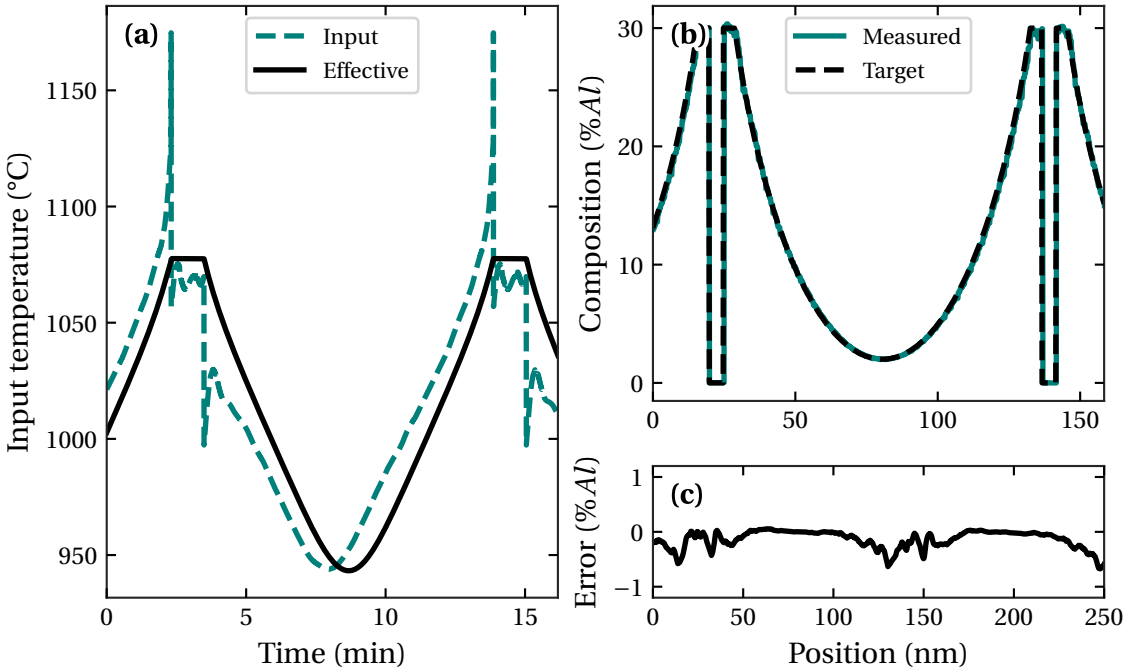

Figure 3.5.. **(a)**: black curve is the cell temperature over time required to grow the mock growth PQWs. The purple dashed one is the input temperature set to the PID to obtain the desired cell temperature according to the transfer function relationship (see Eq. (3.145)). **(b)**: target (dark, dashed) and measured (purple) aluminum composition during a mock growth of a PQW stack. **(c)**: Error in percent between the target and the measured aluminum composition.

Now that the relation has been found, actual PQW structures were mock grown to assess the deviation between the expected and the actual profile composition. Fig. 3.5 (a) shows the targeted cell temperature that would give the right composition profile for a parabolic shaped potential, and the temperature input the PID has to respect for it to be grown. Theses mock growths were used to iteratively bring correction to the model, up to the point where errors were brought from around 2 % below 0.5 % (see Fig. 3.5 (b) and (c)) It has been done by directly correcting not the transfer function, but the input temperature itself.

3.1.4. Modelisation of a PQW structure

The method described in the previous section allows to translate a potential design into an alloy composition design. Assuming the growth method works perfectly, the actual active region would be as good as the potential design. As it was said earlier, most of the quantum well calculations were done using a commercial Schrödinger-Poisson solver: Nextnano++. This software permits calculations using either the single-band effective mass approximation or an 8 band $\boldsymbol{k}.\boldsymbol{p}$ (see

Section 1.2.4). In Fig. 3.6, the dispersion of the three first subbands of a simulated PQW are plotted for the effective mass and the 8 band $\boldsymbol{k} \cdot \boldsymbol{p}$.

While being effective and fast to converge, the effective mass approximation suffers from a lack of accuracy when more than 3 subbands are needed or high $\boldsymbol{k}$-value are explored. This is the case for a PQW structure. As Fig. 3.3 highlights it, up to seven subbands have a non-negligible electron occupation at room temperature.

In order to recover a correct picture, the other energy bands have to get included in the calculation (light hole, heavy hole, split off). That is the goal of the 8 band $\boldsymbol{k} \cdot \boldsymbol{p}$ method. The downside is the computational effort necessary to carry out the calculation. While an effective mass simulation converges in a matter of a minute, an 8 band $\boldsymbol{k} \cdot \boldsymbol{p}$ can take up to several hours using a standard computer. Furthermore, the wavefunctions structure drastically change in the $\boldsymbol{k} \cdot \boldsymbol{p}$, where the resulting envelope functions of the conduction band are not only functions of the position, but also of the wavefunctions of the valence bands (light hole, heavy hole and split off valance bands) [130]. Considering the formalism used to model the PQW absorption (which will be introduced in the next part of this section) was developed using the one subband envelope function, using the built-in $\boldsymbol{k} \cdot \boldsymbol{p}$ is not an option.

Fortunately, it is possible to use the effective mass results as a basis for deriving solutions that take into account a 3 band $\boldsymbol{k}.\boldsymbol{p}$ model [129]. In doing so, the simplicity of the one electron envelope function is conserved while the non-parabolicity at high $\boldsymbol{k}$ is taken into account, providing a good fit with the full 8-band $\boldsymbol{k}.\boldsymbol{p}$ (see Fig. 3.6).

To derive the absorption from the calculation returned by a Schrödinger-Poisson solver, an absorption model has to be used. One simple way to achieve that, and extensively used throughout this thesis is the Zaluzny effective medium approximation as it allows, using parameters extracted from measured absorption, to model the ISB into an electromagnetic solver. A more accurate model, that fits perfectly in the case of a PQW is the multisubband plasmon model. At low temperature, it is expected that only the first subband is populated. However, as the temperature rises, more and more subbands get involved in the absorption process. Although they have the same energy, these transitions are not decoupled and this behavior is not taken into account in the Zaluzny model. The coupling of the different ISB transitions is called a multisubband plasmon and has been extensively studied in Ref. [55, 131, 132, 133]. While providing a complete picture of the plasmon-plasmon coupling using a quantum model, obtaining absorption and effective permittivity values from Nextnano simulations using this model is not an easy task. An equivalent approach is developed in Ref. [134], based on a semi-classical Multisubband Plasmon (MSP) theory. It proved to be easier to use in our case, and equally rigorous. Using only Schrödinger-Poisson simulation results, it allows to obtain the susceptibility tensor of an active region. An effective permittivity can then be derived using an effective medium model similar to the Zaluzny model, which takes into account the MSP coupling.

From the permittivity, an absorption can be obtained by taking the inverse of the imaginary part of the permittivity in the z-direction (growth axis direction). This provides the absorption frequency. However, no models were implemented in the simulation to introduce broadening. Interface roughness, alloy and electron scattering or thermal broadening can not be predicted with the simulation. In order to approximate the measured transmission curve, the calculated absorption is phenomenologically broadened by adding a complex component to the frequency. This imaginary contribution can be used to reproduce the experimental broadening.

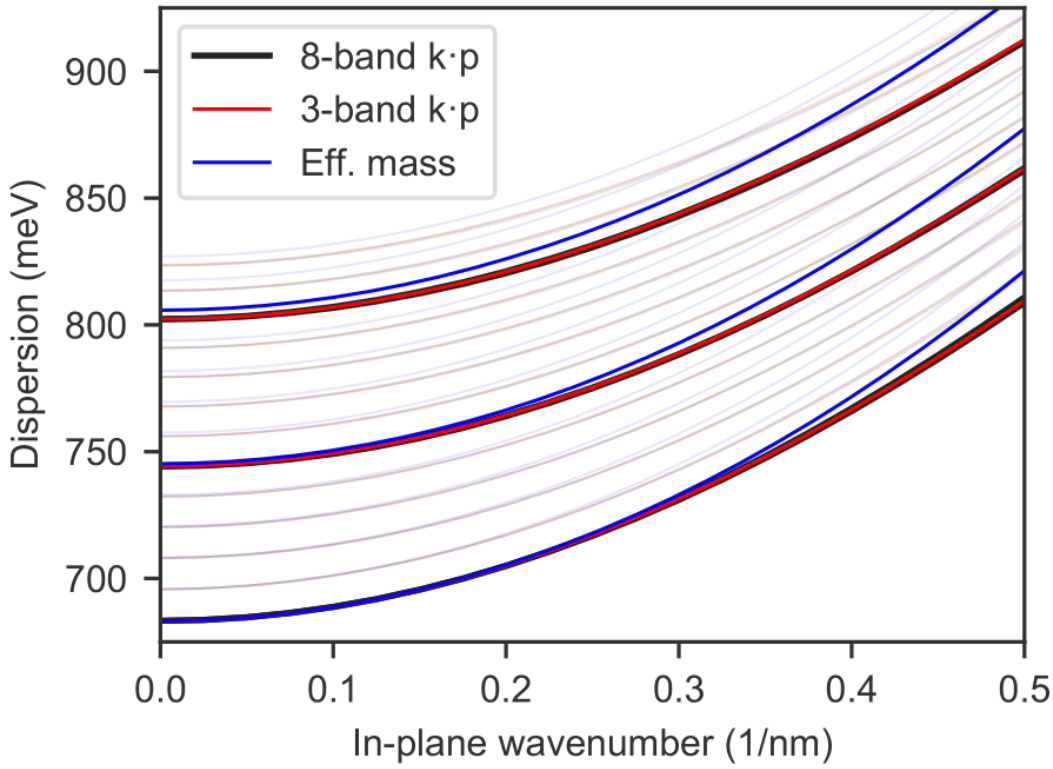

Figure 3.6.. Subband dispersions for an undoped PQW with a 3 THz calculated using (blue) the effective mass approximation, (black) the 8-band $\boldsymbol{k}.\boldsymbol{p}$ and (red) the 3-band $\boldsymbol{k}.\boldsymbol{p}$.

3.2. Experimental Characterization setup

When designing a photonic device, having accurate data on the active region is fundamental. Even if the theoretical absorption and frequency are modeled before the growth, the measured ones are not always what was predicted. Imperfections and errors during the growth can lead to deviations of some expected values. The ability to quickly measure them is important to know if the AR can be used or not. An experimental method, the multipass waveguide measurement, is presented.

3.2.1. Multipass geometry and measurements

In order to study the intersubband transition absorption of an active region, a way to couple light with the QW stack and recover it is necessary. The nature of the intersubband transition requires the selection rule to be respected: it means that a simple transmission experiment with light shined at a normal incidence on an active region will not work. A non-zero projection of the electric field along the growth axis is needed. A solution exists with the Brewster angle transmission measurement, but the high refractive index of semiconductor materials leads to a low angle of incidence within the active region, which means only a small part of the electric field is projected along the QW growth axis [13]. This method is effective for highly doped samples that show strong absorption, like the ones used to achieved ultra strong-coupling in the MIR. The samples presented

in this chapter are not doped heavily enough to be measurable using this technique. For this reason another method was chosen: the multipass measurement. It consists in using the active region as a waveguide in which light undergoes multiple internal reflections [38].

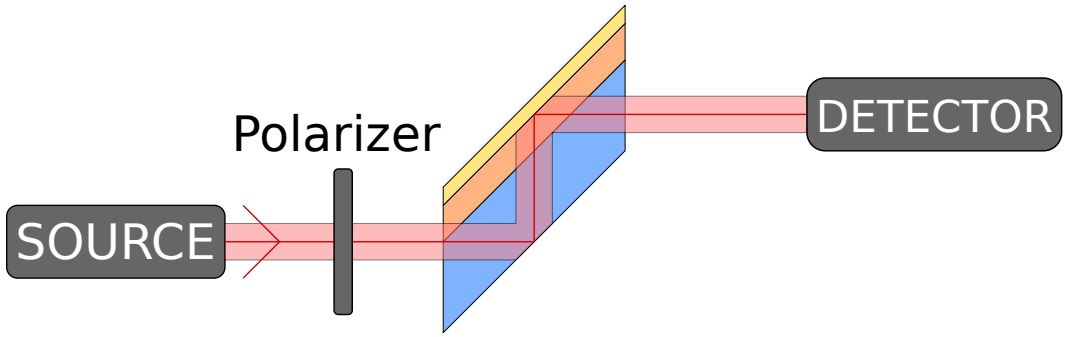

Figure 3.7.. Multipass measurement schematic.

Several geometries exist. In this work, only the parallel facets with 45° angle geometry was used like the one Fig. 3.7. The reason is that the losses at the facets are the same for both impinging polarizations, which is a useful feature for normalizing spectra: TM polarization couples with the ISB while TE polarization does not.

The fabrication process of this prism geometry is straightforward. On the active region side, a layer of evaporated gold is deposited to obtain a maximum of the amplitude of the electric field at the vicinity of the quantum wells for TM polarization. This is an important consideration because the typical thickness of the active region is below 10 µm, much smaller than the typical wavelength at the frequency of interest (At 3 THz, $\lambda = 100\,\mu m$). Without this gold layer that imposes a boundary condition, the total internal reflection would lead to an almost 180° phase change, thus leading to a poor coupling with the active region. The multipass geometry is obtained by lapping a slice of the active region using Al_2O_3 lapping discs with decreasing roughness ranging from 30 µm to 1 µm, ensuring a low level of defects on the facets. During the lapping, the sample is held at a 45° angle on a custom-made jig using crystal bond wax.

In order to highlight the ISB transition, two measurements are performed at two different polarization directions: TE and TM. The ratio TM- over TE-polarization yields a baseline corrected transmission, but does not take into account the optical anisotropy induced by the mirrors and the source. To correct it, a measurement of the empty path in both polarizations is performed and is used to correct the respective polarization measurements The final ratio becomes:

$$Transmission = \frac{TM_{\text{Sample}}/TM_{\text{Empty}}}{TE_{\text{Sample}}/TE_{\text{Empty}}} \tag{3.146}$$

The measurements were done using a Fourier Transform Infrared spectrometer (Bruker IFS66V), with a Beam Condenser unit inside the sample compartment. The source is a standard broadband Globar lamp (SiC) and the detector is a helium cooled Si bolometer (QMC Instrument). The prism is mounted on the cold finger of a cryostat, placed in the optical path of the Beam Condenser. The transmissions obtained can be fitted, using a model presented in Section 3.2.3.

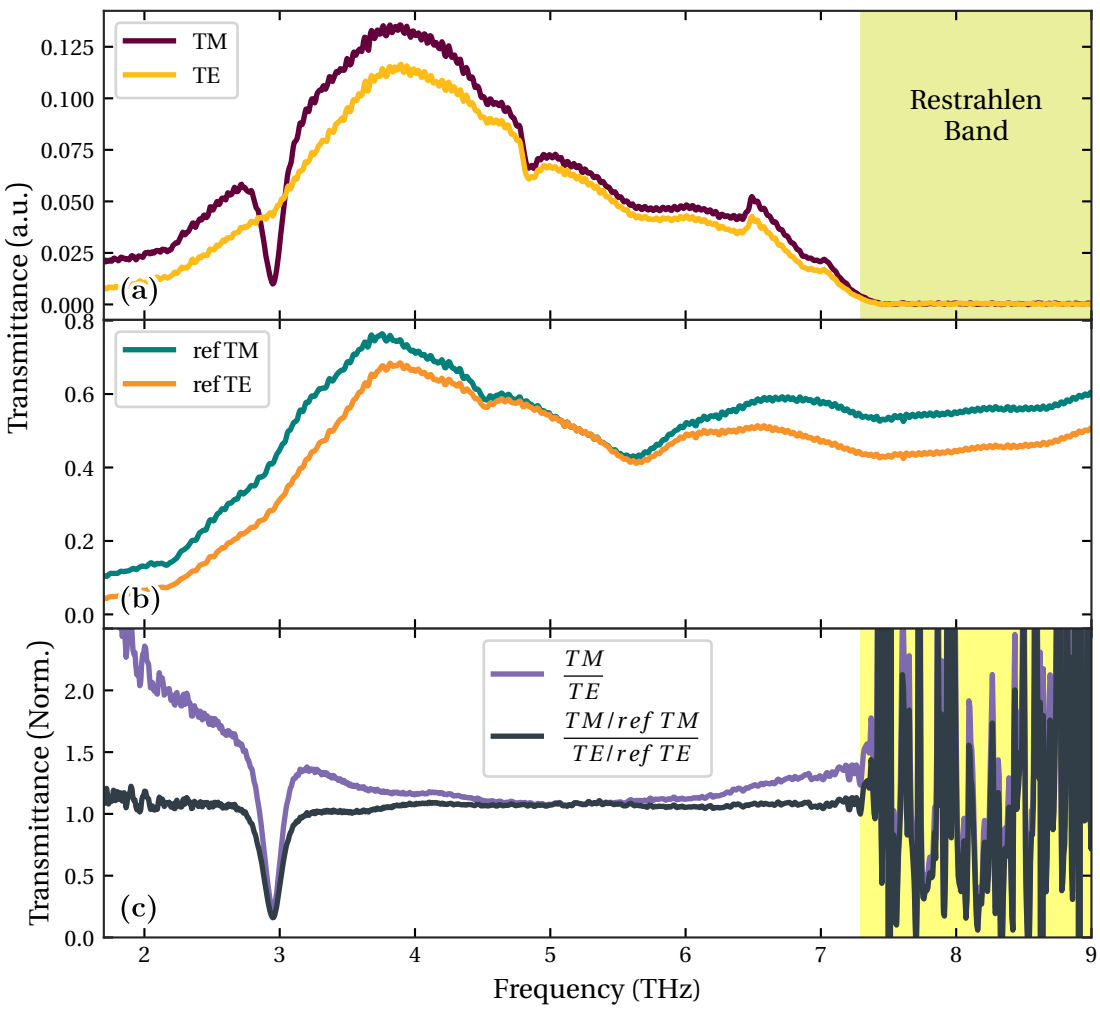

Figure 3.8.. **(a)**: sample TM and TE measurements. The anisotropy of the optical system for the different polarization clearly appears. **(b)**: empty path TM and TE measurements for the correction. **(c)**: corrected and uncorrected ratio. The uncorrected ratio has a non-horizontal baseline, making it unpractical for a good fitting.

3.2.2. High resolution transmission measurements

The development of the parabolic quantum well was an iterative process, with each generation bringing improvements. One that proved to be tricky to capture was the linewidth as it requires to do the measurement with a high resolution if one wants to resolve correctly the absorption. At first, the measurements were done using a cryostat, suspended on a pole, above the FTIR's sample compartment. In this configuration, the cryostat is extremely sensitive to the outside environment : the pump vibrations as well as the helium transfer line from the Dewar brng a lot of vibrational noise on the measurement.

Another strong perturbation comes from the water vapour absorption of the atmosphere. As

explained in the introduction, THz is heavily absorbed in the atmosphere, thus THz measurements are usually performed purging the path with dry air or nitrogen gas. Most of the time this is sufficient to avoid atmosphere absorption. But leading experiments with a resolution below 1 cm^{-1}, periodic oscillations started to perturb the entire spectra, which make the baseline harder to define. It is mainly damageable for the fitting process, as well as room temperature multipass measurements because the absorption is weaker, and thus harder to isolate from the noise.

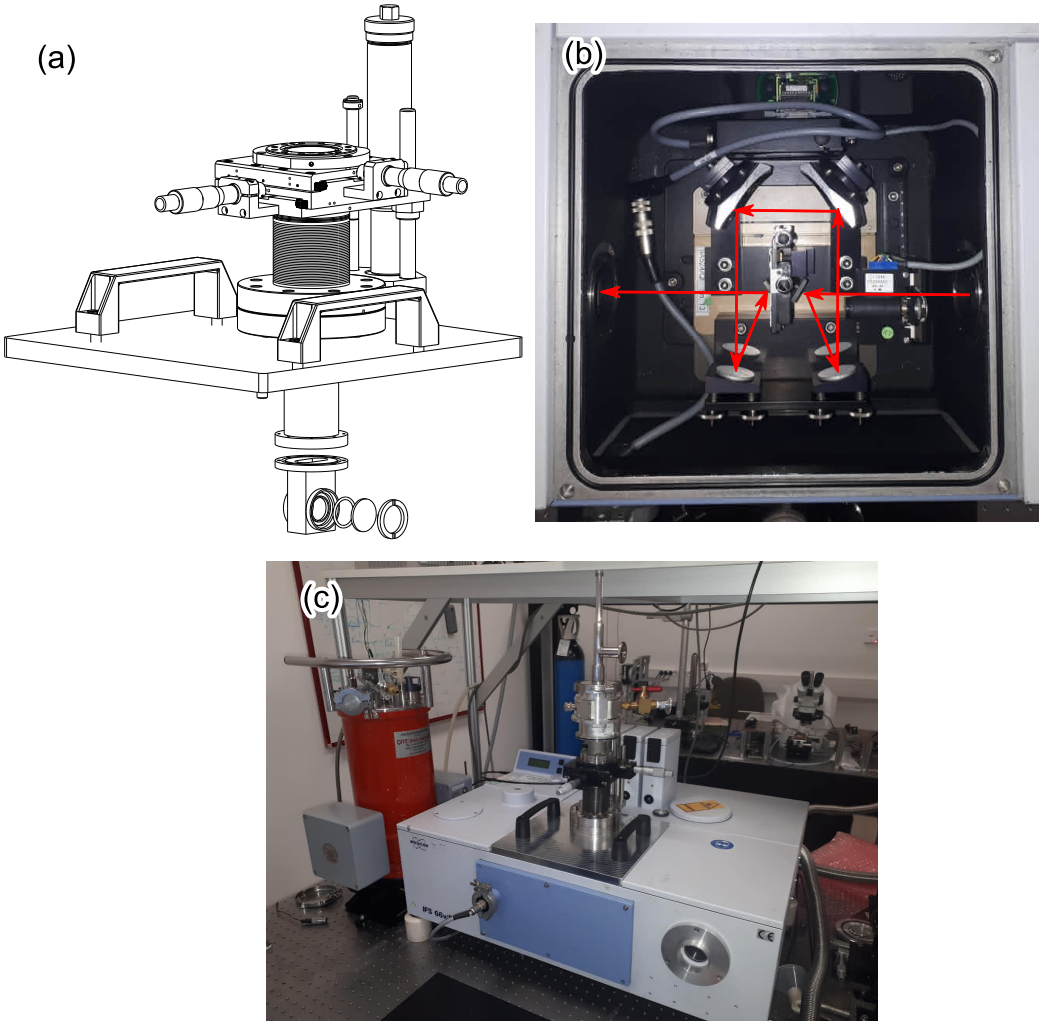

Figure 3.9.. **(a)**: CAD schematic of the 3-axis lid. **(b)**: optical path in the FTIR sample compartment with the beam condenser unit. **(c)**: lid with the cryostat on top of the FTIR.

In order to mitigate these problems, improvements to the existing setup were developed. The Bruker ISF66v has the ability to do measurements under primary vacuum. If the sample compartment is closed, then it is possible to evacuate the interferometer and reduce the impact of water vapour absorption. But primary vacuum is not good enough to avoid ice formation at low temperature, and the FTIR is not made for high vacuum. For these reasons, we have designed the setup with two different vacuum levels: the main challenge is to insert the cryostat within the primary vacuum of the interferometer while being still able to operate micrometer positioning

(See schematic Fig. 3.9 **(a)**).

The assembly that allows this configuration is composed of a stainless steel plate that covers the sample compartment of the FTIR. A 3-axis translator is mounted on it with a cryostat skirt. The assembly is completed with a window holder head that is aligned with the optical path of the beam condenser unit (Fig. 3.9 **(b)**). The windows are made of ZEONEX, a polymer with excellent mechanical properties, allowing us to thin them down to 1.5 mm while bearing the difference of vacuum. Using thinner windows improves their transmissions, leading to a better signal-to-noise ratio. With this system, the cryostat directly sits on the FTIR and is part of a heavy mass, making it more stable (Fig. 3.9 **(c)**). The improvements of the new setup on the measurements can be seen in Fig. 3.10.

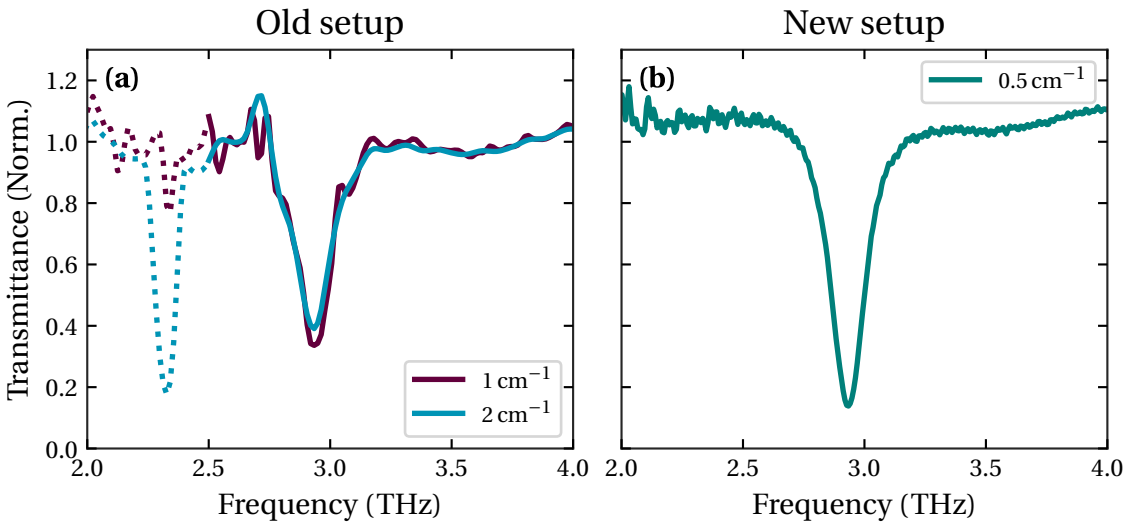

Figure 3.10.. Multipass measurement of G0490 54PQWs at 40 K for **(a)** the old setup using a resolution of 2 and 1 cm^{-1} and **(b)** on the new setup using 0.5 cm^{-1}. The absorption at 2.3 THz for the 2 cm^{-1} measurement is due to vibration of the measurement setup. The absorption frequency remains the same, but the amplitude of the noise is less important with the new setup. Also, the ISB transition appears more contrasted.

A direct comparison between 1 cm^{-1} and 2 cm^{-1} shows a deeper contrast, and this contrast keeps improving at 0.5 cm^{-1}. During the development of this accessory, we took care of having the system coarsely prealigned with the optical path. The reduced noise has led to a reduction of the scan numbers : from 200 or 300 scans with our previous setup we are now integrating with only 50 or 100 scans. All measurements are at least twice faster, increasing the number of runs that can be done with a helium refill of the bolometer.

3.2.3. The effective medium model to fit the experimental absorption

The most widespread method to fit experimental ISB absorptions are the Lorentzian or the Voigt model, both to fit as closely as possible to the absorption shape of the ISB resonance. While this is a good approximation at first sight, using these models do not take into account the fact that the measurement is done using a multipass geometry, which means the signal goes mostly through

the GaAs substrate. While this material is mostly transparent in our frequency window, there is still absorption. Furthermore, the QW/substrate interface induces incoherent reflections which means interferences occur, and they are not included in these simple models.

One way that has been explored at the beginning was to funnel the fitting process through a Transfer Matrix or RCWA code, to take into account the different materials permittivity and the interfaces. This method is highly demanding in terms of computational power which makes it not suitable for analyzing a lot of measurements. For this reason, another solution was used. The reflectivity of a single pass reflection inside the multipass was derived under some assumptions to obtain an analytical solution used directly to fit the absorption. The notation used for the reflectivity are explicated in Fig. 3.11.

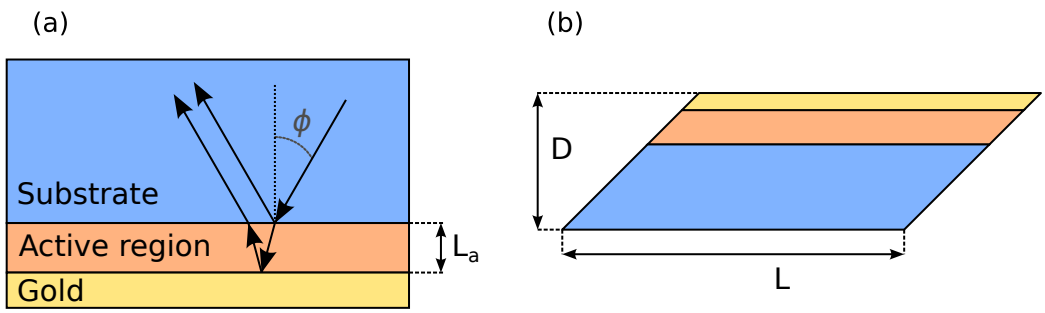

Figure 3.11.. (a): reflection on the substrate / active region layer. The transmission angle is exaggerated for clarity. **(b)**: definition of the dimensions of a multipass waveguide.

The permittivity used for describing the active region is the Zaluzny effective medium approximation [41]:

$$\frac{1}{\varepsilon_{zz}(\omega)} = \frac{1}{\varepsilon_s}\left(1 + \frac{\omega_p^2}{\omega^2 - \omega_{21}^2 + i\gamma\omega}\right) \tag{3.147}$$

$$\varepsilon_{xx} = \varepsilon_{yy} = \varepsilon_s \tag{3.148}$$

where ω_p, ω_{21} and γ are the plasma frequency, the ISB transition pulsation and the ISB linewidth which are our fitting parameters. Here ε_s is the background permittivity, which corresponds to the average of the permittivity of a stack repetition (well plus barrier) The gold layer is treated as a perfect conductor, introducing no losses, and the GaAs substrate modelled using the permittivity described in Section 1.3.2 and is noted ε_{sub}.

The whole derivation of this model can be found in [129] Appendix C. The complex reflection coefficient is then:

$$r = \frac{-k_{z,a}\varepsilon_{sub} + ik_{z,s}\varepsilon_{xx}\cot(k_{z,a}L_a)}{k_{z,a}\varepsilon_{sub} + ik_{z,s}\varepsilon_{xx}\cot(k_{z,a}L_a)} \tag{3.149}$$

where:

$$k_{z,s} = \sqrt{\varepsilon_{\text{sub}}} k_0 \cos(\phi) \quad k_{z,a} = \varepsilon_{xx} \left(1 - \frac{\varepsilon_{\text{sub}}}{\varepsilon_{zz}} \sin^2(\phi)\right) k_0^2 \tag{3.150}$$

with ϕ the incidence angle relative to the growth axis z.

Now that the single pass reflectivity is known, the multipass transmission can be obtained by using the formula:

$$T = |r|^{2N_{\text{reflection}}} \tag{3.151}$$

with $N_{\text{reflection}}$ the number of time a single pass reflection occurs. This number can be derived from the length L and thickness D of the waveguide using the relation:

$$N_{\text{reflection}} = \frac{L}{D} \cot \phi \tag{3.152}$$

with L and D the length and thickness of the multipass waveguide.

Finally, a word on the absorption in a multipass geometry. The absorption of a quantum well can be expressed as:

$$\alpha_{2\text{D}}(\omega) = -\frac{\omega \sqrt{\varepsilon_{\text{s}}} L_{\text{QW}}}{c} \text{Im}\left(\frac{1}{\varepsilon_{zz}(\omega)}\right) \tag{3.153}$$

with L_{QW} the length of a QW period, ε_s the background permittivity and ε_{zz} the permittivity in the z direction. If one considers an effective medium permittivity like the one described in the seminal paper of Zaluzny, then the absorption becomes:

$$\alpha_{2\text{D}}(\omega) = -\frac{\omega_{\text{p}}^2 L_{\text{QW}}}{c\sqrt{\varepsilon_{\text{s}}}} \frac{\gamma \omega^2}{(\omega - \omega_{\text{res}})^2 (\omega + \omega_{\text{res}})^2 + (\gamma\omega)^2} \tag{3.154}$$

Where γ is the width of the absorption and ω_{res} the resonance of the QW. From here, it is possible to demonstrate that:

$$\int_{-\text{inf}}^{+\text{inf}} \alpha_{2\text{D}}(\omega) d\omega = \frac{\omega_{\text{p}}^2 L_{\text{QW}}}{c\sqrt{\varepsilon_{\text{s}}}} \tag{3.155}$$

which is the integrated absorption of one QW. The interesting thing is that this value is linked directly to the plasma frequency and therefore to the number of electrons, which is one of the fitting parameters. It is then possible to assess the absorption using only the plasma frequency. To evaluate coarsely the total absorption of the QW stack, it is only necessary to multiply the integrated absorption by the number of QW N_{QW}. Throughout this chapter, a quantity defined as the absorption strength $\alpha = \sqrt{N_{\text{QW}}}\omega_{\text{p}}$ will be used to monitor the evolution of the absorption behavior of the different samples, depending on the temperature.

3.3. Performances of the Parabolic Quantum Wells

As already mentioned, the development of the continuously graded PQWs was an iterative process: in total 3 generations were made, each of them with changes that led to drastic increase of performances.

3.3.1. First generation: 18-well repetition

In this part, the results of the first PQWs generation will be discussed. The structure, as well as the doping method used to incorporate donor atoms is presented. The experimental results are then showed.

3.3.1.1. Design choices for a PQW structure

This first generation was designed to show an ISB transition at 3 THz, with an 18 well repetition structure. The wells are 122 nm wide, and the barrier are 4.48 nm wide with 30 % Al alloy composition. The structure is modulation doped in a 2 nm GaAs well in a delta-like thickness, in the barrier. The reason of this doping strategy is two-fold:

Modulation doping refers to the spatial separation of the donor atoms from the mobile electrons [135, 109]. For a quantum well structure, as the electrons are confined in the well, modulation doping is done by introducing the impurities in the barrier. This doping method has a beneficial effect on the ISB transition: the confined electrons in the well experience less scattering from the ionized donor, which leads to a reduction of the absorption linewidth [136]. Whether modulation doping is used or not, doping can be done in two manners : over a volume (bulk doping) or on a surface layer (delta doping). The delta doping offers the possibility to embed an important doping concentration in a reduced volume. In doing so, it is possible to push as far away as possible the impurities from the well, decreasing even further the probability of a scattering event [136].

The reason behind the presence of the 2 nm well in the barrier comes from the way donors behave in $Al_xGa_{1-x}As$ alloy when the aluminum composition is above 20 %. At this concentration, donor binding energy becomes so important that the electron is not released from its atom, leading to smaller electron density than expected. These donor states are called DX-centers [137]. In order to avoid this issue, impurities are incorporated in a small well in the barrier.

3.3.1.2. Experimental results

The first structure was G0413, a 18-well repetition of $3 \cdot 10^{11}$ cm^{-2} doped PQWs. As one of the applications of this technique for continuously grown PQW, this active region suffered from an off target composition profile which happened to be problematic for the quality of the ISB absorption. Due to a software issue, the computer controlled operations during the growth were delayed which made the well larger than expected. A less problematic issue is the Al cell non-linearity of the temperature dynamics which is not perfectly compensated, which led to overshoot of the composition at the edge of the well. This growth highlights the effect of the small deviation on the

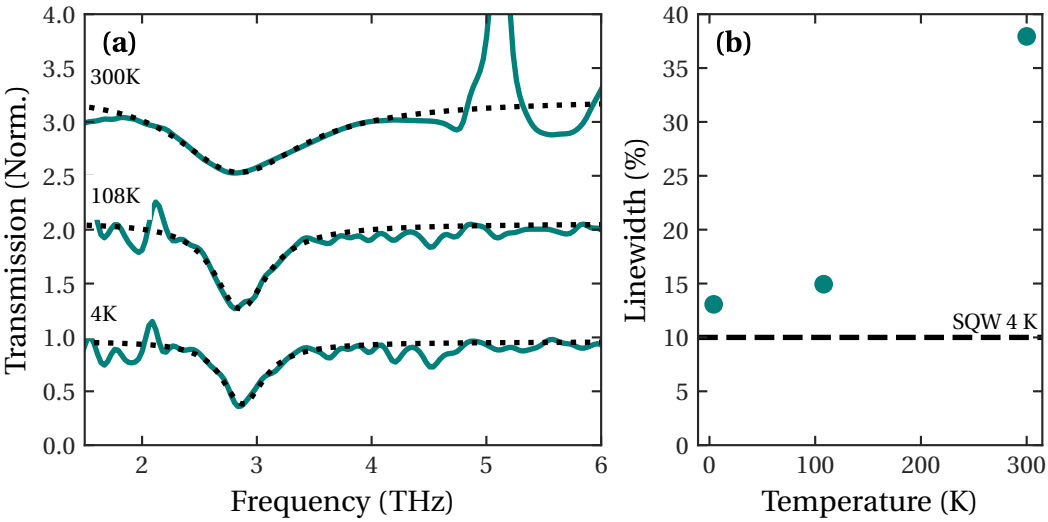

Figure 3.12.. **(a)** Transmission spectra of G0413 multipass at different temperatures. These measurements were done prior the development of the full vacuum setup, hence the high level of noise. It can be noted that room temperature absorption is achieved. **(b)** Linewidth of the ISB absorption. As the sample is cooled, a drastic improvement happened up to 13 % at 4 K without ever reaching the 10 % linewidth of a classic THz square well at 4 K

targeted conduction bandedge: The linewidth is quite broad, even at cryogenic temperatures. But it can also be noted that the resonant frequency is remarkably stable with the temperature.

3.3.2. Second generation: 18-well regrowth and doping level study

The second growth generation was made with corrections for the composition profiles to get closer to the desired profile. This generation is composed of G0489 a 18-repetition of PQWs doped at $3 \cdot 10^{11}$ cm^{-2} (regrowth of G0413), and G0490 a 54-repetition of PQWs doped at 10^{11} cm^{-2} which has the same total surface doping, but spread on more wells. The idea is to assess the effect of the doping on the linewidth, as the impurities can act as scattering centers. The results are reported in Figs. 3.13 and 3.14.

A direct comparison of the G0413 and G0489 active regions shows the impact of the AlGaAs potential distortion that was corrected with this second generation. At 78 K, the linewidth drops from 14.9 % to 11.5 % and would probably provide an even better figure at 4 K. This temperature could not be measured due to a lack of helium. The G0490 active region exhibits an unprecedented linewidth for a THz ISB transition, reaching around 4 % at 5 K and maintaining a 10 % linewidth up to 150 K well above liquid nitrogen temperature. Such linewidth can be obtained with a THz square QW only at a temperature of 10 K. Furthermore, there is no major difference in the absorption between 4 K and 78 K which allows us to envision applications in the THz without the need of Helium cooling. Another point of interest is the relative stability of the central frequency of absorption, with a shift of around 150 GHz over our temperature range. However, careful comparison between the experimental results and the simulated absorption using Nextnano++ unveiled discrepancies.

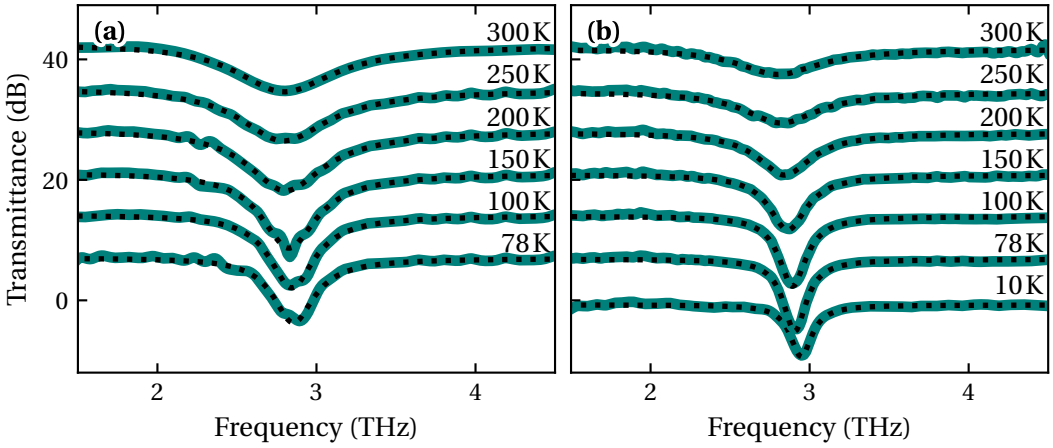

Figure 3.13.. **(a)**: G0489 transmittance (G0413 regrowth with corrections for the potential doped at $3 \cdot 10^{11}$ cm^{-2}). **(b)**: G0490 transmittance (54 PQWs doped at 10^{11} cm^{-2}).

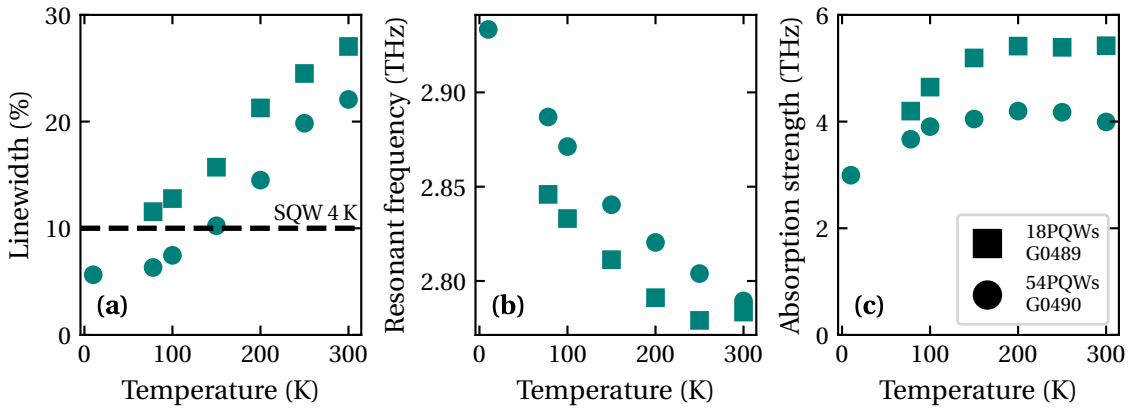

Figure 3.14.. Fitting parameters depending on the temperature of the second generation growths : **(a)** Transition linewidth, **(b)** resonance frequency and **(c)** the absorption strength.

The design that was targeted was a perfectly quadratic conduction band in the absence of doping, which would show an ISB transition at 3.3 THz. Experimentally, we observed a resonant absorption around 2.9 THz, around 0.4 THz lower than what was expected. We decided to look more closely on how Nextnano defines the alloy composition vs band gap for $Al_xGa_{1-x}As$. It appears that Nextnano uses a cubic dependence detailed in Ref. [138], which provides a good approximation over the entire range of composition. But for values below 45 % of Al, Ref. [139] advises to use a linear dependence.

Fig. 3.15 shows the calculated transmittance of the G0490 sample with the same alloy composition profile, but using the two different dependencies. The absorption calculated using the linear dependence appears to fit more closely the experimental data, in terms of central frequency of absorption as well as the shift of this frequency with the temperature. The sample that was designed to have a parabolic potential with the cubic dependence ends up with a wider potential profile leading to a shift of the ISB frequency.

To illustrate the superiority of the 54-well AR performances, a square quantum well designed

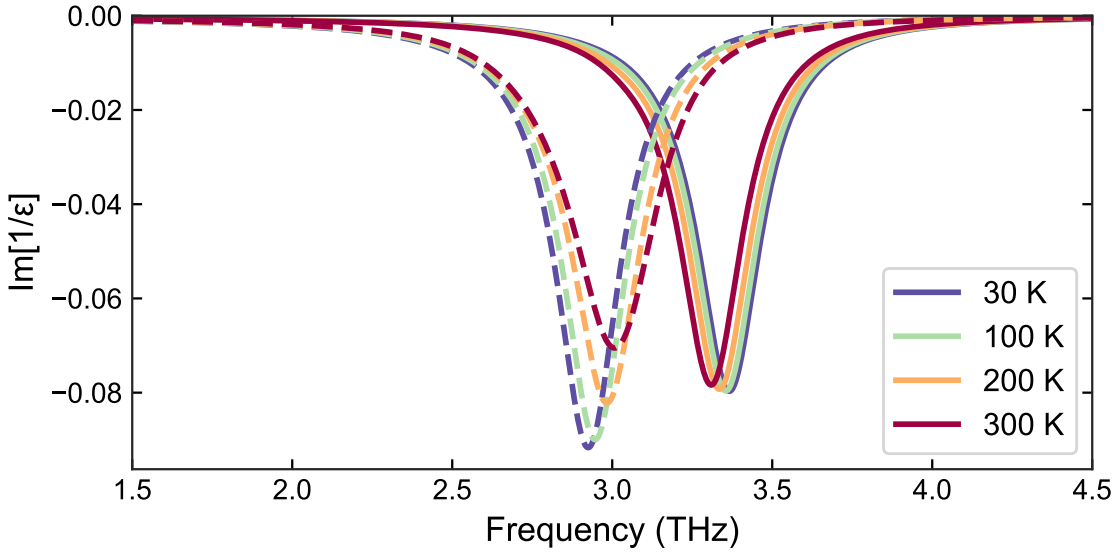

Figure 3.15.. Calculated transmittance of G0490 sample using (solid lines) the cubic dependence [138] and (dashed lines) the linear dependence [139] for the alloy composition vs bandgap energy.

to absorb around 3 THz at 4 K was measured for different temperatures. The results are shown in Fig. 3.16 and are similar to the simulation prediction shown Fig. 3.2. As expected, the SQW sample shows a broad absorption at 4 K that starts to split above 40 K, with the 2→3 transition becoming active. It indicates that the second subband starts to be populated. Around 100 K, the 1→2 transition disappears and above 150 K no absorptions can be measured

It can also be noted that the 1→2 transition shows a significant shift in frequency with the temperature increase, of around 0.4 THz from 4 K to 78 K. On the contrary, the 54-well sample is, as detailed earlier, showing impressive resilience with a frequency shift of less than 0.2 THz from cryogenic to room temperature.

3.3.2.1. TEM measurements

The growth technique accuracy was studied using mock growth, where the substrate was replaced with an ion gauge. While it provided valuable information on the atom flux, this study does not provide information on how the species arrange themselves on the substrate surface. Furthermore, despite the substrate rotation, the flux anisotropy creates a gradient of alloy for a given growth position over the surface.

To experimentally assess the profile composition of the well, Scanning Transmission Electron Microscopy (Scanning Transmission Electron Microscopy (STEM)) pictures were made of an active region slice by L. Largeau, engineer of the PANAM technology platform at C2N. STEM is a type of Transmission Electron Microscopy which consists of an electron beam passing through a thin sample. These electrons are detected to raster an image of the electron interaction with the sample. Several detection methods exist depending on which information one is interested in. The methods that was used here is the High-Angle Annular Dark-Field (HAADF) imaging, which is performed

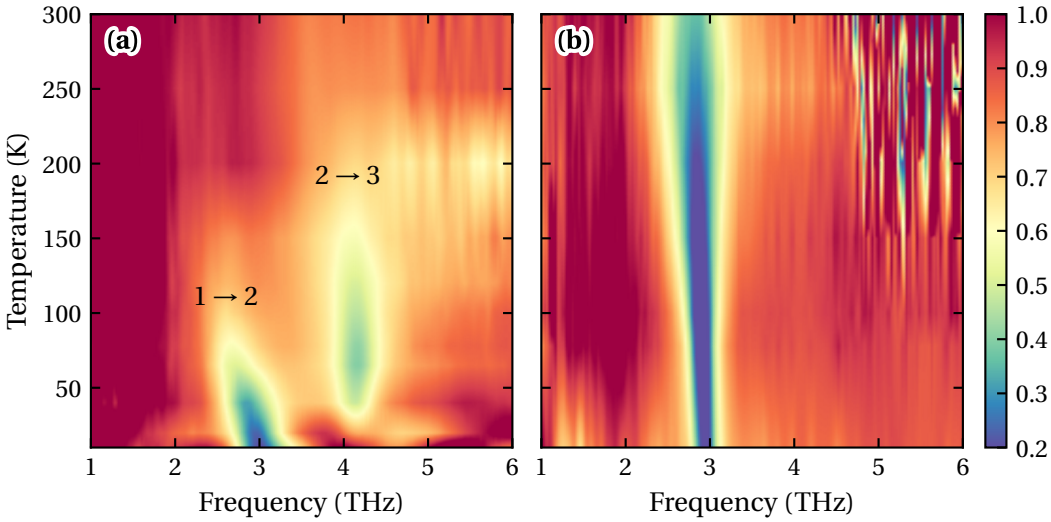

Figure 3.16.. Color plot of the transmittance as a function of the temperature of **(a)** a THz square QW and **(b)** G0490 54PQWs sample.

using an annular detector, collecting the electrons incoherently scattered by nucleus of the atoms. Using this method, a sample mapping where the contrast is directly linked to the atomic number of the atoms can be achieved [140]. The obtained images are called Z-contrast image.

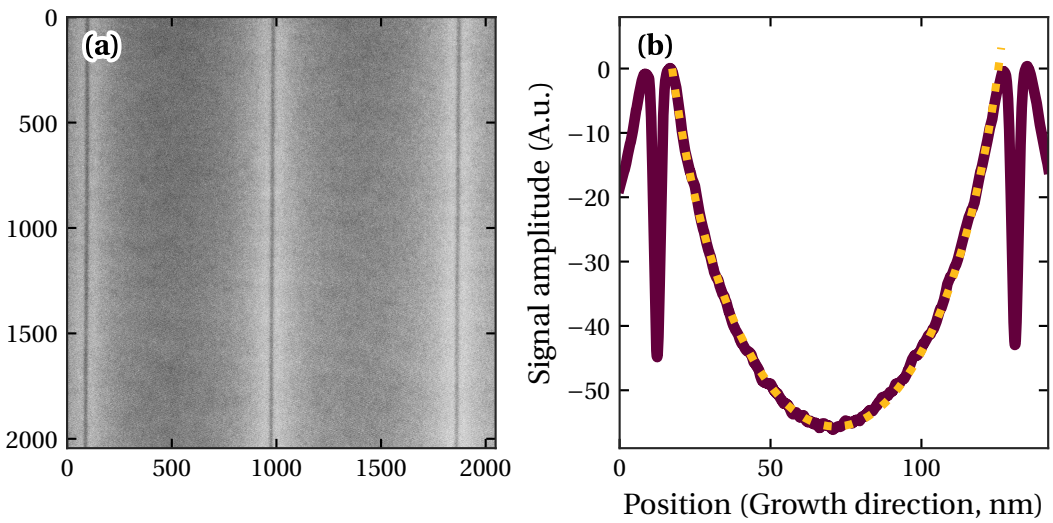

Figure 3.17.. (a): STEM HAADF picture of two well repetition of G0490. **(b)**: Aluminum concentration profile extracted from the STEM picture (solid line). The dashed line is the theoretical profile used as an input during for the growth.

Fig. 3.17 (a) is a picture of two wells of active region G0490. The contrast captures the change of aluminum concentration in the sample. The three narrow dark bands are the doping wells, made of GaAs. The symmetric contrast regions are the parabolic wells, ranging from light (high Al concentration) to dark (low Al concentration).

Using signal analysis on the data contrast, the average and baseline corrected signal amplitude can be extracted from the HAADF image. This cleaned signal is plotted Fig. 3.17 (b). It represents the Al concentration of a single parabolic well, depending on the growth direction. The yellow dotted curve is the expected composition profile for the well. The agreement between the expected and obtained profile over the well length is excellent.

3.3.3. Third generation: corrected Alloy vs bandgap

These findings led to the growth of a third generation of PQWs, in view of an application with LC resonators that will be detailed in the next chapter. The requirements for this generation were specific: to accommodate the LC resonator design the maximum AR thickness has to be below 1.4 µm and the transition frequency was chosen at 2.2 THz to exhibit absorption within the bandwidth of the Time-Domain spectrometer that will be used to characterize the LC resonators.

The changes compared to the previous generation are : the linear dependency for the bandgap vs alloy composition (see Fig. 3.15) was used to obtain a potential profile as close as possible to a true parabola. The barrier composition was $Al_{0.2}Ga_{0.8}As$ and the sample was delta-doped directly in the middle of the barrier and not within a doping well. Two active regions with 4- and 8-wells doped 10^{11} cm^{-2} were grown. The wells and barriers are respectively 130.8 nm and 20 nm wide. These samples, with fewer wells, naturally show a weaker absorption: above 200-250K the signal becomes too noisy for conducting a proper fitting. The parameters extracted from the fitting are plotted in Fig. 3.19. Despite the change for the alloy-potential dependency, these growths still show a red shift of their resonance frequencies with the temperature, but further improvement on the linewidth at cryogenic temperatures were observed in comparison with the 3 THz samples.

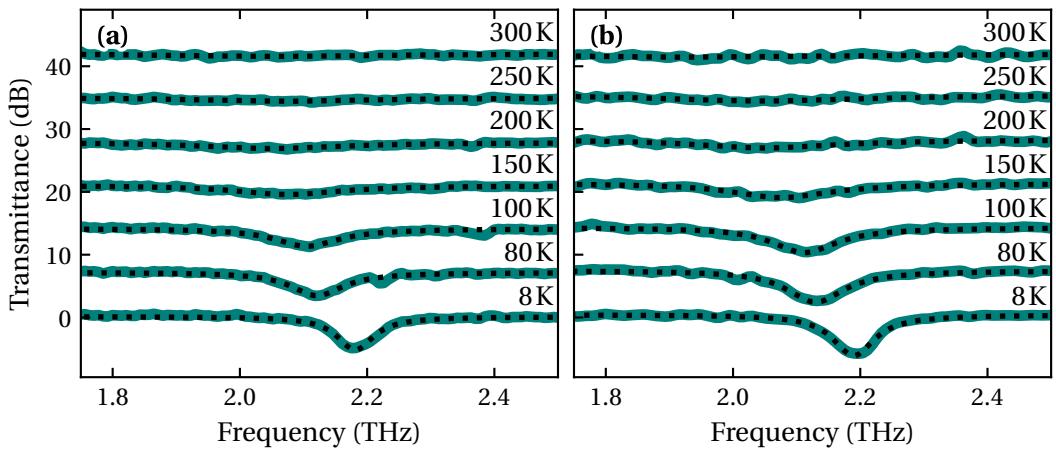

Figure 3.18.. Stacked transmittances of **(a)** the 4-PQW G0642 and **(b)** the 8-PQW G0643.

The linewidth at 4 K and 8 K drops below 3.6 % for both structures, an improvement on the 5 % of the previous generation which seems to be the result of the change from the cubic to the linear relation for the band edge vs alloy composition [139]. Compared to the previous generation, the absorption strength is even more stable with the temperature, and it is around 1.3 % larger for the 8PQWs compared to the 4PQWs, which is close to the expected 1.4 % ($\sqrt{N_{QW_{G0643}}}/\sqrt{N_{QW_{G0642}}}$).

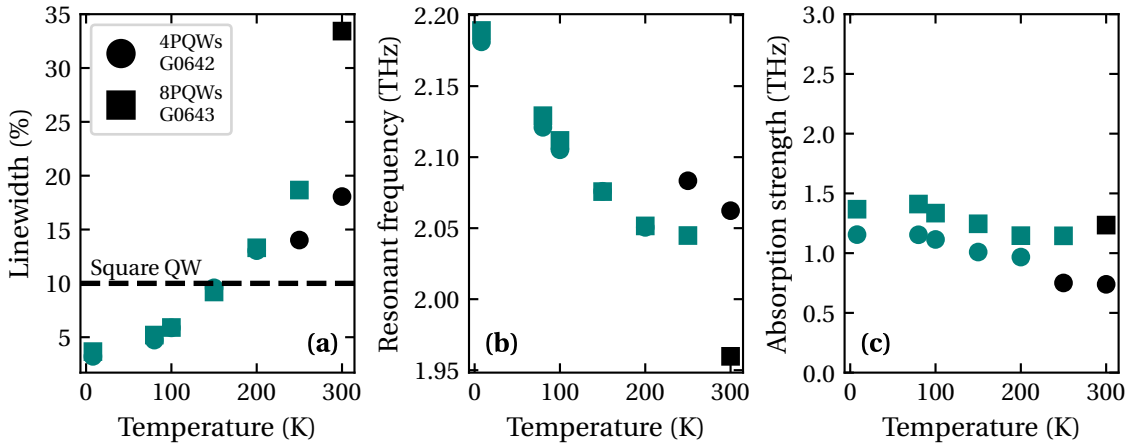

Figure 3.19.. Fitting parameters depending on the temperature of the third generation growths G0642 and G0643: **(a)** Transition linewidth, **(b)** resonance frequency and **(c)** the absorption strength. Black marks correspond to parameters whose values may be inaccurate due to the absorption being too weak at these temperatures for a proper fitting.

Overall these samples seem to be of higher quality than the 18- and 56-PQWs samples, but the reason is still not fully elucidated. The switch from the cubic to linear potential-vs-alloy for the definition of the composition of the wells can be an answer. Another reason could be the larger barriers: because the samples are delta-doped in the middle of the barriers, the impurities are further away from the wells which induces less scattering from the ionized impurities. Another source of improvement could also be the reduced number of wells [141].

These minor issues set aside, the resulting samples provide high quality THz absorption and despite not being usable for room temperature operation, are compatible with liquid Nitrogen cooling which is a requirement from our collaborators in Greece, as we will see in the next chapter.

3.4. Half Parabolic Quantum Wells

Parabolic Quantum Well structures, as it has been demonstrated in the previous section, hold potential for future room temperature THz device and fundamental studies thanks to a high quality ISB transition. However, compared to a square quantum well operating at the same frequency, PQWs have one major problem : their size. Typical PQWs are quite wide, often more than 100 nm, which lead to either thick active region when a minimal number of wells are needed, or active region with only a few wells when the thickness need to be small.

A solution to reduce the size of the well while conserving the temperature behavior that PQWs offer can be found with Half Parabolic Quantum Well profiles. Like their PQWs counterpart, HPQWs should keep evenly spaced energy level, while being half the size.

While this profile can be implemented by simply truncating a full PQW at its center, some care must be taken once dopants are introduced. Two doping methods are traditionally used: the bulk doping where the dopants are introduced directly in the well, and the modulation doping where

the dopants are placed in the barriers. In the first case, electrons and silicon ions are at the same place, while in the case of the modulation doping electrons and ions are spatially separated: ions are in the barrier while electrons are confined in the well. It means that their electrostatic potential are not cancelling each other and will distort the conduction band. An example of this effect can be seen Fig. 3.2 on a square well. The bottom of the well has a parabolic distortion, caused by the electrons grouped in the well, while the barriers are bent by the silicon ion potential (see Fig. 3.20 **(a)** and **(b)**).

In square and parabolic wells, this effect is not a major issue. The square well becomes shallower leading to a red-shift, and the PQW recovers from the Hartree potential thanks to the plasmon-plasmon interaction. But for a half parabolic well, the distortion completely destroys the potential shape and introduces a splitting of the absorption in several lines. For this reason, bulk doping seems to be the way to go. Unfortunately, it implies broadening issues because of the impurity scattering, which cancels out the advantages brought by the parabolic potential. Fortunately, it is possible to conciliate modulation doping and half parabolic potential using a trick: by shifting the bottom of the well. Instead of truncating exactly at the middle of the well, a little more of the parabola is grown.

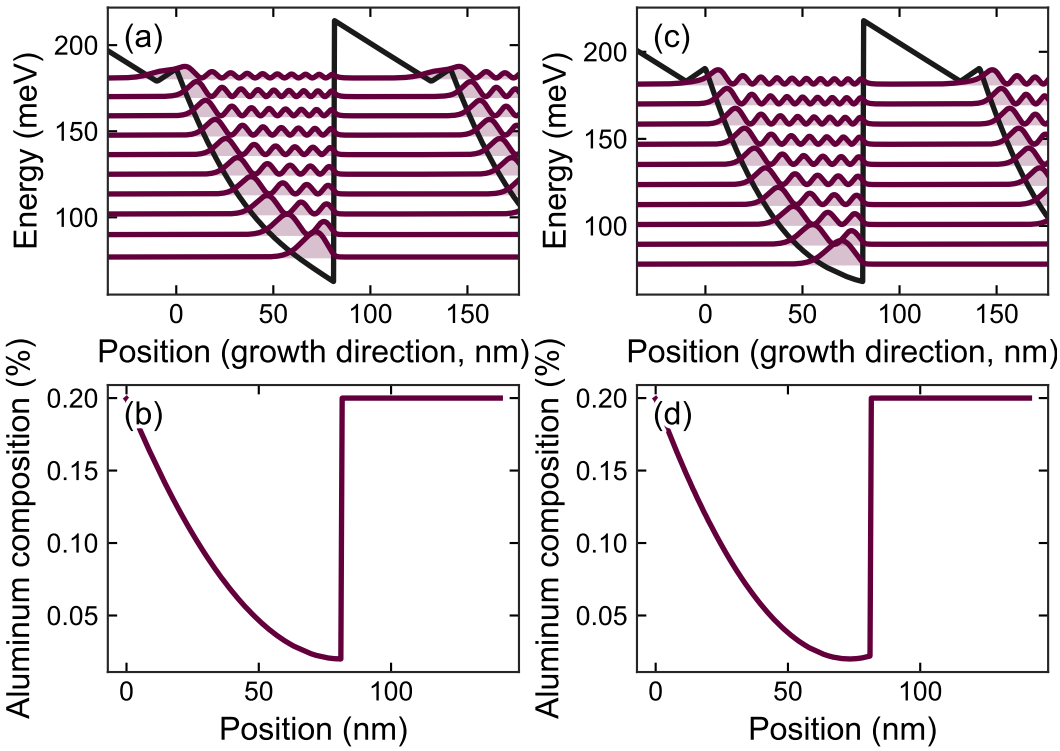

Figure 3.20.. Top panel: Conduction band and wavefunctions for **(a)** a HPQW and **(c)** a shifted HPQW. The bottom of the conduction band of **(a)** is distorted by the Poisson potential of the electrons, while **(c)** remains parabolic. Bottom panel: **(b)** HPQW and **(d)** shifted HPQW aluminum composition. For this simulation, the bottom of the well was shifted by 7 nm.

The result of this operation can be seen Figure Fig. 3.20 (c) and (d). The inflection point that appeared near the bottom of the well with the exactly half PQW is compensated. Of course, it

requires to have a perfect control on the doping and the alloy concentration. As an example, if a structure is designed to compensate for a given doping level, but the effective doping is less important, then the well will be overcompensated and will have a PQW-like shape at the bottom, reintroducing the unwanted symmetry of the potential for the lowest energy states.

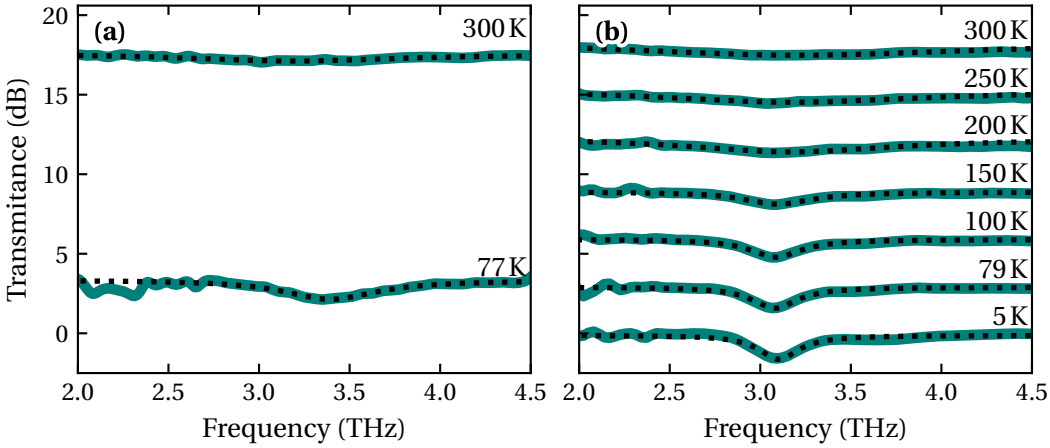

Figure 3.21.. **(a)** Stacked transmitance of G0645 bulk doped and **(b)** G0712 modulation doped HPQW.

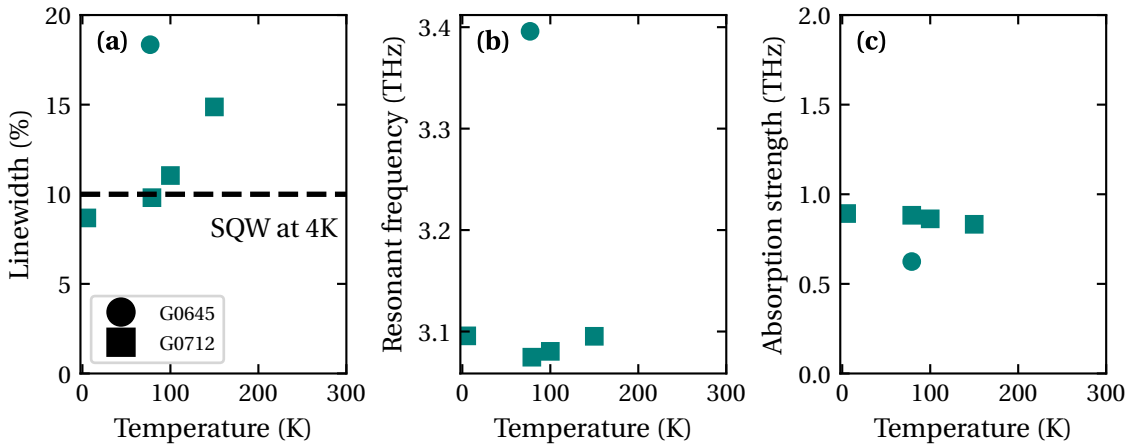

Figure 3.22.. Fitting parameters depending on the temperature of the Half Parabolic Quantum Well (HPQW) growths : **(a)** Transition linewidth, **(b)** resonance frequency and **(c)** the absorption strength.

To test the concept, two samples were grown. The sample G0645 is a 43-repetitions of AlGaAs Half Parabolic Quantum Well (HPQW)s bulk doped at $5 \cdot 10^{11}$ cm^{-2} and the sample G0712 which has the same number of wells, but is delta doped in the barriers at $5 \cdot 10^{11}$ cm^{-2}.

These samples were measured with the same system as the PQWs, using the same multipass geometry. G0645 was measured at 77 K and at room temperature only, while G0712 had a full temperature sweep. The predicted downside of the bulk doping appears clearly: G0645 has a 18 % linewidth at 77 K, almost five times more than what full PQWs can achieve. The ion scattering hampers a lot the transition quality. The modulation doped sample recovers partially the lost

linewidth, with 10 % linewidth at 77 K, down to around 8.7 % at 4 K. Above 150 K, no measurable absorption could be detected. Despite that, G0712 showed the same PQW feature when it comes to the temperature stability of the ISB frequency and the absorption strength: they are both quite stable. The shifted modulation doped structure is still under investigation.

3.5. Strong light-matter coupling regime with PQWs

As discussed in the introductory chapter, ISB polaritons are interesting for several applications at MIR and THz wavelengths. The main reason for the development of these parabolic structures was to obtain the room temperature operation of THz ISB polaritons. Although PQWs are not yet operating systematically at room temperature, the performances obtained at 78 K (Liquid N_2 temperature) surpasses by far the one of square QW. This fact already brings practical advances for the ISB polariton field.

One important piece of information that can be extracted from the strong-coupling regime is the number of electrons participating in the light-matter interaction. In order to make these tests quickly, we chose to use planar metal-dielectric-metal micro-cavities [67], mostly for convenience because they are easy to fabricate, and the measurement is straightforward. More details on these cavities can be found in Section 2.1.2.

For each sample, the cavity was designed using an RCWA code [142] and the active region modeled using the effective medium approximation [41]. Depending on the thickness of the active region, the sample will operate either in a dispersive or non-dispersive regime. In the case of a dispersive cavity, parameters (size and duty cycle of the grating) were optimized to offer the best contrast at 15° due to constrains coming from our measurement setup which allows low temperature measurements only at this angle. For the non-dispersive cavity, since the angle of incidence is not influencing the resonance frequency of the cavity, the parameters were also chosen for best contrast as close as possible to the anti crossing.

3.5.1. 54 PQWs within dispersive cavities: strong-coupling

With 54-well repetitions, this sample is the best candidate for room temperature strong-coupling operation despite a quite broad linewidth at 300 K. First an angle resolved measurement in reflectivity was conducted at room temperature. The results can be seen in Fig. 3.23 (a). While no distinct peaks are visible, the dispersion shows a hint of strong-coupling. Although an absorption was measurable at 300 K, the linewidth is too broad to satisfy the conditions for strong-coupling.

To push further the analysis and reach the necessary conditions for the strong coupling to occur, a temperature sweep was conducted. The experiments were done using a 15° unit, removing the ability to probe the sample in angle. The results are presented in Fig. 3.23 (b). A clear strong-coupling regime appears below 200 K.

From the experimental data (see Fig. 3.23 (c)), the extracted doping value is only a third of the nominal doping. Either the amount of impurities deposited during the growth was not the target value, which seems unlikely because this step is usually well calibrated, or electrons are trapped

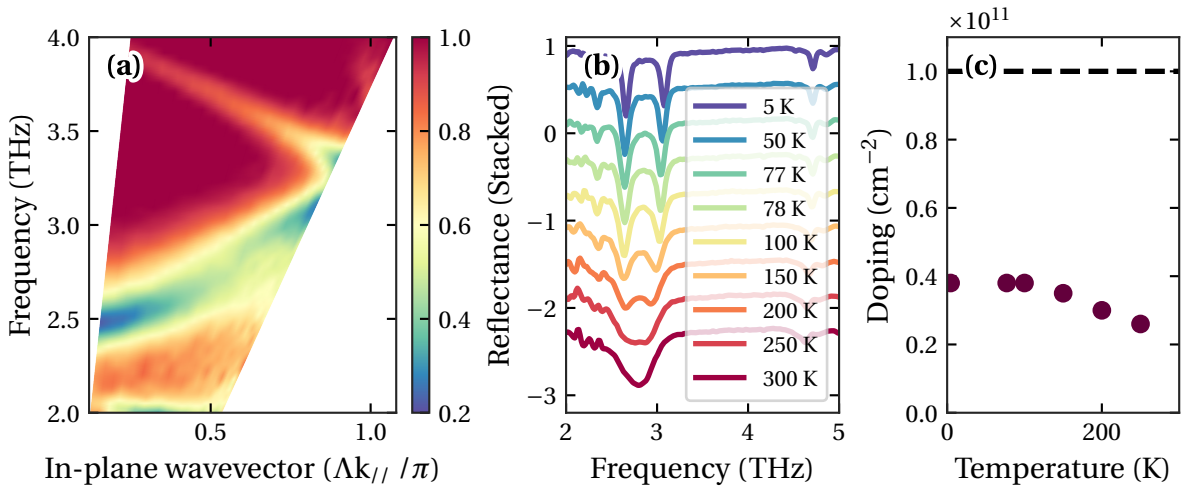

Figure 3.23.. **(a)**: Frequency dispersion of the 54-well PQWs (G0490) in a MIM cavity at room temperature (cavity parameters: period Λ = 42 µm, filling factor ff = 85 %). **(b)**: Reflectivity measurements with a temperature sweep at a fixed angle of 15° (cavity parameters: period Λ = 36 µm, filling factor ff = 85 %). **(c)**: Estimated doping taking part in the light-matter interaction.

somewhere in the lattice reducing the available carriers for the ISB transition despite the right amount of incorporated impurities.

As a benchmark, the square quantum well active region L1412 was also embedded into a dispersive MIM cavity and measured. The results are shown in Fig. 3.24.

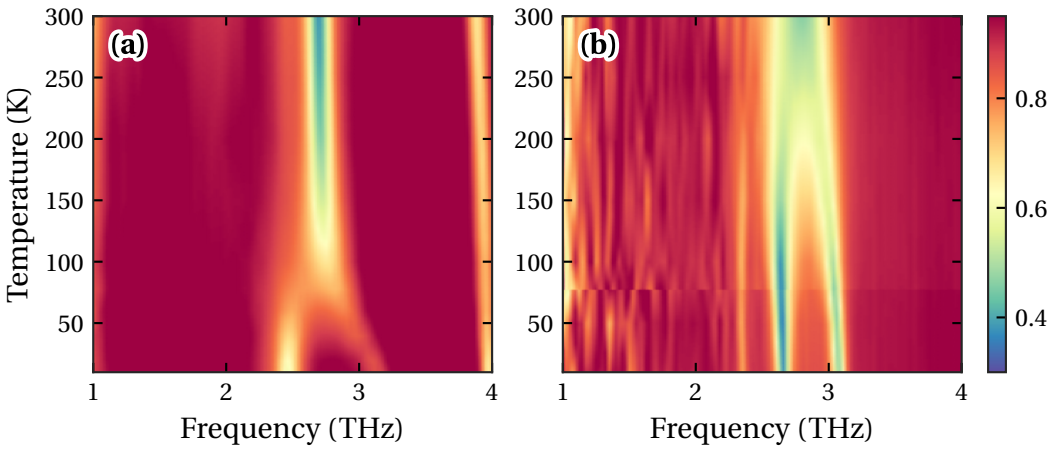

Figure 3.24.. Color plot of the reflectivity as a function of the temperature and the frequency for **(a)** L1412 (square QW) and **(b)** G0490 (PQW) in a MIM cavity

The comparison clearly highlights the advantage of a PQW over a classical square quantum well structure. The PQW based sample is able to stay in the strong-coupling regime at higher temperature. With square quantum wells, the sample can only achieve the strong-coupling regime up to around 90 K, which is the temperature at which this sample stops absorbing for the transition

1 → 2 (see Fig. 3.16).

3.5.2. 4 PQWs in non-dispersive cavity: strong-coupling up to 200 K

On the contrary of the 54-well active region, the 4-well sample was developed for being used in LC resonators which require low electromagnetic volume, thus the need for a thin active region. The period and filling factor of the grating was found using the RCWA code and optimized in order to be as close as possible to the anticrossing. The results are presented in Fig. 3.25.

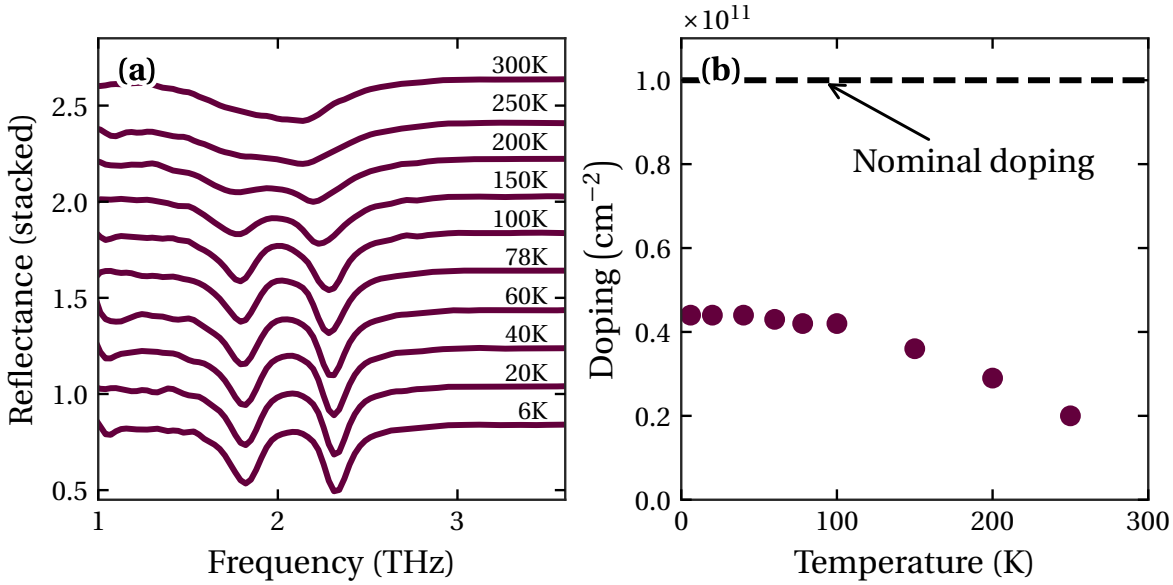

Figure 3.25.. **(a)**: Reflectivity measurements of the 4-well PQWs (G0642) with a temperature sweep at a fixed angle of 15° (cavity parameters: period Λ = 22 µm, filling factor ff = 82 %). **(b)**: Calculated doping from the polaritonic splitting.

Similarly to the 54-well sample, this one shows a very good behavior with temperature: two peaks are still visible at 200 K and the onset of the strong-coupling can be guessed at 300 K. The asymmetric shape of the absorption at 250 and 300 K is another clue that the sample is on the verge of entering the strong coupling regime.

To extract the doping from these measurements, RCWA simulations were done using the doping level as well as the transition frequency as a fitting parameter. The active region was modeled using the Zaluzny effective medium approximation. The static permittivity of the GaAs/AlGaAs stack was approximated using the average value of the permittivity over a well repetition. For G0642, the value is $\varepsilon_{avg} = 12.65$.

On the downside, these measurements revealed that the effective doping of this sample is lower than expected. Only a third of the nominal doping seems to be active. Despite the change of strategy for the doping (directly in the barrier, without doping wells) the outcome is the same: many charges remain trapped within the lattice and do not participate in the light-matter interaction. In turn, this lower effective doping means a lower Rabi splitting which may be problematic for achieving the ultra strong-coupling regime. It is possible to add more impurities to recover from

the loss but as the 18 PQWs demonstrated it, the linewidth would suffer from the heavier doping level.

3.5.3. The strong coupling regime with Half-PQWs inserted in non-dispersive resonators

The importance of the HPQW was discussed previously and is related to the polariton-polariton scattering process under resonant injection of light. Although, the transmittance measurements were not as excellent as the PQW, we have processed the sample within MIM geometry to explore the strong light-matter coupling. The temperature sweep results at an incident angle of 15° can be seen in Fig. 3.26.

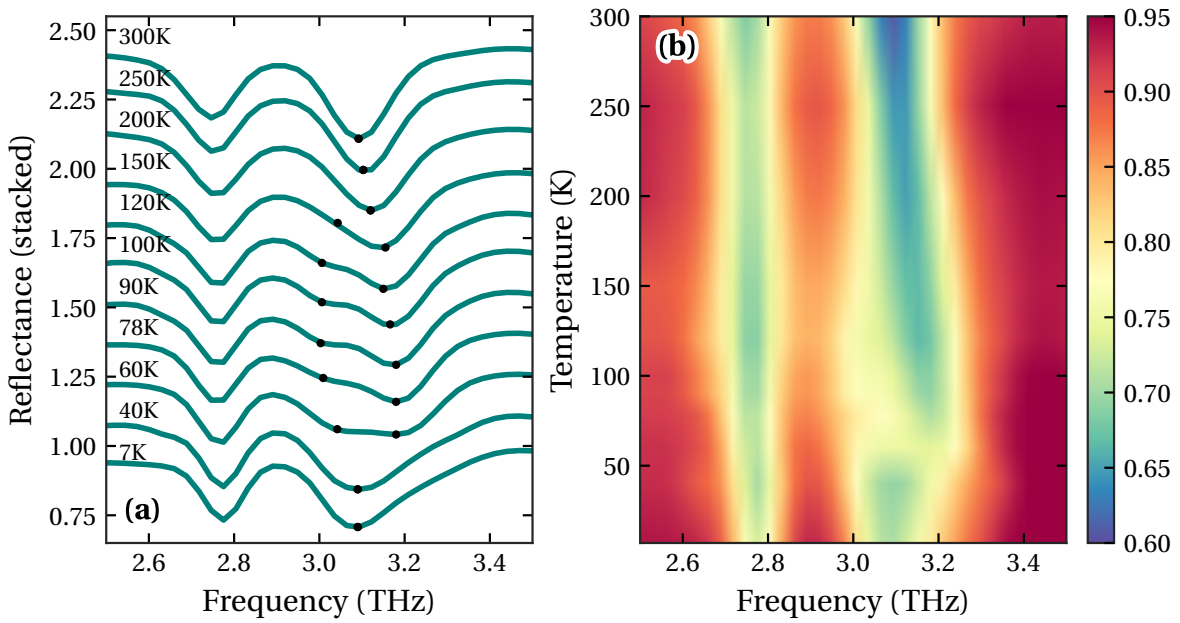

Figure 3.26.. **(a)**: Stacked reflectivity measurements of the 43-well modulation doped HPQWs (G0712) with a temperature sweep at a fixed angle of 15° (cavity parameters: period $\Lambda = 22\,\mu m$, filling factor ff = 82 %). **(b)**: Color plot of the reflectivity as a function of the temperature and the frequency. Despite being weak, a slight splitting happens around 78 K.

First it can be observed that despite being faint, strong coupling seems to occur around a temperature of 100 K. The other noticeable effect is the loss of the strong coupling below 78 K. The origin is unclear: as the temperature drops, the linewidth improves below 78 K, so the reason has to be found somewhere else. The most likely one is that fewer charges are available. Nevertheless, despite a design probably far from perfect, seeing strong coupling is an encouraging step, and it is very likely that after some iteration a high quality ISB transition can be obtained using HPQWs.

3.6. Conclusion

Throughout this chapter, I described how taking advantage of a parabolic potential profile can lead to a significant improvement of the temperature of operation and performance of THz semiconductor QWs. A record-breaking linewidth down to 3.6 % at 2.14 THz was measured at liquid He temperature, and below 10 % up to 150 K while maintaining its resonance frequency quite stable over a wide temperature range. These accomplishments are the results of the development of a new way to control alloy concentration during growth from our collaborators in Waterloo, Canada.

In order to confirm the applicative potential of these samples, some active regions were incorporated in MIM cavities and the reflectivity in the strong-coupling regime was measured. These measurements allowed to reveal some lingering uncertainties regarding the doping which appeared to be consistently lower than expected.

Several interesting applications of this growth method and the high quality active region it produces can be envisioned. First using the same GaAs/AlGaAs material platform, MIR PQW well is a possibility. It could allow to improve the line width of MIR transition, currently around 10 % using square wells, which is currently a limiting in factor in the achievement of gain in phonon-polariton scattering (see Chapter 2). Also, this growth method being general, it can in principle be applied to other materials like InGaAs or InSb. Finally, in order to expect to see PQWs used for QCL lasers, studies on the transport need to be done. This topic was left unexplored as the applications, in the scope of thesis, rely only on optical injection. It is however crucial to have a robust modeling of the electron transport if one wants to use PQWs for QCL or QWIP devices.

Chapter

4

Toward dynamical Casimir: ultrafast switching of a subwavelength THz cavity

4.1. Subwavelength resonators: The 3D LC circuit meta-atom

This section is dedicated to the study of the LC resonator. First the $\lambda/2$n cavity will be discussed: the modes of the square and round patch will be studied and the diffraction limit demonstrated. Then the concept of meta-materials will be introduced followed by a detailed description of what an LC cavity is. Finally, some properties of these cavities will be explained.

4.1.1. The Lambda/2n patch resonator

4.1.1.1. The square patch resonator

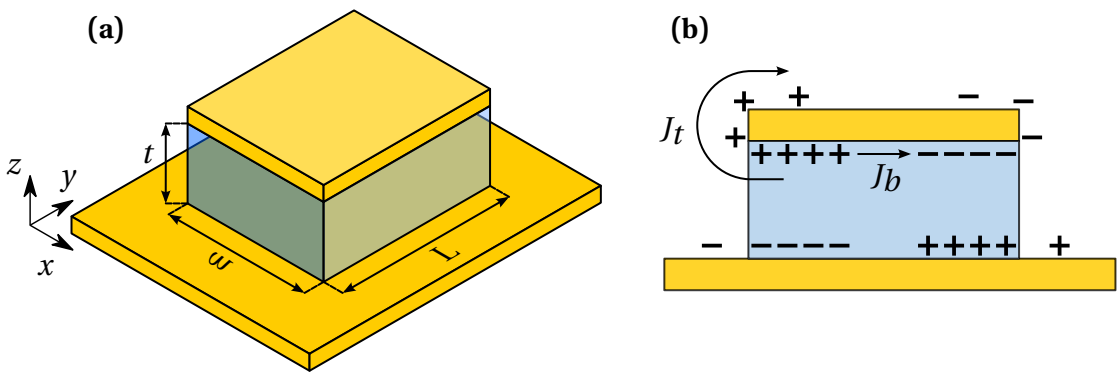

Figure 4.1.. **(a)**: Schematic of a square patch geometry. **(b)**: Current density profile of a parallel plate geometry.

Although the final design of the LC resonator is composed of a circular patch, this part will be devoted to the study of the square patch resonator as it allows to grasp the physics involved while being more accessible on a mathematical point of view. The geometry is depicted in Fig. 4.1. In such a cavity it is possible to solve the Helmholtz equation to find its eigenmodes, but first it is necessary to define the boundary conditions of the problem. The easiest one are for z = 0 and z = d : at these locations the gold layers, approximated as a perfect conductor, impose a zero tangential electric field. Additional physical considerations will provide the four other boundary conditions. If a cavity mode is excited, two charge distributions are created: one on the ground plane, and another on the lower and upper surfaces of the top patch. The shape of the top patch charge distribution depends on two effect: an attractive one between charges of opposite signs between the bottom of the patch and the ground plane, and a repulsive one between charges of same sign on the bottom of the patch [143]. These interactions create two current distributions J_t and J_b represented in Fig. 4.1 (b). In the practical case where the height over width ratio is small, the attractive mechanism will prevail. The current density J_t can be approximated to be negligible thus there are no tangential magnetic field at the edge of the patch. The four sides can be treated as perfect magnetic conductor.

For such a cavity, the modes of interest are those with the E field polarized in the z-direction or TM_z, which is the condition for having a coupling between the cavity mode and an ISB transition. It means the magnetic field in the z-direction is zero ($H_z = 0$). It can be shown that under this condition, the vector potential is reduced to $A = A_z$ [144]. The Helmholtz equation for the vector potential is then:

$$\nabla^2 A_z + k^2 A_z = 0 \tag{4.156}$$

and the solution for TM_z modes are [144]:

$$A_z = \left[A_1 \cos(k_x x) + B_1 \sin(k_x x)\right]\left[A_2 \cos(k_y y) + B_2 \sin(k_y y)\right] \tag{4.157}$$

$$\times \left[A_3 \cos(k_z z) + B_3 \sin(k_z z)\right] \tag{4.158}$$

with k_x, k_y and k_z the wavenumbers for the x-, y- and z-direction. From this, the electric and magnetic field are derived:

$$E_x = -\mathrm{i}\frac{1}{\omega\mu\varepsilon}\frac{\partial^2 A_z}{\partial x\,\partial z} \qquad H_x = \frac{1}{\mu}\frac{\partial A_z}{\partial y} \tag{4.159a}$$

$$E_y = -\mathrm{i}\frac{1}{\omega\mu\varepsilon}\frac{\partial^2 A_z}{\partial y\,\partial z} \qquad H_y = -\frac{1}{\mu}\frac{\partial A_z}{\partial x} \tag{4.159b}$$

$$E_z = -\mathrm{i}\frac{1}{\omega\mu\varepsilon}\left(\frac{\partial^2}{\partial z^2} + k^2\right)A_z \qquad H_z = 0 \tag{4.159c}$$

These expressions of the EM fields are constrained by the following boundary conditions:

$$E_x(z=0) = E_y(z=0) = E_x(z=h) = E_y(z=h) = 0 \tag{4.160}$$
$$H_y(x=0) = H_y(x=w) = 0 \tag{4.161}$$
$$H_x(y=0) = H_x(y=L) = 0 \tag{4.162}$$

Using the two boundary conditions on E_x yields that $B_3 = 0$ and that:

$$k_z = \frac{p\pi}{t} \quad with \quad p = 0, 1, 2, ... \tag{4.163}$$

Similarly, using the two boundary conditions on H_y yields that $B_1 = 0$ and that:

$$k_x = \frac{m\pi}{w} \quad with \quad m = 0, 1, 2, ... \tag{4.164}$$

Finally, using the two boundary conditions on H_x yields that $B_2 = 0$ and that:

$$k_y = \frac{n\pi}{L} \quad with \quad n = 0, 1, 2, ... \tag{4.165}$$

Using the constraint equation $k^2 = k_x^2 + k_y^2 + k_z^2 = \omega\mu\varepsilon$, the resonance frequencies of the cavity are:

$$f_{mnp} = \frac{1}{2\pi\sqrt{\mu\varepsilon}}\sqrt{\left(\frac{m\pi}{W}\right)^2 + \left(\frac{n\pi}{L}\right)^2 + \left(\frac{p\pi}{h}\right)^2} = \frac{c}{2\pi}\sqrt{\left(\frac{m\pi}{W}\right)^2 + \left(\frac{n\pi}{L}\right)^2 + \left(\frac{p\pi}{h}\right)^2} \tag{4.166}$$

where $\varepsilon = \varepsilon_0\varepsilon_r$ and $\mu = \mu_0\mu_r$.

Using the results imposed by the boundary conditions, the vector potential becomes:

$$A_z(x, y, z) = A_{mnp}\cos\left(k_x x\right)\cos\left(k_y y\right)\cos\left(k_z z\right) \tag{4.167}$$

Plugging this vector potential into Eq. (4.159), one obtains the expressions for the electric field in the cavity:

$$E_x = -\mathrm{i}\frac{k_x k_z}{\omega\mu\varepsilon}A_{mnp}\sin\left(k_x x\right)\cos\left(k_y y\right)\sin\left(k_z z\right) \tag{4.168}$$
$$E_y = -\mathrm{i}\frac{k_y k_z}{\omega\mu\varepsilon}A_{mnp}\cos\left(k_x x\right)\sin\left(k_y y\right)\sin\left(k_z z\right) \tag{4.169}$$
$$E_z = -\mathrm{i}\frac{\left(k^2 - k_z^2\right)}{\omega\mu\varepsilon}A_{mnp}\cos\left(k_x x\right)\cos\left(k_y y\right)\cos\left(k_z z\right) \tag{4.170}$$

In this cavity, the different modes are sorted depending on their resonance frequencies. The dominant mode is the mode with the lowest order resonant frequency. In the studied case with

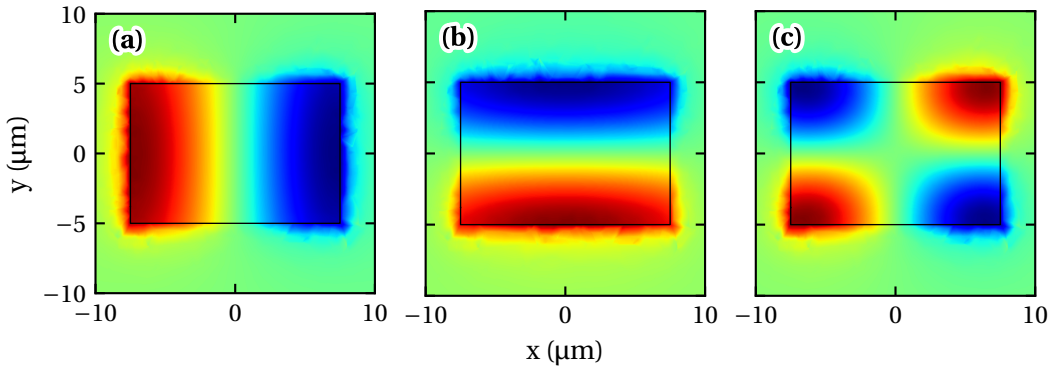

Figure 4.2.. Electric field in the z-direction for a GaAs rectangular patch for the first three modes: **(a)** f_{01}, **(b)** f_{10} and **(c)** f_{11}.

a small height to width ratio, the first modes of this cavity are TEM modes with no electric field components in the x- and y-direction. They behave as standing waves propagating in the xy-plane.

In Fig. 4.2, the E_z component of the electric field is plot for the three first modes TM_{01}, TM_{10} and TM_{11} for a patch cavity with a 0.8 µm thick GaAs core, 15 µm width and 10 µm length. The field maps were calculated using COMSOL Multiphysics.

4.1.1.2. The round patch

Now that the basics of the square patch were presented, the same method can be applied to the circular patch to find what are the modes sustained by this cavity geometry.

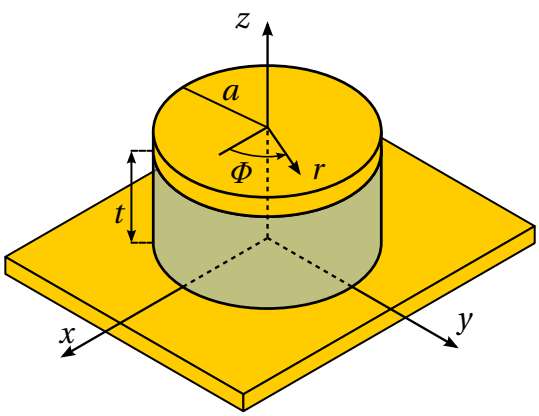

Figure 4.3.. Schematic of a circular patch geometry.

In such a geometry, the natural coordinate system is the cylindrical one (r, θ, z). Once again, we present only the TM_z modes of interest for an ISB based device. In this case, the vector potential is [144] :

$$A_z(r,\theta,z) = [A_1 J_m(k_r r) + B_1 Y_m(k_r r)][A_2 \cos(m\theta) + B_2 sin(m\theta)][A_3 \cos(k_z z) + B_3 \sin(k_z z)] \quad (4.171)$$

with J_m and Y_m the Bessel functions of first and second kind, $k_{r,\theta,z}$ the wavevector in the r-, θ- and z-direction and As and Bs are constants. Using the same physical considerations for the boundary conditions used for the square patch, solving the Helmoltz's equation in this system yields the magnetic vector potential :

$$A_z = B_{mnp} J_m(k_\rho \rho)[A\cos(m\phi) + B\sin(m\phi)]\cos(k_z z) \tag{4.172}$$

and the wavevector expressions are :

$$k_r = \frac{\chi'_{mn}}{a} \quad with \quad m,n = 0,1,2,... \tag{4.173}$$

$$k_z = \frac{p\pi}{t} \quad with \quad p = 0,1,2,... \tag{4.174}$$

where χ'_{mn} are the zeroes of the Bessel function derivative J_m whose first values are:

$$\chi'_{11} = 1.8412 \tag{4.175}$$

$$\chi'_{21} = 3.0542 \tag{4.176}$$

$$\chi'_{01} = 3.8318 \tag{4.177}$$

$$\chi'_{31} = 4.2012 \tag{4.178}$$

Using once again the constraint equation, the resonant frequency under the condition of a small height over width aspect ratio can be derived :

$$f_{mn0} = \frac{1}{2\pi\sqrt{\mu\varepsilon}}\left(\frac{\chi'_{mn}}{R}\right) = \frac{c}{2\pi}\left(\frac{\chi'_{mn}}{R}\right) \tag{4.179}$$

A field map of the numerically calculated E_z electric field of the first four modes is depicted in Fig. 4.4.

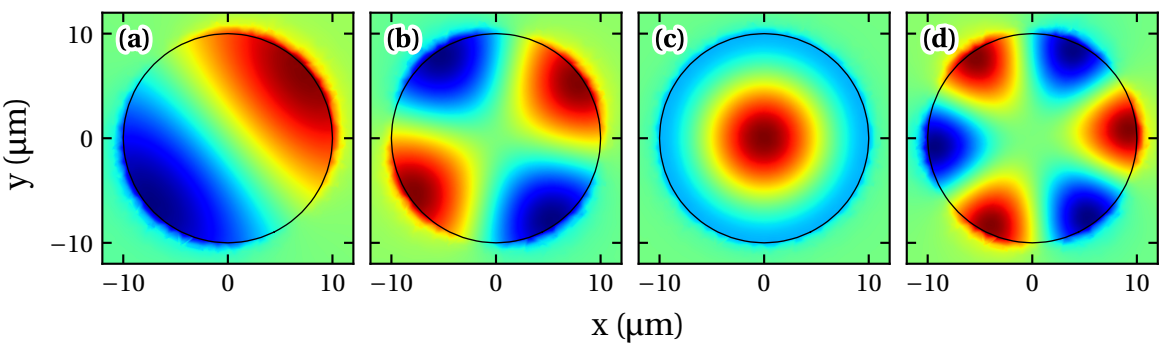

Figure 4.4.. Mode profile in the xy-plane for **(a)** χ'_{11}, **(b)** χ'_{21}, **(c)** χ'_{01} and **(d)** χ'_{31}.

4.1.1.3. The diffraction limit

In general, optical systems are limited in resolution. It is well established that it is constrained by the diffraction limit, which was theorized by Abbe and Rayleigh in the 1890's [145].

In the context of a cavity resonator, a rule can be obtained from the Fourier transform's "uncertainty" relation. Considering the square patch presented earlier Section 4.1.1.1 with a mode propagating in the x-direction, the wavevectors k and k_x must be real. From the relation $k = \sqrt{k_x^2 + k_y^2 + k_z^2}$, it can be shown that $-k \leq k_x \leq k$. In other word, the accessible values for k_x range in the interval $\Delta k_x = 2k$ The uncertainty principle implies that $\Delta x \Delta k_x \geq \pi$ which means that :

$$\Delta x \geq \frac{\lambda}{4n} \tag{4.180}$$

This relation says that for a wave of wavevector k, the spatial extent in which this wave can be contained must respect the condition $x \geq \lambda/2n$.

This relation can be verified for the circular patch cavity. Using the expression of the fundamental mode f_{11} and remembering that $\sqrt{\varepsilon_r} = n$, the diameter of the patch can be written :

$$d = 2a = \frac{c}{\pi f_{11}\sqrt{\varepsilon_r}}\chi'_{11} = \frac{\lambda}{\pi n}\chi'_{11} \tag{4.181}$$

$$\simeq \frac{\lambda}{2n} \quad \text{with} \quad \frac{\chi'_{11}}{\pi} \simeq 0.59 \tag{4.182}$$

As expected, the fundamental mode of the circular patch cavity, derived from the Helmoltz equation, is effectively the mode of smaller frequency that can be confined in the cavity.

At first glance, the diffraction limit imposes a hard limit on the accessible device sizes for a specific operating frequency. Under the assumption that the different components of the wavevector $k_{x,y,z}$ must be real, which supposes that a wave can propagate in the three directions, this is the case. However, if one of the directions has a purely imaginary wavevector, corresponding to an evanescent wave, then the other wavevectors can be larger thus permitting to overcome the diffraction limit. Such a system can be obtained when one considers the propagation of a wave on a metallic surface. This is the domain of surface plasmon photonics [146]. Another domain where the diffraction limit has been overcome is the photonics meta-material.

4.1.2. The concept of meta-material

The optical response of a medium is highly dependent on its physical constituents. Examples introduced in Section 1.3 are the metal and dielectric media, which present sharp features created by the phonon and electron interactions with an impinging electric field, materialized by a strong modification of the permittivity around specific frequencies. Such behavior can be artificially mimicked by creating a material made of several resonators called meta-atoms, arranged in a

rational way in order to provide specific properties to the medium. Those media are called metamaterials. Novel properties were introduced using this concept, ranging from superlensing [147, 148] to cloaking [149].

It was quickly realized that such control on the flow of light could be achieved using a monolayer of meta-atoms. Those metasurfaces are compatible with clean room processes, thus can be obtained with standard semiconductor fabrication. Among the many properties offered by metasurfaces, one has a great potential for semiconductor applications: the field enhancement [150] Thanks to the reduced volume where the EM field is confined, the field intensity is drastically increased. This property has led to major advances in terms of performance for detectors [151, 152, 153] and emitters [154].

Another domain in which metamaterials are a useful concept is the implementation of advanced features such as switching and reconfigurability, either using electrical, mechanical, thermal or optical methods [155, 156, 157, 158]. This is the property that will be used for achieving the fast modulation in the follow up of this chapter.

4.1.3. Toward the LC resonator

We have shown in the previous section that the device dimension for a given resonance frequency is constrained by the diffraction limit. This limit is set for any propagative mode in a cavity. An alternative regime can be obtained with standing modes in subwavelength cavities, called LC resonators due to similar features they share with the electronic LC circuit.

4.1.3.1. Lumped elements

The lumped element model is a convenient tool that allows to see a complex system as made of distributed individual elements, connected together. The properties of these elements are described by their impedance and follow the association rules of the electrical components. Famous applications of this model can be found in RF engineering or in thermodynamic system to simplify the study of complex systems

In the electromagnetic world this regime is achieved under one assumption: if the size of the system is much smaller than the effective wavelength. Under this assumption, the electric and magnetic fields vary slowly over the system dimensions, thus justifying that the time derivative of the electromagnetic field is zero. The Maxwell equations become:

$$\boldsymbol{\nabla} \cdot \boldsymbol{H} = 0 \tag{4.183}$$

$$\boldsymbol{\nabla} \cdot \boldsymbol{E} = \frac{\rho}{\varepsilon} \tag{4.184}$$

$$\boldsymbol{\nabla} \times \boldsymbol{H} = \boldsymbol{J} \tag{4.185}$$

$$\boldsymbol{\nabla} \times \boldsymbol{E} = 0 \tag{4.186}$$

The time varying dependence between $\boldsymbol{E}$ and $\boldsymbol{H}$, which is responsible for the wave like behavior of the electromagnetic field, disappeared. The magnetic and electric fields are uncoupled. This

regime is called the quasi-static regime and it is the realm of electronics. From these equations, it is possible to demonstrate the Kirchhoff law which justifies the use of the impedance to describe the system.

4.1.3.2. The patch cavity as a capacitance

A classic example used to introduce the capacitor in electromagnetism is to consider two circular parallel plates made of a conducting material separated with an insulator. In the DC regime, opposite sign charges are built on the two plates leading to a uniform electric field from one plate to the other. In the AC regime, it is more subtle. In the small frequency regime, the time varying electric field can be approximated as:

$$E(\omega) = E_0 \exp(\mathrm{i}\omega t) \tag{4.187}$$

where E_0 is the magnitude of the electric field and ω the pulsation of the driving bias.

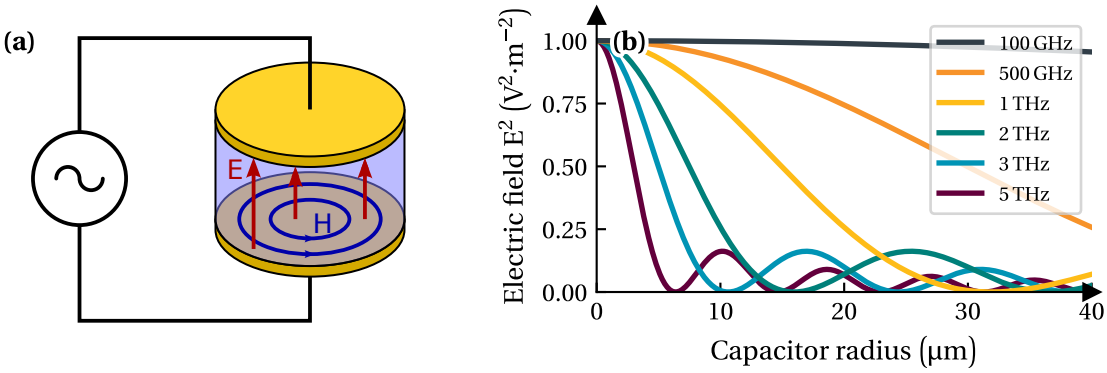

Figure 4.5.. (a) Capacitor driven by an AC generator with the electric and magnetic fields. **(b)** Electric field amplitude depending on the radial position or several frequencies.

In reality, this electric field expression is not taking into account the effect of the induced magnetic field created by the electric field oscillation, which can be calculated using the Ampere law. This magnetic field amplitude depends on the system frequency and its radius, and follows the expression $B(r) = \frac{\mathrm{i}\omega r}{2c^2} E_0 \exp^{\mathrm{i}\omega t}$. For small capacitor size or low frequency, this induced magnetic field has a negligible amplitude, justifying the Eq. (4.187) in the low frequency approximation.

At higher frequency, the magnetic field has to be taken into account, as it will influence the electromagnetic environment. This modification takes the form of a correction of the electric field, which yields the following expression:

$$E(r,\omega) = E_0 \exp^{\mathrm{i}\omega t} J_0\left(\frac{\omega r}{c}\right) \tag{4.188}$$

with J_0 the first kind Bessel function. The electric field at different frequencies for a GaAs capacitor can be seen in Fig. 4.5 (b). At low frequencies (around 100 GHz), the electric field remains almost constant on a wide radius range, changing its sign around 300 µm. At higher frequencies, the field

oscillates faster. For instance at 3 THz, the electric field do a complete oscillation approximately in 15 µm, which is close to the resonance frequency of the TM_{01} mode in a circular patch cavity.

4.1.3.3. Energy conservation in a patch cavity

In a circular patch cavity, it has been shown in Section 4.1.1.3 that for a given dimension it exists a frequency limit below which no mode can be confined. For this demonstration, assumptions on the accessible wavenumbers were made. It is possible to obtain the same results using a different reasoning. The reasoning will be similar to the study in Ref. [159].

In a patch cavity with a radius $a \geqslant \lambda/2n$ the electric field can be written in the form $E(z,t) = E_0 \sin(kz)\mathrm{e}^{-\mathrm{i}\omega t}$. Using Faraday's law the magnetic field can be derived $H(z,t) = H_0 \cos(kz)\mathrm{e}^{-\mathrm{i}\omega t}$ with $H_0 = \sqrt{\varepsilon/\mu}E_0$. In such a system, the electric and magnetic energy per volume unit w_e and w_m are:

$$w_e \backsim \frac{\varepsilon E_0^2}{2} \tag{4.189}$$

$$w_m \backsim \frac{\mu H_0^2}{2} \tag{4.190}$$

with ε and μ the permittivity and permeability of the material. Remembering that $H_0 = \sqrt{\varepsilon/\mu}E_0$, it turns out $w_\mathrm{e} = w_\mathrm{m}$. For a photonic mode in a cavity, there is a periodic exchange of energy between the electric and magnetic fields. Those are the confined modes described in Section 4.1.1.2.

Now if one considers a sub $\lambda/2n$ cavity of radius a, the electric field becomes:

$$E(z,t) = E_0 sin(kz)e^{-i\omega t} \backsimeq E_0 \sin(\pi z/a)e^{-\mathrm{i}\omega t} \tag{4.191}$$

and the Faraday law yields $H(z,t) \backsimeq H_0 \cos(\pi z/a)e^{-\mathrm{i}\omega t}$ with $H_0 = \sqrt{\varepsilon/\mu}E_0(2na/\lambda)$ [159]. Using the energy relation, one obtains:

$$w_m = \left(\frac{2na}{\lambda}\right)^2 w_e \tag{4.192}$$

It means that for a hypothetical mode in a cavity whose size is below the diffraction limit, there is no conservation of the energy between the magnetic and electric field. During an oscillation, the total energy confined in the cavity decreases: part of the electric field is radiated away from the cavity. While this property is interesting in the case of an antenna, it is a problem for a cavity whose purpose is to confine. Fortunately, it is possible to recover the energy conservation in the system, by adding another reservoir of magnetic energy: an inductance.

4.1.3.4. The air bridge antenna

So far, the patch cavity does not allow carriers movements: as shown in the previous section, charge separation gives rise to an oscillating electromagnetic field for modes above the diffraction limit and radiative ones for modes below the diffraction limit due to an unbalanced energy conservation. Loading the patch cavity with an inductance allows the electrons to circulate in the system, which provides an additional reservoir of energy for the system. During an oscillation, the stored energy in the electric field is converted into electron motion in the inductance. This motion in turn generates a magnetic field stored in the inductance.

For a capacitor of capacitance C, the stored energy is dependent on the charge $q(t)$ and follows the formula $w_e = q(t)^2/2C$. Similarly, an inductor of inductance L stores an energy $w_i = Li(t)^2/2$ which depends on the current $i(t)$.

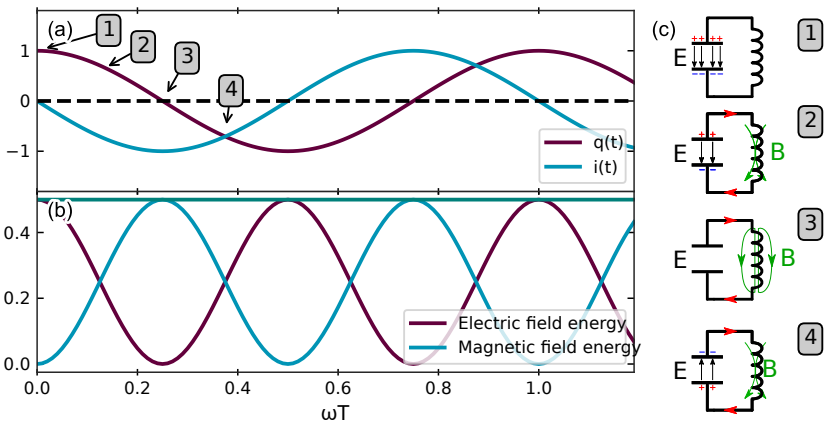

Figure 4.6.. (a): evolution of the capacitor charge and current in the circuit for an LC circuit. **(b)**: evolution of the electric and magnetic field energy. **(c)**: LC circuit and the current, charge and associated electromagnetic fields.

The process is similar to an RLC circuit where there is a periodic energy exchange between the capacitive part (the patch) and the inductive part (the inductance). If the initial state is the capacitor fully charged, all the energy of the system is stored in the capacitor. As the capacitor starts to release its charges, an electrical current flows in the inductor generating a magnetic field. During this stage, w_e decreases while w_i increases up to the point where the capacitor charge is zero and the inductor stores all the energy of the system in its magnetic field. At this point the current is maximal. As it starts to decrease, the magnetic field decreases too and the capacitor builds back its charge, with opposite charges sign on its plates. In this system the oscillations are sustained indefinitely.

Obviously, in the real world the oscillation cannot be sustained forever, due to imperfections and the ohmic losses of the metal. After the initial excitation, the total energy decreases exponentially, with a rate proportional to the damping factor $\alpha = R/2L$ with R the total resistance of the circuit, hence providing a resonant mode with a finite lifetime.

The design of the LC resonator is shown Fig. 4.8 (a). The antenna is a suspended metal stripe with one end resting on the patch and the other on the ground plane. More detail on its fabrication are provided in Section 4.2.2.1.

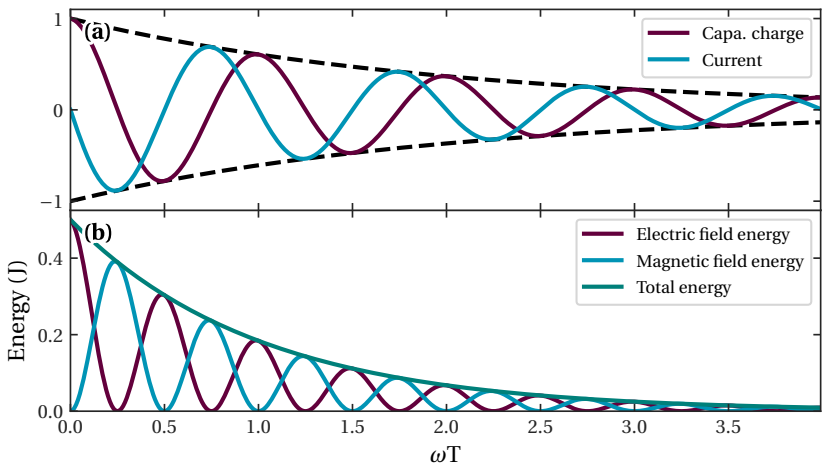

Figure 4.7.. Damping of the **(a)** capacitor charge and current in the circuit and **(b)** of the electric and magnetic field energy.

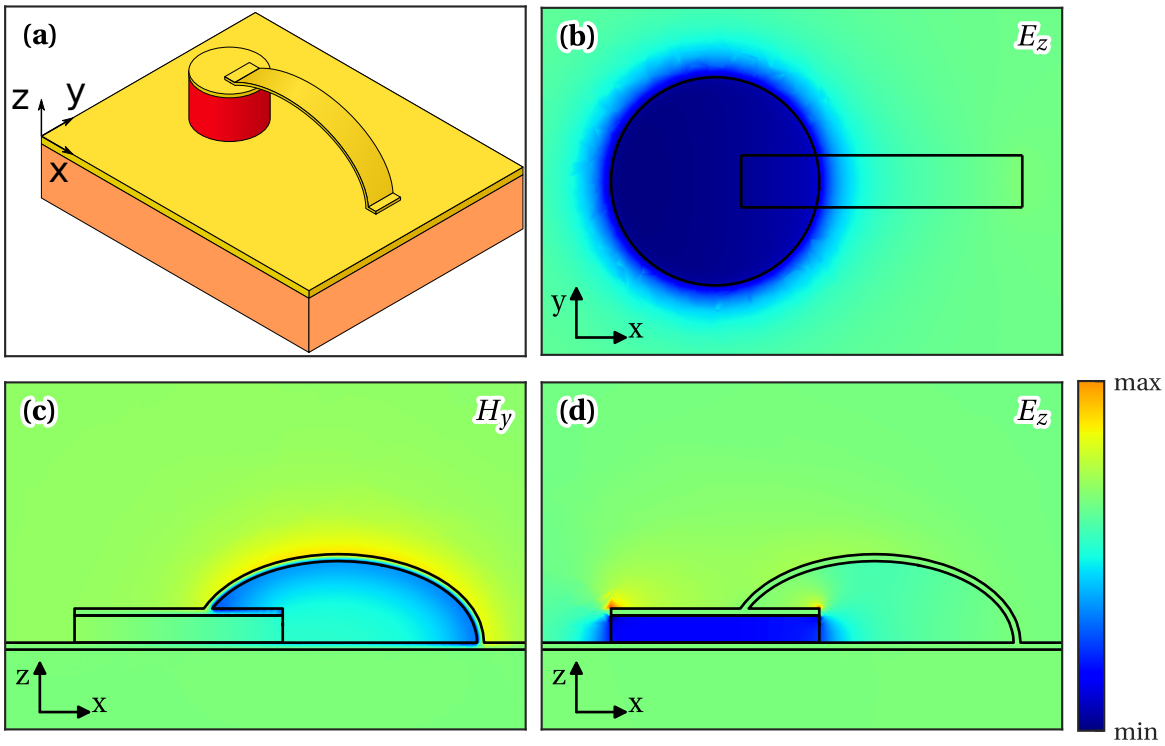

Figure 4.8.. **(a)**: Schematic of the LC resonator. **(b)** and **(d)**: field map of the electric field in the z-direction for a xy- and xz-plane cut. **(c)**: field map of the magnetic field in the y-direction for a xz-plane cut.

In Fig. 4.8 (b), (c) and (d) the electric and magnetic fields of a simulated LC resonator are depicted. The patch has a 3 µm radius, a SiO_2 core of 1 µm thickness, and an 8 µm long and 1.5 µm wide antenna. It can be seen that bot fields are spatially separated as expected: the electric field is confined in the patch capacitance and the magnetic field in the antenna inductance.

4.1.4. Considerations on the THz LC resonator

The previous part was devoted to the concept of LC resonators as a system allowing to confine electromagnetic energy in a volume below the diffraction limit, by spatially separating the electric and magnetic fields. While the concept was still theoretical, some practical insights for a real device will be presented in this section.

4.1.4.1. Circuit tuning of an LC cavity

As a physical object, an LC cavity shares many properties with their electrical counterpart, the LC circuit. Among them, the basic laws of impedance and capacitance shall apply.

Starting with the capacitive section of the cavity, the circular patch is a textbook representation of the parallel plate capacitor. Considering a cavity of surface S, with a dielectric core of permittivity $\varepsilon = \varepsilon_0 \varepsilon_r$ and thickness t, the equivalent capacitance can be written :

$$C = \frac{\varepsilon S}{t} \tag{4.193}$$

This is under the assumption that the fringing fields at the patch edges are not taken into account. This is a reasonable assumption considering that it has been stated that patch cavities with a small height over width ratio are considered. From Eq. (4.193), three tuning knobs are available to tune the capacitance value. The geometrical parameters (surface and height) as well as the material used for the dielectric core allow to reach a wide range of accessible capacitance values. However, one has to keep in mind that these cavities are to be fabricated. Not all materials are compatible between each other or available for deposition, making the permittivity a tricky tuning knob. It is even stricter once a specific active region has to be used. Since these LC cavities are developed for ISB strong coupling applications, the dielectric core is expected to embed semiconductor quantum wells. For a specific application, the active region (AR) material is not a free parameter thus the permittivity cannot be changed at will. Using the same argument, the core material thickness is more or less fixed. Thus, only the device surface can be employed to tune the capacitance value.

On the inductive section, the inductance of the suspended antenna is not easily tailorable. The closest counterpart in the electronic world would be the wire single loop inductance. However, this model does not take into account the thickness of the antenna. The best way to approximate it is to model it as a rectangular conductor. Most of the time, extremely complicated formula result from the exact analysis using the geometric mean distance [160]. In our case, a simplified expression can be obtained [161] :

$$L = 0.2l\left(\ln\frac{2l}{w+t} + 0.5 + \frac{w+t}{3l}\right) \tag{4.194}$$

where l, w and t are respectively the length, width and thickness of the metal strip. Realistically, the thickness is not a parameter that can be changed over a wide range of values. In the THz range, the typical metal thickness is around 200-300 nm in order to be above the skin depth, and below 400 nm in order to be compatible with standard clean room processes. Another constrain on the

air bridge design is the ratio height over length, as it will be explained in the fabrication section. Too steep bridges will collapse or break.

Following the circuital equivalent of LC resonators, the resonance frequency is :

$$f = \frac{1}{2\pi\sqrt{LC}} \tag{4.195}$$

4.1.4.2. Coupling

To characterize the resonators, optical reflectivity measurements will be performed using an FTIR. To obtain the best results, it is important to find what is the most suitable polarization and incident angle offering the best coupling. A simplified picture of an LC cavity is the coupling of an electric and magnetic dipole. In this section, the four possible configurations are presented in Fig. 4.9.

To obtain general rules on the absorption depending on the polarization and the incidence angle, the results of B. Paulillo will be presented [162, 163].

First let's consider the magnetic dipole materialized by the loop antenna. From an antenna theory point of view, the suspended bridge can be seen as a circular loop antenna with a dipole moment oriented perpendicularly to the enclosed surface. In order to couple a magnetic field with a dipole, there must be a non-zero projection in the antenna loop. It is the case for the configuration (a) and (d) depicted Fig. 4.9. In order to study the effect of the angle on the coupling strength, the results of the angle resolved experimental results of the configuration (d) are presented in Fig. 4.10 (a). The coupling between the magnetic field and the magnetic dipole follows an angular dependence proportional to $\cos(\theta)$ with θ the angle between the dipole moment and the magnetic field. Thus, the maximum coupling between the magnetic field and the magnetic dipole occurs when both vectors are aligned ($\theta = 0°$)

Using the same idea, the configuration (c) was used to study the coupling between the electric field and the electric dipole materialized by the patch cavity. From the experimental results visible in Fig. 4.10 (b), the maximum of the absorption happens at high angle of incidence, and diminish as the angle get closer to the quasi-normal incidence. This is consistent with the fact that the patch can be seen as an electric dipole.. The maximum coupling with the incident electric field occurs at grazing angle.

Of the two remaining configurations, the case depicted in Fig. 4.9 (c) is the only one that offer no coupling at all with both the electric and magnetic dipole. It leaves the configuration (a) that can couple with both the antenna and the capacitance. It is the most favorable configuration and will be the one used experimentally for probing the LC mode.

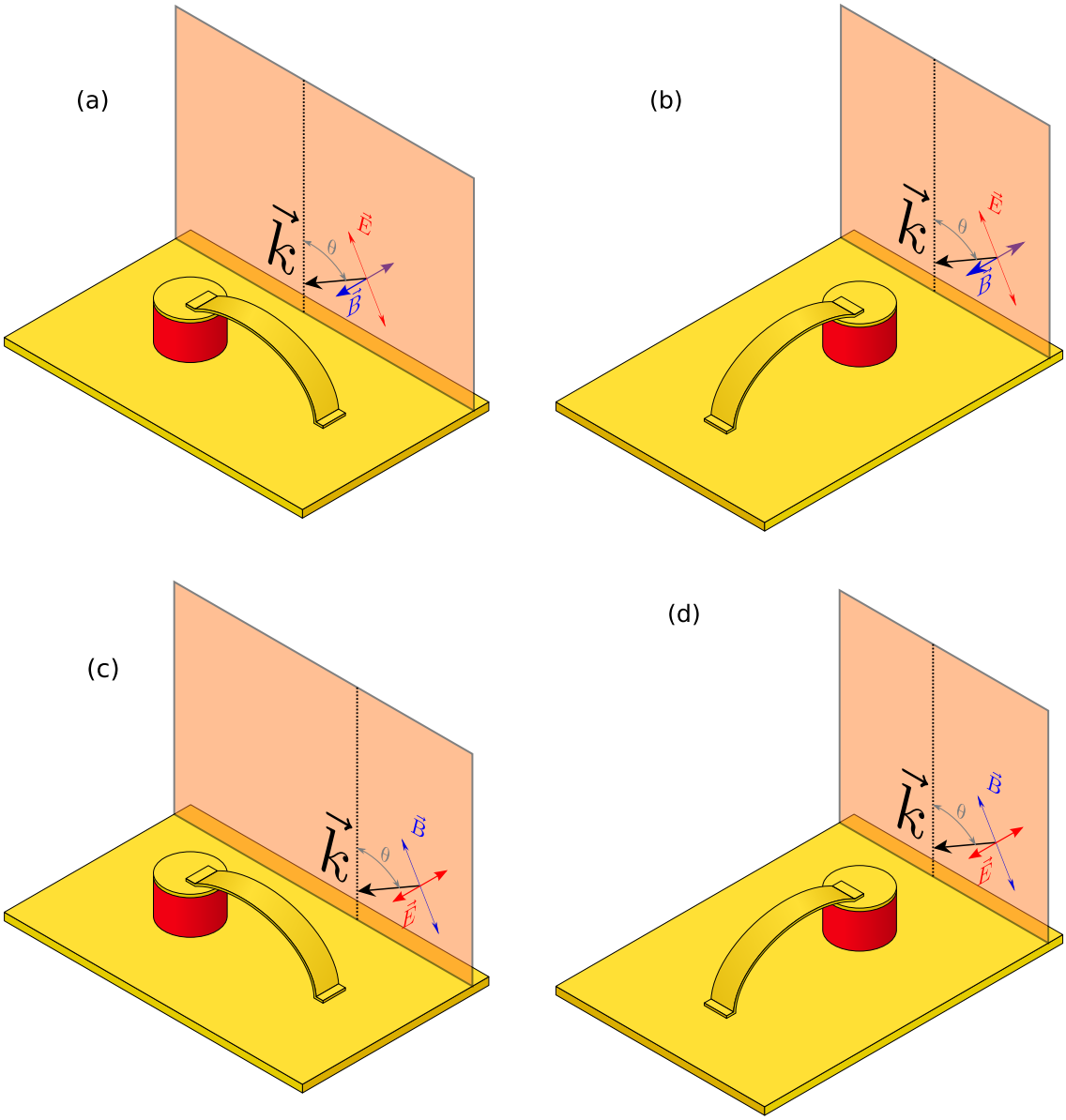

Figure 4.9.. Different coupling and polarization configurations for the air bridge and devices.

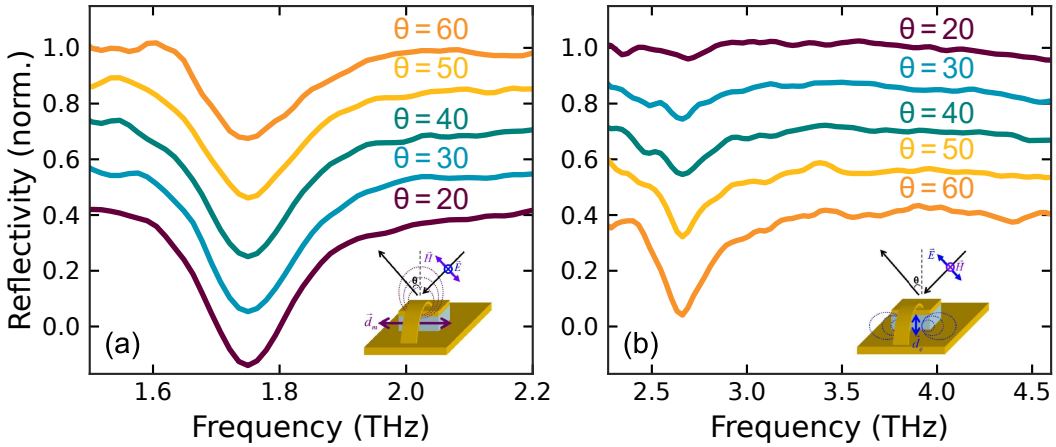

Figure 4.10.. Angle resolved reflectivity measurements of an LC resonator in configuration where only **(a)** the magnetic dipole or **(b)** the electric dipole are excited.

4.2. Functionalization of the LC resonator

4.2.1. Frequency modulation of the optical properties of metasurfaces

Soon after the demonstration of the first metamaterial surfaces, the development of ways to alter their optical responses attracted a lot of attention. The demonstration of an active metamaterial was first reported in the RF frequency range [164, 165, 166] followed shortly after in the THz []. In these early studies, whose metamaterials were based on planar SRRs, the strategy was to change the equivalent capacitance of the circuit.

The first demonstrations were based on electrical modulation of the capacitance of the LC equivalent circuit, by using varactors as an additional tunable capacitor [164, 165] or by creating depletion layer in a semiconductor [167].

Optically controlled modulation was then achieved using free carrier generation in semiconductors. Total turn off of the metamaterial resonance was achieved by shorting entirely the resonator, pumping either the whole substrate [168] or an element inserted in the gap of an SRR [166]. Real frequency modulation was then obtained by selectively photoexciting a carefully inserted semiconductor element, inducing a total capacitance change without shorting the entire resonator [169, 157].

Thermal induced metamaterial modulation with SRR was also reported, using the phase transition of VO_2 layers, which transition from insulator to conductor above 62 °C [170].

Another approach to tune metamaterial properties is to change mechanically the dimensions of the resonant inclusions. Applications of this method to metamaterials can be found in lens design, using stretchable substrate [171] or MEMS [172].

Another area where dynamic metamaterials found interesting applications is in the ultrafast modulation of their properties. The ultrafast property comes from 'damaged' semiconductor (low temperature grown or ion implantation), where defects act as fast trapping centers [173]. More recently, ultrafast switching was also achieved using topological insulator [174].

4.2.2. Optical switching implementation on an LC resonator

In this part we will introduce the design that has been chosen for implementing the fast switching property for the 3D LC resonators previously discussed along with the materials choice. The inspiration of the approach used to implement the frequency switching can be traced back to the 2D SRR. By adding several loops or gap openings in a SRR, its resonance frequency can be changed. Applied to the 3D LC resonator, it can take one of the form presented in Fig. 4.11

For instance, a structure with two antennas would yield an equivalent circuit composed of one capacitor and two inductors in parallel. Assuming the two antennas are strictly identical with an inductance value L and by following the summation rule, the equivalent inductance is $L_{eq} = L/2$. It is equivalent to having a smaller antenna. In certain configurations, interesting properties like magnetic dipole cancellation can be implemented, yielding an electrically resonant split ring [163]. While being interesting, no switching properties can be added by modifying the inductance of the LC circuit.

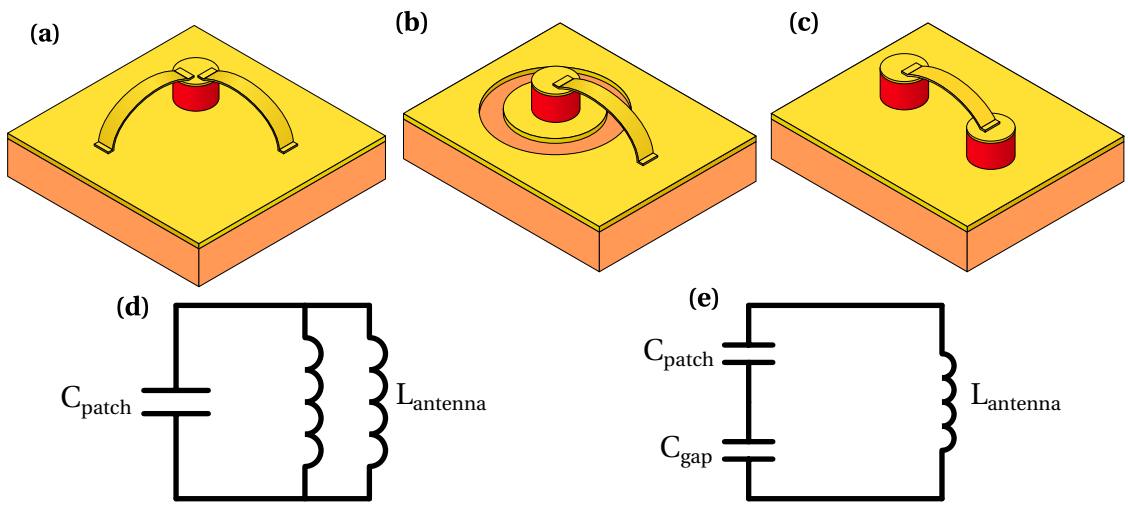

Figure 4.11.. **(a)**: Modified LC resonator with an additional inductance taking the form of another air bridge, and **(b)** the equivalent circuit of the two antenna resonator. Modified LC resonator with an additional capacitance created by **(c)** a ring shaped opening in the ground plane or **(d)** a second patch cavity. **(d)**: circuit of the two capacitor resonator.

Something similar can be achieved with the capacitive part, by introducing an additional electrical capacitance. For a 3D LC resonator, it can take the geometry presented in Fig. 4.11 (b) and (c). If a semiconductor material is used for the substrate material ((b), like [168]) or is used as the core material of one patch ((c) like [156, 157]), then optical switching is achievable.

Of the two presented configurations, the chosen geometry was the one presented Fig. 4.11 (c) for its compatibility with active region (see Section 4.4.1).

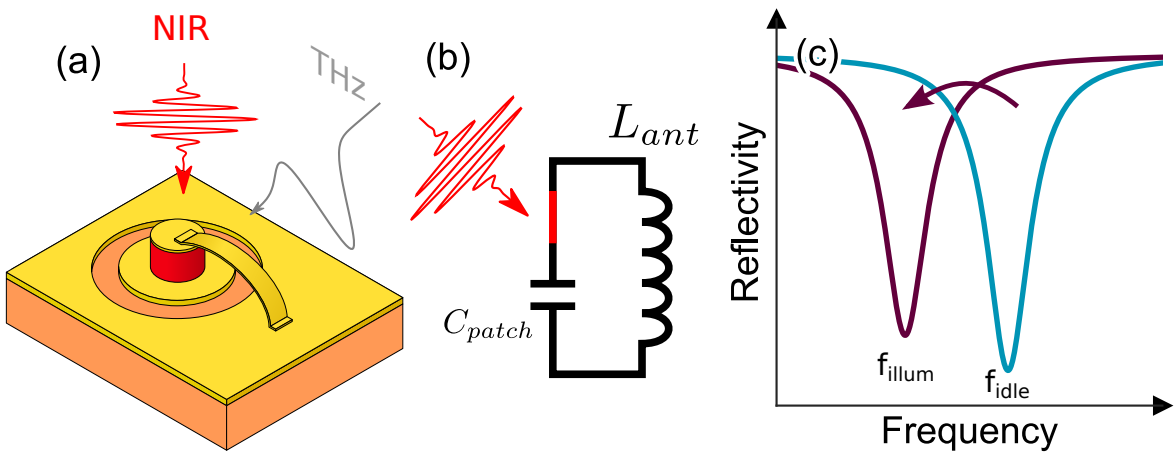

Figure 4.12.. **(a)**: experiment configuration. A NIR pulse generates carriers in the substrate while a THz pulse probe the optical response of the resonator. **(b)**: equivalent circuit of the resonator with the ring capacitance photoexcited. **(c)**: expected change of resonance frequency between the idle mode and the photoexcited mode.

The operating principle is similar to the one presented in Ref. [156, 157] and is detailed in Fig. 4.12. By using an optical pump, carriers are generated in the substrate under the gold plane, selectively shorting the capacitance created by the ring shaped opening, thus changing the total capacitance of the equivalent circuit (Fig. 4.12 (b)). As the resonance frequency depends on the total capacitance value, the LC mode frequency changes (Fig. 4.12 (c)).

4.2.2.1. Clean room fabrication of state-of-the-art LC resonators

Throughout this thesis, sample fabrications was done in three different cleanrooms: the old and new C2N research facility and in Paris 7 university. The fabrication steps are illustrated Fig. 4.13.

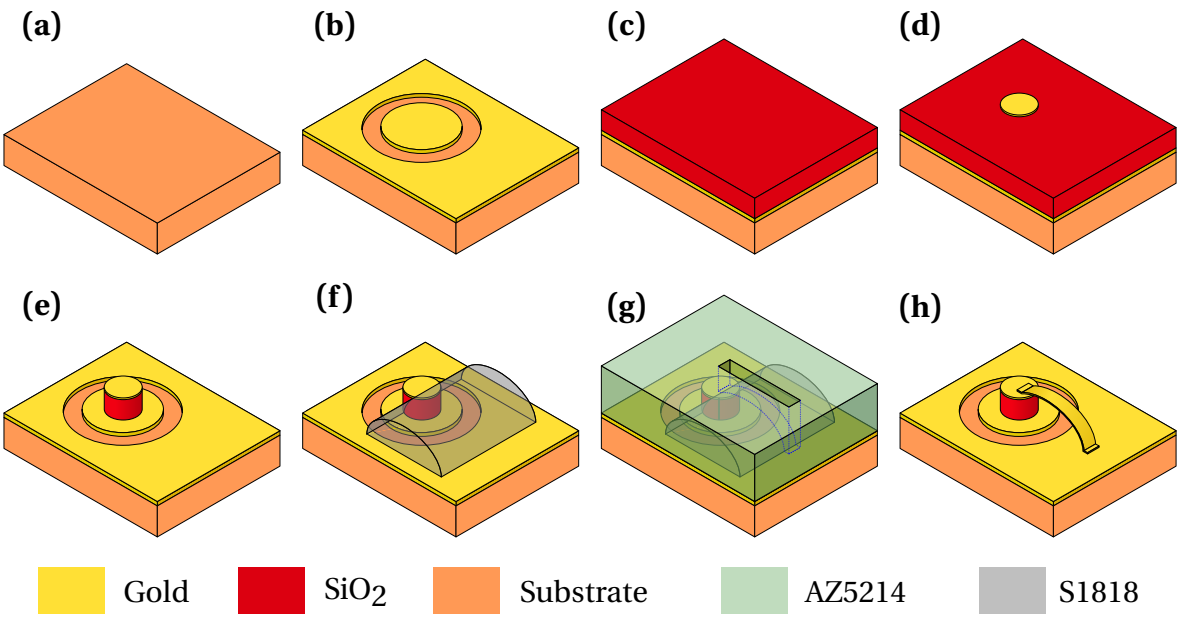

Figure 4.13.. Different steps of the fabrication of an SW cavity.

The starting point is a wafer of the switching material (in this thesis, Si and GaAs will be the switching material). The ground plane with the ring opening for the switchable capacitance is obtained using a lift-off of evaporated 10 nm/300 nm Titanium/Gold layers . The lithography was done using AZ5214E resist in reversal mode. Then, a SiO_2 layer is deposited by Plasma-enhanced chemical vapor deposition (PECVD) on the whole sample's surface. The thickness depends on the target resonance frequency. On this layer, another AZ5214E resist in reversal mode is used to fabricate the top metal of the patch capacitance. The evaporated metals are 10 nm/300 nm thick Titanium/Gold layers. Next, the capacitance is made by etching the SiO_2 layer with a Reactive Ion Etching (RIE) etching with a CHF_3 and SF_6 plasma. To protect the top metal, an S1818 positive resist layer is used to recover it. The final step is the antenna deposition. First, resist cuboids are fabricated using S1818 positive resist which partially recover the patch capacitance. Then, the resist is reflowed by doing baking sequence to give a rounded shape to the resist. Finally, a layer of AZ5214E photoresist used in reversal mode is patterned to expose the top metal, ground plane and the S1818 scaffolds. The antenna is obtained with an evaporation of 10 nm/300 nm thick Titanium/Gold layers. To strengthen the junctions between the scaffold and the antenna and ground plane, the evaporation is done at -30,0 and 30°.

A Scanning electron microscope (SEM) side view of a LC and a switch cavity (SW) is shown Fig. 4.14

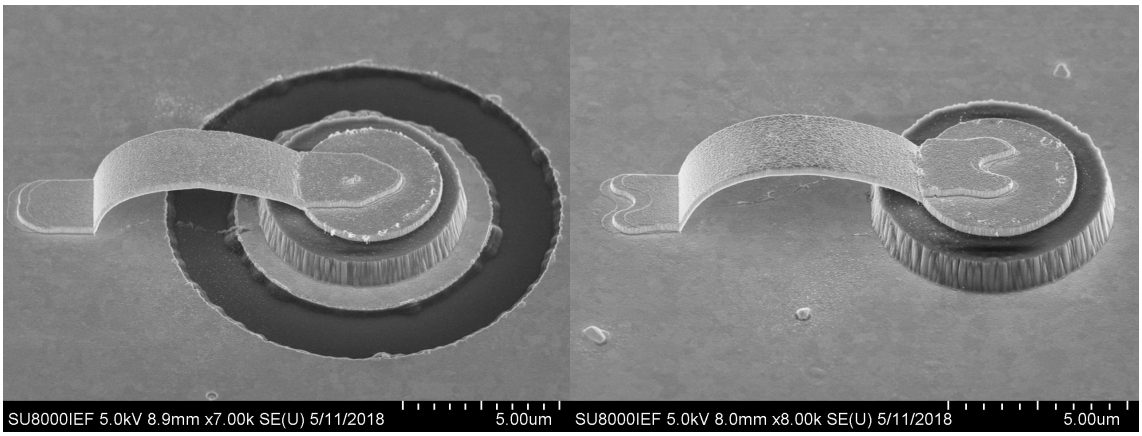

Figure 4.14.. SEM pictures of a fabricated switch (SW) and LC cavity.

4.2.2.2. Numerical simulation of the LC resonator device

In order to be predictive with the samples, an FEM model has been developed using COMSOL Multiphysics and its RF and electrostatic modules. The RF module is used to find the eigenfrequencies and simulate the reflectance and absorption of the resonators in the frequency domain, while the electrostatic module is used to calculate the capacitance of the patch and ring opening. This tool proved to be extremely useful considering that the LC switch cavity resonance frequency are not easily predictable as it will be shown later on.

The simulation space is composed of a single unit cell artificially repeated using Floquet boundary conditions. Materials were simulated using the permittivity defined in Section 1.3 and the switching is modeled by changing the conductivity of the substrate.

In order to assess what would be the frequency modulation between the idle and photo-excited LC cavity, the simulation was run at different conductivity value for the substrate. The substrate had a 10 S·m conductivity at rest while the photoexcited substrate was simulated with 10^6 S·m. With this conductivity value, there is no difference for the LC mode between the photo-excited SW cavity and the one capacitor LC cavity.

Quickly it appeared that the initial guess of the patch and ring shaped opening being equivalent to the two capacitors in series circuit was not accurate. In Fig. 4.15 are presented electrostatic simulation of the ring and patch capacitance, and the frequency difference between the idle and photo-excited modes for different patch radius with fixed antenna. In the case where C_{ring} and C_{patch} are equal, the frequency difference is expected to be non-zero. However, simulations reveals that this case corresponds to a situation where frequency difference between both modes $\Delta\nu$ is close to zero.

While the derivation of a model a lumped element model for the SW cavity would be of great theoretical interest, numerical simulations are predictive enough to the design and the development of the ultra-fast modulation property.

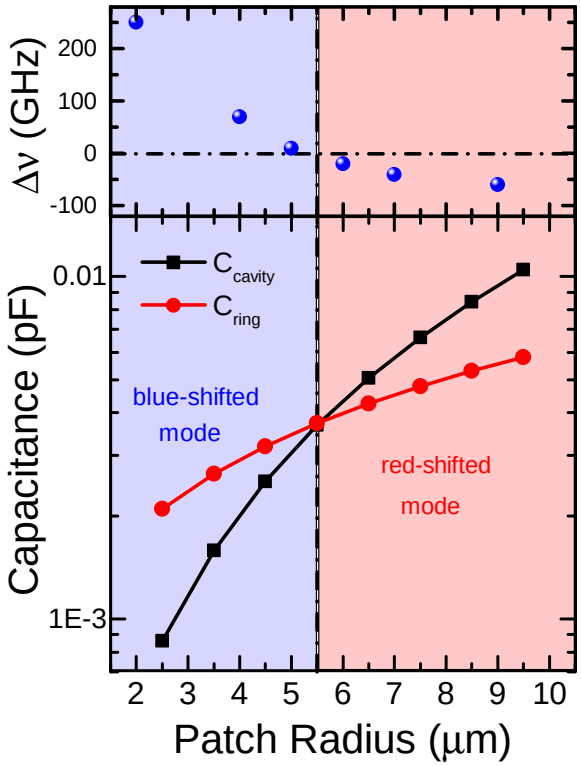

Figure 4.15.. Frequency difference $\Delta\nu$ between the idle and photoexcited modes depending on the patch radius.

4.3. Time domain characterization of the LC switch dynamic

The previous section was dedicated to the LC resonators functionalization with another capacitor made of a ring shape opening, revealing a semiconductor material. Up to now, no carrier generation was done with this material, the measurements were done on a switch and an LC structure in order to have an idea of what would be the results of switching experiments if the carrier generation inside the semiconductor was enough to reach a metal conductivity. Of course, it is clear that the photo excited semiconductor will not reach the same level of conductivity as the metal though it is still a good approximation of how the resonator behave under illumination. These measurements were done by our collaborators of the Institute of Electronic structures and laser in Greece.

4.3.1. Time domain spectrometer and the generation of THz pulses

Time Domain Spectroscopy is a measurement method widely used for characterizing dynamical systems, especially ultra-fast processes. The goal is to record the electric field and reconstruct the interferogram, the electric field amplitude versus time. Then a Fourier transform of this signal yields the corresponding spectrum. The setup can be divided into 2 parts: (i) THz generation and (ii) detection.

A complete schematic of the setup can be found in Fig. 4.16

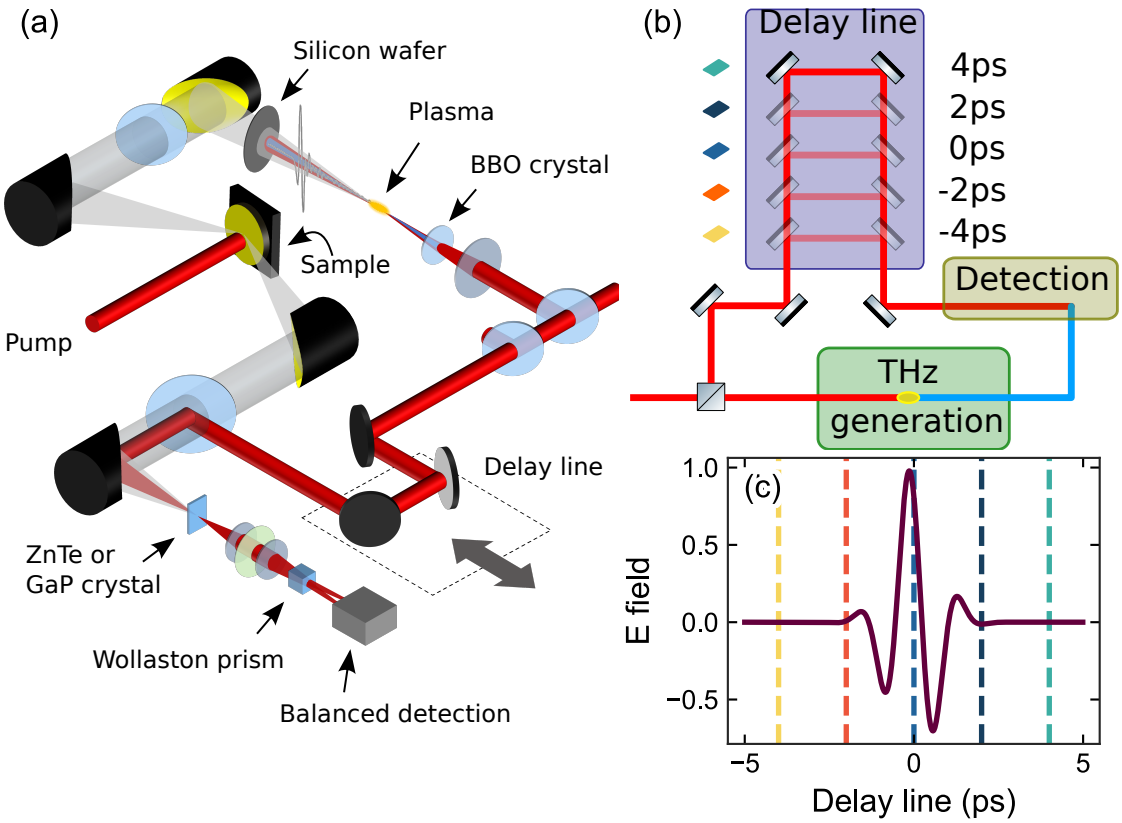

Figure 4.16.. **(a)**: schematic of the time-domain spectroscopy (TDS) setup. **(b)**: THz detection scheme with the delay line at 5 different positions. **(c)**: corresponding point on the THz E-field amplitude.

A walkthought of the setup can be found in Ref. [175].

4.3.1.1. THz pulses generation

In the THz time-domain spectroscopy (TDS) community, there are two major techniques to generate intense THz pulses. The first one relies on optical rectification using non-linear crystals, and allows the generation of high energy pulses with a narrow bandwidth [176, 177]. The other one, which is the one that is used by our collaborators in Greece, is based on two color filamentation [178, 179]. While providing a less intense pulse, the bandwidth of the resulting pulses exceeds 20 THz.

The operating principle of the two color filamentation scheme is based on the mixing of a laser pulse and its second harmonic in a gas, most of the time the ambient air, after tight focusing. A Ti-Sapphire laser produces an input pulse 80 fs wide with an energy of 2.3 mJ at 800 nm that is separated using a beam splitter. One part of this pulse will be used for the coherent detection and the sample pumping, while the other part (that will be used for the THz pulse generation) is focused using a lens. Between the focal spot and the lens, a BBO crystal is inserted and is used to generate a second harmonic pulse. At the focal point, the interaction of the two pulses creates a

plasma in which an electrical transient emits a THz pulse in the same direction as the two NIR pulses. The obtained THz pulse has a 20 THz bandwidth with an amplitude of approximately 200 kV·cm^{-1}. A Si wafer is then used to block the remaining NIR signal. The generated THz pulse is collimated using a parabolic mirror and focused on the sample at 45° angle.

4.3.1.2. Electric-field sampling of the THz pulses

Most of the time, it is interesting to measure the amplitude and phase of an optical signal. This permits, for instance, to employ THz spectroscopy to extract information like the conductivity of a material. In order to do that, coherent detection methods are necessary. Several techniques exist. Those that can be used with our measurement setup are the electro-optic (EO) sampling and the air biased coherent detection (ABCD) method.

The EO detection relies on the birefringence modulation of a crystal by the electric field or the optical beam to be detected. This index modulation is then probed by monitoring the polarization change of a NIR pulse. The two polarization orthogonal components are then separated using a Wollaston prism and are measured using a balanced detector, allowing to recover the amplitude and the phase of the THz pulse. This method is extremely sensitive, permitting to measure extremely weak THz waves. However, it is limited in terms of bandwidth because of the phonon resonances occurring in the crystals and the different group velocity dispersion of the THz and optical pulses. The bandwidth of the ZnTe and GaP crystals that were used are 2.8 THz and 8 THz, respectively.

The ABCD detection on the other hand, is based on third order non-linearity of a gas modulated by an electric field [180]. The interaction of the THz and optical pulses generates a second harmonic NIR pulse whose amplitude is proportional to the THz electric field amplitude. Then, the same balanced detection scheme using a Wollaston prism is used, providing a measurement of the phase and amplitude of the THz field. While the overall sensitivity and Signal to Noise (S/N) ratio of this method is lower than what the EO detection can achieve, the bandwidth is significantly greater approaching 30 THz.

With both of these methods, by varying the time delay of the NIR pulse with respect to the THz one, it is possible to reconstruct the time variation of the THz electric field. A Fourier transform of the recorded electric field yields the amplitude spectrum and the phase. Measuring both a sample and a gold reference, the reflectance of a sample can be assessed. The spectral resolution depends on the length of the time domain trace, but the internal reflections on the different optical components of the setup introduce echoes which limit the length, thus the resolution. With the EO detection method one solution is to make the crystal thicker, pushing the echoes further away in the time domain.

4.3.1.3. Pump-Probe experiments

The main advantage of the TDS measurements is that it is possible to synchronize the THz pulse with the optical source to impinge on the sample at the same time. The optical pulse acts as a pump, photoexciting the sample, while the THz pulse acts as a probe, measuring the change of the sample response in the THz range and probing the dynamics of our switching device.

4.3.2. First attempt of cavity photoswitching: the SOI based device

The effective modulation of the cavities relies on the ability of the material under the ground plane to change its conductivity under illumination. This is an inherent property of semiconductor materials. In order to have a better idea of the dynamics that can be expected from this carrier generation effect, the silicon on insulator (SOI) material alone was measured. Then the reflectivity of a SW cavity with and without illumination is performed in order to verify if the simulations match the experiment.

4.3.2.1. Semiconductor photo-excitation capabilities

The carrier generation in semiconductor materials is a well known effect, arising from the promotion of an electron from the valence to the conduction band when an electromagnetic wave of energy larger than the semiconductor energy gap hits the sample. In the case of SOI, the photoexcited material is silicon, which is an indirect band gap material with a band gap energy of 1.17 eV which corresponds to a wavelength of 1060 nm. Any wave with a wavelength lower than this value will be absorbed and generates an electron-hole pair.

To assess the switching capabilities of the SOI, the time amplitude of the THz electric field for different fluences of the optical pump, as well as the time amplitude of a plain gold mirror. After calculating the amplitude spectra $E(\omega)$ performing a Fourier transform of the time amplitude, the spectra were normalized by the gold spectra and the differential reflectivity $\Delta R/R$ was calculated using the formula:

$$\frac{\Delta R}{R} = \frac{R - R_0}{R_0} \tag{4.196}$$

where R_0 is the reflectivity of the SOI without pump. These results can be seen in Fig. 4.17 (a).

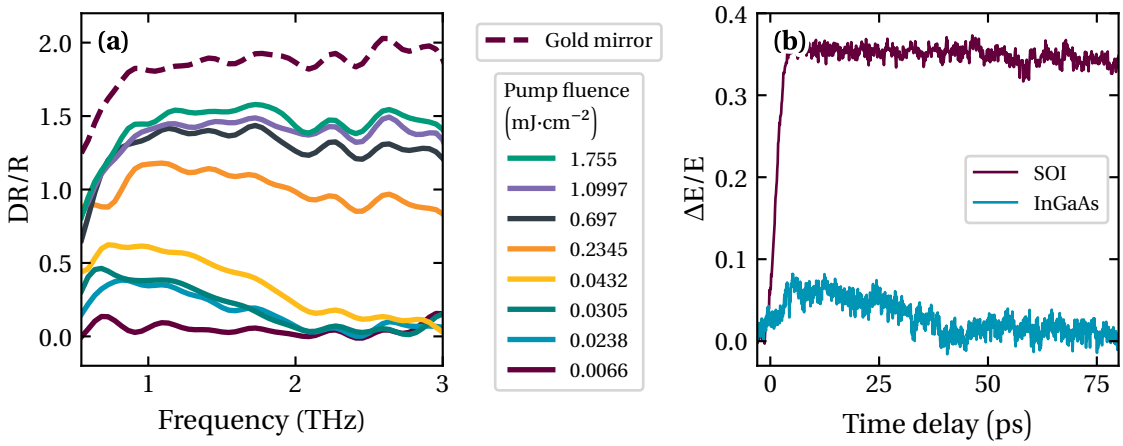

Figure 4.17.. **(a)**: differential reflectivity for several pump fluences and a gold mirror. **(b)**: Carriers dynamic within SOI and InGaAs as a function of the time delay.

The pump fluence ranged from 0.007 to 1.76 mJ·cm^{-2}. As expected, the relative reflectivity of the silicon layer increases with increasing fluence of the optical pump, meaning that the free carrier population grows and the conductivity increases. It can also be noted that around 0.7 mJ·cm^{-2}, a saturation of the reflectivity starts to occur: using a higher fluence does not increase the reflectivity. To assess how the photo-excited SOI behaves compared to a real metal, the $\Delta R/R$ of the gold mirror was also calculated. As expected, the photo-excited silicon layer does not reach the conductivity of a metallic mirror.

While the carrier generation in the material happens on a very short timescale, quickly it was noticed that the recovery of the initial state could not be observed with the TDS setup. The reason is that the lifetime of the photogenerated carriers is way longer than what can be obtained with the delay line. Fig. 4.17 (b) shows the THz electric field transient before and after the pump generating carrier in the sample. After 80 ps the electric field variation remains the same, while an InGaAs sample recovers the photo-excitation in less than 40 ps. The reason for the very long carrier's lifetime in these materials lies in the non-radiative recombination process. The most prominent mechanism at high carrier density is the Auger recombination: it is a 3-carrier process where an electron and a hole recombined, while the energy of the recombination is transferred to a third carrier without changing its energy band [36]. This third excited carrier will lose its energy via thermal vibration. Although the most important feature is the fast generation of carriers, having the ability to observe the recovery would yield valuable information on the dynamic behavior of the cavity modulation.

4.3.2.2. Ultrafast-Switching of the cavity under illumination

Despite a relatively slow recombination dynamics, the switching capability of the sample was measured the same way the SOI dynamic was tested, in order to have a better insight of what to expect with the carrier generation in the SOI material. In the past, similar cavity switching in the THz using silicon as switching material for 2D LC circuits has been reported [157].

The measurements of the samples with a 12 µm patch radius are presented in Fig. 4.18. To allow a direct comparison between bare material and resonator, the same fluences are used. It can be observed that the evolution of the SW cavity contrast follows closely the SOI response to the pump fluence. From 0 to 44 µJ·cm^{-2}, the mode fades progressively following the increase of the relative reflectivity of the substrate. Around 0.7 mJ·cm^{-2}, the mode completely vanishes and does not reappear with the increasing fluence. Just like the SOI measurements showed, the material seems to saturate and pumping harder does not increase the conductivity of the material leaving the SW in a state where the SOI is not an insulator nor a conductor. The result is a poor quality factor which broadens the LC mode so much that it becomes impossible to measure.

In order to find the conductivity that corresponds to the resonator response under the maximum of fluence, a FEM simulation where the photo-active Si layer conductivity is varied was run. The results of this simulation can be found in Fig. 4.18. We reproduced the experimental results with a material conductivity of $10 \cdot 10^5$ S·m. A conductivity value an order of magnitude larger is needed to obtain a clear and measurable photo-switched mode.

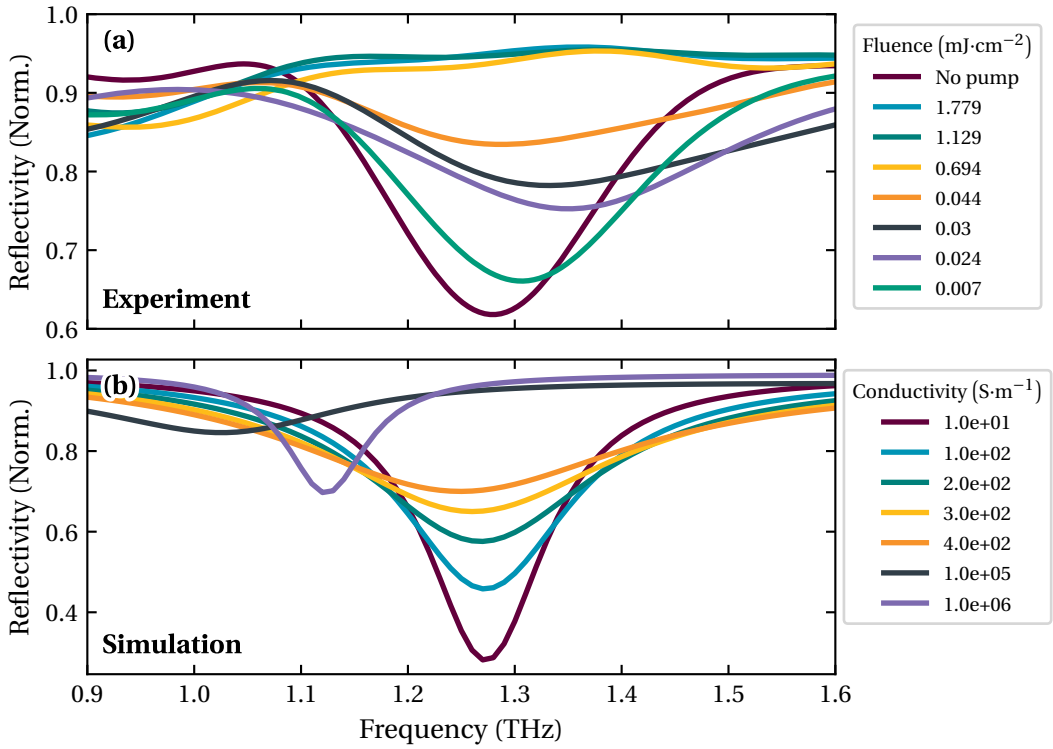

Figure 4.18.. **(a)**: reflectivity measurement of the SW on SOI sample in TDS with different pump fluences. **(b)**: reflectivity obtained from an finite element method simulation of the LC resonator with an increasing conductivity of the photo-active layer.

4.3.3. Toward sub-picosecond photoswitching dynamics

The conclusion we could establish on the SOI based devices is that the maximum conductivity achievable was not sufficient for observing the full mode switching. Furthermore, the recombination dynamics of the photocarriers is too slow for setup to be measured, due to the slow Auger recombination mechanism. In this part we will discuss the use of an alternative material known for its ultrafast dynamics: the low temperature grown Gallium Arsenide (LT-GaAs).

4.3.3.1. Addressing the dynamics hurdles using LT-GaAs

The maximum conductivity problem of the silicon mostly comes down to its absorbance: as the conduction band of the semiconductor is being filled, the semiconductor absorption decreases [181], thus setting a hard limit on the maximum conductivity through photoexcitation. The same effect is expected to happen using other semiconductor materials [182].

However, a change of material can be the solution to obtain the missing order of magnitude to observe the photo-switched mode. For a given carrier density, the conductivity depends on the electron mobility. Semi-insulating silicon has an electron mobility $\mu_e = 1206\,\mathrm{cm^2{\cdot}V^{-1}{\cdot}s^{-1}}$. One material, compatible with our cleanroom process, which has a higher electron mobility is GaAs, with a reported electron mobility $\mu_e = 5000\,\mathrm{cm^2{\cdot}V^{-1}{\cdot}s^{-1}}$. Transitioning to this material is expected

to reach the necessary conductivity. Compared to the silicon, GaAs exhibits a larger conductivity with the same pump fluence [183]. This is a clear advantage for our target application.

However on the time dynamics, no significant changes are expected. GaAs recombination of photo-excited carriers is the same as silicon, thus similar recombination dynamic of several hundred of picoseconds are expected [184]. Fortunately, there is a way to radically modify the recombination dynamics in the material, by performing the epitaxial growth at low temperature.

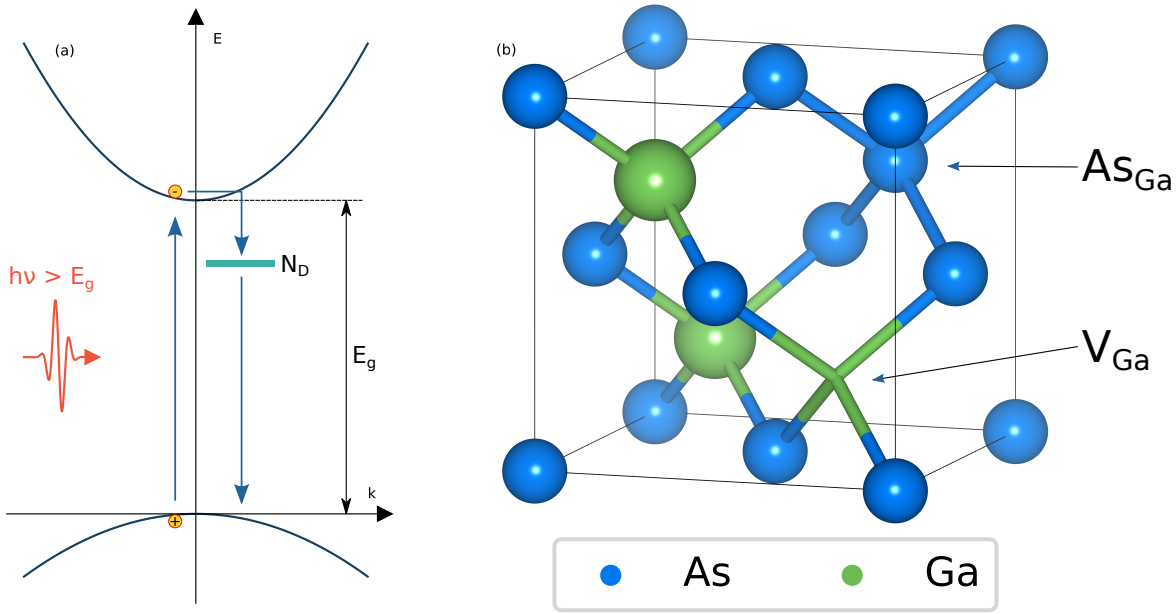

Figure 4.19.. (a): band structure of LT-GaAs. The point defects form an energy level lying between the conduction and valence band. **(b)**: crystal lattice of LT-GaAs.

If the GaAs growth is performed at a temperature below 400 °C under an excess of arsenic, atoms on the wafer surface will not have the necessary energy to migrate and form a perfect crystal structure. The result is a high concentration of point defects in the lattice, in particular ionized As_{Ga}^{+} antisites that act as fast trapping centers for the photoexcited carriers [185]. This very fast trapping mechanism is then followed by a slower recombination process between the shallow defect band and the valence band.

This slow recombination process is an important factor to take into account because it will limit the fast dynamics of the material at high pumping fluence. If more carriers than As_{Ga}^{+} antisites are photoexcited in the material, these trapping centers will be all filled in very quickly, but because of the slow electron-hole recombination to the valence band, the remaining carriers will stay in the conduction band longer thus slowing the whole dynamics. In order to keep the fast dynamics even at high fluence pumping, it is then interesting to have a high defect concentration, which is achievable by doing the epitaxial growth at lower temperature.

However, other physical properties degrade with an increasing number of defects. First, the carrier mobility decreases with an increasing number of antisites. The reason is that the imperfect crystal lattice increases the electron scattering. The second degradation is the decrease of the resistivity.

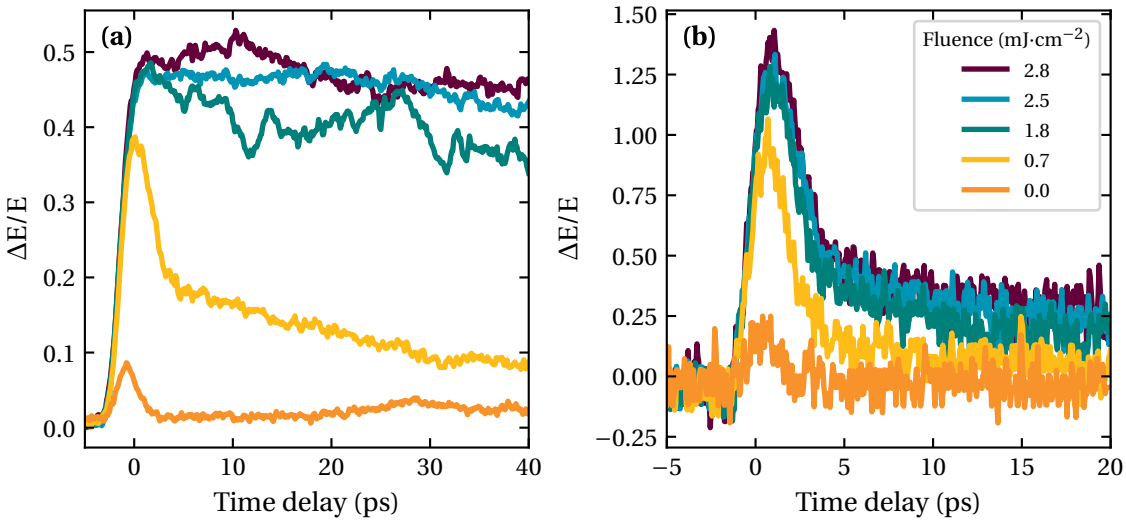

Figure 4.20.. Relative reflectivity measurements for various pump fluences of **(a)** annealed LT-GaAs and **(b)** as grown LT-GaAs

The reason is that electrons can move through hopping between the trapped states, providing an additional conduction channel [186].

To circumvent this, it is a common practice to reduce the amount of antisites with an annealing. The provided energy allows the arsenic antisites to migrate and form As clusters, reducing drastically their numbers thus decreasing the probability of electron hopping from one to another [186]. Of course this reduction means the carrier lifetime increases but at the same time the mobility improves thanks to a cleaner crystal structure. In the application to the fast cavity switching, the trade-off went in favor of the faster carrier dynamic.

Fig. 4.20 shows the comparison between the LT-GaAs annealed and as grown for different pump fluences. In this graph, the importance of the point defect concentration appears clearly: while the as grown LT-GaAs keeps a fast recombination, the annealed sample starts to saturate after the fast trapping mechanism. At high fluence, its dynamics becomes very similar to the SOI one. For this reason, we chose the as grown LT-GaAs as the switching material within our device.

4.3.3.2. The importance of the setup configuration for the ultrafast dynamics measurements

Using the same process described in Section 4.2.2.1 for the LC resonators on SOI, a sample using as grown LT-GaAs was fabricated. While the LT-GaAs provided a huge improvement on the dynamics side, the measured numbers were still far from the values reported in the literature reported (around 0.4 ps) [187]. However, early measurements of the cavity switching showed that the photoexcited mode starts to become visible, thanks to the better conductivity the GaAs offers under illumination.

Fig. 4.21 shows the SW cavity with and without the illumination and the LC cavity. Compared to the SOI based sample, the new LT−GaAs sample shows improvements: instead of just observing the

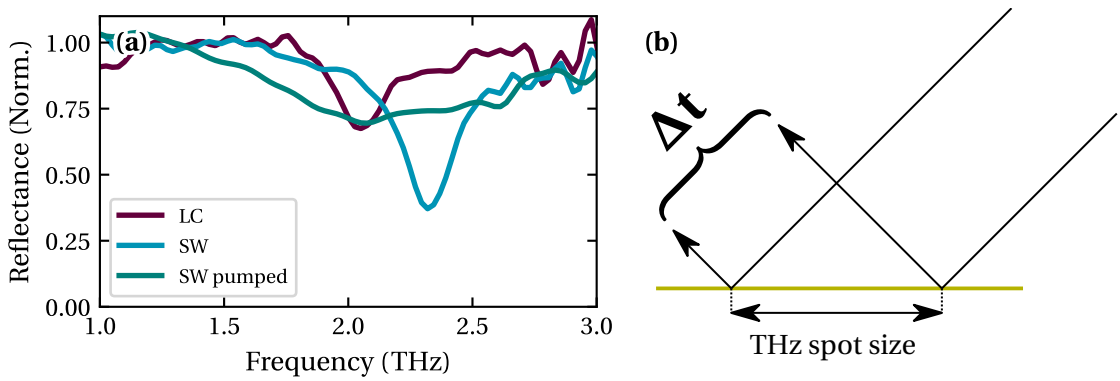

Figure 4.21.. (a): LC and SW cavity with and without photocarriers excitation with a non-collinear pump and probe. **(b)**: schematic of the time difference between the two ends of the THz pulse. The sample is not probed at the same time everywhere.

SW mode disappearing, a new mode aligned with the LC mode is measured. While this behavior is an improvement compared to what was achieved before, several hints pointed toward the fact that something was not being correctly done.

First, measurements of our LT-GaAs showed a very different behavior than what was reported in the literature. Many papers report sub-ps dynamics while our measurements always show a longer generation-recombination cycle. Then the shape of the photo excited mode is quite peculiar. The exact position of the LC mode can be distinguished in the broad photo excited mode, almost as if what was actually measured was an integrated value of the THz probe not at a single time delay, but in a Δt range.

In fact, it is directly related to the experimental configuration. In the current setup, the pump signal is shined on the sample at normal incidence while the probe is at 45°. Despite the fact that the probe spatially overlaps the pump, which ensures that the probed area of the sample is pumped, the non-collinearity of the two signals prevents a temporal overlap. Fig. 4.21 (b) represents the time delay between the two ends of the THz beam after the reflection of the sample surface. For a 1 mm wide spot, the time difference is around 4.7 ps, which compared to the expected sub-ps LT-GaAs dynamic, means that the THz probe interacts with a sample experiencing a full carrier generation and recombination cycle. In this configuration, the TDS measurement is the integrated optical response of a sample during the mode switching. In order to circumvent this problem the solution is to have collinear pump and probe. The TDS setup was adapted accordingly.

Another point introducing uncertainty on the dynamical measurement is the detector used for the balanced detection. As introduced in Section 4.3.1.2, two detection schemes were used in this thesis. Up to now, only the ZnTe EO detection was used because of its higher sensitivity, which was deemed important due to how hard the measurements of the switched mode was. The downside of the EO detection, compared to the ABCD detection is the bandwidth, of around 30 THz for this setup, compared to the 2.8 THz the ZnTe crystal can provide.

Fig. 4.22 (a) and (b) illustrate the difference of detection for the same THz pulse and pump energy on the bare LT-GaAs dynamic measurement with the two detection methods at a 45° angle. Especially the relative reflectivity clearly demonstrates the improved time dynamics offered by the ABCD detection over the ZnTe EO detection. While an exponential fit of the ZnTe measurement yields

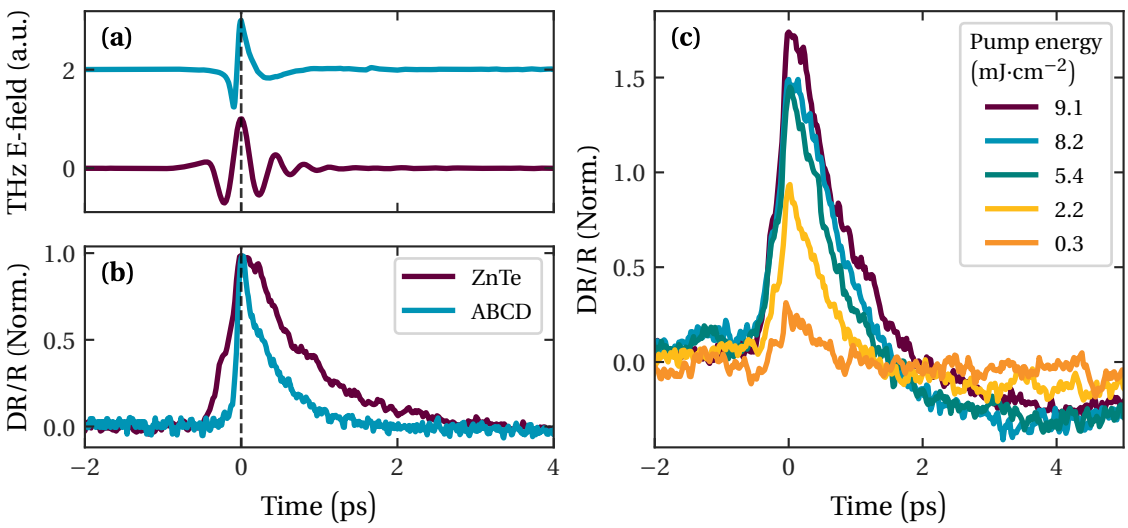

Figure 4.22.. **(a)** THz transient comparison and **(b)** relative difference of electric field amplitude between the EO detection with the ZnTe crystal and the ABCD detection. **(c)**: time dynamics of as grown LT-GaAs using the ABCD detection and a collinear pump-probe.

a 0.81 ps time constant, the ABCD measurement returns a 0.45 ps time constant, close to what the literature reports on as-grown LT-GaAs [187]. The important point to keep in mind with this detector comparison is that the probed physical phenomena in these experiments are convoluted with the detector dynamics. While the ABCD detection provided a faster time dynamics, it is possible that the real recombination time is even faster.

4.3.3.3. Observation of the full switching dynamics

Now that the TDS setup is able to correctly capture the dynamics of the cavity switching, it is possible to reliably measure the transition between the two LC modes. The results are presented in Fig. 4.23 (a). The change of alignment of the pump and probe did not modify the results on the LC and SW mode, but it was of great importance for the photo excited mode. A well-defined absorption is now measured around 2.07 THz, detuned by 20 GHz with respect to the target LC mode at 2.09 THz. While the width of the two modes are comparable, the contrast of the pumped mode does not reach the contrast of the LC mode.

To gather a deeper insight of the evolution of the SW optical response during the switching process, a two-dimensional (2D) dynamic measurement was performed. While the previous measurements were done with the pump pulse synchronized with the probe to interact with the sample at the same time, the 2D map shows the optical response at different time delays between the pump and the probe. This is particularly interesting because it allows observing how the resonator behaves during the recombination of the carriers.

Fig. 4.23 (b) depicts the results of this experiment. Before the arrival of the pump signal, the idle SW mode is visible at 2.35 THz. It is followed by a 200 fs transition which ends up on the

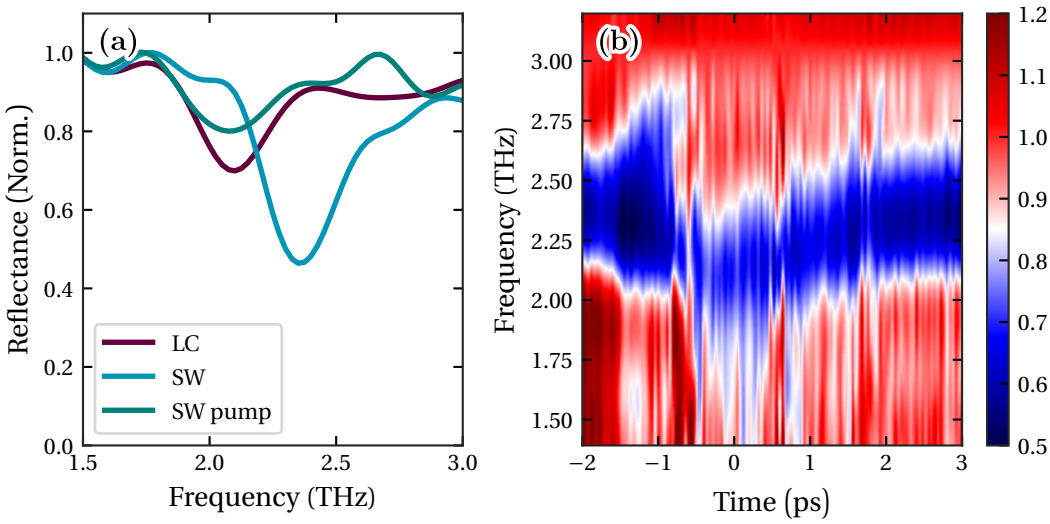

Figure 4.23.. (a): SW cavity with and without photoexcitation compared to the equivalent LC cavity. **(b)**: Color plot of the 2D map of the reflectivity depending on the time delay.

photoactivated mode 2.07 THz. This mode is sustained for a duration of 1.2 ps, and finally recovers in approximately 800 fs.

A few interesting observations can be made on this 2D measurement. First, the transition between the two eigenfrequencies of the SW cavity is achieved in 200 fs, which is the value measured by the ABCD detection scheme (and probably less than that, as the measurement is convoluted with the detector response time, see Section 4.3.3.2). Ref. [51] predicts that the mode switching must be done on a timescale smaller than the oscillation period of the lower polaritonic mode in order to trigger the emission of the virtual photon of the ground state population. If one considers a cavity using the 4PQWs active region which was characterized in the strong-coupling regime in Section 3.5.2, with a lower polaritonic mode at 1.9 THz, its oscillation period is 526 fs. The sample has a time dynamics compatible with the non-adiabatic emission of photons.

The second observation is the recovery time toward the idle SW mode. Despite the measured 450 fs for the bare sample LT-GaAs recombination dynamic, the photoexcited mode remains active for 1.2 ps, and takes a further 800 ps to go back toward the idle SW resonance frequency. A probable explanation can be found in Ref. [188]. The LT-GaAs layer used for this sample is 2 µm thick, grown on a GaAs substrate and while only a small fraction of the incoming pump reaches the GaAs substrate (around 7 %), it is enough to generate carriers in the material, creating a carrier reservoir. This reservoir has a much longer recombination time (around 1 ns) and can provide the LT-GaAs with electrons even after the theoretical recombination time, keeping the photo-activated mode alive.

4.4. PQW LC cavity

The switching demonstration on a short timescale was the first step toward the study of non-adiabatic switching, where the devices would operate in the strong coupling regime. Hence, the

patch material has to be replaced with an active region to observe the time formation of polaritons.

4.4.1. Backside illumination geometry

In this first part the limitation of the current system is described, and a solution is presented.

4.4.1.1. Front side illumination issue with GaAs substrate and cavity material

Until now, the patch material was made of SiO_2 for two reasons: first it is a well known material in the semiconductor world and its processing is highly compatible with gold and GaAs material. Second, earlier attempts to develop LC photoswitchable cavities using GaAs patch and substrate highlighted a real incompatibility with a front side illumination. In this configuration carriers are excited in both patch and substrate, shorting the equivalent capacitance of the LC resonator, which leads to an undetectable photo-activated mode. Fig. 4.24 shows optical switching on such an LC resonator. The contrast of the LC mode decreases with the pump fluence. To confirm that the loss of the LC mode is not due to a poorly photo activated substrate, similar to the SOI based devices presented Section 4.3.2.2, the TM_{01} was also measured. This mode is unrelated to the LC mode, and depends only on the patch. Similarly, the mode contrast follows the same behavior as the LC mode, which is consistent with the generation of carriers in the patch.

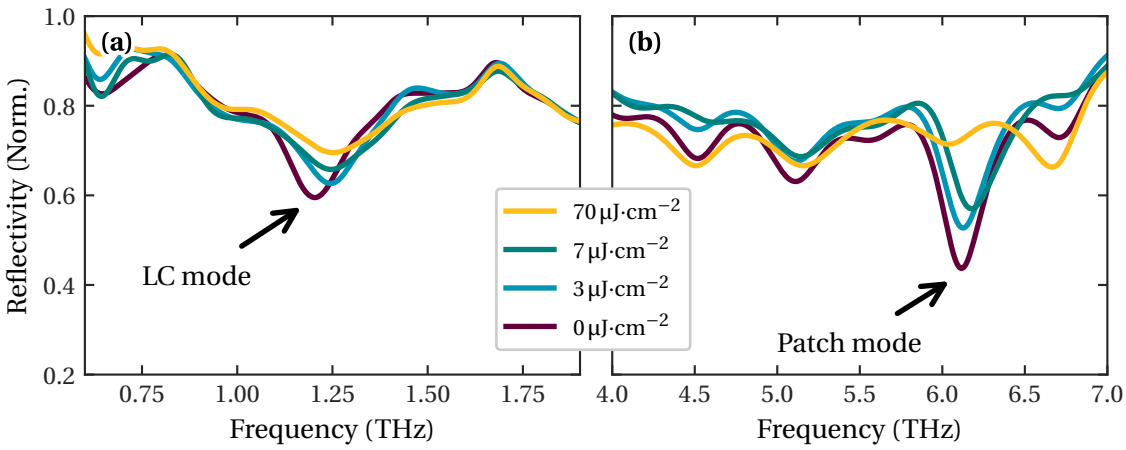

Figure 4.24.. Measured TDS reflectivity on an LC resonator using GaAs for the patch capacitance and the substrate. The LC mode as well as the TM_{01} mode are bleached which point toward the generation of carriers in the GaAs gap in the ground plane and in the GaAs patch. From [163].

To circumvent this problem and recover the possibility to observe a photo excited mode while keeping the GaAs based substrate and active region, the only solution is to change from which side the pump impinges on the sample. The next section will be devoted to the development of a sample compatible with a backside illumination.

4.4.1.2. LT-GaAs on Sapphire: dynamics measurements

Obviously the backside illumination needs a substrate material that is transparent at the pump wavelength, and compatible with a bonding method for keeping the LT-GaAs on top of it. The retained solution was a sapphire substrate which is transparent in the NIR, compatible with sample cooling and inert to most of the clean room processes used to fabricate samples.

Before moving further in the sample fabrication, dynamics measurement of LT-GaAs on sapphire were performed to find to what extent the backside pumping affects the carrier generation. Just like the resonator on LT-GaAs, the starting point is an epitaxial layer of LT-GaAs grown on a GaAs substrate. A piece of this material is bonded on a 650 µm thick sapphire substrate with benzocyclobutene (BCB). BCB is a widely used material for bonding in the semiconductor industry for its process compatibility as well as its great transmission in the visible frequency range of the electromagnetic spectrum. Finally, the GaAs substrate is removed using mechanical lapping followed by a chemical etching. In order to provide a deeper insight of the pumping from the backside, the epi layer which was 2 µm thick was divided into four regions of different thicknesses: 2 µm, 1 µm, 600 nm and 300 nm.

To carry out this experiment, the TDS setup was adapted to allow the illumination from the backside with a 0° incidence angle. Despite the fact that the 0° is not the best configuration for the dynamic measurements as it was highlighted in Section 4.3.3.2, the backside sapphire makes the exact angle hard to control due to the Snell's law.

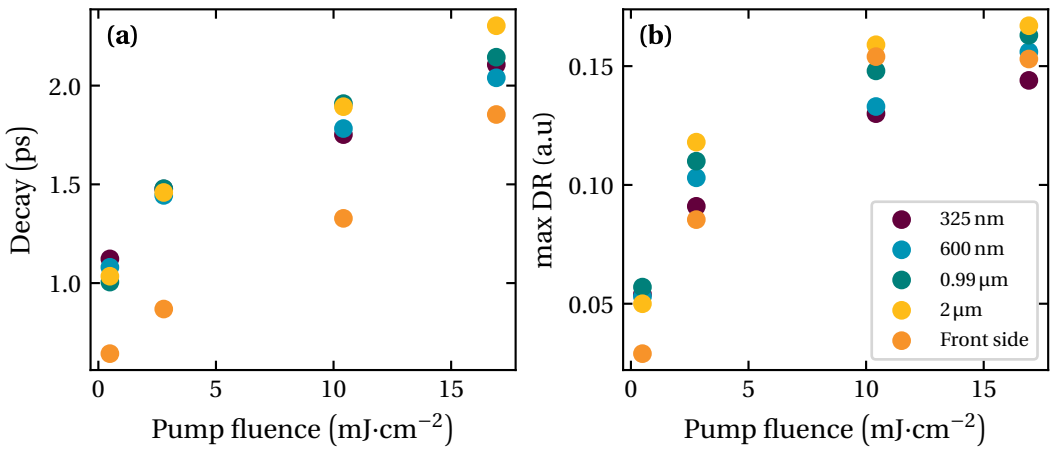

Figure 4.25.. Comparison between front side illumination and backside illumination at different fluences of **(a)** the recombination time and **(b)** the maximum variation of reflectivity.

Fig. 4.25 shows the changes that the backside illumination of the LT−GaAs, through the sapphire, induces on the time dynamics and the maximum amount of carriers. The first clear difference is the time dynamics of the backside illumination compared to the front side illumination. The first guess to explain this difference would be the pump pulse stretching due to the sapphire medium. The pulse length after passing the sapphire slab can be calculated using the following formula [189]:

$$\tau(L) = \tau_0 \sqrt{1 + \left(\frac{4\ln(2)\Psi L}{\tau_0^2}\right)^2} \tag{4.197}$$

where τ_0 is the pulse duration in the free space, L the thickness of material to go through and Ψ the group velocity dispersion (GVD), the pulse time barely change after going through the sapphire material. For a 650 µm thick sapphire it corresponds to an increase of 0.13 fs, which is too small to explain the 350 fs difference within the time dynamic. We are still investigating to find the reason of this increase of the decay time.

However, the comparison of the differential reflectivity between the different thickness with backside illumination and the front side illumination shows similar changes of reflectivity for every pump fluences. It confirms that despite the slower dynamics, the same level of switching is obtained with a backside illumination. A sample fabricated on LT-GaAs on sapphire should offer the same capabilities that has been demonstrated in Section 4.3.3.3.

4.4.2. LC strong coupling measurements with PQWs

In the first subsection, the fabrication process will be discussed, followed by the static measurements performed in the FTIR system.

4.4.2.1. Fabrication of the LC resonators on LT-GaAs and on sapphire substrate

Until now, the fabrication of the resonators was quite straightforward: beside the air bridge, no process step was really critical. The different material layers were either evaporated or deposited, using E-Beam evaporation and PECVD. Now that a real active region material is used, a thermo-compression wafer bonding [190] is necessary which makes the gold patterning of the ring shaped opening less straightforward. Etching is now necessary in order to carve the gold plane and form the necessary ring opening. The different steps of the LC resonator processing are depicted in Fig. 4.26.

The starting point of the fabrication is the gold-gold waferbonding of the active region wafer and the LT−GaAs wafer. Traditionally, 300 nm layers or more of gold are evaporated on both wafers to provide enough material for heat dissipation in laser applications, but would complicate the etching step in the present approach. For this reason, and to stay in the same range of gold thickness used before, a 125 nm gold layer was evaporated on both wafers.

To expose the LT-GaAs layer, a substrate removal is performed on the LT-GaAs side, followed by a BCB bonding of the exposed layer to the sapphire slab. Then another GaAs substrate removal is done, to expose the 4PQW active region surface.

The patch cavity is implemented using a gold evaporation followed by inductively coupled plasma – reactive ion etching (ICP-RIE) etching with the metal as a hardmask using a soft etching recipe to avoid metal sputtering. The ring openings are made thanks to an optical lithography and an ion beam etching (IBE). The resist removal was done using resist remover solution assisted by an ultrasonic bath to break the gold fences created on the resist walls by the gold redeposition.

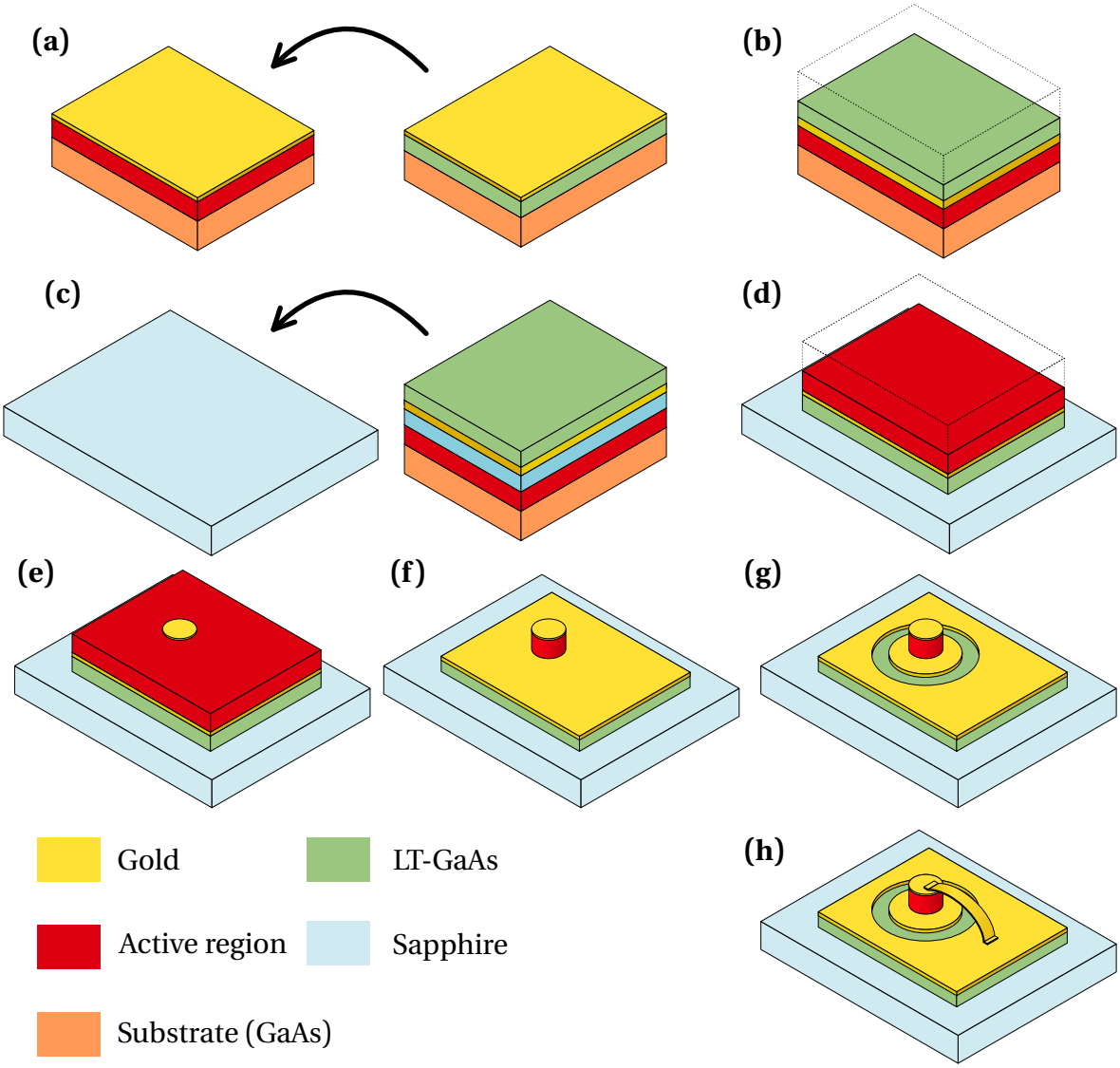

Figure 4.26.. **(a)**: thermocompression waferbonding of the LT-GaAs and 4PQW active region wafers. **(b)**: substrate removal on the LT-GaAs side. **(c)**: BCB bonding of the exposed LT-GaAs layer on a sapphire slab. **(d)**: substrate removal on the 4PQW active region side. **(e)**: metal evaporation of the top patch of the capacitance. **(f)**: inductively coupled plasma – reactive ion etching (ICP-RIE) etching of the active region. **(g)**: ion beam etching (IBE) etching of the ground metal layer to define the ring capacitance. **(h)**: antenna fabrication.

Finally, the same air bridge fabrication technique presented Section 4.2.2.1 was used for fabricating the antenna. In order to improve the electromagnetic overlap with the active region, the width of the antenna was reduced, down to 1.5 µm reaching the optical aligner resolution limit for such a thick resist.

Fig. 4.27 shows SEM images of the fabricated samples.

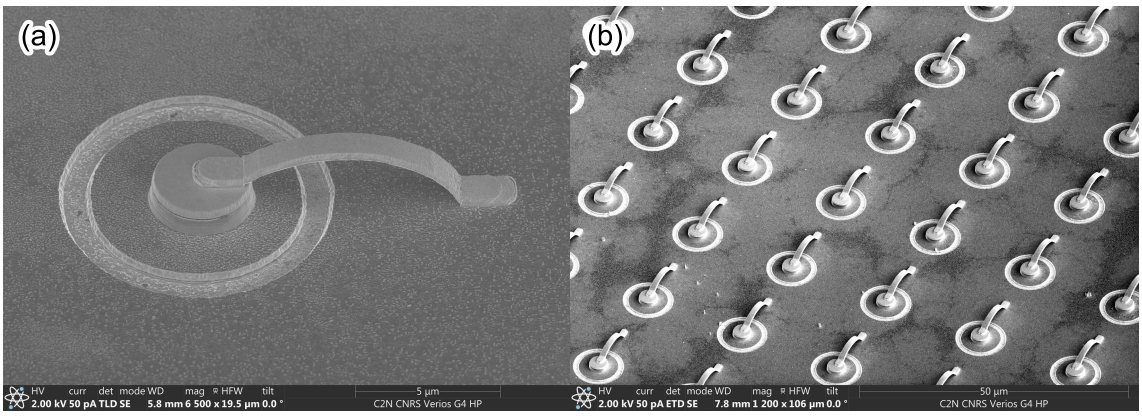

Figure 4.27.. **(a)**: global view of the 4 PQW sample. **(b)**: close view of one resonator. Despite the use of IBE for the gold plane opening, the edges quality is comparable to what the gold lift-off provided.

4.4.2.2. Static FTIR measurements

Contrary to previous FTIR measurements of the LC resonators, that could be done under vacuum with the grazing angle unit, this new sample needs to be measured at low temperature to assess its performance. Due to its configuration, a cryostat is not compatible with this setup, so another unit had to be used. This unit allows to do the measurements at a fixed 15° angle. This raised two problems: First 15° is not the best angle for the measurements as shown in Section 4.1.4.2. Also, in such configuration, it is not possible to vacuum the FTIR sample compartment. Dry air purging was used, which has impacted the quality of the measurement.

The experiments were done from 4 K to 300 K, using the SiC globar source and a helium cooled Si-Bolometer detector under dry air atmosphere. The results are presented in Fig. 4.28

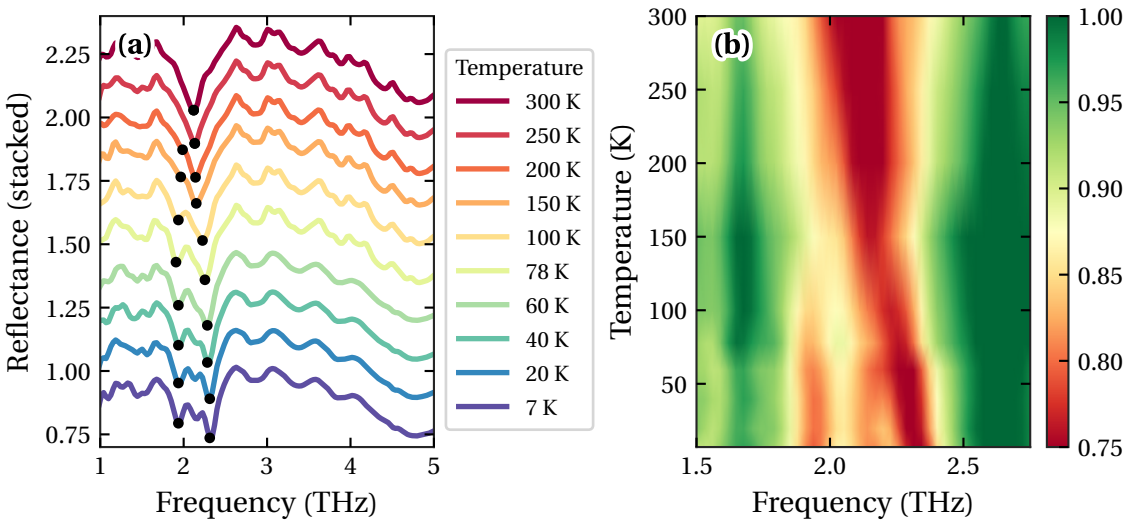

Figure 4.28.. **(a)** stacked reflectivity and **(b)** color plot of the 4PQW SW cavity sample reflectivity measurements from 4 K to room temperature.

The reflectivity measurements show that the strong light-matter coupling regime is achieved at temperatures as high as 100 K. The minimum splitting, Ω_{Rabi}, is measured at 0.35 THz up to 78 K. The onset becomes impossible to measure above 100 K, while it was still possible to observe it at this temperature with the MIM non-dispersive cavity (see Section 3.5.2).

The reflectivity measurements show a strong coupling of a splitting higher than $\Omega_R = 0.35$ THz up to 78 K. The onset becomes impossible to measure above 100 K, while it was still possible to observe it at this temperature with the MIM non-dispersive cavity. It is probable that a measurement at 45° would have provided similar results in terms of contrast, with observable strong coupling at 150 K. Nevertheless, these measurements are encouraging and open the perspective of nitrogen cooled measurements instead of helium cooled.

The sample is currently in Greece at our collaborators' laboratory for TDS measurements and dynamic switching.

4.5. Conclusions and perspectives

The development of an LC resonator showing sub-picosecond modulation capability proved to be a challenge, especially in terms of design. The first real challenge was the optimization of the contrast versus switch splitting of the SW cavity. Different configurations like the two antenna design could lead to improvements. An attempt was made to measure an SW cavity with the opening deported around the antenna's feet. Despite the excellent performance simulations showed with a near 1 THz splitting, the fabricated sample exhibited no LC mode. Due to a lack of time, no further investigations were conducted, even though there could be a great geometry to exploit.

Optimization of the switching performances can also be done using another material. Several materials were not considered in this work, but could be potential candidates. LT-InGaAs for instance has similar carrier lifetime and would bring flexibility in terms of design thanks to its different permittivity and smaller energy gap. Also, doped ErAs nano-island InGaAs and GaAs proved to be interesting materials as they retain the ultrafast carrier dynamics while increasing the electron mobility [191, 192]. Self induced switching using InSb could also be an interesting way to produce a fast switching of the cavity, using the probe to pump carriers within side valleys of the conduction band [193].

The measurements were also the point where a lot of work had to be done, and these results would not have been obtained without the tenacity of our collaborators of IESL/FORTH. When measuring extremely fast phenomena with a high spectral or time resolution, a great amount of optimizations must be done and the impact of the non-collinear pump-probe shows how an apparently insignificant detail leads to the impossibility of obtaining results.

Chapter 5

Conclusions

My thesis work was devoted to the development of crucial building-blocks towards the implementation of MIR and THz polaritonic emitting devices, i.e. semiconductor-based emitters that operated in the strong light-matter coupling regime. I studied and elucidated several fundamental aspects that currently constitute bottlenecks towards the development of such devices.

After a global introduction in **chapter 1**, in **chapter 2**, the emphasis was set on the MIR frequency range and the study and development of polaritonic emitters that rely on the mechanism of phonon-polariton scattering. While the concept was demonstrated by the team in 2018, the lasing threshold was still out of range. To lower the pump threshold to more realistic values, I explored two strategies.

The first one aims at increasing the phonon-polariton scattering rate by the use of non-dispersive cavities, that permit an engineering of the density of states of the system. I was able develop polaritonic emitters relying on phonon-polariton scattering in these resonators. I demonstrated similar results to the ones achieved with dispersive cavities, but I did not get a major increase in the phonon-polariton scattering rate. The reason, that I could elucidate, is that in this geometry it is necessary to induce a polariton population in the final state. This result motivated the development, that is currently ongoing, of a pump-probe measurement setup to fully take advantage of this architecture.

The second strategy that I explored is to radically increase the Q-factor of the cavity used for mid-IR polaritonics, as this would yield an important improvement of the polariton lifetime. My activity was theoretical: I numerically designed and studied high Q-factor cavities, inspired by what is employed by the photonic crystal community at shorter visible/near-infrared wavelengths. My initial results suggest that this improvement could be what it is necessary to reach the lasing threshold of a prospective ISB polariton lasers.

In the rest of the thesis I moved my attention to devices operating in the THz range of the electromagnetic spectrum.

Chapter 3 focused on the development of a new method to grow parabolic quantum wells in the THz range, in collaboration with colleagues of Waterloo university, Canada. In a series of

iterations this method was optimized up to the point where high quality THz ISB transitions were demonstrated up to 150 K, well above the current state of art of standard square quantum wells, that operate at much lower temperatures and with larger linewidths. A more exotic structure was also explored, namely half parabolic quantum wells.

Chapter 4 was devoted to the development and study of cavities suitable for the exploration of the dynamical Casimir effect in the THz range. This effort was made in collaboration with the IESL/FORTH research facility in Greece. Based on the 3D LC resonator concept, developed by a former PhD student of our team, I designed a system capable of modulating its optical resonance frequency (in essence, its optical density of states) on a sub-picosecond timescale, taking advantage of the fast carrier dynamics of LT-GaAs. Then, a sample embedding a PQW active region was fabricated. This sample has been characterized with our FTIR setup and the strong-coupling regime was measured.

In summary, in Chapter 3 and Chapter 4 I developed two crucial building blocks for the observation of the dynamic Casimir effect in the THz range: an active region that provides efficient optical dipoles up to high temperature in the THz, and a cavity whose optical density of states can be modulated on ultra-fast timescales. To observe the time dynamics of the strong-coupling regime modulation, the first step towards dynamic Casimir, the sample was sent to our collaborators, and it is currently being measured in time domain.

From the different exploratory works I studied, several exciting perspectives can be envisioned.

While being currently demonstrated for GaAs/AlGaAs material systems, the growth method outlined in **chapter 3** is general and thus can be in theory applied to other materials. An exciting prospect is the application of this method to the development of MIR PQW. If a similar linewidth improvement could be translated to MIR, it would be a great leap forward for the development polariton lasers.

On the polariton laser side, the two strategies I explored to reduce the lasing threshold are now to be further developed. While the use of photonic crystal cavities will require additional important technological developments, in particulas as far as the cleanroom fabrication is concerned, real improvements are expected as the achievable Q-factors are ten times higher than the current state of art.

Finally on the dynamical Casimir effect study, it is probably optimistic to expect Casimir photons from the first real sample I could design, fabricate and pre-test. However, the crucial building blocks are in place, and it is now a matter of optimizing the design. This will have to be done iteratively with the ultra-fast pump/probe measurements.

Appendix

A

Active region growthsheets

A.1. L1006 Interdigitated PQWs

Table A.1:

Comment	Repeats	Material	Thickness (Å)	Doping
Substrate		GaAs (SI)		
Buffer		GaAs cavity	2500	
Etch stop		AlGaAs: 50%	5000	
Cavity filler		GaAs cavity	500	
Barrier	11	AlGaAs: 15%	29.5	
Well	...	GaAs	1.5	
Barrier	...	AlGaAs: 15%	25	
Well	...	GaAs	5	
Barrier	...	AlGaAs: 15%	20.4	
Well	...	GaAs	9.6	
Barrier	...	AlGaAs: 15%	16.7	
Well	...	GaAs	13.3	
Barrier	...	AlGaAs: 15%	13.4	
Well	...	GaAs	16.6	
Barrier	...	AlGaAs: 15%	10.4	
Well	...	GaAs	17.6	
Dop. Well	...	GaAs	2	$4.0e17cm^{-3}$

Continued on next page

Table A.1: (Continued)

Barrier	...	AlGaAs: 15%	7.8	
Well	...	GaAs	17.2	
Dop. Well	...	GaAs	5	$4.0e17cm^{-3}$
Barrier	...	AlGaAs: 15%	3.7	
Well	...	GaAs	21.3	
Dop. Well	...	GaAs	5	$4.0e17cm^{-3}$
Barrier	...	AlGaAs: 15%	2.8	
Well	...	GaAs	20.2	
Dop. Well	...	GaAs	7	$4.0e17cm^{-3}$
Barrier	...	AlGaAs: 15%	1.5	
Well	...	GaAs	18.5	
Dop. Well	...	GaAs	10	$4.0e17cm^{-3}$
Barrier	...	AlGaAs: 15%	1.5	
Well	...	GaAs	81	
Dop. Well	...	GaAs	20	$4.0e17cm^{-3}$
Well	...	GaAs	81	
Barrier	...	AlGaAs: 15%	1.5	
Dop. Well	...	GaAs	10	$4.0e17cm^{-3}$
Well	...	GaAs	18.5	
Barrier	...	AlGaAs: 15%	1.5	
Dop. Well	...	GaAs	7	$4.0e17cm^{-3}$
Well	...	GaAs	20.2	
Barrier	...	AlGaAs: 15%	2.8	
Dop. Well	...	GaAs	5	$4.0e17cm^{-3}$
Well	...	GaAs	21.3	
Barrier	...	AlGaAs: 15%	3.7	
Dop. Well	...	GaAs	5	$4.0e17cm^{-3}$
Well	...	GaAs	19.4	
Barrier	...	AlGaAs: 15%	5.6	
Dop. Well	...	GaAs	5	$4.0e17cm^{-3}$
Well	...	GaAs	17.2	
Barrier	...	AlGaAs: 15%	7.8	
Dop. Well	...	GaAs	2	$4.0e17cm^{-3}$

Continued on next page

Table A.1: (Continued)

Well	...	GaAs	17.6
Barrier	...	AlGaAs: 15%	10.4
Well	...	GaAs	16.6
Barrier	...	AlGaAs: 15%	13.4
Well	...	GaAs	13.3
Barrier	...	AlGaAs: 15%	16.7
Well	...	GaAs	9.6
Barrier	...	AlGaAs: 15%	20.4
Well	...	GaAs	5
Barrier	...	AlGaAs: 15%	25
Well	...	GaAs	1.5
Barrier	...	AlGaAs: 15%	144.5
Cladding		AlGaAs: 15%	100
Cap		GaAs	500

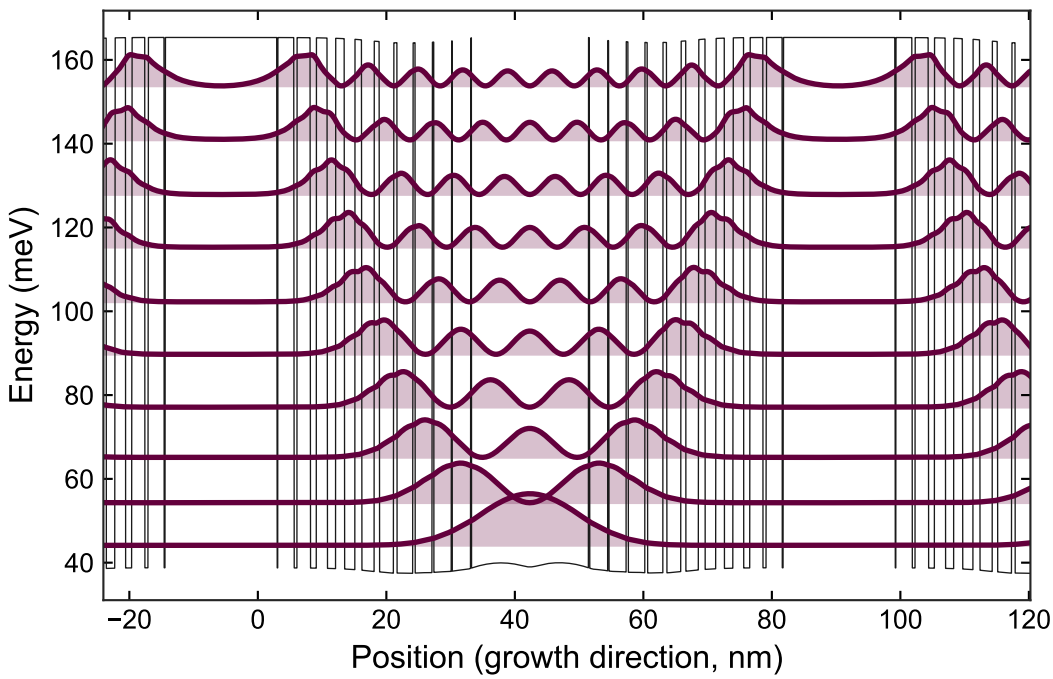

Figure A.1.. Bandstructure of L1006.

A.2. G0413 18 PQWs

Comment	Repeats	Material	Thickness (Å)	Doping
Substrate		GaAs (SI)		
Buffer		GaAs	2000	
High temp. cap		AlAs	30	
Etch stop		AlGaAs: 50%	4000	
Cavity filler		GaAs cavity	66000	
Cavity filler		GaAs cavity	1500	
Cladding		AlGaAs: 30%	1000	
Barrier		AlGaAs: 30%	12.4	
Doping well		GaAs	5.65	
Doping well		Si delta	0	$3.0e11cm^{-2}$
Doping well		GaAs	14.35	
Barrier		AlGaAs: 30%	12.4	
Parabolic QW		AlGaAs: parabolic	1038.3	
Barrier	17	AlGaAs: 30%	12.4	
Doping well	...	GaAs	5.65	
Doping well	...	Si delta	0	$3.0e11cm^{-2}$
Doping well	...	GaAs	14.35	
Barrier	...	AlGaAs: 30%	12.4	
Parabolic QW	...	AlGaAs: parabolic	1038.3	
Barrier		AlGaAs: 30%	12.4	
Doping well		GaAs	5.65	
Doping well		Si delta	0	$3.0e11cm^{-2}$
Doping well		GaAs	14.35	
Barrier		AlGaAs: 30%	12.4	
Cladding		AlGaAs: 30%	1000	
Doped cap		GaAs (SI)	100	$5.0e18cm^{-3}$
Cap		GaAs	400	

A.3. G0489 18 PQWs

Comment	Repeats	Material	Thickness (Å)	Doping
Substrate		GaAs (SI)		
Buffer		GaAs cavity	2000	
Etch stop		AlGaAs: 50%	4000	
Cavity filler		GaAs cavity	67500	
Cladding		AlGaAs: 30%	1000	
Barrier	18	AlGaAs: 30%	40	
Doping well	...	GaAs	5.65	
Doping well	...	Si delta	0	$3.0e11cm^{-2}$
Doping well	...	GaAs	14.35	
Barrier	...	AlGaAs: 30%	40	
Parabolic QW	...	AlGaAs: PQW (2-30%)	1038.28	
Barrier		AlGaAs: 30%	40	
Doping well		GaAs	5.65	
Doping well		Si delta	0	$3.0e11cm^{-2}$
Doping well		GaAs	14.35	
Barrier		AlGaAs: 30%	40	
Cladding		AlGaAs: 30%	1000	
Doped cap		GaAs (SI)	100	$2.0e18cm^{-3}$
Cap		GaAs	400	

A.4. G0490 54 PQWs

Comment	Repeats	Material	Thickness (Å)	Doping
Substrate		GaAs (SI)		
Buffer A		GaAs cavity	1000	
Buffer B		GaAs cavity	1000	
Etch stop		AlGaAs: 50%	4000	
Cavity filler A		GaAs cavity	8000	
Cavity filler B		GaAs cavity	17000	
Cavity filler C		GaAs cavity	1500	
Cladding		AlGaAs: 30%	1000	
Barrier	54	AlGaAs: 30%	40	
Doping well	...	GaAs	5.65	
Doping well	...	Si delta	0	$1.0e11cm^{-2}$
Doping well	...	GaAs	14.35	
Barrier	...	AlGaAs: 30%	40	
Parabolic QW	...	AlGaAs: PQW (2-30%)	1038.28	
Barrier		AlGaAs: 30%	40	
Doping well		GaAs	5.65	
Doping well		Si delta	0	$1.0e11cm^{-2}$
Doping well		GaAs	14.35	
Barrier		AlGaAs: 30%	40	
Cladding		AlGaAs: 30%	1000	
Doped cap		GaAs (SI)	100	$2.0e18cm^{-3}$
Cap		GaAs	400	

A.5. G0642 4 PQWs

Comment	Repeats	Material	Thickness (Å)	Doping
Substrate		GaAs (SI)		
Buffer A		GaAs cavity	1000	
Buffer B		GaAs cavity	1000	
Etch stop		AlGaAs: 50%	4000	
Doped cap		GaAs	300	$3.3e18cm^{-3}$
Cladding		AlGaAs: 20%	500	
Barrier	4	AlGaAs: 20%	90	
Doping well	...	AlGaAs: 20%	5.65	
Doping well	...	Si delta	0	$1.0e11cm^{-2}$
Doping well	...	AlGaAs: 20%	14.35	
Barrier	...	AlGaAs: 20%	90	
Parabolic QW	...	AlGaAs: PQW (2-20%)	1307.5	
Barrier		AlGaAs: 20%	90	
Doping well		AlGaAs: 20%	5.65	
Doping well		Si delta	0	$1.0e11cm^{-2}$
Doping well		AlGaAs: 20%	14.35	
Barrier		AlGaAs: 20%	90	
Cladding		AlGaAs: 20%	500	
Doped cap		GaAs (SI)	300	$3.3e18cm^{-3}$

A.6. G0643 8 PQWs

Comment	Repeats	Material	Thickness (Å)	Doping
Substrate		GaAs (SI)		
Buffer A		GaAs cavity	1000	
Buffer B		GaAs cavity	1000	
Etch stop		AlGaAs: 50%	4000	
Doped cap		GaAs	300	$3.3e18cm^{-3}$
Cladding		AlGaAs: 20%	500	
Barrier	8	AlGaAs: 20%	90	
Doping well	...	AlGaAs: 20%	5.65	
Doping well	...	Si delta	0	$1.0e11cm^{-2}$
Doping well	...	AlGaAs: 20%	14.35	
Barrier	...	AlGaAs: 20%	90	
Parabolic QW	...	AlGaAs: PQW (2-20%)	1307.5	
Barrier		AlGaAs: 20%	90	
Doping well		AlGaAs: 20%	5.65	
Doping well		Si delta	0	$1.0e11cm^{-2}$
Doping well		AlGaAs: 20%	14.35	
Barrier		AlGaAs: 20%	90	
Cladding		AlGaAs: 20%	500	
Doped cap		GaAs (SI)	300	$3.3e18cm^{-3}$

A.7. G0645 43 HPQWs bulk doped

Comment	Repeats	Material	Thickness (Å)	Doping
Substrate		GaAs (SI)		
Buffer A		GaAs cavity	1000	
Buffer B		GaAs cavity	1000	
Etch stop		AlGaAs: 50%	4000	
Cavity filler A		GaAs cavity	4000	
Cavity filler B		GaAs cavity	42500	
Cavity filler C		GaAs cavity	1500	
Cladding		AlGaAs: 20%	400	
Barrier	43	AlGaAs: 20%	600	
Parabolic QW	...	AlGaAs: HPQW (2-20%)	812.8	$5.0e10cm^{-2}$
Barrier		AlGaAs: 20%	600	
Cladding		AlGaAs: 20%	400	
Doped cap		GaAs (SI)	300	$3.3e18cm^{-3}$

A.8. G0712 43 HPQWs mod. dop.

Comment	Repeats	Material	Thickness (Å)	Doping
Substrate		GaAs (SI)		
Buffer A		GaAs cavity	1000	
Buffer B		GaAs cavity	1000	
Etch stop		AlGaAs: 50%	4000	
Cavity filler A		GaAs cavity	6000	
Cavity filler B		GaAs cavity	40500	
Cavity filler C		GaAs cavity	1500	
Cladding		AlGaAs: 20%	400	
Barrier	43	AlGaAs: 20%	500	
Mod. Dop.	...	Si delta	0	$5.0e10cm^{-2}$
Barrier	...	AlGaAs: 20%	100	
Parabolic QW	...	AlGaAs: HPQW (2-20%)	812.83	
Barrier		AlGaAs: 20%	500	
Mod. Dop.		Si delta	0	$5.0e10cm^{-2}$
Barrier		AlGaAs: 20%	100	
Cladding		AlGaAs: 20%	400	
Doped cap		GaAs (SI)	300	$3.3e18cm^{-3}$

A.9. HM4162

Comment	Repeats	Material	Thickness (Å)	Doping
Substrate		GaAs (SI)		
Buffer		GaAs cavity	2500	
Etch stop		AlGaAs: 50%	5000	
Cap layer		GaAs	500	
Barrier	7	AlGaAs: 33%	100	
Mod. Dop.	...	Si delta	0	$4.4e12cm^{-2}$
Barrier	...	AlGaAs: 33%	100	
Well	...	GaAs	83	
Barrier		AlGaAs: 33%	200	
Doped cap		GaAs (SI)	200	

Bibliography

[1] *MIR atmospheric transmission measurement at the Gemini South telescope (Chile)*. URL: https://www.gemini.edu/observing/telescopes-and-sites/sites (cit. on p. 3).

[2] *THz atmospheric transmission measurement at the Concordia Research Station (South Pole)*. URL: http://transmissioncurves.free.fr/ (cit. on p. 3).

[3] D.J. McCaa and J.H. Shaw. "The infrared spectrum of ozone." In: *Journal of Molecular Spectroscopy* 25.3 (Mar. 1, 1968), pp. 374–397. ISSN: 0022-2852. DOI: 10.1016/S0022-2852(68)80050-5 (cit. on p. 2).

[4] Tadao Nagatsuma, Guillaume Ducournau, and Cyril C. Renaud. "Advances in terahertz communications accelerated by photonics." In: *Nature Photonics* 10.6 (June 1, 2016), pp. 371–379. ISSN: 1749-4893. DOI: 10.1038/nphoton.2016.65 (cit. on p. 2).

[5] Jane Hodgkinson and Ralph P. Tatam. "Optical gas sensing: a review." In: *Measurement Science and Technology* 24.1 (Nov. 2012). Publisher: IOP Publishing, p. 012004. DOI: 10.1088/0957-0233/24/1/012004 (cit. on p. 4).

[6] Bruce Napier et al. "Ultra-broadband infrared gas sensor for pollution detection: the TRIAGE project." In: *Journal of Physics: Photonics* 3.3 (June 2021). Publisher: IOP Publishing, p. 031003. DOI: 10.1088/2515-7647/ac0542 (cit. on p. 4).

[7] Hannaneh Dortaj et al. "High-speed and high-precision PbSe/PbI2 solution process mid-infrared camera." In: *Scientific Reports* 11.1 (Jan. 15, 2021), p. 1533. ISSN: 2045-2322. DOI: 10.1038/s41598-020-80847-4 (cit. on p. 4).

[8] NASA. *Infrared Astronomy*. URL: https://webbtelescope.org/webb-science/the-observatory/infrared-astronomy (cit. on p. 4).

[9] Hongtao Lin et al. "Mid-infrared integrated photonics on silicon: a perspective." In: *Nanophotonics* 7.2 (2018), pp. 393–420. DOI: 10.1515/nanoph-2017-0085 (cit. on p. 4).

[10] Craig Kulesa. "Terahertz Spectroscopy for Astronomy: From Comets to Cosmology." In: *IEEE Transactions on Terahertz Science and Technology* 1.1 (Sept. 2011), pp. 232–240. ISSN: 2156-3446. DOI: 10.1109/TTHZ.2011.2159648 (cit. on p. 4).

[11] John F. Federici et al. "THz imaging and sensing for security applications—explosives, weapons and drugs." In: *Semiconductor Science and Technology* 20.7 (June 2005). Publisher: IOP Publishing, S266–S280. DOI: 10.1088/0268-1242/20/7/018 (cit. on p. 4).

[12] Harsh Tataria et al. "6G Wireless Systems: Vision, Requirements, Challenges, Insights, and Opportunities." In: *Proceedings of the IEEE* 109.7 (July 2021), pp. 1166–1199. ISSN: 1558-2256. DOI: 10.1109/JPROC.2021.3061701 (cit. on p. 4).

[13] Jerome Faist et al. "Quantum Cascade Laser." In: *Science* 264.5158 (1994), pp. 553–556. DOI: 10.1126/science.264.5158.553 (cit. on pp. 4, 70).

[14] F. Wang et al. "Room temperature quantum cascade lasers with 22% wall plug efficiency in continuous-wave operation." In: *Opt. Express* 28.12 (June 2020). Publisher: OSA, pp. 17532–17538. DOI: 10.1364/OE.394916 (cit. on p. 4).

[15] Daylight. *Advance Your Application with Mid-IR Laser Technology*. URL: https://daylightsolutions.com/product/mircat/ (cit. on p. 4).

[16] W. D. Lawson et al. "Preparation and properties of HgTe and mixed crystals of HgTe-CdTe." In: *Journal of Physics and Chemistry of Solids* 9.3 (1959), pp. 325–329. ISSN: 0022-3697. DOI: https://doi.org/10.1016/0022-3697(59)90110-6 (cit. on p. 4).

[17] Daniele Palaferri et al. "Room-temperature nine-µm-wavelength photodetectors and GHz-frequency heterodyne receivers." In: *Nature* 556.7699 (Apr. 1, 2018), pp. 85–88. ISSN: 1476-4687. DOI: 10.1038/nature25790 (cit. on p. 4).

[18] Etienne Rodriguez et al. "Room-Temperature, Wide-Band, Quantum Well Infrared Photodetector for Microwave Optical Links at 4.9 um Wavelength." In: *ACS Photonics* 5.9 (2018), pp. 3689–3694. DOI: 10.1021/acsphotonics.8b00704 (cit. on p. 4).

[19] Michael Hakl et al. "Ultrafast Quantum-Well Photodetectors Operating at 10 <pre>μ</pre>m with a Flat Frequency Response up to 70 GHz at Room Temperature." In: *ACS Photonics* 8.2 (Feb. 17, 2021). Publisher: American Chemical Society, pp. 464–471. DOI: 10.1021/acsphotonics.0c01299 (cit. on p. 4).

[20] J. Hawecker et al. "Cavity-based photoconductive sources for real-time terahertz imaging." In: *Photon. Res.* 8.6 (June 2020). Publisher: OSA, pp. 858–863. DOI: 10.1364/PRJ.388219 (cit. on p. 4).

[21] Rüdeger Köhler et al. "Terahertz semiconductor-heterostructure laser." In: *Nature* 417.6885 (May 1, 2002), pp. 156–159. ISSN: 1476-4687. DOI: 10.1038/417156a (cit. on p. 4).

[22] H. Luo et al. "Background-limited terahertz quantum-well photodetector." In: *Applied Physics Letters* 86.23 (2005), p. 231103. DOI: 10.1063/1.1947377 (cit. on p. 4).

[23] Mathieu Jeannin et al. "High temperature metamaterial terahertz quantum detector." In: *Applied Physics Letters* 117.25 (2020), p. 251102. DOI: 10.1063/5.0033367 (cit. on p. 5).

[24] Peter YU and Manuel Cardona. *Fundamentals of Semiconductors*. Springer-Verlag Berlin Heidelberg. ISBN: 978-3-642-00709-5. URL: 10.1007/978-3-642-00710-1 (cit. on pp. 5, 7).

[25] Emmanuel Rosencher and Borge Vinter. *Optoelectronics*. Trans. by P. G. Piva. Cambridge: Cambridge University Press, 2002. ISBN: 978-0-521-77129-0. DOI: 10.1017/CBO9780511754647 (cit. on p. 6).

[26] N. W. Ashcroft and N. D. Mermin. *Solid State Physics*. Philadelphia: Saunders College, 1976 (cit. on p. 6).

[27] Lok C Lew Yan Voon and Morten Willatzen. *The kp method: electronic properties of semiconductors*. Springer Science & Business Media, 2009. ISBN: 3-540-92872-3 (cit. on p. 7).

[28] Evan O. Kane. "Band structure of indium antimonide." In: *Journal of Physics and Chemistry of Solids* 1.4 (Jan. 1, 1957), pp. 249–261. ISSN: 0022-3697. DOI: 10.1016/0022-3697(57)90013-6 (cit. on p. 8).

[29] A.Y. Cho and J.R. Arthur. "Molecular beam epitaxy." In: *Progress in Solid State Chemistry* 10 (Jan. 1, 1975), pp. 157–191. ISSN: 0079-6786. DOI: 10.1016/0079-6786(75)90005-9 (cit. on p. 8).

[30] G. Bastard. *Wave mechanics applied to semiconductor heterostructures*. United States: John Wiley and Sons Inc, 1990. ISBN: 0-471-21708-1. URL: http://inis.iaea.org/search/search.aspx?orig_q=RN:23010919 (cit. on p. 9).

[31] D. J. BenDaniel and C. B. Duke. "Space-Charge Effects on Electron Tunneling." In: *Phys. Rev.* 152.2 (Dec. 1966). Publisher: American Physical Society, pp. 683–692. DOI: 10.1103/PhysRev.152.683 (cit. on p. 9).

[32] R. H. Lyddane, R. G. Sachs, and E. Teller. "On the Polar Vibrations of Alkali Halides." In: *Phys. Rev.* 59.8 (Apr. 1941). Publisher: American Physical Society, pp. 673–676. DOI: 10.1103/PhysRev.59.673 (cit. on p. 13).

[33] E.D. Palik. *Handbook of Optical Constants of Solids: Volume 1*. vol. 1. Elsevier Science, 2012. ISBN: 978-0-08-054721-3. URL: https://books.google.fr/books?id=h8mEd9no5-kC (cit. on p. 13).

[34] C. Patel et al. "Phonon Frequencies in GaAs." In: *physica status solidi (b)* 122.2 (1984), pp. 461–467. DOI: https://doi.org/10.1002/pssb.2221220210 (cit. on p. 13).

[35] D. J. Lockwood, Guolin Yu, and N. L. Rowell. "Optical phonon frequencies and damping in AlAs, GaP, GaAs, InP, InAs and InSb studied by oblique incidence infrared spectroscopy." In: *Solid State Communications* 136.7 (2005), pp. 404–409. ISSN: 0038-1098. DOI: https://doi.org/10.1016/j.ssc.2005.08.030 (cit. on p. 13).

[36] Mauro Nisoli. *Semiconductor photonics. Principles and Applications*. Società Editrice Esculapio, 2016. ISBN: 978-88-9385-004-9. URL: https://books.google.fr/books?id=ZmNADwAAQBAJ (cit. on pp. 17, 115).

[37] Mark Fox. *Optical Properties of Solids*. Oxford Master Series in Physics. Oxford University Press, 2010. ISBN: 978-0-19-957336-3. URL: https://books.google.fr/books?id=5WkVDAAAQBAJ (cit. on pp. 18, 20, 41).

[38] Manfred Helm. "The Basic Physics of Intersubband Transitions." In: *Intersubband Transitions in Quantum Wells: Physics and Device Applications I*. Ed. by H. C. Liu and Federico Capasso. Vol. 62. Semiconductors and Semimetals. ISSN: 0080-8784. Elsevier, 1999, pp. 1–99. DOI: https://doi.org/10.1016/S0080-8784(08)60304-X (cit. on pp. 18, 20, 71).

[39] Tsuneya Ando, Alan B. Fowler, and Frank Stern. "Electronic properties of two-dimensional systems." In: *Rev. Mod. Phys.* 54.2 (Apr. 1982). Publisher: American Physical Society, pp. 437–672. DOI: 10.1103/RevModPhys.54.437 (cit. on p. 20).

[40] Aymeric Delteil. "Exaltation multicorps du couplage lumière-matière." PhD thesis. 2012. 1 vol. (XIV-199 p.) URL: http://www.theses.fr/2012PA077214 (cit. on p. 20).

[41] M Zaluzny and C Nalewajko. "Coupling of infrared radiation to intersubband transitions in multiple quantum wells: The effective-medium approach." In: *PHYSICAL REVIEW B* 59.20 (May 15, 1999), pp. 13043–13053. ISSN: 1098-0121. DOI: 10.1103/PhysRevB.59.13043 (cit. on pp. 21, 75, 86).

[42] E. M. Purcell. "Spontaneous Emission Probabilities at Radio Frequencies." In: *Confined Electrons and Photons: New Physics and Applications*. Ed. by Elias Burstein and Claude Weisbuch. Boston, MA: Springer US, 1995, pp. 839–839. ISBN: 978-1-4615-1963-8. DOI: 10.1007/978-1-4615-1963-8_40 (cit. on pp. 22, 26).

[43] Serge Haroche and Daniel Kleppner. "Cavity Quantum Electrodynamics." In: *Physics Today* 42.1 (1989), pp. 24–30. DOI: 10.1063/1.881201 (cit. on p. 22).

[44] Y. Kaluzny et al. "Observation of Self-Induced Rabi Oscillations in Two-Level Atoms Excited Inside a Resonant Cavity: The Ringing Regime of Superradiance." In: *Phys. Rev. Lett.* 51.13 (Sept. 1983). Publisher: American Physical Society, pp. 1175–1178. DOI: 10.1103/PhysRevLett.51.1175 (cit. on p. 23).

[45] D. Meschede, H. Walther, and G. Müller. "One-Atom Maser." In: *Phys. Rev. Lett.* 54.6 (Feb. 1985). Publisher: American Physical Society, pp. 551–554. DOI: 10.1103/PhysRevLett.54.551 (cit. on p. 23).

[46] J. J. Hopfield. "Theory of the Contribution of Excitons to the Complex Dielectric Constant of Crystals." In: *Phys. Rev.* 112.5 (Dec. 1958). Publisher: American Physical Society, pp. 1555–1567. DOI: 10.1103/PhysRev.112.1555 (cit. on pp. 23, 27).

[47] E.T. Jaynes and F.W. Cummings. "Comparison of quantum and semiclassical radiation theories with application to the beam maser." In: *Proceedings of the IEEE* 51.1 (1963), pp. 89–109. DOI: 10.1109/PROC.1963.1664 (cit. on p. 23).

[48] C. Weisbuch et al. "Observation of the coupled exciton-photon mode splitting in a semiconductor quantum microcavity." In: *Phys. Rev. Lett.* 69.23 (Dec. 1992). Publisher: American Physical Society, pp. 3314–3317. DOI: 10.1103/PhysRevLett.69.3314 (cit. on p. 23).

[49] D Dini et al. "Microcavity polariton splitting of intersubband transitions." In: *PHYSICAL REVIEW LETTERS* 90.11 (Mar. 21, 2003). ISSN: 0031-9007. DOI: 10.1103/PhysRevLett.90.116401 (cit. on pp. 23, 43).

[50] R. H. Dicke. "Coherence in Spontaneous Radiation Processes." In: *Phys. Rev.* 93.1 (Jan. 1954). Publisher: American Physical Society, pp. 99–110. DOI: 10.1103/PhysRev.93.99 (cit. on p. 28).

[51] C Ciuti, G Bastard, and I Carusotto. "Quantum vacuum properties of the intersubband cavity polariton field." In: *PHYSICAL REVIEW B* 72.11 (Sept. 2005). Place: ONE PHYSICS ELLIPSE, COLLEGE PK, MD 20740-3844 USA Publisher: AMER PHYSICAL SOC Type: Article. ISSN: 2469-9950. DOI: 10.1103/PhysRevB.72.115303 (cit. on pp. 29, 32, 33, 121).

[52] Y. Todorov et al. "Ultrastrong Light-Matter Coupling Regime with Polariton Dots." In: *Phys. Rev. Lett.* 105.19 (Nov. 2010). Publisher: American Physical Society, p. 196402. DOI: 10.1103/PhysRevLett.105.196402 (cit. on p. 29).

[53] C. Cohen-Tannoudji, J. Dupont-Roc, and G. Grynberg. *Photons et atomes. Introduction à l'électrodynamique quantique: Introduction à l'électrodynamique quantique.* SAVOIRS ACTUELS. EDP Sciences, 2012. ISBN: 978-2-7598-0135-0. URL: https://books.google.fr/books?id=F-qe7iVyiHoC (cit. on p. 29).

[54] Simone De Liberato. "Cavity quantum electrodynamics and intersubband polaritonics of a two dimensional electron gas." Theses. Université Paris-Diderot - Paris VII, June 2009. URL: https://tel.archives-ouvertes.fr/tel-00421386 (cit. on p. 30).

[55] Yanko Todorov and Carlo Sirtori. "Intersubband polaritons in the electrical dipole gauge." In: *Phys. Rev. B* 85.4 (Jan. 2012). Publisher: American Physical Society, p. 045304. DOI: 10.1103/PhysRevB.85.045304 (cit. on pp. 30, 69).

[56] Simone Zanotto. "Intersubband polaritons in photonic crystal cavities." PhD thesis. Scuola Normale Superiore, 2014. 157 pp. URL: https://metapublishing.org/index.php/MP/catalog/book/45 (cit. on pp. 33, 38).

[57] Aji A. Anappara et al. "Electrical control of polariton coupling in intersubband microcavities." In: *Applied Physics Letters* 87.5 (Aug. 1, 2005). Publisher: American Institute of Physics, p. 051105. ISSN: 0003-6951. DOI: 10.1063/1.2006976 (cit. on p. 33).

[58] Aji A. Anappara et al. "Controlling polariton coupling in intersubband microcavities." In: *Proceedings of the 6th International Conference on Physics of Light-Matter Coupling in Nanostructures* 41.5 (May 1, 2007), pp. 308–312. ISSN: 0749-6036. DOI: 10.1016/j.spmi.2007.03.005 (cit. on p. 33).

[59] Aji A. Anappara et al. "Tunnel-assisted manipulation of intersubband polaritons in asymmetric coupled quantum wells." In: *Applied Physics Letters* 89.17 (Oct. 23, 2006). Publisher: American Institute of Physics, p. 171109. ISSN: 0003-6951. DOI: 10.1063/1.2367664 (cit. on p. 33).

[60] G. Günter et al. "Sub-cycle switch-on of ultrastrong light–matter interaction." In: *Nature* 458.7235 (Mar. 1, 2009), pp. 178–181. ISSN: 1476-4687. DOI: 10.1038/nature07838 (cit. on p. 33).

[61] Gerald T. Moore. "Quantum Theory of the Electromagnetic Field in a Variable-Length One-Dimensional Cavity." In: *Journal of Mathematical Physics* 11.9 (Sept. 1, 1970). Publisher: American Institute of Physics, pp. 2679–2691. ISSN: 0022-2488. DOI: 10.1063/1.1665432 (cit. on p. 33).

[62] Michael Uhlmann et al. "Resonant Cavity Photon Creation via the Dynamical Casimir Effect." In: *Phys. Rev. Lett.* 93.19 (Nov. 2004). Publisher: American Physical Society, p. 193601. DOI: 10.1103/PhysRevLett.93.193601 (cit. on p. 33).

[63] V. V. Dodonov. "The dynamical Casimir effect and resonance frequency shifts in cavities with thin photo-excited semiconductor layers." In: *Physica Scripta* T135 (July 2009). Publisher: IOP Publishing, p. 014014. DOI: 10.1088/0031-8949/2009/t135/014014 (cit. on p. 33).

[64] C Braggio et al. "A novel experimental approach for the detection of the dynamical Casimir effect." In: *Europhysics Letters (EPL)* 70.6 (June 2005). Publisher: IOP Publishing, pp. 754–760. ISSN: 0295-5075. DOI: 10.1209/epl/i2005-10048-8 (cit. on p. 33).

[65] C. M. Wilson et al. "Observation of the dynamical Casimir effect in a superconducting circuit." In: *Nature* 479.7373 (Nov. 1, 2011), pp. 376–379. ISSN: 1476-4687. DOI: 10.1038/nature10561 (cit. on p. 33).

[66] Yannick Chassagneux. "Photonique pour les lasers à cascade quantique térahertz." Theses. Université Paris Sud - Paris XI, Nov. 2009. URL: https://tel.archives-ouvertes.fr/tel-00740111 (cit. on p. 37).

[67] Y. Todorov et al. "Optical properties of metal-dielectric-metal microcavities in the THz frequency range." In: *OPTICS EXPRESS* 18.13 (June 21, 2010), pp. 13886–13907. ISSN: 1094-4087. DOI: 10.1364/OE.18.013886 (cit. on pp. 37, 38, 47, 86).

[68] W. L. Barnes et al. "Surface Plasmon Polaritons and Their Role in the Enhanced Transmission of Light through Periodic Arrays of Subwavelength Holes in a Metal Film." In: *Phys. Rev. Lett.* 92.10 (Mar. 2004). Publisher: American Physical Society, p. 107401. DOI: 10.1103/PhysRevLett.92.107401 (cit. on p. 38).

[69] Stéphane Collin. "Nanostructure arrays in free-space: optical properties and applications." In: 77.12 (Nov. 2014). Publisher: IOP Publishing, p. 126402. DOI: 10.1088/0034-4885/77/12/126402 (cit. on p. 39).

[70] Anderson M. H. et al. "Observation of Bose-Einstein Condensation in a Dilute Atomic Vapor." In: *Science* 269.5221 (July 14, 1995). Publisher: American Association for the Advancement of Science, pp. 198–201. DOI: 10.1126/science.269.5221.198 (cit. on p. 41).

[71] K. B. Davis et al. "Bose-Einstein Condensation in a Gas of Sodium Atoms." In: *Phys. Rev. Lett.* 75.22 (Nov. 1995). Publisher: American Physical Society, pp. 3969–3973. DOI: 10.1103/PhysRevLett.75.3969 (cit. on p. 41).

[72] G Malpuech et al. "Polariton laser: thermodynamics and quantum kinetic theory." In: *Semiconductor Science and Technology* 18.10 (Sept. 3, 2003). Publisher: IOP Publishing, S395–S404. ISSN: 0268-1242. DOI: 10.1088/0268-1242/18/10/314 (cit. on p. 41).

[73] Iacopo Carusotto and Cristiano Ciuti. "Quantum fluids of light." In: *Rev. Mod. Phys.* 85.1 (Feb. 2013). Publisher: American Physical Society, pp. 299–366. DOI: 10.1103/RevModPhys.85.299 (cit. on p. 42).

[74] A. Imamoglu et al. "Nonequilibrium condensates and lasers without inversion: Exciton-polariton lasers." In: *Phys. Rev. A* 53.6 (June 1996). Publisher: American Physical Society, pp. 4250–4253. DOI: 10.1103/PhysRevA.53.4250 (cit. on p. 41).

[75] F. Tassone and Y. Yamamoto. "Exciton-exciton scattering dynamics in a semiconductor microcavity and stimulated scattering into polaritons." In: *Phys. Rev. B* 59.16 (Apr. 1999). Publisher: American Physical Society, pp. 10830–10842. DOI: 10.1103/PhysRevB.59.10830 (cit. on p. 41).

[76] J. Kasprzak et al. "Bose–Einstein condensation of exciton polaritons." In: *Nature* 443.7110 (Sept. 1, 2006), pp. 409–414. ISSN: 1476-4687. DOI: 10.1038/nature05131 (cit. on pp. 41, 42).

[77] Hui Deng, Hartmut Haug, and Yoshihisa Yamamoto. "Exciton-polariton Bose-Einstein condensation." In: *Rev. Mod. Phys.* 82.2 (May 2010). Publisher: American Physical Society, pp. 1489–1537. DOI: 10.1103/RevModPhys.82.1489 (cit. on p. 41).

[78] Daniele Bajoni. "Polariton lasers. Hybrid light–matter lasers without inversion." In: *Journal of Physics D: Applied Physics* 45.31 (July 2012). Publisher: IOP Publishing, p. 313001. DOI: 10.1088/0022-3727/45/31/313001 (cit. on p. 41).

[79] S. Christopoulos et al. "Room-Temperature Polariton Lasing in Semiconductor Microcavities." In: *Phys. Rev. Lett.* 98.12 (Mar. 2007). Publisher: American Physical Society, p. 126405. DOI: 10.1103/PhysRevLett.98.126405 (cit. on p. 42).

[80] Christian Schneider et al. "An electrically pumped polariton laser." In: *Nature* 497.7449 (May 1, 2013), pp. 348–352. ISSN: 1476-4687. DOI: 10.1038/nature12036 (cit. on p. 42).

[81] Pallab Bhattacharya et al. "Solid State Electrically Injected Exciton-Polariton Laser." In: *Phys. Rev. Lett.* 110.20 (May 2013). Publisher: American Physical Society, p. 206403. DOI: 10.1103/PhysRevLett.110.206403 (cit. on p. 42).

[82] Pallab Bhattacharya et al. "Room Temperature Electrically Injected Polariton Laser." In: *Phys. Rev. Lett.* 112.23 (June 2014). Publisher: American Physical Society, p. 236802. DOI: 10.1103/PhysRevLett.112.236802 (cit. on p. 42).

[83] F. Tassone et al. "Bottleneck effects in the relaxation and photoluminescence of microcavity polaritons." In: *Phys. Rev. B* 56.12 (Sept. 1997). Publisher: American Physical Society, pp. 7554–7563. DOI: 10.1103/PhysRevB.56.7554 (cit. on p. 43).

[84] Simone De Liberato and Cristiano Ciuti. “Stimulated Scattering and Lasing of Intersubband Cavity Polaritons.” In: *Phys. Rev. Lett.* 102.13 (Mar. 2009). Publisher: American Physical Society, p. 136403. DOI: 10.1103/PhysRevLett.102.136403 (cit. on p. 43).

[85] R Colombelli et al. “Quantum cascade intersubband polariton light emitters.” In: *Semiconductor Science and Technology* 20.10 (Aug. 19, 2005). Publisher: IOP Publishing, pp. 985–990. ISSN: 0268-1242. DOI: 10.1088/0268-1242/20/10/001 (cit. on p. 43).

[86] P. Jouy et al. “Intersubband electroluminescent devices operating in the strong-coupling regime.” In: *Phys. Rev. B* 82.4 (July 2010). Publisher: American Physical Society, p. 045322. DOI: 10.1103/PhysRevB.82.045322 (cit. on p. 43).

[87] A. Delteil et al. “Optical phonon scattering of cavity polaritons in an electroluminescent device.” In: *Phys. Rev. B* 83.8 (Feb. 2011). Publisher: American Physical Society, p. 081404. DOI: 10.1103/PhysRevB.83.081404 (cit. on p. 43).

[88] D. Chastanet et al. “Surface emitting thermally assisted polaritonic light-emitting device.” In: *Applied Physics Letters* 110.8 (Feb. 20, 2017). Publisher: American Institute of Physics, p. 081108. ISSN: 0003-6951. DOI: 10.1063/1.4976585 (cit. on p. 43).

[89] J. -M. Manceau et al. “Resonant intersubband polariton-LO phonon scattering in an optically pumped polaritonic device.” In: *APPLIED PHYSICS LETTERS* 112.19 (May 7, 2018). ISSN: 0003-6951. DOI: 10.1063/1.5029893 (cit. on pp. 43–49, 51).

[90] Raffaele Colombelli and Jean-Michel Manceau. “Perspectives for Intersubband Polariton Lasers.” In: *PHYSICAL REVIEW X* 5.1 (Mar. 23, 2015). ISSN: 2160-3308. DOI: 10.1103/PhysRevX.5.011031 (cit. on pp. 43, 44).

[91] Michiel Wouters and Iacopo Carusotto. “Parametric oscillation threshold of semiconductor microcavities in the strong coupling regime.” In: *Phys. Rev. B* 75.7 (Feb. 2007). Publisher: American Physical Society, p. 075332. DOI: 10.1103/PhysRevB.75.075332 (cit. on p. 44).

[92] Kim Rahmelow. “Electronic influences on an infrared detector signal: nonlinearity and amplification.” In: *Applied Optics* 36.10 (Apr. 1, 1997). Publisher: OSA, pp. 2123–2132. DOI: 10.1364/AO.36.002123 (cit. on p. 50).

[93] M. Knorr et al. “Intersubband polariton-polariton scattering in a dispersive microcavity.” In: (2022). _eprint: 2201.05056 (cit. on pp. 53, 54, 60).

[94] Alongkarn Chutinan and Susumu Noda. “Highly confined waveguides and waveguide bends in three-dimensional photonic crystal.” In: *Applied Physics Letters* 75.24 (Dec. 13, 1999). Publisher: American Institute of Physics, pp. 3739–3741. ISSN: 0003-6951. DOI: 10.1063/1.125441 (cit. on p. 55).

[95] Mehmet Bayindir, B. Temelkuran, and E. Ozbay. “Photonic-crystal-based beam splitters.” In: *Applied Physics Letters* 77.24 (Dec. 11, 2000). Publisher: American Institute of Physics, pp. 3902–3904. ISSN: 0003-6951. DOI: 10.1063/1.1332821 (cit. on p. 55).

[96] Hatice Altug and Jelena Vučković. “Two-dimensional coupled photonic crystal resonator arrays.” In: *Applied Physics Letters* 84.2 (Jan. 12, 2004). Publisher: American Institute of Physics, pp. 161–163. ISSN: 0003-6951. DOI: 10.1063/1.1639505 (cit. on p. 55).

[97] Steven G. Johnson et al. “Guided modes in photonic crystal slabs.” In: *Phys. Rev. B* 60.8 (Aug. 1999). Publisher: American Physical Society, pp. 5751–5758. DOI: 10.1103/PhysRevB.60.5751 (cit. on p. 55).

[98] Siti Chalimah et al. “Midinfrared Dispersion Relations in $\mathrmIn\mathrmP$-Based Photonic Crystal Slabs Revealed by Fourier-Transform Angle-Resolved Reflection Spectroscopy.” In: *Phys. Rev. Applied* 15.6 (June 2021). Publisher: American Physical Society, p. 064076. DOI: 10.1103/PhysRevApplied.15.064076 (cit. on p. 56).

[99] Victor Liu and Shanhui Fan. “S4 : A free electromagnetic solver for layered periodic structures.” In: *Computer Physics Communications* 183.10 (2012), pp. 2233–2244. ISSN: 0010-4655. DOI: 10.1016/j.cpc.2012.04.026 (cit. on p. 56).

[100] Roman Gansch et al. “Measurement of bound states in the continuum by a detector embedded in a photonic crystal.” In: *Light: Science & Applications* 5.9 (Sept. 1, 2016), e16147–e16147. ISSN: 2047-7538. DOI: 10.1038/lsa.2016.147 (cit. on p. 56).

[101] Shanhui Fan and J. D. Joannopoulos. “Analysis of guided resonances in photonic crystal slabs.” In: *Phys. Rev. B* 65.23 (June 2002). Publisher: American Physical Society, p. 235112. DOI: 10.1103/PhysRevB.65.235112 (cit. on p. 57).

[102] M. Galli et al. “Measurement of photonic mode dispersion and linewidths in silicon-on-insulator photonic crystal slabs.” In: *IEEE Journal on Selected Areas in Communications* 23.7 (2005), pp. 1402–1410. DOI: 10.1109/JSAC.2005.851164 (cit. on p. 57).

[103] S. Kalchmair et al. “Photonic crystal slab quantum well infrared photodetector.” In: *Applied Physics Letters* 98.1 (Jan. 3, 2011). Publisher: American Institute of Physics, p. 011105. ISSN: 0003-6951. DOI: 10.1063/1.3537954 (cit. on p. 58).

[104] J.D. Joannopoulos et al. *Photonic Crystals: Molding the Flow of Light - Second Edition*. Princeton University Press, 2011. ISBN: 978-1-4008-2824-1. URL: https://books.google.fr/books?id=owhE36qiTP8C (cit. on p. 59).

[105] Ali Khalatpour et al. “High-power portable terahertz laser systems.” In: *Nature Photonics* 15.1 (Jan. 1, 2021), pp. 16–20. ISSN: 1749-4893. DOI: 10.1038/s41566-020-00707-5 (cit. on p. 64).

[106] Walter Kohn. “Cyclotron Resonance and de Haas-van Alphen Oscillations of an Interacting Electron Gas.” In: *Phys. Rev.* 123.4 (Aug. 1961), pp. 1242–1244. DOI: 10.1103/PhysRev.123.1242 (cit. on p. 65).

[107] L. Brey, N. F. Johnson, and B. I. Halperin. “Optical and magneto-optical absorption in parabolic quantum wells.” In: *Phys. Rev. B* 40.15 (Nov. 1989). Publisher: American Physical Society, pp. 10647–10649. DOI: 10.1103/PhysRevB.40.10647 (cit. on p. 65).

[108] R. C. Miller et al. “Parabolic quantum wells with the $\mathrmG\mathrma\mathrmA\mathrms\ensuremath-\mathrmAl_x\mathrmGa_1\ensuremath-x\mathrmAs$ system.” In: *Phys. Rev. B* 29.6 (Mar. 1984), pp. 3740–3743. DOI: 10.1103/PhysRevB.29.3740 (cit. on p. 66).

[109] A. C. Gossard. “Modulation Doping of Semiconductor Heterostructures.” In: *Molecular Beam Epitaxy and Heterostructures*. Ed. by Leroy L. Chang and Klaus Ploog. Dordrecht: Springer Netherlands, 1985, pp. 499–531. ISBN: 978-94-009-5073-3. DOI: 10.1007/978-94-009-5073-3_14 (cit. on pp. 66, 77).

[110] A.C. Gossard, R.C. Miller, and W. Wiegmann. “MBE growth and energy levels of quantum wells with special shapes.” In: *Surface Science* 174.1 (Aug. 3, 1986), pp. 131–135. ISSN: 0039-6028. DOI: 10.1016/0039-6028(86)90397-3 (cit. on p. 66).

[111] Arthur C. Gossard, Mani Sundaram, and Peter F. Hopkins. "Chapter 2 Wide Graded Potential Wells." In: *Epitaxial Microstructures*. Ed. by Arthur C. Gossard. Vol. 40. Semiconductors and Semimetals. ISSN: 0080-8784. Elsevier, 1994, pp. 153–217. DOI: https://doi.org/10.1016/S0080-8784(08)62663-0 (cit. on p. 66).

[112] T. Sajoto et al. "High quality electron system with variable electron layer thickness in a parabolic quantum well." In: *Applied Physics Letters* 55.14 (1989), pp. 1430–1432. DOI: 10.1063/1.101577 (cit. on p. 66).

[113] E. G. Gwinn et al. "Characterization of the electron gas in wide parabolic GaAs/$\mathrmAl_\mathitx$$\mathrmGa_1\mathrm\ensuremath-\mathitx$As quantum wells." In: *Phys. Rev. B* 41.15 (May 1990). Publisher: American Physical Society, pp. 10700–10705. DOI: 10.1103/PhysRevB.41.10700 (cit. on p. 66).

[114] J. Menéndez et al. "Light scattering in GaAs parabolic quantum wells." In: *Solid State Communications* 61.10 (Mar. 1, 1987), pp. 601–605. ISSN: 0038-1098. DOI: 10.1016/0038-1098(87)90369-3 (cit. on p. 66).

[115] K. Karraï et al. "Cyclotron effective mass in wide parabolic quantum wells." In: *Phys. Rev. B* 42.15 (Nov. 1990). Publisher: American Physical Society, pp. 9732–9735. DOI: 10.1103/PhysRevB.42.9732 (cit. on p. 66).

[116] Susanta Sen et al. "Observation of resonant tunneling through a compositionally graded parabolic quantum well." In: *Applied Physics Letters* 51.18 (1987), pp. 1428–1430. DOI: 10.1063/1.98646 (cit. on p. 66).

[117] G. Neofotistos et al. "Resonant tunneling in double-barrier parabolic well structures." In: *IEEE Transactions on Electron Devices* 36.4 (Apr. 1989), pp. 745–749. ISSN: 1557-9646. DOI: 10.1109/16.22480 (cit. on p. 66).

[118] K. D. Maranowski et al. "Far-infrared emission from parabolically graded quantum wells." In: *Applied Physics Letters* 69.23 (1996), pp. 3522–3524. DOI: 10.1063/1.117232 (cit. on p. 66).

[119] J. H. Burnett et al. "Photoluminescence excitation spectroscopy of remotely doped wide parabolic GaAs/$\mathrmAl_\mathitx$$\mathrmGa_1\mathrm\ensuremath-\mathitx$As quantum wells." In: *Phys. Rev. B* 43.14 (May 1991). Publisher: American Physical Society, pp. 12033–12035. DOI: 10.1103/PhysRevB.43.12033 (cit. on p. 66).

[120] W. Q. Chen et al. "Inverse parabolic quantum wells grown by molecular-beam epitaxy using digital and analog techniques." In: *Phys. Rev. B* 48.19 (Nov. 1993). Publisher: American Physical Society, pp. 14264–14268. DOI: 10.1103/PhysRevB.48.14264 (cit. on p. 66).

[121] W. Q. Chen et al. "Inverse parabolic quantum well and its quantum-confined Stark effect." In: *Journal of Applied Physics* 74.10 (1993), pp. 6247–6250. DOI: 10.1063/1.355167 (cit. on p. 66).

[122] Markus Geiser et al. "Strong light-matter coupling at terahertz frequencies at room temperature in electronic LC resonators." In: *Applied Physics Letters* 97.19 (2010), p. 191107. DOI: 10.1063/1.3511446 (cit. on pp. 66, 67).

[123] B. Paulillo et al. "Room temperature strong light-matter coupling in three dimensional terahertz meta-atoms." In: *Applied Physics Letters* 108.10 (2016), p. 101101. DOI: 10.1063/1.4943167 (cit. on pp. 66, 67).

[124] K. L. Campman et al. "Interface roughness and alloy-disorder scattering contributions to intersubband transition linewidths." In: *Applied Physics Letters* 69.17 (1996), pp. 2554–2556. DOI: 10.1063/1.117737 (cit. on p. 67).

[125] Takeya Unuma et al. "Effects of interface roughness and phonon scattering on intersubband absorption linewidth in a GaAs quantum well." In: *Applied Physics Letters* 78.22 (2001), pp. 3448–3450. DOI: 10.1063/1.1376154 (cit. on p. 67).

[126] Takeya Unuma et al. "Intersubband absorption linewidth in GaAs quantum wells due to scattering by interface roughness, phonons, alloy disorder, and impurities." In: *Journal of Applied Physics* 93.3 (2003), pp. 1586–1597. DOI: 10.1063/1.1535733 (cit. on p. 67).

[127] S. M. Wang et al. "Growth of analog AlxGa1-xAs/GaAs parabolic quantum wells by molecular beam epitaxy." In: *Applied Physics Letters* 62.1 (1993). _eprint: https://doi.org/10.1063/1.108819, pp. 61–62. DOI: 10.1063/1.108819 (cit. on p. 67).

[128] C. Deimert and Z. R. Wasilewski. "MBE growth of continuously-graded parabolic quantum well arrays in AlGaAs." In: *Journal of Crystal Growth* 514 (2019), pp. 103–108. ISSN: 0022-0248. DOI: https://doi.org/10.1016/j.jcrysgro.2019.02.045 (cit. on p. 67).

[129] C. Deimert. "Growth of graded quantum wells for THz polaritonics." PhD thesis. Waterloo (cit. on pp. 67, 69, 75).

[130] Shun Lien Chuang. *Physics of photonic devices*. Vol. 80. John Wiley & Sons, 2012. ISBN: 1-118-58565-8 (cit. on p. 69).

[131] G. Pegolotti et al. "Quantum model of coupled intersubband plasmons." In: *Phys. Rev. B* 90.3 (July 2014). Publisher: American Physical Society, p. 035305. DOI: 10.1103/PhysRevB.90.035305 (cit. on p. 69).

[132] Yanko Todorov. "Dipolar quantum electrodynamics theory of the three-dimensional electron gas." In: *Phys. Rev. B* 89.7 (Feb. 2014). Publisher: American Physical Society, p. 075115. DOI: 10.1103/PhysRevB.89.075115 (cit. on p. 69).

[133] Yanko Todorov. "Dipolar quantum electrodynamics of the two-dimensional electron gas." In: *Phys. Rev. B* 91.12 (Mar. 2015). Publisher: American Physical Society, p. 125409. DOI: 10.1103/PhysRevB.91.125409 (cit. on p. 69).

[134] Filippo Alpeggiani and Lucio Claudio Andreani. "Semiclassical theory of multisubband plasmons: Nonlocal electrodynamics and radiative effects." In: *PHYSICAL REVIEW B* 90.11 (Sept. 25, 2014). ISSN: 2469-9950. DOI: 10.1103/PhysRevB.90.115311 (cit. on p. 69).

[135] R. Dingle et al. "Electron mobilities in modulation-doped semiconductor heterojunction superlattices." In: *Applied Physics Letters* 33.7 (1978), pp. 665–667. DOI: 10.1063/1.90457 (cit. on p. 77).

[136] E. B. Dupont et al. "Influence of ionized impurities on the linewidth of intersubband transitions in GaAs/GaAlAs quantum wells." In: *Applied Physics Letters* 60.17 (1992), pp. 2121–2122. DOI: 10.1063/1.107082 (cit. on p. 77).

[137] Michael J. Manfra. "Molecular Beam Epitaxy of Ultra-High-Quality AlGaAs/GaAs Heterostructures: Enabling Physics in Low-Dimensional Electronic Systems." In: *Annual Review of Condensed Matter Physics* 5.1 (2014), pp. 347–373. DOI: 10.1146/annurev-conmatphys-031113-133905 (cit. on p. 77).

[138] I. Vurgaftman, J. R. Meyer, and L. R. Ram-Mohan. "Band parameters for III–V compound semiconductors and their alloys." In: *Journal of Applied Physics* 89.11 (2001), pp. 5815–5875. DOI: 10.1063/1.1368156 (cit. on pp. 79, 80).

[139] Z. R. Wasilewski et al. "Composition of AlGaAs." In: *Journal of Applied Physics* 81.4 (1997), pp. 1683–1694. DOI: 10.1063/1.364012 (cit. on pp. 79, 80, 82).

[140] S. J. Pennycook and D. E. Jesson. "High-resolution Z-contrast imaging of crystals." In: *Ultramicroscopy* 37.1 (1991), pp. 14–38. ISSN: 0304-3991. DOI: 10.1016/0304-3991(91)90004-P (cit. on p. 81).

[141] Jean-Michel Manceau et al. "Immunity of intersubband polaritons to inhomogeneous broadening." In: *PHYSICAL REVIEW B* 96.23 (Dec. 1, 2017). ISSN: 2469-9950. DOI: 10.1103/PhysRevB.96.235301 (cit. on p. 83).

[142] S. Zanotto. *PPML - Periodically Patterned Multi Layer*. URL: https://fr.mathworks.com/matlabcentral/fileexchange/55401-ppml-periodically-patterned-multi-layer (cit. on p. 86).

[143] William F. Richards. "Microstrip Antennas." In: *Antenna Handbook: Theory, Applications, and Design*. Ed. by Y. T. Lo and S. W. Lee. Boston, MA: Springer US, 1988, pp. 639–712. ISBN: 978-1-4615-6459-1. DOI: 10.1007/978-1-4615-6459-1_10 (cit. on p. 93).

[144] Constantine A. Balanis. *Advanced Engineering Electromagnetics*. Wiley, 2012. URL: https://books.google.fr/books?id=_q35KChOfVwC (cit. on pp. 93, 95).

[145] Lukas Novotny and Bert Hecht. *Principles of Nano-Optics*. 2nd ed. Cambridge: Cambridge University Press, 2012. ISBN: 978-1-107-00546-4. DOI: 10.1017/CBO9780511794193 (cit. on p. 97).

[146] William L. Barnes, Alain Dereux, and Thomas W. Ebbesen. "Surface plasmon subwavelength optics." In: *Nature* 424.6950 (Aug. 1, 2003), pp. 824–830. ISSN: 1476-4687. DOI: 10.1038/nature01937 (cit. on p. 97).

[147] J. B. Pendry. "Negative Refraction Makes a Perfect Lens." In: *Phys. Rev. Lett.* 85.18 (Oct. 2000). Publisher: American Physical Society, pp. 3966–3969. DOI: 10.1103/PhysRevLett.85.3966 (cit. on p. 98).

[148] Fang Nicholas et al. "Sub-Diffraction-Limited Optical Imaging with a Silver Superlens." In: *Science* 308.5721 (Apr. 22, 2005). Publisher: American Association for the Advancement of Science, pp. 534–537. DOI: 10.1126/science.1108759 (cit. on p. 98).

[149] Schurig D. et al. "Metamaterial Electromagnetic Cloak at Microwave Frequencies." In: *Science* 314.5801 (Nov. 10, 2006). Publisher: American Association for the Advancement of Science, pp. 977–980. DOI: 10.1126/science.1133628 (cit. on p. 98).

[150] A. Benz et al. "Strong coupling in the sub-wavelength limit using metamaterial nanocavities." In: *Nature Communications* 4.1 (Nov. 29, 2013), p. 2882. ISSN: 2041-1723. DOI: 10.1038/ncomms3882 (cit. on p. 98).

[151] D. Palaferri et al. "Patch antenna terahertz photodetectors." In: *Applied Physics Letters* 106.16 (2015), p. 161102. DOI: 10.1063/1.4918983 (cit. on p. 98).

[152] Daniele Palaferri et al. "Ultra-subwavelength resonators for high temperature high performance quantum detectors." In: *New Journal of Physics* 18.11 (Nov. 2016). Publisher: IOP Publishing, p. 113016. DOI: 10.1088/1367-2630/18/11/113016 (cit. on p. 98).

[153] A. Benz et al. "Resonant metamaterial detectors based on THz quantum-cascade structures." In: *Scientific Reports* 4.1 (Mar. 10, 2014), p. 4269. ISSN: 2045-2322. DOI: 10.1038/srep04269 (cit. on p. 98).

[154] Amir Ali Tavallaee et al. "Zero-Index Terahertz Quantum-Cascade Metamaterial Lasers." In: *IEEE Journal of Quantum Electronics* 46.7 (2010), pp. 1091–1098. DOI: 10.1109/JQE.2010.2043642 (cit. on p. 98).

[155] Hou-Tong Chen et al. "A metamaterial solid-state terahertz phase modulator." In: *Nature Photonics* 3.3 (Mar. 1, 2009), pp. 148–151. ISSN: 1749-4893. DOI: 10.1038/nphoton.2009.3 (cit. on p. 98).

[156] Nian-Hai Shen et al. "Broadband blueshift tunable metamaterials and dual-band switches." In: *Phys. Rev. B* 79.16 (Apr. 2009). Publisher: American Physical Society, p. 161102. DOI: 10.1103/PhysRevB.79.161102 (cit. on pp. 98, 108, 109).

[157] Nian-Hai Shen et al. "Optically Implemented Broadband Blueshift Switch in the Terahertz Regime." In: *Phys. Rev. Lett.* 106.3 (Jan. 2011). Publisher: American Physical Society, p. 037403. DOI: 10.1103/PhysRevLett.106.037403 (cit. on pp. 98, 107–109, 115).

[158] Jeremiah P. Turpin et al. "Reconfigurable and Tunable Metamaterials: A Review of the Theory and Applications." In: *International Journal of Antennas and Propagation* 2014 (May 22, 2014). Ed. by Giacomo Oliveri. Publisher: Hindawi Publishing Corporation, p. 429837. ISSN: 1687-5869. DOI: 10.1155/2014/429837 (cit. on p. 98).

[159] Jacob B. Khurgin. "How to deal with the loss in plasmonics and metamaterials." In: *NATURE NANOTECHNOLOGY* 10.1 (Jan. 2015), pp. 2–6. ISSN: 1748-3387. DOI: 10.1038/nnano.2014.310 (cit. on p. 100).

[160] C.R. Paul. *Inductance: Loop and Partial*. IEEE Press. Wiley, 2011. ISBN: 978-1-118-21128-1. URL: https://books.google.fr/books?id=3a7z8TzxaDMC (cit. on p. 103).

[161] Katrin Steinberg, Marc Scheffler, and Martin Dressel. "Microwave inductance of thin metal strips." In: *Journal of Applied Physics* 108.9 (2010), p. 096102. DOI: 10.1063/1.3505706 (cit. on p. 103).

[162] B. Paulillo et al. "Circuit-tunable sub-wavelength THz resonators: hybridizing optical cavities and loop antennas." In: *OPTICS EXPRESS* 22.18 (Sept. 8, 2014), pp. 21302–21312. ISSN: 1094-4087. DOI: 10.1364/OE.22.021302 (cit. on p. 104).

[163] Bruno Paulillo. "Circuit-tunable subwavelength terahertz devices." PhD thesis. 2016. URL: http://www.theses.fr/2016SACLS130/document (cit. on pp. 104, 107, 122).

[164] Sungjoon Lim, C. Caloz, and T. Itoh. "Metamaterial-based electronically controlled transmission-line structure as a novel leaky-wave antenna with tunable radiation angle and beamwidth." In: *IEEE Transactions on Microwave Theory and Techniques* 52.12 (2004), pp. 2678–2690. DOI: 10.1109/TMTT.2004.838302 (cit. on p. 107).

[165] Ilya V. Shadrivov, Steven K. Morrison, and Yuri S. Kivshar. "Tunable split-ring resonators for nonlinear negative-index metamaterials." In: *Opt. Express* 14.20 (Oct. 2006). Publisher: OSA, pp. 9344–9349. DOI: 10.1364/OE.14.009344 (cit. on p. 107).

[166] Aloyse Degiron, Jack J. Mock, and David R. Smith. "Modulating and tuning the response of metamaterials at the unit cell level." In: *Opt. Express* 15.3 (Feb. 2007). Publisher: OSA, pp. 1115–1127. DOI: 10.1364/OE.15.001115 (cit. on p. 107).

[167] Hou-Tong Chen et al. "Active terahertz metamaterial devices." In: *Nature* 444.7119 (Nov. 1, 2006), pp. 597–600. ISSN: 1476-4687. DOI: 10.1038/nature05343 (cit. on p. 107).

[168] W. J. Padilla et al. "Dynamical Electric and Magnetic Metamaterial Response at Terahertz Frequencies." In: *Phys. Rev. Lett.* 96.10 (Mar. 2006). Publisher: American Physical Society, p. 107401. DOI: 10.1103/PhysRevLett.96.107401 (cit. on pp. 107, 108).

[169] Hou-Tong Chen et al. "Experimental demonstration of frequency-agile terahertz metamaterials." In: *Nature Photonics* 2.5 (May 1, 2008), pp. 295–298. ISSN: 1749-4893. DOI: 10.1038/nphoton.2008.52 (cit. on p. 107).

[170] Laurent Boulley. "Développement de dispositifs à base de dioxyde de vanadium VO$_{2}$ et de méta-surfaces dans le moyen infrarouge : applications passives et intégration sur des lasers à cascade quantique." PhD thesis. 2019. URL: http://www.theses.fr/2019SACLS150/document (cit. on p. 107).

[171] Ho-Seok Ee and Ritesh Agarwal. "Tunable Metasurface and Flat Optical Zoom Lens on a Stretchable Substrate." In: *Nano Letters* 16.4 (Apr. 13, 2016). Publisher: American Chemical Society, pp. 2818–2823. ISSN: 1530-6984. DOI: 10.1021/acs.nanolett.6b00618 (cit. on p. 107).

[172] Zheyi Han et al. "MEMS-actuated metasurface Alvarez lens." In: *Microsystems & Nanoengineering* 6.1 (Oct. 5, 2020), p. 79. ISSN: 2055-7434. DOI: 10.1038/s41378-020-00190-6 (cit. on p. 107).

[173] Hou-Tong Chen et al. "Ultrafast optical switching of terahertz metamaterials fabricated on ErAs/GaAs nanoisland superlattices." In: *Optics Letters* 32.12 (June 15, 2007). Publisher: OSA, pp. 1620–1622. DOI: 10.1364/OL.32.001620 (cit. on p. 107).

[174] Yuze Hu et al. "Bi2Se3-Functionalized Metasurfaces for Ultrafast All-Optical Switching and Efficient Modulation of Terahertz Waves." In: *ACS Photonics* 8.3 (Mar. 17, 2021). Publisher: American Chemical Society, pp. 771–780. DOI: 10.1021/acsphotonics.0c01194 (cit. on p. 107).

[175] Anastasios Koulouklidis. "Broadband intense THz fields from laser plasma interactions." PhD thesis. Dec. 13, 2016. URL: http://dx.doi.org/10.12681/eadd/39960 (cit. on p. 112).

[176] J. A. Fülöp et al. "Efficient generation of THz pulses with 0.4 mJ energy." In: *Optics Express* 22.17 (Aug. 25, 2014). Publisher: OSA, pp. 20155–20163. DOI: 10.1364/OE.22.020155 (cit. on p. 112).

[177] C. Vicario et al. "Generation of 0.9-mJ THz pulses in DSTMS pumped by a Cr:Mg2SiO4 laser." In: *Optics Letters* 39.23 (Dec. 1, 2014). Publisher: OSA, pp. 6632–6635. DOI: 10.1364/OL.39.006632 (cit. on p. 112).

[178] K. Y. Kim et al. "Coherent control of terahertz supercontinuum generation in ultrafast laser–gas interactions." In: *Nature Photonics* 2.10 (Oct. 1, 2008), pp. 605–609. ISSN: 1749-4893. DOI: 10.1038/nphoton.2008.153 (cit. on p. 112).

[179] D. Kuk et al. "Generation of scalable terahertz radiation from cylindrically focused two-color laser pulses in air." In: *Applied Physics Letters* 108.12 (Mar. 21, 2016). Publisher: American Institute of Physics, p. 121106. ISSN: 0003-6951. DOI: 10.1063/1.4944843 (cit. on p. 112).

[180] I-Chen Ho, Xiaoyu Guo, and X.-C. Zhang. "Design and performance of reflective terahertz air-biased-coherent-detection for time-domain spectroscopy." In: *Optics Express* 18.3 (Feb. 1, 2010). Publisher: OSA, pp. 2872–2883. DOI: 10.1364/OE.18.002872 (cit. on p. 113).

[181] Dmitry S. Polyakov and Evgeny B. Yakovlev. "Influence of Burstein–Moss effect on photoexcitation and heating of silicon by short and ultrashort laser pulses at wavelength 1.06 $$\upmu \mathrm{m}$$." In: *Applied Physics A* 124.12 (Nov. 8, 2018), p. 803. ISSN: 1432-0630. DOI: 10.1007/s00339-018-2225-x (cit. on p. 116).

[182] B. R. Bennett, R. A. Soref, and J. A. Del Alamo. "Carrier-induced change in refractive index of InP, GaAs and InGaAsP." In: *IEEE Journal of Quantum Electronics* 26.1 (Jan. 1990), pp. 113–122. ISSN: 1558-1713. DOI: 10.1109/3.44924 (cit. on p. 116).

[183] Brian G. Alberding, W. Robert Thurber, and Edwin J. Heilweil. "Direct comparison of time-resolved terahertz spectroscopy and Hall Van der Pauw methods for measurement of carrier conductivity and mobility in bulk semiconductors." In: *J. Opt. Soc. Am. B* 34.7 (July 2017). Publisher: OSA, pp. 1392–1406. DOI: 10.1364/JOSAB.34.001392 (cit. on p. 117).

[184] M Tani et al. "Emission characteristics of photoconductive antennas based on low-temperature-grown GaAs and semi-insulating GaAs." In: *APPLIED OPTICS* 36.30 (Oct. 20, 1997), pp. 7853–7859. ISSN: 0003-6935. DOI: 10.1364/AO.36.007853 (cit. on p. 117).

[185] U. Siegner et al. "Ultrafast high-intensity nonlinear absorption dynamics in low-temperature grown gallium arsenide." In: *Applied Physics Letters* 69.17 (1996), pp. 2566–2568. DOI: 10.1063/1.117701 (cit. on p. 117).

[186] J. K. Luo et al. "Transport properties of GaAs layers grown by molecular beam epitaxy at low temperature and the effects of annealing." In: *Journal of Applied Physics* 79.7 (1996), pp. 3622–3629. DOI: 10.1063/1.361417 (cit. on p. 118).

[187] S. Gupta et al. "Subpicosecond carrier lifetime in GaAs grown by molecular beam epitaxy at low temperatures." In: *Applied Physics Letters* 59.25 (Dec. 16, 1991). Publisher: American Institute of Physics, pp. 3276–3278. ISSN: 0003-6951. DOI: 10.1063/1.105729 (cit. on pp. 118, 120).

[188] Matthew C. Beard, Gordon M. Turner, and Charles A. Schmuttenmaer. "Subpicosecond carrier dynamics in low-temperature grown GaAs as measured by time-resolved terahertz spectroscopy." In: *Journal of Applied Physics* 90.12 (2001), pp. 5915–5923. DOI: 10.1063/1.1416140 (cit. on p. 121).

[189] A. Yariv and P. Yeh. *Photonics: Optical Electronics in Modern Communications*. Oxford series in electrical and computer engineering. Oxford University Press, 2007. ISBN: 978-0-19-517946-0. URL: https://books.google.fr/books?id=B2xwQgAACAAJ (cit. on p. 123).

[190] C.H. Tsau, S.M. Spearing, and M.A. Schmidt. "Characterization of wafer-level thermocompression bonds." In: *Journal of Microelectromechanical Systems* 13.6 (2004), pp. 963–971. DOI: 10.1109/JMEMS.2004.838393 (cit. on p. 124).

[191] Abul K. Azad et al. "Carrier dynamics in InGaAs with embedded ErAs nanoislands." In: *Applied Physics Letters* 93.12 (2008), p. 121108. DOI: 10.1063/1.2989127 (cit. on p. 127).

[192] D. C. Driscoll et al. "Ultrafast photoresponse at 1.55 µm in InGaAs with embedded semimetallic ErAs nanoparticles." In: *Applied Physics Letters* 86.5 (2005), p. 051908. DOI: 10.1063/1.1852092 (cit. on p. 127).

[193] Matthias C. Hoffmann et al. “Impact ionization in InSb probed by terahertz pump—terahertz probe spectroscopy.” In: *Phys. Rev. B* 79.16 (Apr. 2009). Publisher: American Physical Society, p. 161201. DOI: 10.1103/PhysRevB.79.161201 (cit. on p. 127).